

# Numerical Analysis and Design of Antenna Systems for Micro/Nano Satellites

THÈSE N° 5680 (2013)

PRÉSENTÉE LE 22 MARS 2013

À LA FACULTÉ DES SCIENCES ET TECHNIQUES DE L'INGÉNIEUR  
LABORATOIRE D'ÉLECTROMAGNÉTISME ET ACOUSTIQUE  
PROGRAMME DOCTORAL EN GÉNIE ÉLECTRIQUE

ÉCOLE POLYTECHNIQUE FÉDÉRALE DE LAUSANNE

POUR L'OBTENTION DU GRADE DE DOCTEUR ÈS SCIENCES

PAR

**Gabriele ROSATI**

acceptée sur proposition du jury:

Dr S.-R. Cherkaoui, président du jury  
Prof. J. R. Mosig, directeur de thèse  
Prof. A. Freni, rapporteur  
Prof. F. Rachidi-Haeri, rapporteur  
Dr I. Stevanovic, rapporteur



ÉCOLE POLYTECHNIQUE  
FÉDÉRALE DE LAUSANNE

Suisse  
2013



[...] vincer potero dentro a me l'ardore  
ch'i' ebbi a divenir del mondo esperto  
e de li vizi umani e del valore;

ma misi me per l'alto mare aperto

*Dante, Commedia, Inferno, Canto XXVI*



# Abstract

Recent space research and activities have been characterized by a growing emphasis on the development of small spacecrafts. Since the year 2000, more than 30 micro/nano satellites were built and launched. Today, constellations of micro-satellites are an efficient alternative to traditional platforms for short missions involving security and survey, imaging and data acquisition or telecommunications. Typical functionalities like TT&C or inter-satellite cross-link require multi-functional antenna systems for the concurrent generation of different antenna modes; the extremely stringent accommodation requirements pose a significant challenge as the integration of the antenna with the spacecraft can critically affect the radiation performance, especially when the size of the satellite platform becomes comparable with the wavelength.

The lack of established methodologies for the design of antenna systems for small satellites, providing specific radiation patterns, inspired the research performed in this thesis work.

In the frame of the ESA project MAST, requiring the design of a typical antenna system for small platform, we developed a specific design strategy, based on the use of platform-independent antennas, which led to the implementation of the simulation software SatAF. Targeting the accurate predictions of the radiation performance of large arrays of identical elements, together with a competitive computational time, the simple 3D Array Theory was integrated in SatAF with original implementations of the Method of Moments.

In view of dedicated applications to slot antennas, a novel, simplified slot excitation model was developed, allowing the realistic representation of the physical feeding mechanism without the necessity of including the feeding structure in the simulation model.

The “Magic Distance Inspired” method, an original formulation of the Nyström method for the numerical approximation of Integral Equations, allowed the replacement of the time-demanding computation of the four fold integrals, necessary in canonical MoM algorithms, with point-to-point computations performed according to special point grids. Together with a significative reduction of computational time, the formulation offers a number of advantages, like an efficient computation of the singular, quasi- and non-singular entries of the MoM matrix with a single formulation, and the possibility of extension to complex environment where, for instance, potentials and MPIE encounter difficulties.

The development of SatAF-MDI as alternative to brute force full-wave software constitutes the original contribution of this thesis.

**Keywords:** Micro-satellites, Slot antennas, Computational electromagnetics, Method of Moments, EFIE, MPIE, Nyström method.



# Sintesi

La recente attività di ricerca in ambito spaziale è stata caratterizzata da una crescente enfasi posta sullo sviluppo di micro-/nano-satelliti, con un totale di più di 30 missioni effettuate dall'inizio del secolo. Costellazioni di microsattelliti rappresentano oggi una valida soluzione in missioni di sicurezza, sorveglianza, acquisizione di dati o telecomunicazioni.

Funzionalità quali TT&C o cross-link inter-satellitare richiedono sistemi multi-funzionali di antenne per la generazione simultanea dei diversi modi di radiazione; gli stringenti requisiti di alloggiamento costituiscono inoltre una vera e propria sfida in quanto l'integrazione dell'antenna con la navicella può compromettere severamente la radiazione.

L'attività di ricerca compiuta in questa tesi è stata ispirata dalla mancanza di ben affermate metodologie di design di sistemi di antenne per micro-satelliti.

Nell'ambito del progetto ESA "MAST", che richiedeva il progetto di un sistema di antenne per micro-satelliti, abbiamo sviluppato una strategia basata sull'uso di antenne indipendenti dalle caratteristiche della struttura circostante, che ha condotto all'implementazione del software di simulazione SatAF. Mirando ad un'accurata previsione delle caratteristiche di radiazione di array costituiti da un elevato numero di elementi identici fra loro, oltre che a un competitivo tempo di calcolo, i semplici elementi di Teoria degli Array tridimensionale sono stati integrati in SatAF insieme con un'originale implementazione del Metodo dei Momenti. Nella prospettiva di un'applicazione orientata in particolare ad antenne ad apertura, è stato sviluppato un innovativo e semplificato modello per l'eccitazione della slot, che permette una realistica rappresentazione del fenomeno fisico di accoppiamento senza la necessità di includere nel modello di simulazione la struttura di alimentazione.

Il metodo "Magic Distance Inspired", una originale formulazione del metodo di Nyström per la soluzione di Equazioni Integrali ha permesso di sostituire il calcolo degli integrali in quattro dimensioni, necessari per gli algoritmi canonici del MoM, con calcoli punto-punto effettuati sulla base di speciali griglie. Insieme a una significativa riduzione del tempo di calcolo, la formulazione offre una serie di vantaggi quali un efficiente calcolo dei termini, singolari, e non, del MoM con un'unica formulazione valida in ambienti complessi dove, ad esempio, i potenziali e la formulazione MPIE entrano in crisi.

Lo sviluppo di SatAF-MDI come alternativa ai software full-wave costituisce il contributo originale di questa tesi.

**Parole chiave:** Micro-satelliti, antenna ad apertura, metodi numerici per l'elettromagnetismo, Metodo dei Momenti, EFIE, MPIE, metodo di Nyström .





# Acknowledgements

First and foremost, to my thesis advisor Prof. Juan R. Mosig for his trust, inspiration and invaluable support during these years. His true passion for electromagnetism was a great motivation for this work and scientific discussions we shared were a unique experience. Thank you Juan.

My appreciation goes to the committee members Prof. Angelo Freni, from University of Florence, Prof. Farhad Rachidi from EPFL and Dr. Ivica Stevanovic from ABB Schweiz for having accepted to examine this work and for all their useful remarks which contributed to improve the value of this thesis; I would also like to thank Prof. Rachid Cherkaoui for chairing this Jury. My gratitude to Angelo, thank you for introducing me to electromagnetism and guiding my studies during and after the university.

Thanks to all the permanent members of LEMA: Prof. Anja Skrivervik for her support and professional advice, Michael der Zauberlehrling, l'enfant terrible, Hervé, Julien, J.-F. Zürcher for his availability and professionalism during the measurements of the satellite antenna system, David, our and in particular to Eulalia for running flawlessly the most delicate matters.

Huge thanks to the LEMA guys. To Marco, my office mate and the best bike trainer, with whom rooftops became bike trips: grazie Campione. To the Docs: Eden, for all our philosophic conversations, you better than anyone else deserve the "Ph" in your title, Roberto; always and forever there to lend a hand; Benji, le foie gras in Toulouse will never be enough for us, Thanos, Francesco, Sergio, all the Acoustic group with whom I wish I had spent more time together. To the Docs wannabes: Ioannis, always waiting for you down the slopes but the most contagious laugh ever, Rafal my first ski teacher, David, Apo, Marc, Jovanche, Nuno, Eduardo, Anton, Michele, Baptiste, my past and present office mates Mohsen and Nuno: guys you really made this four years a great and unforgettable experience. Special mention for the beautiful LEMA girls: Madda, Laleh, Ruzica, Gabriela and most recently Elena and Maria for cheering up the atmosphere here at LEMA.

Thanks to the JAST team, Stefano Vaccaro, Ferdinando Tiezzi, José Padilla, Frédéric Bongard and Carolina Viganò for the very nice collaboration during the project MAST and the MILAS, MASSA, MAST-X proposals we prepared together.

Finally, the most grateful thanks to my family, who raised and guided me: without your support I would never have made it here. Thanks to my uncle and aunt, to my cousins Letizia and Cristiano. To all of them is dedicated this thesis.



# Contents

<b>1. Introduction</b>	<b>1</b>
1.1. General context . . . . .	1
1.2. State of the Art: existing and up-coming small satellite missions . . . . .	1
1.3. Miniaturized antennas for micro/nano satellites . . . . .	6
1.4. A typical example: the ESA project MAST . . . . .	7
1.5. Outline and motivation of the thesis: original contributions . . . . .	9
<b>2. A possible design approach for antennas on small satellites: the SatAF software</b>	<b>13</b>
2.1. The design strategy . . . . .	13
2.1.1. Platform size effect . . . . .	14
2.1.2. Sensitivity of induced platform surface currents . . . . .	16
2.1.3. Interference effects when combining omnidirectional patterns . . . . .	16
2.2. Final design guidelines . . . . .	18
2.3. The Satellite Array Factor (SatAF) software . . . . .	20
2.3.1. Description of the software . . . . .	21
2.3.2. Analytical formulation . . . . .	24
2.3.3. Validation . . . . .	26
2.4. A typical SatAF application: the design of the ESA-MAST antenna system . . . . .	33
2.4.1. Satellite architectures and arrays . . . . .	33
2.4.2. Practical possible choices for the radiating element . . . . .	38
2.4.3. Patch antennas designs . . . . .	40
2.4.4. Slot antennas designs . . . . .	43
2.4.5. The final antenna system and the measurement campaign . . . . .	50
2.5. MAST measurements compared with SatAF . . . . .	52
2.6. SatAF final assessment and potential improvements . . . . .	54
2.7. Conclusions . . . . .	62
<b>3. Integral Equations and Method of Moments</b>	<b>67</b>
3.1. Electromagnetics fundamentals . . . . .	67
3.1.1. Maxwell equations . . . . .	67
3.1.2. Potentials formulation . . . . .	69
3.1.3. Green's Functions . . . . .	71
3.1.4. The electrostatics problem . . . . .	74

3.2. Integral Equations . . . . .	75
3.2.1. SIE for conducting bodies in free space . . . . .	76
3.2.2. The Electric Field Integral Equation (EFIE) . . . . .	77
3.2.3. The Magnetic Field Integral Equation (MFIE) . . . . .	78
3.2.4. The Mixed Potential Integral Equation (MPIE) . . . . .	79
3.2.5. The Electrostatic Potential Integral Equation (EPIE) . . . . .	80
3.2.6. Open surfaces and slots . . . . .	81
3.3. The Method of Moments . . . . .	82
3.3.1. Basis functions . . . . .	83
3.3.2. The test function . . . . .	85
3.3.3. Galerkin-MoM formulation of IEs . . . . .	90
3.4. Implementation of MoM . . . . .	91
3.5. Comparison of the different IE formulations . . . . .	93
3.6. Conclusions . . . . .	94
<b>4. Towards an improved version of SatAF</b>	<b>97</b>
4.1. Introduction . . . . .	97
4.2. Dealing with slots: the excitation problem . . . . .	98
4.2.1. Validation . . . . .	100
4.3. Combination with Array Theory . . . . .	105
4.4. Conclusions . . . . .	110
<b>5. The Magic Distance Inspired method</b>	<b>113</b>
5.1. Introduction . . . . .	113
5.2. On mesh and discretization . . . . .	115
5.3. General formulation . . . . .	116
5.3.1. The self term . . . . .	119
5.3.2. The weights . . . . .	123
5.3.3. Asymptotic condition . . . . .	123
5.3.4. Phase Correction . . . . .	124
5.4. The electrostatic case: the EPIE . . . . .	129
5.4.1. Configurations for the electrostatic problem . . . . .	130
5.5. Infinite Ground Plane . . . . .	137
5.5.1. Application to rectangular cells . . . . .	138
5.5.2. Resume . . . . .	139
5.6. The full-wave problem: the EFIE . . . . .	140
5.6.1. The benchmark model . . . . .	141
5.6.2. Full-wave implementation of the MDI method . . . . .	142
5.6.3. Electrostatics configurations . . . . .	143
5.6.4. Single-source configurations . . . . .	146
5.6.5. Multi-source configurations . . . . .	155
5.6.6. The impact of phase correction . . . . .	155

---

5.6.7. Application to small cells . . . . .	160
5.7. Summary of the full-wave benchmarks . . . . .	162
5.8. Conclusions . . . . .	162
<b>6. Improved SatAF-MDI results</b>	<b>165</b>
6.1. Final comparison of accelerated formulations of the MoM . . . . .	165
6.2. The MDI method applied to MAST . . . . .	169
<b>7. Conclusions and Perspectives</b>	<b>175</b>
7.1. Thesis assessment . . . . .	176
7.2. Perspectives . . . . .	178
<b>Appendices</b>	
<b>Appendix A. MAST antenna system technical details</b>	<b>181</b>
A.1. Slot antennas designs . . . . .	181
A.2. Array design . . . . .	187
A.3. Directive and TT&C modes . . . . .	189
A.4. The Proof-Of-Concept . . . . .	190
A.5. Measurement setup . . . . .	191
A.6. Measurements . . . . .	194
A.6.1. Mode A . . . . .	194
A.6.2. Mode B . . . . .	196
A.6.3. Mode C . . . . .	197
A.7. Final assessment . . . . .	198
<b>Appendix B. SatAF source code</b>	<b>201</b>
<b>Bibliography</b>	<b>211</b>
<b>Curriculum Vitae</b>	<b>221</b>
<b>List of Publications</b>	<b>225</b>



# 1. Introduction

## 1.1. General context

Like in many other technological fields, the trend in satellites is towards miniaturization. The words micro-satellites (less than 100 Kg), nano-satellites (less than 10 Kg) and even pico-satellites (around 1 Kg) are frequently encountered in the literature, while Cubesats ( $10 \times 10 \times 10$  cm) have become a standard for university research groups.

Recent industrial space research and activities have been characterized by a growing emphasis on the development of micro- and nano-satellites: with strongly reduced mass, size, cost and time-line, clusters of these platforms are a very promising alternative to classic, larger spacecraft in short space mission involving security and survey, data acquisition and transmission, etc. In typical scenarios, a constellation of micro-satellites can cover different functions including Telemetry, Tracking and Command (TT&C), Global Positioning System (GPS), Global Navigation Satellite Systems (GNSS), and inter-satellite cross links [1–3]. From the electromagnetic point of view, it is often required the generation of different radiation patterns, such as multi-beam and omnidirectional patterns or high directive beams. Multi-functional antenna systems [4, 5], allowing the concurrent generation of different radiation modes, are an efficient solution for such requirements.

The different communication functionalities are usually performed in classic spacecraft by distributed antenna systems.

Micro/nano satellites pose the further challenge of extremely stringent accommodation requirements, leading to the need of antenna system miniaturisation and multiple functionality. In fact, micro/nano satellite antennas have very specific design requirements [6, 7]. In some cases, very small size of the platform even makes the whole satellite act as an antenna, impacting on the radiation pattern much more than usually seen on antenna systems in classic satellites.

## 1.2. State of the Art: existing and up-coming small satellite missions

Since the year 2000, more than 30 micro/nano satellites were built and launched [3, 8]; one of the most remarkable events took place in 2008 and included 7 Cubesats on board of the

Indian launch vehicle PSLV. Now, technology maturity and miniaturization allows even small student groups to create their own satellite, while special efforts are directed towards the realization of combinations of two or more Cubesats to allow a larger payload allocation and a better solar power accumulation.

The establishment of a telecommunication uplink and down-link capability is one of the major challenges that most design teams have to face, due to severe restrictions on weight, power and accommodation; for these reasons, UHF and VHF bands are preferred in many applications. This holds in particular for Cubesats, whose antenna systems often operate in the range of AM frequencies, also known as Radio Amateurs band. These frequencies only allow 1200 ~ 9600 Kbit/s down-link and are subject to high levels of noise. S-Band on the other hand requires a lot of power (for Cubesat capabilities) and only a few of such spacecrafts employed S-band antennas. Among them, it is worth mentioning GeneSat, which has used a transmitter Microhard MHX-2400, allowing 2.4 GHz operations [1].

One of the most well-known space missions employing micro-satellites is PROBA, started in 2001 with the launch of a spacecraft of size  $60 \times 60 \times 80$  cm and a weight of 100 Kg. It uses an S-band antenna allowing a 4 Kbit/s uplink and 1 Mbit/s down-link; on the ground, a 2.4 m portable parabolic dish closes the communication loop. A 2.4 m dish antenna [9] is used in the follow-up PROBA-2 [10, 11] which was launched in 2009.

The European Student Earth Orbiter (ESEO) [12] is another small satellite which uses two S-band antenna subsystems to establish a telemetry down-link using 2400.1 MHz band with a data rate of 9.6 Kbit/s. The first one [13] is a set of three directional patch antennas, producing a total of 3 W of circularly polarised radiation with a half-power beam width of approximately 70 degrees. The second radiator is a circularly-polarized compact High-Gain Antenna (HGA), realized by stacking two coaxial Shorted Annular Patches (SAP) [14] where the top one is placed half a wavelength above the lower one. The antenna is illustrated in Fig. 1.1 together with the satellite.

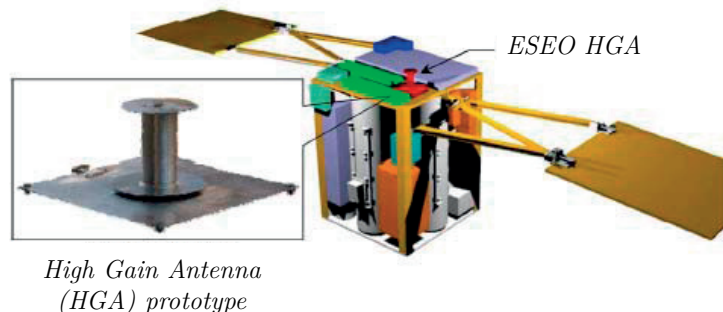


**Figure 1.1.:** ESEO satellite and HGA antenna [12].



The SSETI Express satellite [15] was an educational mission launched in 2005 that deployed Cubesat pico-satellites developed by universities to take pictures of the Earth. The operational down-link speed is 38.4 Kbit/s [16] using the standard AX-25 protocol for communications. Two S-band antennas are allocated onboard the satellite (Fig. 1.2): the patch antenna system "S-band ANT", adapted from the ESEO micro-satellite, a second patch "S-band TX", plus an UHF system providing the uplink of commands from the ground station.

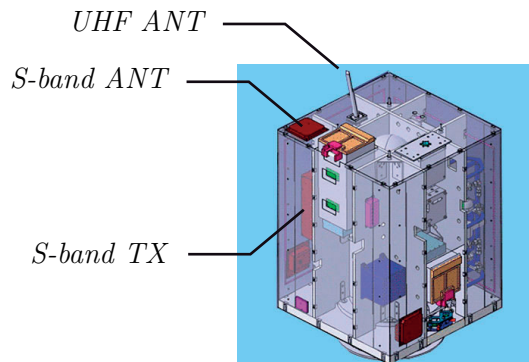


**Figure 1.2.:** UHF and S-band antennas on SSETI EXPRESS [15].

Slightly bigger than PROBA, with a mass of 125 Kg, is the British satellite TopSat [17], launched in 2005. It uses an X-band antenna to down-link the high-resolution images acquired by the spacecraft. The spacecraft is slewed to point the antenna towards the mobile user directly after imaging is completed.

Also using X-band antenna is the ST5 (Space Technology 5) constellation, launched in 2006 and consisting of 3 micro-satellites with a weight of 25 Kg each, within a cylinder shape of 50 cm of diameter by 50 cm of height. These satellites operated flawlessly during the three-months mission. The antenna [18], shown in Fig. 1.3, satisfies the requirements of large beam-width, circular-polarization, and large bandwidth. These satellites fly in geostationary orbit and communicate with 34 m ground-based dish antenna [19].

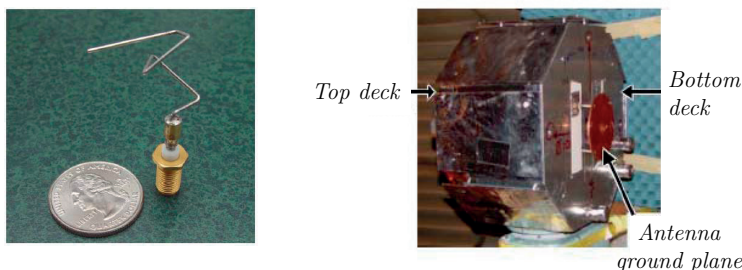


**Figure 1.3.:** X-band antenna on one of the ST5 micro-satellites [18].

AISSat-1 [20] is a 6 Kg Norwegian nano-satellite, constructed on behalf of the government of Norway by UTIAS/SFL, whose primary mission is to investigate the feasibility and performance of a spacecraft-based Automatic Identification System (AIS) sensor in low-Earth orbit as a means of tracking maritime assets, and secondly the integration of the AIS data into a national maritime tracking information system. AISSat-1 is intended as both a research and development platform and a demonstration mission for a larger operational capability. The satellite design is based on the Generic Nano-satellite Bus (GNB), which measures  $200 \times 200 \times 200$  mm in size and mounts a VHF antenna system (see Fig. 1.4).

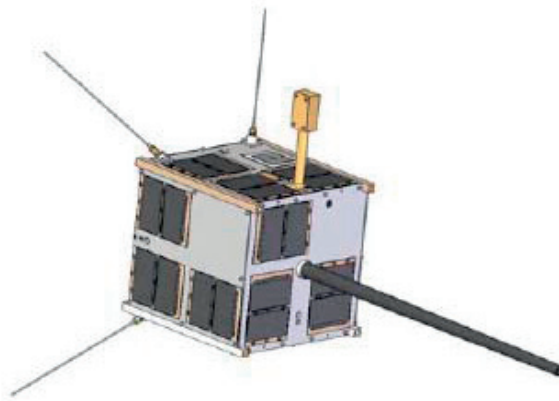


**Figure 1.4.:** The generic Nano-Satellite Bus used for AISSat-1 [20].

Pathfinder2 (Fig. 1.5), developed by LuxSpace, was launched in September 2009. It entered operational service in October the same year and since then provides acquisition of AIS messages on a global scale. With a down-link of 115 Kbit/s and internal memory, it has the capability to collect and download all AIS messages. It is equipped with a 2 channels AIS receiver fed by a monopole antenna, a UHF down-link and a GPS system. The platform has a dimension of  $55 \times 35 \times 7$  cm and is powered by 12 W solar panels.

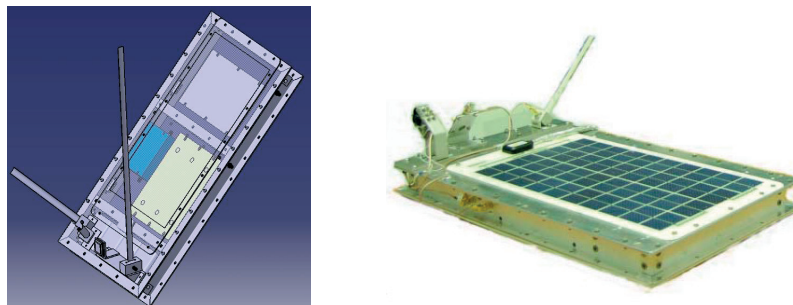


**Figure 1.5.:** The Pathfinder 2.

In 2009, the EPFL Space Center completed a three year project and built its own nano-satellite, the SwissCube [10,21]. The SwissCube passed its Qualification Test and was flown on September, 23. The satellite has been entirely designed and built by the EPFL Space Center in cooperation with many universities and schools of advanced technology in Switzerland. The primary scientific objective of this satellite is to image solar wind induced glow at the Earth's atmospheric boundary; the successful technologies used in SwissCube payload will be used for future orientation sensors on larger satellites.

SwissCube uses two dipole antennas are used to communicate with the ground stations; due to the stowed size requirement of 10 cm, an antenna deployment system is required. Fig. 1.6 shows the spacecraft: the VHF antenna is 610 mm long when in the straight ideal position, while the deployed UHF antenna reaches 176 mm.



**Figure 1.6.:** The SwissCube [21].

The GapFiller program (2011) relies on a very rugged and flexible platform. A view of the satellite model in launch configuration is shown in Fig. 1.7. The platform weight is 27 Kg, with a size of  $30 \times 30 \times 45$  cm fully equipped (excluding protrusions); the payload includes 2 UHF receivers and 2 UHF high speed transmitters (up to 512 Kbit/s), realized with an array of  $2 \times 2$  dipoles, generating a radiation pattern characterized by sharp nulls and a narrow beam width.

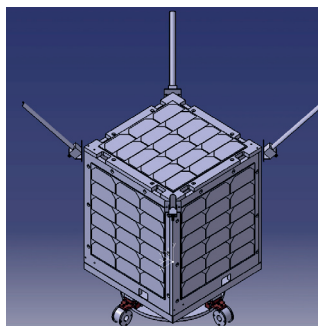


**Figure 1.7.:** The Gapfiller in launch configuration.

The State-of-the-Art research performed and illustrated in this section allowed us to derive useful guidelines for the design of the antenna system, setting the basis for the design of the ESA-MAST antenna system described in Chap. 2 which constitutes one of the main topics of this thesis work.

### 1.3. Miniaturized antennas for micro/nano satellites

According to the State-of-the-Art survey, Tab. 1.1 summarizes the satellites' characteristics the most relevant for this thesis work. From our investigation, it already appears that two

**Table 1.1.:** Resume of the relevant features of the satellites illustrated in the State of the Art.

Mission name and year	Weight	Max satellite linear dimensions	Antenna characteristics: Type, frequency, coverage and size
PROBA 2001	100 Kg	80 cm	S-band
PROBA-2 2009	100 Kg	80 cm	Reflector, S-band, directive, 2.4 m
ESEO 2009	< 100 Kg	100 cm	3 patches, S-band, omni SAP, S-band, directive
SSETI Express 2005	86 Kg	90 cm	Patch, S-band Patch, S-band, directive Monopole, UHF
TopSat 2005	125 Kg		X-band, directive
ST5 2006	3 × 25 Kg	50 cm	Wire, X-band, low-gain
AISSat-1	16 Kg	20 cm	Monopole, VHF
PathFinder2 2009		55 cm	2 × Monopole, UHF/GPS,
GapFiller 2011	27 Kg	45 cm	2 × 2λ Dipoles, UHF
SwissCube 2009	1 Kg	10 cm	Wire, VHF, 61 cm Wire, UHF, omni, 17.6 cm

strategies can be used in the design of antenna systems for micro/nano satellites. Antennas are either deployable and have dimensions comparable to wavelengths, or they are integrated on the satellite surface: in this case, they must be miniaturized (especially in the low VHF and UHF bands) and they usually behave as point sources.

As for the radiation pattern, two situations should be considered. In the first case, antennas can exhibit radiation characteristics rather independent of the satellite platform: this can be obtained by a proper design or when the electrical dimensions of the platform are very small. On the opposite situation, the antennas' radiation can be critically affected by the

platform and strongly dependent on it. This usually happens with low directivity antennas on spacecrafts of size comparable to the wavelength. In this case, the design of the antenna cannot be made without including in the simulation model the platform, which becomes de facto a part of the antenna.

An intermediate situation can occur with mildly directive antennas, which couple only weakly with the platform and can be modeled using essentially a good estimation of their embedded pattern and classical array theory.

## 1.4. A typical example: the ESA project MAST

The European Space Agency awarded the project MAST (Miniaturized multi-functional Antenna System for micro/nano satellites) to LEMA-EPFL in 2009. It constitutes the paradigm of small satellite missions and set the frame for the antenna engineering challenges faced in this thesis.

An overview of the project, based on the parent documents [22–26], follows hereafter.

The objective of MAST is to study and demonstrate a proof-of-concept miniaturised antenna system suitable for Telemetry, Tracking and Command (TT&C) and data transmission, fitting the extremely tight accommodation requirements of micro/nano-satellites.

Antenna modeling capabilities required also to be developed, eventually on the bases of existing and proven tools used for 'classical' distributed antenna systems, where necessary to achieve the essential design capability.

In fact, one of the MAST goals was to develop a simple but accurate enough model to characterize the radiation of antennas located on small platforms. Opposite to standard full-wave algorithms (as existing in most commercial software tools), MAST called for a software able to decide quickly on the feasibility of a given radiation pattern once the antenna platform and the number and type of antenna elements were known.

Typical requirements for the antenna, as provided by ESA, were:

### Accommodation requirements

- Platform size: micro-nano satellite platform with dimensions variable between a cube of 25 cm side and a box of  $60 \times 60 \times 10$  cm.
- Mass: the antenna system shall have a mass lower than 200 g (goal 100 g).
- The antenna system shall be integrated with other sub-systems, i.e. sharing the same area on the platform, including eventually solar panels.
- Minimum space occupation is required, e.g. antennas could be simple slots in the spacecraft walls.

### Antenna system functional requirements

S-band was targeted as a good compromise corresponding to current developments. This makes platform dimension comparable to wavelength (usually between 0.5 and 2.0 free space wavelengths). The 3 following radiation patterns were of relevance for the functionalities required in this type of satellites:

- Mode A: Full-sphere coverage in single or double polarisation.
- Mode B: Directional coverage in single polarisation (60 deg cone).
- Mode C: RF-tracking coverage (4 tracking lobes within a 60 deg cone).

Circular polarization is required for all modes, either single or double (any of the R- or L-HCP).

Minimum gain level and ripple are set for the three modes as:

- Mode A: Gain  $-3$  dBi, ripple 6 dB.
- Mode B: Gain 5 dBi, ripple 3 dB.
- Mode C: Gain 3 dBi, ripple 1 dB.

Although, of course, specifications can be also added in other aspects, like matching/return loss or frequency bandwidth, the main goal of the ESA activity was to characterize the antenna system in terms of the radiation performances including radiation patterns, Axial Ratio in circular polarization, discrimination between Right- and Left-Hand Circular Polarization, Gain ripple versus angle and maximum Gain variation versus frequency.

Accordingly, antenna performances will be usually expressed in this work in terms of radiation pattern; also, where not differently specified, all the radiation patterns appearing in this thesis work are Directivity patterns expressed in [dBi].

Special attention was finally paid to the concept of "Global Coverage", which, referring to the omnidirectional antenna mode (Mode A), indicates the portion of the ideal radiation sphere where requirements are satisfied. The Global Coverage being a non-standard parameter, we provide here its definition.

Indicating with  $G_{CP}$  the Polarization Gain\* and with  $G_0 = \max\{G\}$  the maximum (total) Gain, we define the function:

$$f(\theta, \varphi) = \begin{cases} 1 & 10 \log_{10} \left( \frac{G_{CP}(\theta, \varphi)}{G_0} \right) \in [-6, 0] \\ 0 & \text{otherwise} \end{cases} \quad (1.1)$$

---

\* $G_{CP}(\theta, \phi) = 4\pi |E_{CP}(\theta, \phi)|^2 / \oint_{\Omega} d\Omega |E_{CP}(\theta, \phi)|^2$

and finally the Global Coverage:

$$C = \frac{1}{4\pi} \oint_{\Omega} d\theta d\varphi f(\theta, \varphi) \quad (1.2)$$

Note that a normalization of  $f$  with respect to the maximum *polarization* Gain would have been misleading.

The Global Coverage quantifies the degree of fulfillment of the specifications allowing a comparison between different solutions.

An appropriate design strategy was developed aiming specifically at these goals and led to the implementation of SatAF, a very efficient algorithm that was delivered to ESA as a MATLAB software and that constitutes one of the original contributions of this thesis.

## 1.5. Outline and motivation of the thesis: original contributions

The leading thread of this thesis work is the development and improvement of the simulation software SatAF (Satellite Array Factor), designed for the fast computation of the radiation pattern generated by antenna systems allocated on small spacecrafts.

The first version of the software was developed in the frame of the ESA project MAST (Chap. 2). The adopted design strategy called strongly for speed and approximation, rather than accurate but computationally demanding full-wave methods.

In its basic formulation, SatAF implements a 3D Array Theory algorithm where sources are represented by simple antennas (e.g. dipoles, patches, slots) radiating in an ideal environment, either free-space (low-frequency approximation, the satellite is electrically small) or on an infinite ground plane (high frequency approximation, very large satellite). With this choice, direct radiation is assumed to be the predominant component of the radiated fields, while diffraction or mutual coupling are considered second-order phenomena and neglected.

The software allows the full characterization of the radiation performance, including the discrimination between polarization and the automatic evaluation of the strongest component as well as the Global Coverage (1.2).

Thanks to its modular approach, SatAF represents a valid tool for the characterization of the radiation pattern. SatAF allowed the design and realization of the multi-functional antenna system for micro-satellites [26], consisting of the customized slot antenna described in [4].

A successful measurement campaign proved the solidity of the design and validated the reliability and usefulness of SatAF. At the same time, the design experience revealed some limitations of the software, in particular the impossibility of handling non-standard radiators or the restriction to moderate or high directive elements in order to verify the hypotheses on

the radiation mechanism.

The clever combination of SatAF with full-wave software was readily identified as a possibility for a two-fold improvement: the extension of the range of applicability to any type of radiator and an increased accuracy in the predictions. The main idea consists in performing *local* full-wave simulations of sub-sets of elements to generate the radiated fields which, once imported in SatAF, allow the computation of the total radiation pattern.

The Surface Integral Equation in its Mixed Potential formulation, solved with the Method of Moments, is known as one of the most efficient algorithms for the analysis of metallic structures in free space and was selected as the full-wave method to be combined with SatAF. Targeting in particular the analysis of slot antenna system, in Chap. 4 we developed [27] a novel model for the excitation of aperture antennas, based on charge accumulation and perfectly compatible with the MoM-MPIE framework. Integrated in the MoM and combined with SatAF, it demonstrated in a series of test configurations the expected improvement of the software.

Even in its combination with the MoM, SatAF proved to be competitive in terms of computational time with the most renown commercial software. Yet, we considered the possibility of a further acceleration of the method, which we achieved with a reformulation of the MoM canonical algorithm. The expensive 4D integration required for the computation of the interaction matrix entries is replaced [28, 29] with a point-to-point computation scheme inspired by the Nyström method: the Magic Distance Inspired method, described in Chap. 5. The formulation allows a strong reduction of calculations with respect to classical quadrature algorithms, e.g. Gauss-Legendre, with a minor impact on the accuracy of the solution (the currents induced on the satellite surface), furthermore mitigated on the far field.

The ultimate version of SatAF, combining the features here introduced, was used in a final validation in Chap. 6 to compute the radiation pattern of the MAST antenna system: a final comparison with measurements demonstrated the solidity of the method.







## 2. A possible design approach for antennas on small satellites: the SatAF software

In this section we describe the work performed in the frame of the ESA project MAST [22–26], which led to the design of a multi-functional antenna system for micro/nano satellites, according to the project requirements introduced in Sec. 1.4. After introducing the possible design strategies (Sec. 2.1) we discuss in Sec. 2.2 the adopted methodology. In Sec. 2.3, we illustrate the in-house MATLAB tool SatAF, developed in the frame of this thesis work, which allowed the design of the antenna system (Par. 2.4.1), prototyped and characterized with a measurement campaign.

A final assessment on the reliability of SatAF (Sec. 2.5) paves the way to the discussion of the possible improvements (Sec. 2.6). Sec. 2.7 summarizes and closes the chapter.

### 2.1. The design strategy

The antenna systems designed for the missions illustrated in the State-of-the-Art (Sec. 1.2) usually consist of an array of elementary radiators, especially patches and dipoles, used to generate the required antenna modes.

On the basis of the literature overview, we decided from the very beginning that the strategy we had followed for the design of the antenna system consisted in using an array of elementary sources, such as patches or slot antennas, which properly displaced on the spacecraft surface and with the right excitation shall produce the required radiation patterns. In fact, while the directive beam (Mode B) and the tracking lobes (Mode C) can be obtained using a simple planar array whose technology is mature and consolidated, the generation of an omnidirectional radiation pattern (Mode A), in circular polarization and in the presence of a small metallic scatterer constituted the real challenge: as no established guidelines were available in the literature, an in-depth study on the feasibility of the possible approaches and their performances was required .

Using omnidirectional elements could appear a simple and obvious way to achieve full-sphere coverage. For extreme satellite sizes, antennas placed on a satellite’s surface can behave almost as in free space (low frequency or very small satellite) or they can see the platform as an infinite ground plane (large satellites, high frequencies). In both cases, it is quite easy to design antennas that show an isotropic 2D or even 3D behavior (close to full coverage). As an example, many antennas designed for W-LAN applications [30–33] can be

included in one of these two categories.

We found in [34–36] an useful insight on the design of antenna arrays allocated on small spacecrafts and on the way the sources orientation and displacement affects the radiation pattern. In these papers, circularly polarized patch antennas operating in S-band are chosen as radiating elements and their position is optimized on a cube satellite of dimension  $50 \times 50 \times 60$  cm. It is interesting to notice how in [36], the radiation performance of three elements placed around a corner of the satellite is significantly enhanced adding a fourth element on the opposite corner (Fig. 2.1).

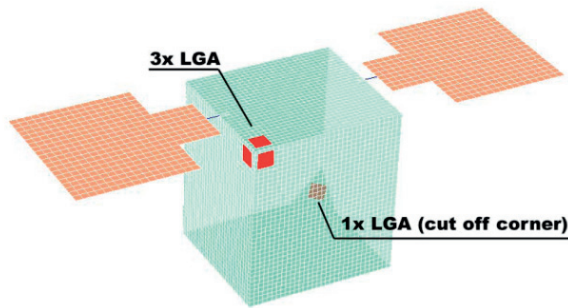


**Figure 2.1.:** Displacement of four antennas on a cubic satellite for optimal omnidirectional coverage.

Following the thread, we performed a feasibility study on the use of elements which present, at least in a stand-alone environment, a low-gain radiation pattern and, more in depth, on the consequences of using surface currents spread on the satellite as primary radiator. A positive output could translate in the possibility of reducing the size of the RF-emitters to the bare minimum. Unfortunately, the platforms considered in this thesis, with dimensions in the order of the wavelength, lie in the midpoint between the two extreme situations mentioned above. Moreover, low directive sources are prone to induce currents in the satellite platform which in turn will produce a secondary or spurious radiation. While it is theoretically possible to use this phenomenon to improve the satellite radiation characteristics, this would lead to very complex and platform-dependent procedures, at the opposite of our strategy aiming at a modular approach, as independent as possible from platform details. Finally, the joint use of several omnidirectional antennas can lead to severe interference problems. These potential drawbacks are illustrated in the following examples.

### 2.1.1. Platform size effect

A simple example of the impact of a metallic platform on radiation is observed when considering a short electric dipole of length  $0.45\lambda$  at a frequency  $f = 2.45$  GHz. When the dipole radiates in free space (Fig. 2.2a), it generates a pattern like Fig. 2.2b (results

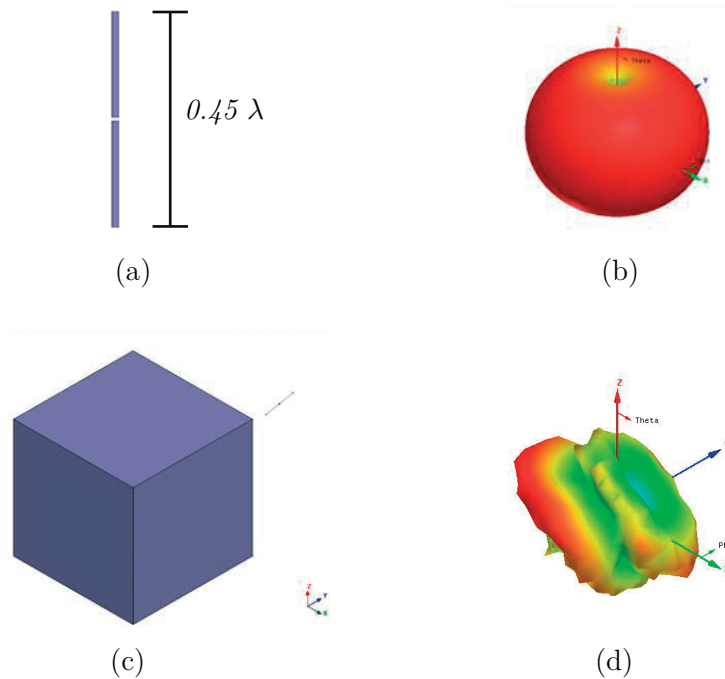


**Figure 2.2.:** Effect of the satellite scattering on a stand-alone low gain source. (a) Dipole in free space and (b) associated radiation pattern; (c) dipole in presence of a 25 cm cubic metallic scatterer and (d) radiation pattern.

generated using Ansoft HFSS). It appears that, already with one simple element, a good degree of coverage is obtained (the concept of coverage was introduced in Sec. 1.4 as an estimation of the performance of the antenna system with respect to Mode A specifications), at least on one plane and around 65% of the full sphere.

Unfortunately, the presence of an electrically large metallic body critically perturbs the radiation, causing a significant degradation of performance. Fig. 2.2d shows the radiation pattern generated by the same dipole in presence of a 25 cm ( $2\lambda$ ) cubic satellite: it is evident that the perturbation is severe (Fig. 2.2d): coverage is reduced below 35% and the maximum radiation occurs opposite to the position of the dipole.

We can also shortly comment the fact that the antenna used for SwissCube, very similar to this example, is working with excellent performance. The difference lies in the operational band, UHF: in fact, at a frequency of 900 MHz, the 10 cm satellite is only a "point" of  $\lambda/30$  size and hence has a negligible influence on the antenna, while in the example the satellite is (at least) a  $2\lambda$  side cube.

A thin rectangular slot on an infinite ground plane is another antenna which exhibits on one cut (its H-plane) an omnidirectional pattern. It is well known anyway that the radiation on the H-plane is severely affected by the size of the ground plane and ceases to be omnidirectional as soon as it becomes of finite size.

### 2.1.2. Sensitivity of induced platform surface currents

Using surface currents induced on the satellite as primary radiator is a very appealing solution and could in fact allow to reduce the size of the RF-emitters to the bare minimum. Such a choice implies that the satellite itself becomes the antenna, excited by a number of sources. Using a structure as an antenna means, on the other hand, fixing its shape and dimensions according to the constraints imposed by the antenna design. This is not an issue in those cases where full control by the antenna designer on the structure which is destined to work as an antenna is assumed. This is obviously not the case if the structure which has to act as an antenna is the entire satellite, due to the obvious necessity of allocating different payloads on the satellite (instruments, telescopes, solar cells) whose disposition follows logics which do not take into account the electromagnetic point of view. It is therefore critical as first action to understand to which extent small perturbations in the satellite structure can affect the radiation pattern.

The previous paragraph already contains an account on the way the current induced on the satellite surface by a source affects the radiation pattern. Moreover, the representation of the satellite with a completely metallic, perfectly smooth surfaces is only an idealization, since on its surfaces are usually allocated solar cells, electronic components or instruments. These elements are not electromagnetic-invisible and currents induced on the platform will be affected by their presence, generating a certain perturbation, in some cases severe, of the radiation pattern. This is shown in the following examples, with two basic cases where currents interact with cuts on the surface or metallic pins. To make the examples meaningful, cuts and pins are intentionally placed in regions where surface currents are strong, as a realistic representation of the phenomenon we want to describe.

A cut on the satellite surface can represent a generic discontinuity or a part of the platform filled with dielectric. Using a thin  $\lambda/2$  slot to excite currents on the satellite, we show in Fig. 2.3 (models solved with HFSS) the effect of the introduction of cuts of in the order of  $0.8\lambda \times \lambda/4$  (a) and (b) and  $\lambda/2 \times \lambda/4$  (c).

As further proof, we show the impact of a small metallic object on the pattern. Two cases are considered and shown in Fig. 2.4: a cylinder of radius  $0.1\lambda$  and height  $0.2\lambda$  (a), and a cuboid of dimensions  $0.6 \times 0.1 \times 0.1$  wavelengths (b). Note that, especially in the cylinder case, the electrical dimensions are quite small; nevertheless, the surface currents are severely affected by their presence.

### 2.1.3. Interference effects when combining omnidirectional patterns

As shown in the previous section, any element in presence of a large metallic scatter becomes more directive. As a consequence, using only two elements on opposite faces produces a poorly omnidirectional pattern: this makes the use of four elements on the side faces not an

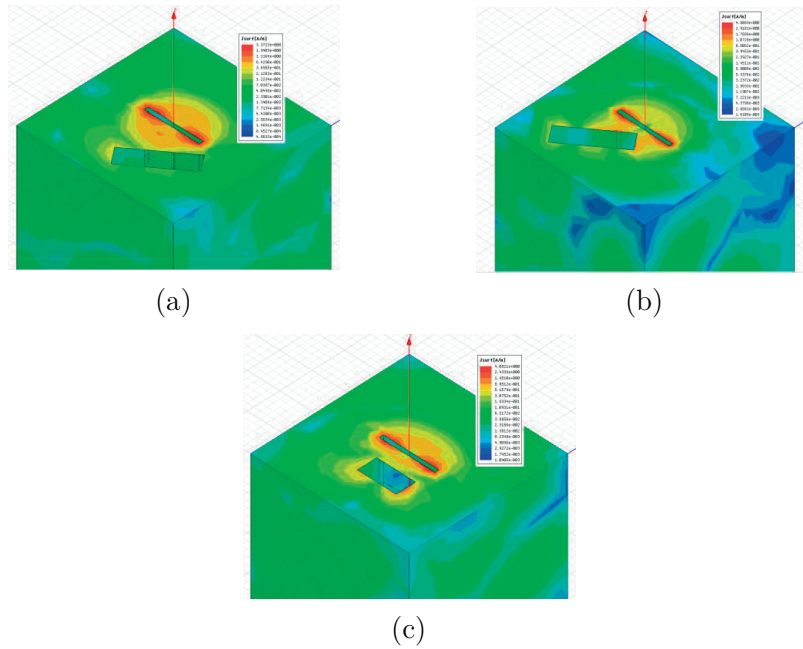


**Figure 2.3.:** Perturbation of currents induced on the satellite surface produced by different cuts.

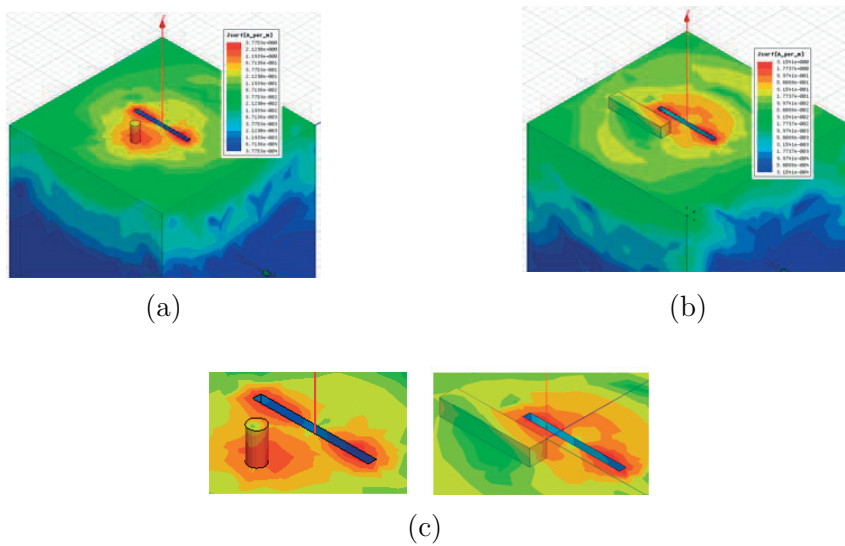


**Figure 2.4.:** Perturbation of the currents induced on the satellite surface produced by metallic objects: (a) a pin, (b) a cuboid and (c) detail.

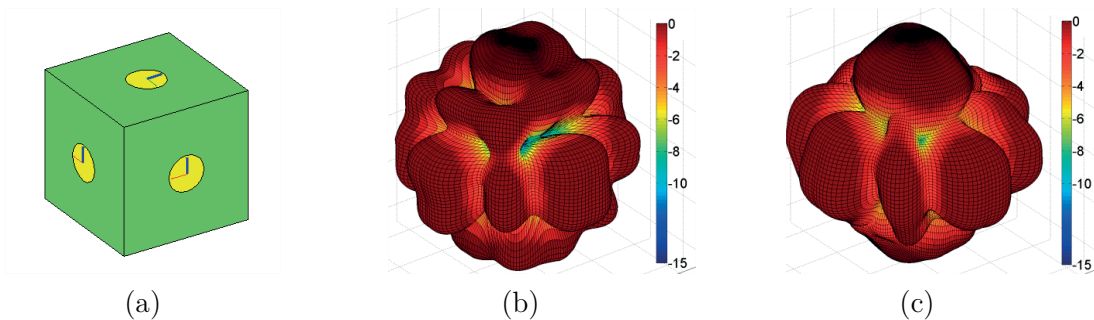


**Figure 2.5.:** The benefit of combining right- and left-hand circular polarization. (a) layout: six patch antennas on a cubic platform, (b) radiation pattern when all antennas are RHCP, (c) radiation pattern when top and bottom elements are LHCP.

optional but an essential expedient to achieve a good performance.

When combining radiation from different sources, the problem of interference arises. It is well-known from planar array theory [37] that, when the element spacing is larger than  $\lambda/2$ , the pattern inevitably presents nulls; the same condition holds, even though with a slightly different formulation, for three-dimensional arrays. To reduce the ripple and the null regions in the pattern is therefore necessary an accurate study on pattern superposition, which depends on element position and orientation. We found that the expedient of taking the strongest between right- and left-hand circular polarization components of the field (Sec. 1.4) significantly improves performances: since a purely RHCP polarized field has no LHCP component, the interference and the presence of radiation nulls is greatly reduced.

Anticipating its description in Sec. 2.3, we use in the following example our in-house MATLAB software SatAF to highlight the interference effect. Six patch antennas are allocated on the faces of a cubic platform (Fig. 2.5a): when all the elements are RHCP, several null regions are present in the radiation pattern (Fig. 2.5b). If the top/bottom elements are LHCP and the strongest component between right- and left-hand polarizations is taken, the pattern assumes the more uniform shape as in Fig. 2.5c.

## 2.2. Final design guidelines

In the previous sections, we have investigated the dependency and stability of the radiation pattern, generated by a low directive element, against modifications in its environment. These modifications are mainly due to modifications of a given platform (non-smoothness of surfaces and presence of metallic objects or holes) and they are responsible for perturbations which can critically affect the radiation pattern.

It appears obvious that a design which is essentially based on the use of low-gain sources to induce surface currents in the platform, transforming the whole satellite into a unique



antenna is unpractical if the platform's parameters and characteristics are not exactly specified. On the other hand, considering the satellite surface as perfectly smooth is an unrealistic assumption which can reveal critical for performance. Even assuming the exact knowledge of the platform characteristics, such a strategy would require the use of powerful full-wave softwares to fully analyze the effect of the platform on the antennas for every position of them. Although this is a possible strategy and has been followed in an ESA companion project [5], it won't be adopted here, as incompatible with the use of simple but very fast quasi-analytical models that we are targeting. Moreover, the tuning elements used to better adapt to platform changes are an expensive and delicate option.

Because of these issues, the use of this class of sources as primary radiators, even if appealing in principle, does not appear as the right way to accomplish the task. Also, the same argumentation leads to the conclusion that it is unreliable to use scattering and diffraction phenomena as secondary radiation sources, for instance for filling those nulls which are direct consequence of using combined discrete elementary radiators.

We can conclude at this point with the strategy which we considered the most suited for the problem and led to the identification of the antenna configuration. This methodology can be summarized with the following statements:

- The design must be based on platform-independent antennas and radiation from the platform has to be minimized.
- Effect of surface currents and diffraction will be considered as a degradation component for the targeted radiation pattern.
- Relatively high Gain antennas are associated with currents concentrated in limited regions of the platform surface and allow to minimize the effect of scattering and spurious radiation. Such antennas should be combined and used for isotropic modes (mode A in the ESA project).
- A subset of Mode A antennas can be a good candidate for the generation of more directive modes (B and C).

This design procedure will likely allow a robust design which can be easily adapted to different platforms and whose performance is expected to have a good degree of stability in case of arbitrary satellite surfaces.

The characteristics and the development of a software performing this task is one original development of this thesis that will be described in the next section.

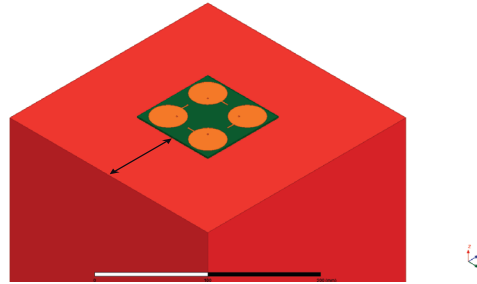


**Figure 2.6.:** A  $2 \times 2$  circular patch array is simulated in 6 different positions between the center and the edge (as indicated by the arrow) of a metallic platform.

### 2.3. The Satellite Array Factor (SatAF) software

Radiation from sources displaced around the satellite body can be thought as the result of three components:

- Direct radiation from sources
- Diffraction of the fields radiated by the sources impinging on the satellite metallic surface
- Mutual coupling between sources

According to the adopted design strategy and on the basis of the discussion of the previous section, the first component is expected to be the most influential contribution to the radiated fields. On the other hand, accounting for the other two contributions requires a precise electromagnetic model and the development of an accurate analysis tool and therefore a considerable amount of computational time and resources to simulate each configuration.

A quantification of the error introduced by this hypothesis in typical MAST scenarios can be obtained anticipating one of the radiating elements proposed for a preliminary design of the antenna system. A directive element, a sub-array of  $2 \times 2$  circular patch antennas on a small cubic platform, is simulated in different positions on a cubic platform (black arrow in Fig. 2.6) with the commercial, full-wave software Ansoft HFSS. The radiation patterns shown in Fig. 2.7 exhibit a very good degree of stability with respect to the change of position, confirming that in the class of problems under investigation, direct radiation can actually be considered predominant on edge diffraction.

We considered therefore of great relevance, at least in the stage of the project involving the the study of optimal disposition of sources around the platform and oriented to the fulfillment of the radiation specifications, to dispose of a simulation tool able to quickly predict the 3D radiated field, even if in the approximation of the sole direct radiation.

The radiating elements will be represented in a first approximation by "ideal" entities lying in a homogeneous environment, for which is available an analytical expression for the representation of radiated fields: examples are patch and aperture antennas on infinite ground planes.

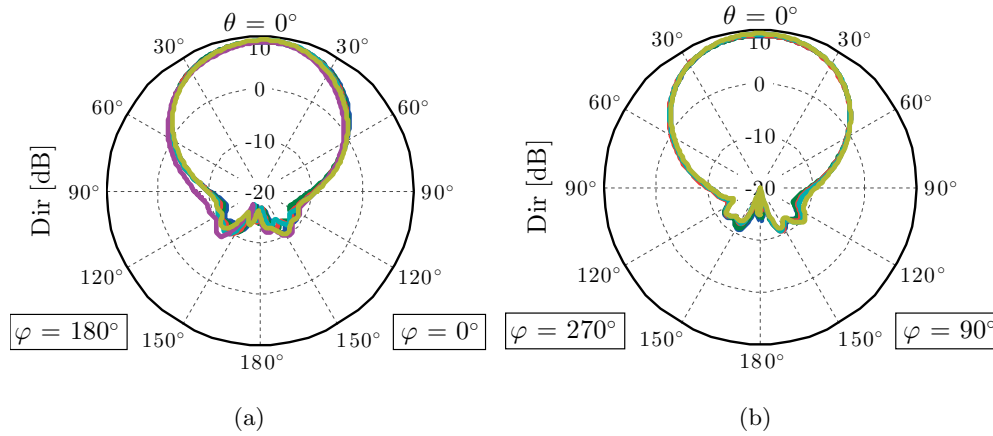


**Figure 2.7.:** Radiation patterns generated by the 6 configurations described in Fig. 2.6

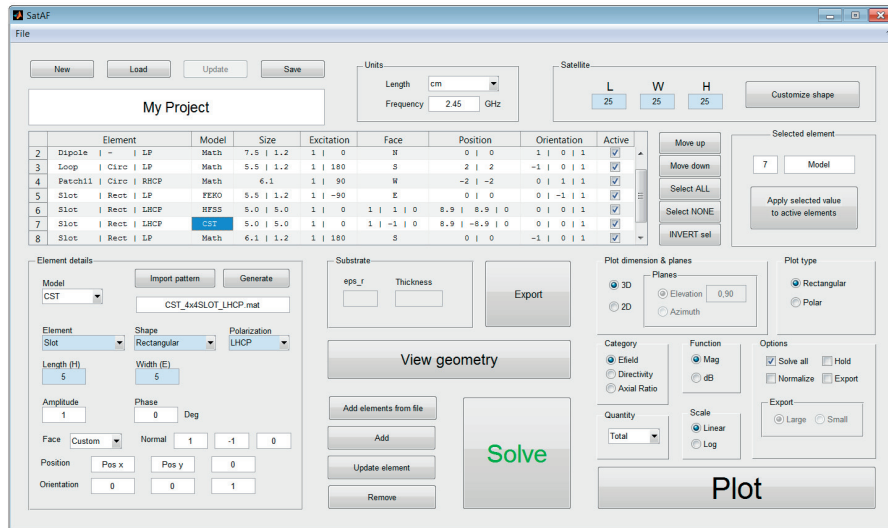
These elementary sources will be used to identify the best performing architecture in terms of sources displacement, postponing the detailed analysis and design of the real radiator to a later stage of the project.

### 2.3.1. Description of the software

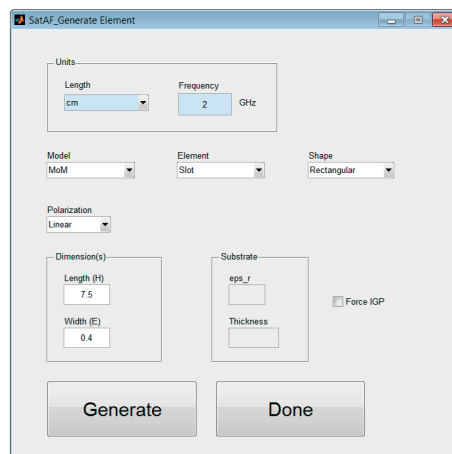
On the basis of all the aforementioned considerations, we developed SatAF (Satellite Array Factor), a MATLAB simulation software for fast calculation of 3D radiation pattern. The tool disposes of a User Interface (UI), shown in Fig. 2.8a which allows the definition of any number of different types of elementary radiators (point sources, dipoles, patches, slots and others), and the control of the relevant parameters (such as dimensions and excitation). Additionally, the tool offers an UI for the customization of the satellite shape (Fig. 2.8b) and a third one (Fig. 2.8c) which handles the import/export of patterns and the creation of SatAF elements. Once the array has been designed, the software calculates the pattern generated by each radiating element, depending on their orientation with respect to a global reference system and generates the total field accounting for the phase delays introduced by the position of elements.

We prefer to anticipate in this section, among the various functionalities of SatAF, the description of a feature which was developed in the frame of the improvement of SatAF. We implemented the possibility of importing radiation patterns generated with external software, supplied in the form of a data table containing the electric far field components in the whole radiation sphere. The procedure consists of an algorithm which interpolates the values of the data table, which refer to the *local* coordinate system used in the external simulator, in order to generate the values in the points of the *global* coordinate system associated with the satellite.

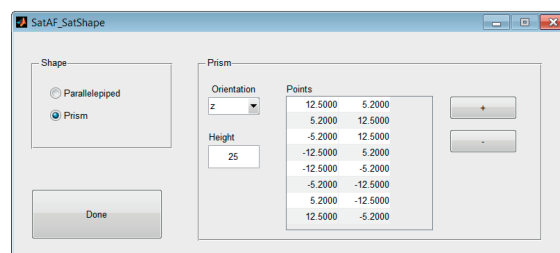
A more detailed illustration of the algorithm is given in Par. 2.3.2.



(a)



(b)



(c)

**Figure 2.8.:** SatAF user interfaces: (a) main window, (b) satellite shape customization and (c) import/export and element generation interface.

It follows here a schematic resume of the possibilities and characteristics offered by the tool.

### Features

- User Interfaces
  - Main interface for controlling the array elements' parameters
  - UI for the design of the satellite platform
  - UI for the creation, import and export of radiation patterns generated with external software
- Management of projects and direct transfer of elements between them

### Array characteristics

- Satellite shape and size
- Elements position and orientation
- Excitations amplitude and phase

### Elements library

- Point source
- Dipole
  - Infinitesimal dipole
  - Finite size dipole
- Loop antenna
- Slot antenna
  - Rectangular or circular aperture
  - Linear, RH or LH circular polarization
- Patch antenna
  - Rectangular patch
  - Circular patch
    - \* Fundamental (TM11) and higher order modes (TM21, TM02, ...)
  - Substrate type and thickness
  - Linear, RH or LH circular polarization

**External software interface**

- Ansoft HFSS [38]
- CST Microwave Studio [39]
- EMSS FEKO [40]
- Agilent ADS [41]
- Possibility of exporting / importing data produced by SatAF itself

**Outputs**

- Layout of the satellite and array elements
- Radiation patterns
  - Quantities
    - \* Radiated field, total or in its  $\theta, \phi$  components
    - \* Directivity, total or in its  $\theta, \phi$  components
    - \* Axial ratio
  - Format
    - \* 3D polar radiation pattern
    - \* 2D rectangular map
    - \* 1D plot of a cut-plane, rectangular or polar and in different scales

**2.3.2. Analytical formulation**

The core of SatAF is the algorithm handling the 3D rotation of the elements. We describe here the theoretical aspects implemented in the software; the source code is included in App. B.

We find convenient expressing the position of an element and its orientation in the 3D space by defining the following quantities, depicted in Fig. 2.9:

- $r_E$ : distance of the element from the center of the reference system
- $\theta_E, \varphi_E$ : angular position of the element in spherical coordinates
- $\alpha_E$ : rotation of the element around the unit vector  $\mathbf{r}$  (which can be associated for planar elements with the normal to their surface).

While the parameters  $r_E, \theta_E, \varphi_E$  localize the element,  $\alpha_E$  defines the orientation and can be associated in some cases (e.g. a circular patch) with the polarization of the element itself.

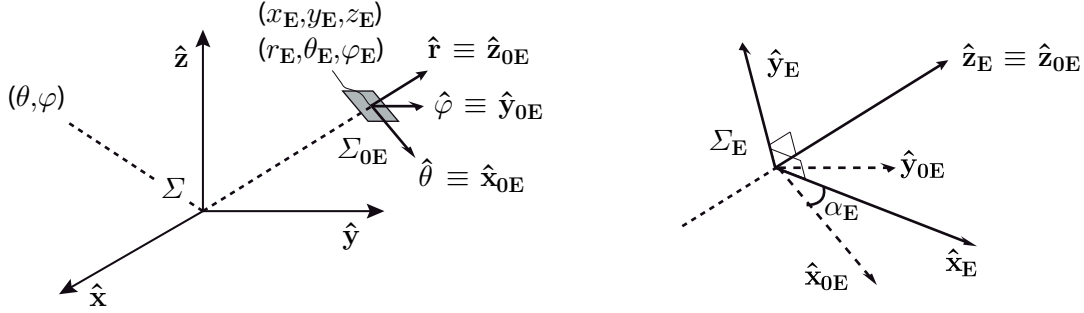


**Figure 2.9.:** A generic radiator in the 3D space: coordinate systems and quantities used to identify its position and orientation.

We suppose that the electric field  $\mathbf{E}_0$  radiated by a generic source is available in closed form with respect to a local reference system  $\Sigma_0 = (\hat{\mathbf{x}}_0, \hat{\mathbf{y}}_0, \hat{\mathbf{z}}_0)$ . The same element is then placed in a point  $(\mathbf{r}_E, \theta_E, \varphi_E)$  expressed in terms of the global reference system  $\Sigma = (\hat{\mathbf{x}}, \hat{\mathbf{y}}, \hat{\mathbf{z}})$  and oriented according to the angle  $\alpha_E$ . The first step consists in translating the observation point  $(\theta, \varphi)$  from the global to the local reference system  $(\theta_0, \varphi_0)$ , where the field is evaluated. Before the rotation ( $\alpha_E = 0$ ), the local coordinate system  $\Sigma_{0E}$  is:

$$\begin{aligned}\hat{\mathbf{x}}_{0E} &= \hat{\boldsymbol{\theta}}_E \\ \hat{\mathbf{y}}_{0E} &= \hat{\boldsymbol{\varphi}}_E \\ \hat{\mathbf{z}}_{0E} &= \hat{\mathbf{r}}_E\end{aligned}\quad (2.1)$$

The relation between  $\Sigma$  and  $\Sigma_{0E}$  is given by the rotation matrix  $R_{SC}$ :

$$R_{SC}(\theta_E, \varphi_E) = \begin{pmatrix} \cos \theta_E \cos \varphi_E & \cos \theta_E \sin \varphi_E & -\sin \theta_E \\ -\sin \varphi_E & \cos \varphi_E & 0 \\ \sin \theta_E \cos \varphi_E & \sin \theta_E \sin \varphi_E & \cos \theta_E \end{pmatrix}\quad (2.2)$$

The rotation does not affect  $\hat{\mathbf{z}}_{0E}$  and allows to define the rotation matrix  $R_{0E}$ :

$$R_{0E}(\alpha_E) = \begin{pmatrix} \cos \alpha_E & \sin \alpha_E & 0 \\ -\sin \alpha_E & \cos \alpha_E & 0 \\ 0 & 0 & 1 \end{pmatrix}\quad (2.3)$$

The local coordinate system can therefore be expressed as a function of the global coordinate system:

$$\Sigma_0(\theta_E, \varphi_E, \alpha_E) = R_{0E}(\alpha_E) \cdot R_{SC}(\theta_E, \varphi_E) \cdot \Sigma\quad (2.4)$$

Using the classic formulas for the transformation between Cartesian and Spherical coordinate  $T_{C2S}$  and viceversa  $T_{S2C}$ , the desired far field field in the point (in global coordinate system)

$\mathbf{E}(\theta, \phi)$  is found by computing  $\mathbf{E}_0(\theta_0, \phi_0)$  with:

$$\begin{pmatrix} 1 \\ \theta_0 \\ \varphi_0 \end{pmatrix} = T_{C2S} \cdot R_{0E}(\alpha_E) \cdot R_{SC}(\theta_E, \varphi_E) \cdot T_{S2C} \cdot \begin{pmatrix} 1 \\ \theta \\ \varphi \end{pmatrix} \quad (2.5)$$

The field derived is a vector with components along the *local* unit vectors  $\hat{\boldsymbol{\theta}}_0, \hat{\boldsymbol{\phi}}_0$ . By reversing the reasoning, the global coordinate system is expressed as:

$$\Sigma = [R_{SC}(\theta_E, \varphi_E)]^{-1} \cdot [R_{0E}(\alpha_E)]^{-1} \cdot \Sigma_0 \quad (2.6)$$

When combined with the formulas for transformation of cartesian to spherical components  $V_{C2S}$  and the inverse  $V_{S2C}$ , we obtain finally:

$$\mathbf{E}(\theta, \varphi) = \begin{pmatrix} 0 \\ E_\theta(\theta, \varphi) \\ E_\varphi(\theta, \varphi) \end{pmatrix} = V_{C2S}(\theta, \varphi) \cdot [R_{SC}(\theta_E, \varphi_E)]^{-1} \cdot [R_{0E}(\alpha_E)]^{-1} \cdot V_{S2C}(\theta, \varphi) \begin{pmatrix} 0 \\ E_{\theta_0}(\theta, \varphi) \\ E_{\varphi_0}(\theta_0, \varphi_0) \end{pmatrix} \quad (2.7)$$

### 2.3.3. Validation

A exhaustive benchmark campaign has been performed in order to validate on one side the correct formulation and implementation of the 3D Array Theory and on the other the actual accuracy and usefulness of the approximate method. We report here those results we find pertinent to the illustration of this thesis work; in particular, we omit the part of the campaign validating the bare implementation, showing instead the cases more closely related to the design process we followed and proving the consistency of the hypotheses on the radiation mechanism. As the preliminary designs of the antenna system envisaged the use of circular patch antennas, the software was tested using mainly such a radiating element; slot antennas have also been considered in some test cases.

The configurations we present involve circular patch antennas in R- or LHCP polarization either in planar or spatial array distribution. The patches are fed with 4 coaxial lines excited in sequential rotation 0, 90, 180, 270 deg which provide the circular polarization; in this context, with "patch orientation" we refer to the orientation of the ideal vector connecting the center of the patch with the coaxial with 0 deg excitation. The characteristic dimensions of the patches, coaxial lines and substrate are given in Tab. 2.1; the "Position" parameter refers to the distance from the center of the ground plane (Patch row) or from the center of the patch (Coaxial row).

In SatAF, the patches are represented with a mathematical model which includes all the information about the dimensions but assumes the presence of an infinite ground plane. As



**Table 2.1.:** Characteristic dimensions used for the benchmark configurations. The parameter "Position" refers to the distance from the center of the ground plane (Patch row) or from the center of the patch (Coaxial row).

Element	Parameter	Value
Patch	Radius	18.5 mm
	Position	12 cm
Substrate	$\varepsilon_r$	4.4
	Thickness	1.6 mm
Coaxial	Inner radius	0.7 mm
	Outer radius	1.6 mm
	Position	9.3 mm

a reference, the configurations are simulated with the commercial, full-wave software Ansoft HFSS and the radiated fields on the main cuts are compared.

The operative frequency is 2.45 GHz.

The first configuration envisages an array of 4 patches on a 36 cm ( $3\lambda$ ) ground plane, as depicted in Fig. 2.10. The patches are oriented in different directions for a more complex test case. As shown in Fig. 2.11, the radiation pattern predicted with SatAF is in excellent agreement with the reference in all the cuts and in the whole region above the ground plane, while the weakness of the fields below it ( $< -10$  dB) demonstrates that the assumption of an infinite ground plane is in fact realistic.

The second benchmark configuration consists of a spatial array of three groups of two patches on three sides of a cubic platform of 25 cm side ( $2\lambda$ ), the actual dimension requested for the MAST satellite. The patches are moved cm away from the center towards a corner of the respective face, as shown in Fig. 2.12. Like in the previous configuration, polarizations and patch orientations are mixed for a more complex test case. Results are again in excellent agreement with the reference in the regions of direct radiation, as it is illustrated in Fig. 2.13.

The third test case is identical to the previous one but the satellite is now smaller ( $15$  cm  $\approx 1.2\lambda$ ) in order the patches to be located very close to the platform edges and one to each other, as shown in Fig. 2.14. The effect of diffraction and mutual coupling is therefore expected to affect the radiation pattern in a stronger way than in the previous cases. In fact, now deviations are observed in some cuts (Fig. 2.15), but the overall behavior is again well predicted and the agreement with HFSS is still acceptable.

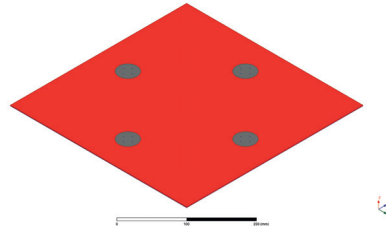


**Figure 2.10.:** Benchmark configuration 1: four patches on a 36 cm ground plane.

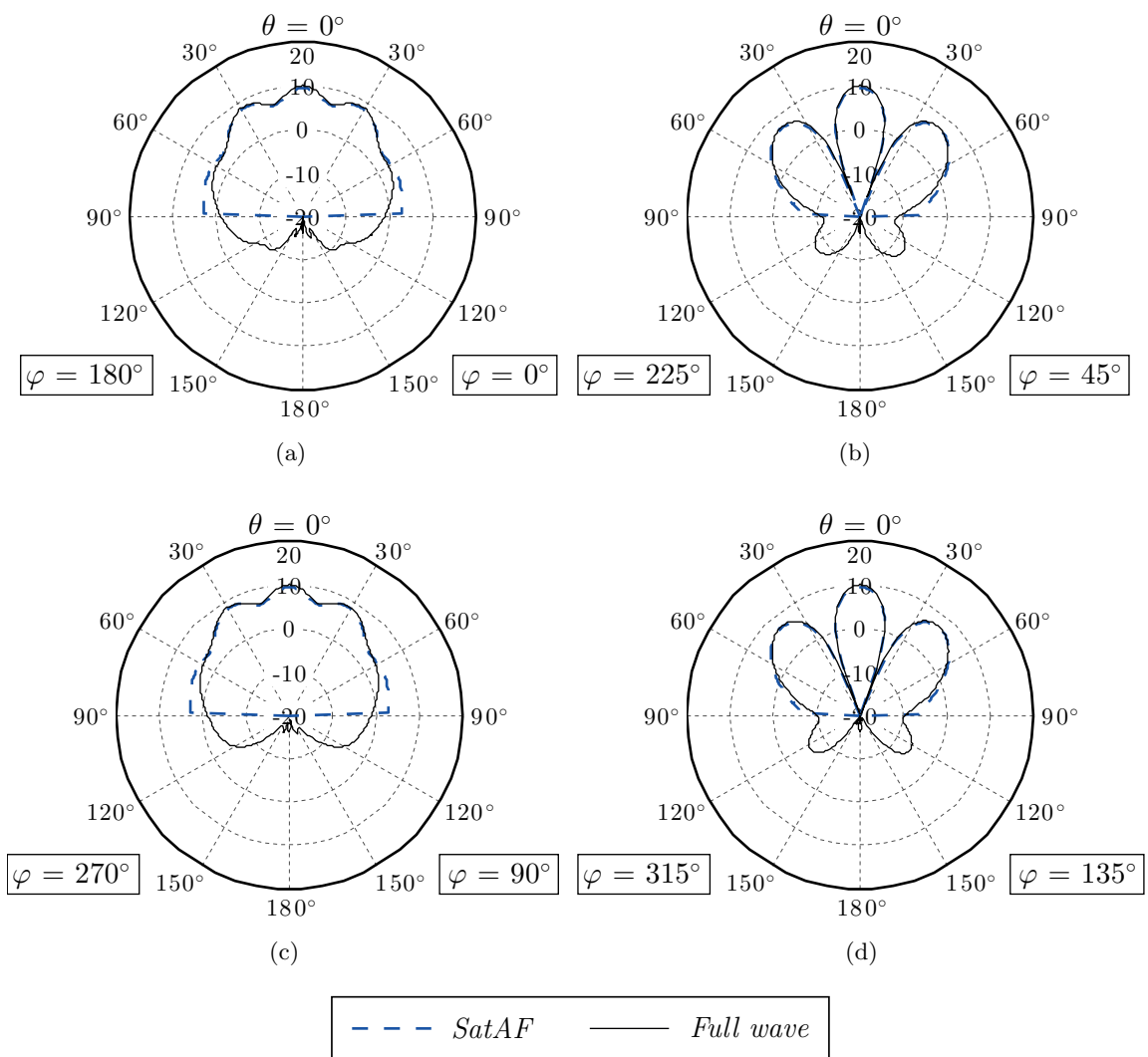


**Figure 2.11.:** Benchmark configuration 1: radiation pattern on the elevation cuts (a)  $\varphi = 0$  deg, (b)  $\varphi = 45$  deg, (c)  $\varphi = 90$  deg, (d)  $\varphi = 135$  deg.

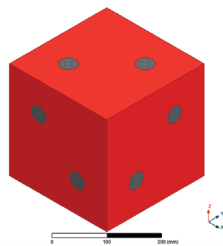


Figure 2.12.: Benchmark configuration 2: six patches on three faces of a 25 cm cubic platform.

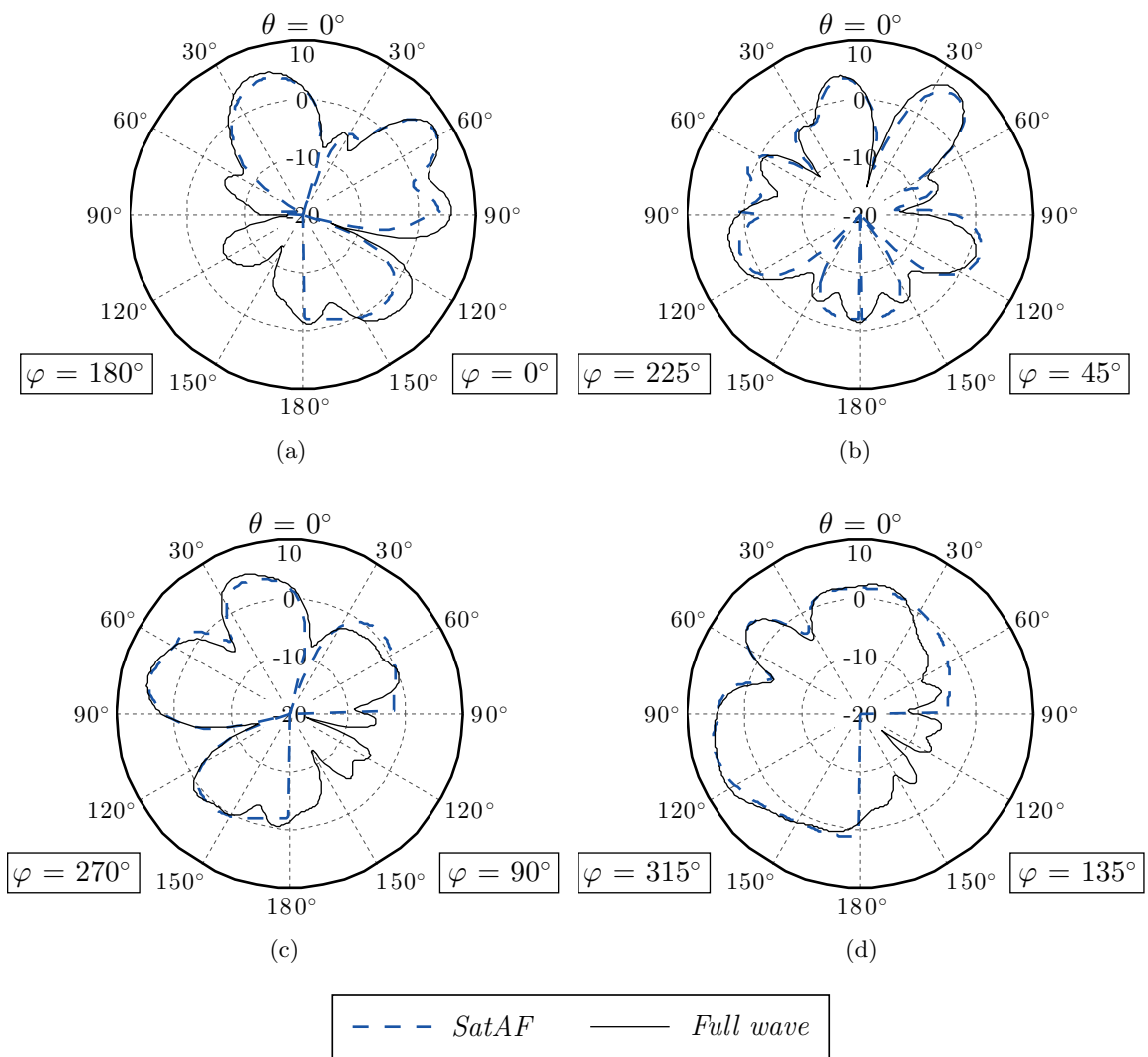
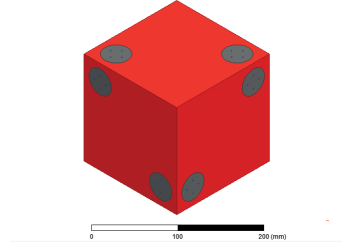
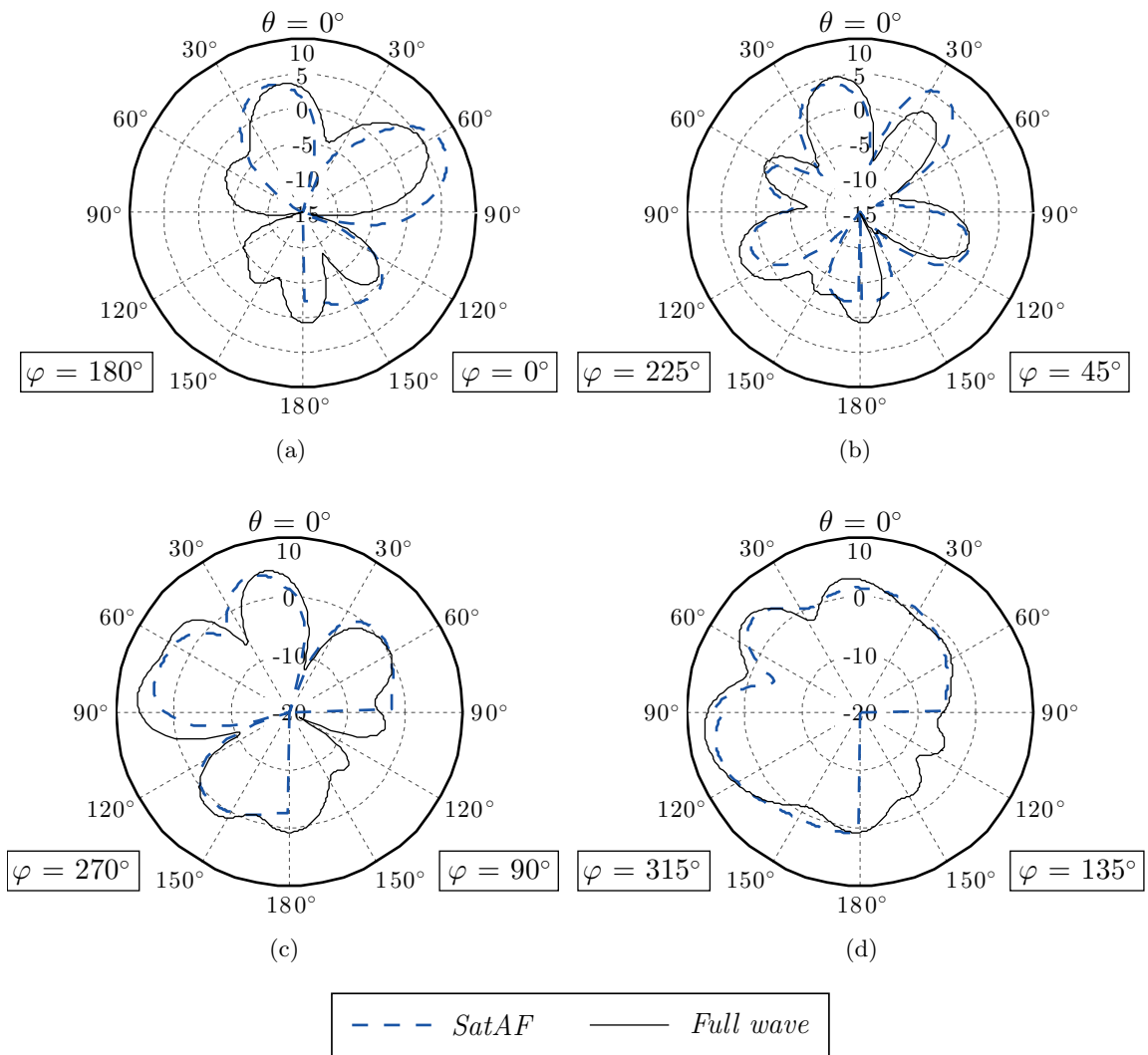


Figure 2.13.: Benchmark configuration 2: radiation pattern on the elevation cuts (a)  $\varphi = 0$  deg, (b)  $\varphi = 45$  deg, (c)  $\varphi = 90$  deg, (d)  $\varphi = 135$  deg.



**Figure 2.14.:** Benchmark configuration 3: six patches on three faces of a 15 cm cubic platform.



**Figure 2.15.:** Benchmark configuration 3: radiation pattern on the elevation cuts (a)  $\varphi = 0$  deg, (b)  $\varphi = 45$  deg, (c)  $\varphi = 90$  deg, (d)  $\varphi = 135$  deg.

These three test cases demonstrate that the assumptions made for the development of SatAF actually hold in the cases of interest for the project: in those regions of space illuminated by direct radiation, the accuracy of the predictions is very good confirming that the diffraction can be safely neglected for the most part of the cases.

When sources are located close to the edges of the satellite, the assumptions made are pushed to the limits and minor deviations eventually appear in the comparisons. Nevertheless, the positions of lobes and nulls is well predicted and the overall accuracy can still be considered satisfying.

The last part of the benchmark involves the impact of mutual coupling and the capability of SatAF to handle radiation patterns generated with external software. Two elements, also studied for the final design of the antenna system have been used: a sub-array of  $2 \times 2$  RHCP circular patches, Fig. 2.16a (a stub is used to induce RHCP), and a sub-array of  $2 \times 2$  C-shaped slots, Fig. 2.16b.

Two of these elements lie on two faces of a cubic platform. The single elements are simulated when lying in the *center* of the satellite face using the commercial, full-wave softwares Ansoft HFSS and CST Microwave Studio respectively; radiation patterns are then imported in SatAF which handles the rotation and Array Factor effects. The same software is then used to simulate the whole structures and radiation patterns are computed as reference.

Edge diffraction is now (roughly) accounted for by the full-wave software and only mutual coupling is actually neglected.

The comparison of the radiation patterns is shown in Fig. 2.16 for the patch array (patterns on the left, Fig. 2.16c and Fig. 2.16e) and for the slot array (patterns on the right, Fig. 2.16d and Fig. 2.16f). The comparison with the full wave software confirms the negligible impact of mutual coupling, validating the solidity of the approach used and the correct software implementation.

Through the benchmark campaign, SatAF proved to be a solid and reliable software and was established as a valuable design tool to be extensively used during the project.

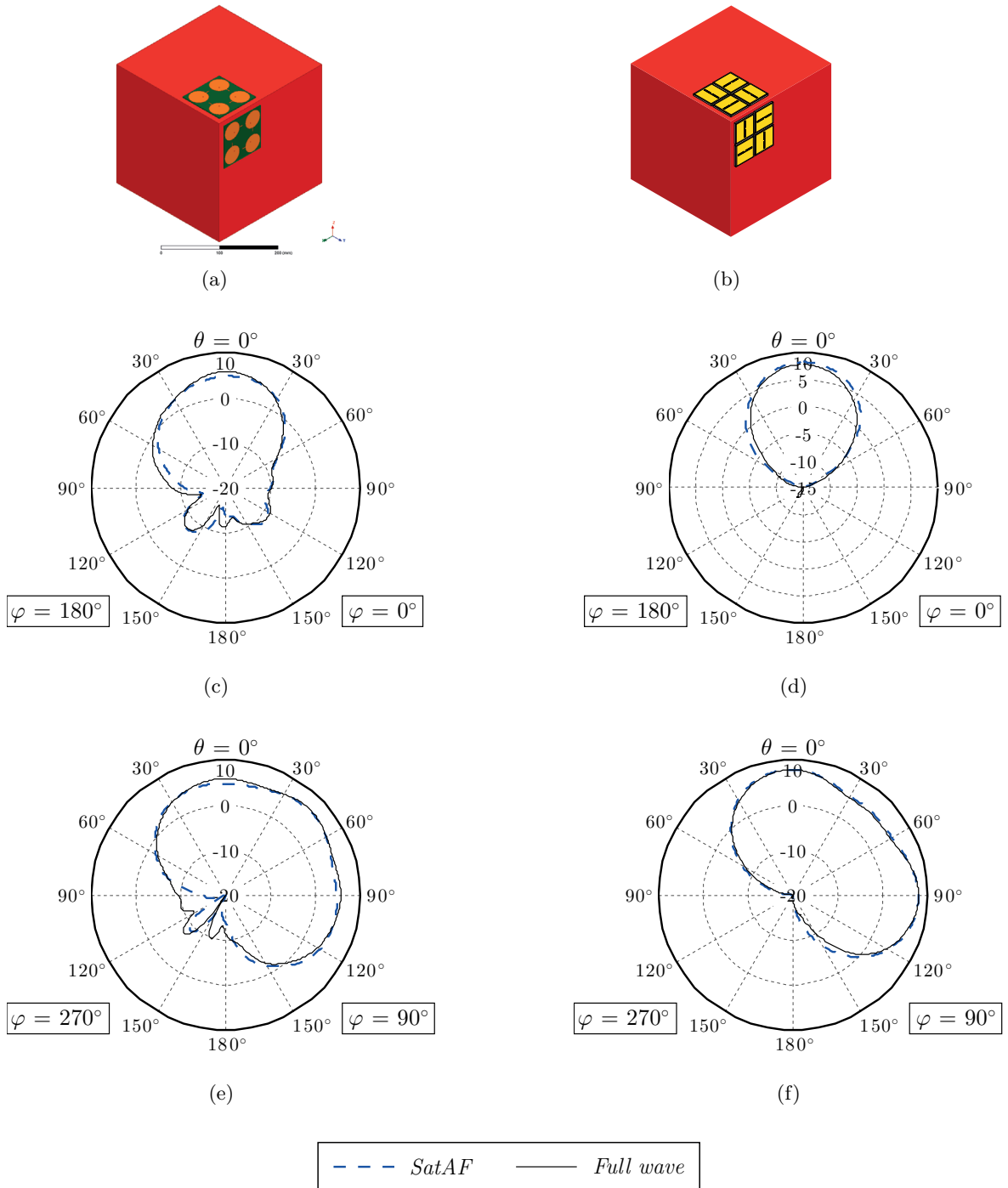


**Figure 2.16.:** Benchmark configuration 4 and 5: 2 sub-arrays of 4 elements, (a) circular paths, (b) C-shaped slots. Radiation patterns: configuration 4, (c)  $\varphi = 0$  deg, (e)  $\varphi = 90$  deg; configuration 5, (d)  $\varphi = 0$  deg, (f)  $\varphi = 90$  deg.

## 2.4. A typical SatAF application: the design of the ESA-MAST antenna system

In this section we resume the work that led to the final design of the MAST Mode A (omnidirectional) antenna system.

Reflecting the actual design process, the first part of the section illustrates the configurations, in terms of the distribution of the array elements, which better fulfill the antenna mode requirements. The investigation was performed with the in-house MATLAB tool SatAF using ideal elements as radiators; consequently to the choice of circular patch antennas for the preliminary design, ideal patches (lying on an infinite ground plane) were mainly used throughout the design.

Once the optimal array and especially the optimal radiation pattern was identified, in the second part of the design we focused on the realization of the real radiator able to produce the desired pattern and, simultaneously, fulfilling the requirements in terms of reflection losses and bandwidth. These latter aspects, even if less pertinent to the radiation performance, drove some of the key design decision and are therefore addressed.

During the element design phase, slot antennas were found to be better performing than patches from the technological point of view and were finally preferred. This choice did not interfere in any way with the investigation conducted in the first part of the design, whose output was an optimal radiation pattern rather than the element producing it.

We limit the information illustrated in this section to that pertinent to the discussion of the thesis. The reader can refer to App. A for the complete documentation about the design of Mode B and C antenna system and a more detailed technical description of the Proof-Of-Concept and the measurement campaign.

### 2.4.1. Satellite architectures and arrays

The Mode A, or omnidirectional coverage, can be considered as the most challenging and difficult to be achieved; not only for the good performance required in terms of power coverage, but also for the circular polarization purity. After the deep study of the state-of-the-art carried out, no references to antenna systems combining a good performance in terms of circular polarization and full-sphere coverage have been found, as well as mature guidelines for the design.

On account of these facts, we have concentrated most of the efforts on the omnidirectional mode, focusing on the achievement the required level of Directivity and polarization purity, trusting on the fact that once this mode was accomplished, the directional and multi-beam modes could have been generated by sub-sets of elements. The requirements provided by ESA (Sec. 1.4) target a minimum gain of  $-3$  dBi with a ripple not higher than 6 dB, either in right or left hand circular polarization.

Thanks to SatAF, a high number of different array configurations have been simulated; we present here the best performing solutions for the omnidirectional mode, evaluated according to the following figures of merit:

- Performance, indicated by the Global Coverage (1.2) and shown on a 2D rectangular diagram representing the 3D space in  $\theta, \varphi$  coordinates
- Number of elements
- Encumbrance of satellite surfaces

The pattern used in the presented solutions is produced by three models of circular patches, all lying on a substrate with relative permittivity  $\epsilon_r = 4.4$  and thickness 1.6 mm. The radius of the patches and the excited mode are summarized in Tab. 2.2. In the following layouts, the patch is depicted as a yellow circle, where two arms represent the orientation of the 0 deg current (blue) and the polarization, red for RHCP, green for LHCP. The computations are performed at the frequency of 2 GHz.

**Table 2.2.:** Parameters of the three models of patch antennas used in the presented arrays.

Patch	Radius	Mode
Type 1	2.7 cm	TM 11
Type 2	3.5 cm	TM 11
Type 3	4.5 cm	TM 21

### Octagonal satellite

The best performance achieved for the omnidirectional mode involves the use of an octagonal platform. The shape is less usual than the standard cubic platform but has already been used in other missions, for instance [18], as seen in the State-of-the-Art, Sec. 1.2. The size of the platform is  $25 \times 25 \times 25$  cm and eight Type 1 RHCP patches are located on the side faces of the prism, plus two LHCP ones on the top and bottom faces. The layout is illustrated in Fig. 2.17a, while Fig. 2.17b shows that this configuration produces a coverage higher than 95%. Such performance is balanced by some drawbacks: the shape of the satellite is not a standard one, a high number of elements is required and, consequently, a high amount of surface is occupied by the antenna system.

### Cubic satellite, edge elements

A very good performance can be obtained using a cubic satellite where six Type 2 patches, differently R/LHCP polarized, are allocated in proximity of the platform edges, as it is depicted in Fig. 2.18. Coverage is inferior to Architecture 1 but still is higher than 90% (Fig. 2.19).



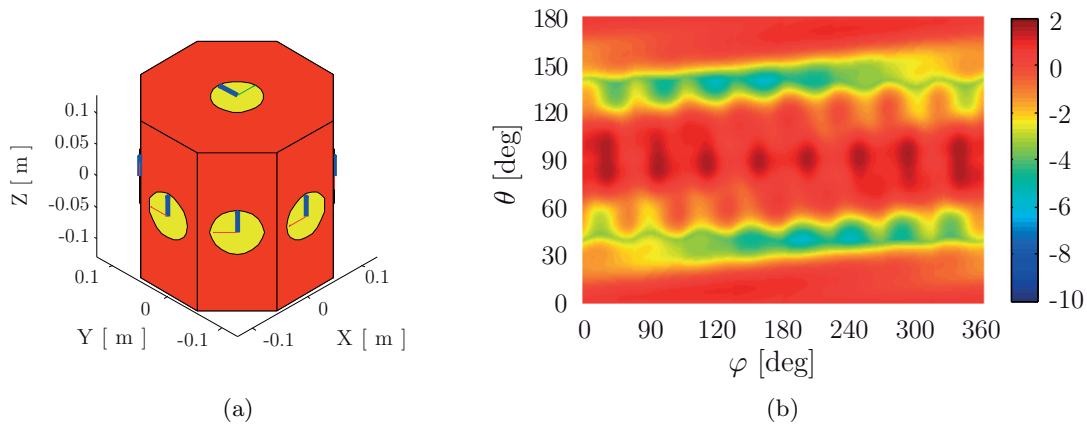


**Figure 2.17.:** Architecture 1, octagonal satellite. (a) layout and (b) Directivity 2D map of the highest R/LHCP radiated field component.

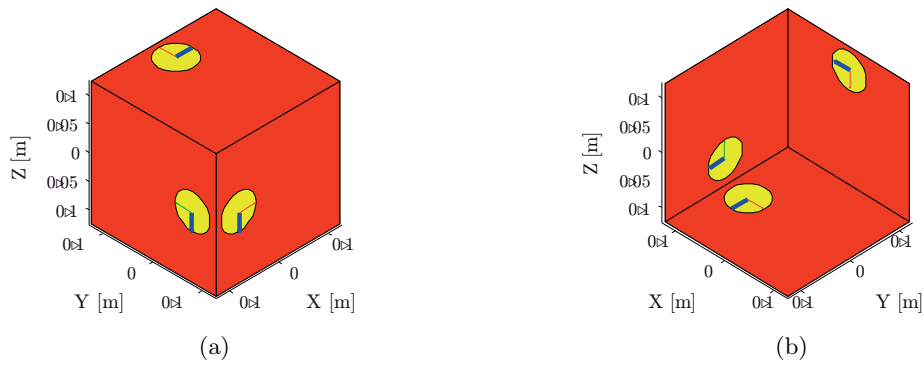


**Figure 2.18.:** Architecture 2, six patches around the edges of a cubic platform, layout: (a) front and (b) back view.

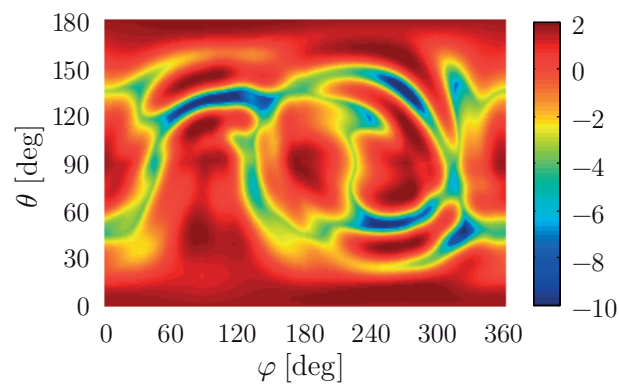


**Figure 2.19.:** Architecture 2, six patches around the edges of a cubic platform. Directivity 2D map of the highest R/LHCP radiated field component.

### Cubic satellite, corner elements

An interesting solution envisages the use of six Type 2 patches allocated around two opposite corners of a cubic satellite, as it is depicted in Fig. 2.20. The main advantage of this configuration is that elements are confined within two limited regions of the satellite, minimizing the surface occupation. Again, patches are differently R/LHCP polarized. A little price is paid in terms of coverage, now reduced to 86% (Fig. 2.21).

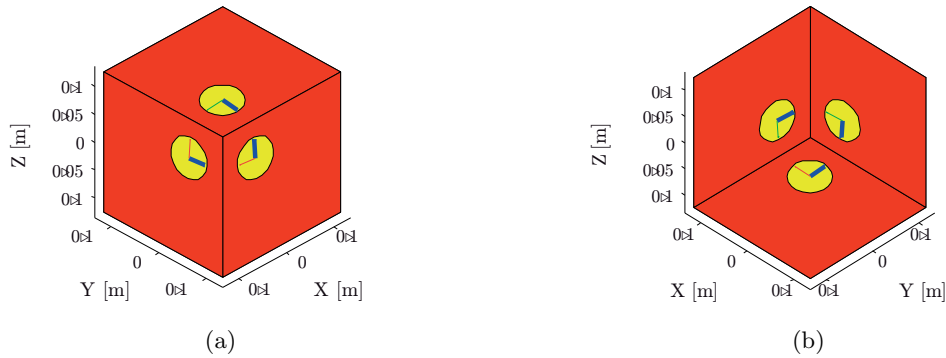


**Figure 2.20.:** Architecture 3, six patches around the corners of a cubic platform, layout: (a) front and (b) back view.

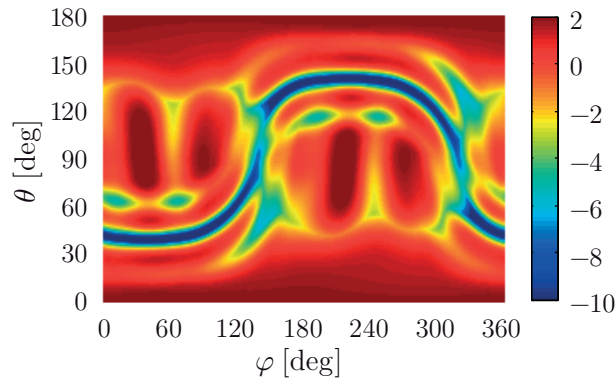


**Figure 2.21.:** Architecture 3, six patches around the corners of a cubic platform. Directivity 2D map of the highest R/LHCP radiated field component.

### Hexagonal satellite

As requested by the ESA, we investigated also creative solutions and in this context one of the most interesting is illustrated in Fig. 2.22: the platform is now an irregular hexagon allocating four Type 3 patches, excited with the TM<sub>21</sub> Mode. The number of elements is minimized (4 patches) and the results, shown in Fig. 2.23, are very promising with a coverage higher than 85%.

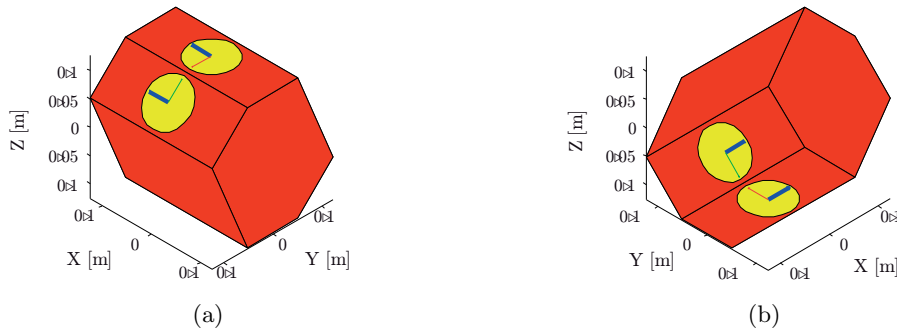


**Figure 2.22.:** Architecture 4, four TM21 patches on an hexagonal platform, layout: (a) front and (b) back view.

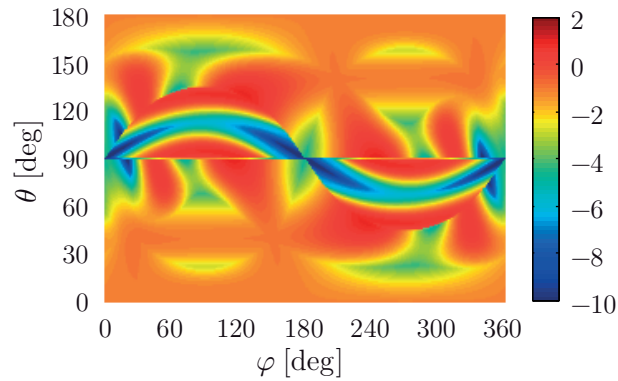


**Figure 2.23.:** Architecture 4, four TM21 patches on an hexagonal platform, Directivity 2D map of the highest R/LHCP radiated field component.

### Summary and final remarks

We presented in this section the configurations producing the best performing patterns with respect to the omnidirectional mode, Mode A. The architectures are resumed with their characteristic parameters in Tab. 2.3.

**Table 2.3.:** Architectures proposed for the Mode A.

Architecture	Patch	N° of elements	Coverage
Octagonal prism	Type 1	10	96%
Cube, edge	Type 2	6	90%
Cube, corners	Type 2	6	86%
Hexagonal prism	Type 3	4	85%

The solutions represent different trade-off solutions between performance, number of elements and encumbrance on the satellite surface. Other configurations, resorting either on sources protruding from the satellite surface, or allocated on unusual cuts (like the design in [36]) were discarded for technological issues.

The architecture selected as best candidate was Architecture 2. This choice identified in particular in the Type 2 radiation pattern the one to be synthesized and it is shown in Fig. 2.24. For the realization of the Proof-Of-Concept (Par. 2.4.5 and App. A), a simpler configuration was chosen, in order to ease the manufacturing process' time and cost and it was decided that an agreement between simulations and measurements could constitute a sufficient proof of validity and reliability of the other proposed architectures.

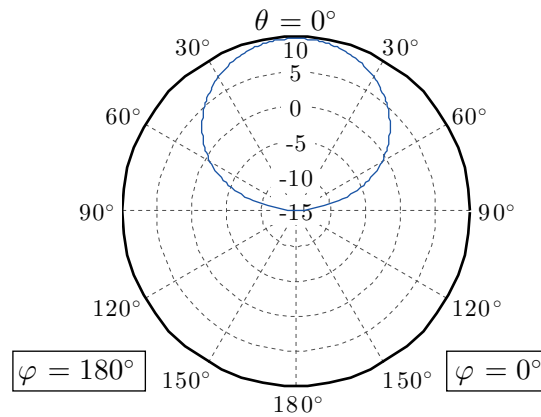


**Figure 2.24.:** The target radiation pattern, as it is generated by the Type 2 patch.

#### 2.4.2. Practical possible choices for the radiating element

The first phase of the design led to the identification of the optimal radiation pattern to be targeted in the design of the radiating element. In this section, we resume the process which led to the design of the radiator best reproducing the ideal pattern and, at the same time, fulfilling the specifications on antenna matching and bandwidth.

Even though the ideal pattern was originally associated with a patch antenna, different types of radiators have been considered, including Printed Inverted F-Antennas (PIFAs) and printed dipoles. Two possible implementations have finally been investigated in depth, one consisting of patch antennas, the second envisaging the use of slot antennas.

### Suitable technologies

A detailed investigation was initially carried out with the goal of identifying key points and weaknesses of the different available technologies. In Tab. 2.4 is resumed the study on the most important trade-off parameters on the most suitable candidates for be the basic radiating element. Printed dipoles and PIFAs can be considered similar technologies except

**Table 2.4.:** Evaluation of the most important trade-off parameters of the most suitable radiating sources candidates.

		Slots	Patches	Printed dipoles	PIFAs
Size	Surface	+	-	+	+
	Thickness	-	+	-	+
Integration level (SP, instruments, edges...)		+	-	+	+
Performance (Gain, BW)		+	+	+	+
Polarization purity		+	+	+	+
BFN design		+	+	+	-
Mechanical imple- mentation		+	+	+	-
Robustness		+	-	-	-

for their mounting and mechanical implementation. If on one hand both are easy to integrate due to their reduced dimensions, the vertical mounting is not compatible with the satellite separation method especially for very small satellites and CubeSats; moreover, they are known to be sensitive to other metallic structures in their surroundings. Finally, the lack of circular polarization purity can be only fairly improved by resorting to an appropriate array disposition.

Slot antennas offer the best performance in terms of robustness and integration ease, while the main advantage of patches are the polarization purity and low-profile.

It is also important to note that some other radiating elements like helix antennas and (non-printed) dipoles have been discarded due to their non-friendly integration on such small satellites.

### 2.4.3. Patch antennas designs

The first step was the design of a single radiating element with a relatively low gain and thin profile, suitable at the same time for placement on small spacecrafts walls with permissible outline limits. Although examples of elements of this type (often called Low Gain Antennas, LGA) can be found in literature, we preferred to design our own single radiating element.

The first logical attempt to traduce the ideal pattern generated by a theoretical patch antenna into a physical radiator was trying to use a patch with characteristics similar to the ideal one. The target pattern being a rather narrow beam, it became quickly evident that a sub-array of low-gain sources could be more efficiently employed, both for its easier and more standard design (with respect to a large patch) and for the possibility of taking advantage of sequential rotation to improve the polarization purity. As a figure of merit of the degree of similarity with the ideal element we take into account the Gain on the principal cuts.

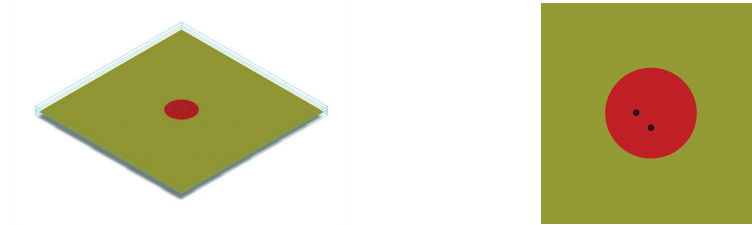


**Figure 2.25.:** Layout of the single CP patch on the finite ground plane.

The layout of the antenna is illustrated in Fig. 2.25; the substrate used is the Rogers Duroid 5880 (Tab. 2.5), which thanks to its very low permittivity and thickness, allowed us to achieve a low degree of encumbrance on the satellite walls and a high efficiency of the antenna system. The details and characteristic dimension of the antenna are given in Tab. 2.6.

**Table 2.5.:** Characteristics of the substrate employed for printing the single CP patch.

<b>Duroid 5880</b>	
Relative permittivity	$\varepsilon_r = 2.20$
Thickness	$h = 3.15 \text{ mm}$
Dielectric losses	$\tan \delta = 0.0005$

**Table 2.6.:** Single CP patch, characteristic dimensions.

<b>Single patch</b>	
Radius	22.5 mm
Probe dist. from center	7.14 mm

The design has been performed using the commercial software Agilent ADS, assuming as layout a finite ground plane with the dimensions of the target satellite face (most of the cases  $250 \times 250$  mm).

In order to generate the circular polarization, two probes were placed at the proper distance from the center, in order to excite the two main orthogonal modes with a 90 deg delay and produce the field rotation in counterclockwise sense for RHCP. The antenna is matched at the operating frequency according to specifications, as it is reported in Fig. 2.26. The Axial Ratio (AR) values are well satisfying the specifications in the band of interest; besides, the power characteristics show a maximum Directivity of 7.2 dB and an efficiency levels higher than 85% at the center frequency (Fig. 2.27).

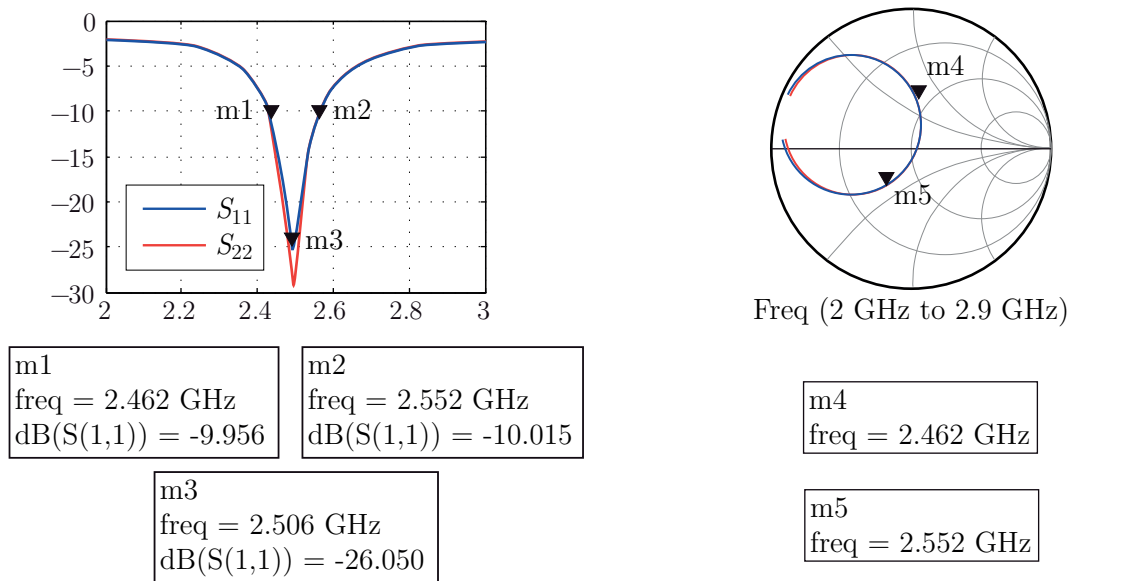


Figure 2.26.: Simulated input return losses of the single circular CP patch.

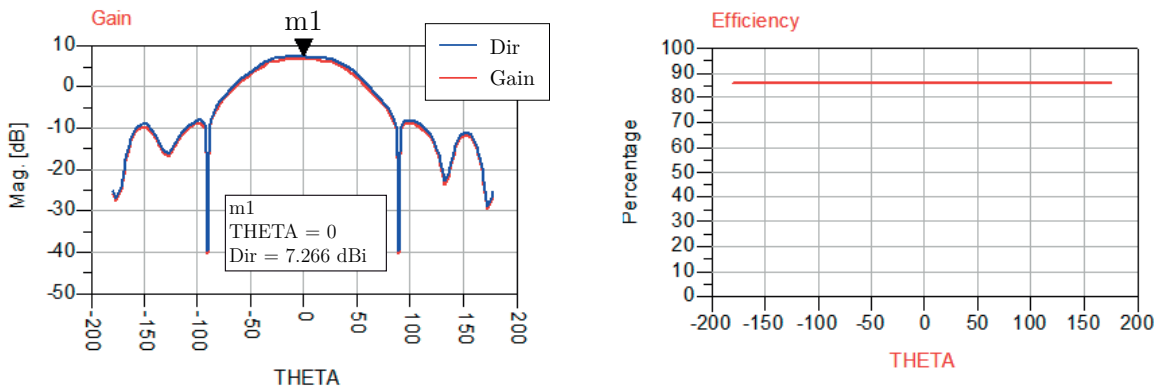


Figure 2.27.: Simulated radiation pattern and power levels of the single circular CP patch, elevation plane.

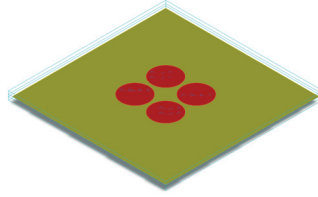


Figure 2.28.: Array of  $2 \times 2$  round CP patches, layout.

Once the suitable radiating source was identified, we focused on the design of the sub-array capable to produce the required Directivity, with an eye on the size occupied in order to reduce the surface occupation. The target pattern was achieved by disposing four round patches at a distance of 50 mm in a  $2 \times 2$  arrangement as presented in Fig. 2.28. Moreover, in order to improve the circular polarization performance, the elements are fed in sequential rotation. As well-known [42], by feeding the elements with increasing phase in the circular polarization sense, the composition of fields is made in a coherent way that improves the AR. The most significant information on the radiation performance is shown in Fig. 2.29.

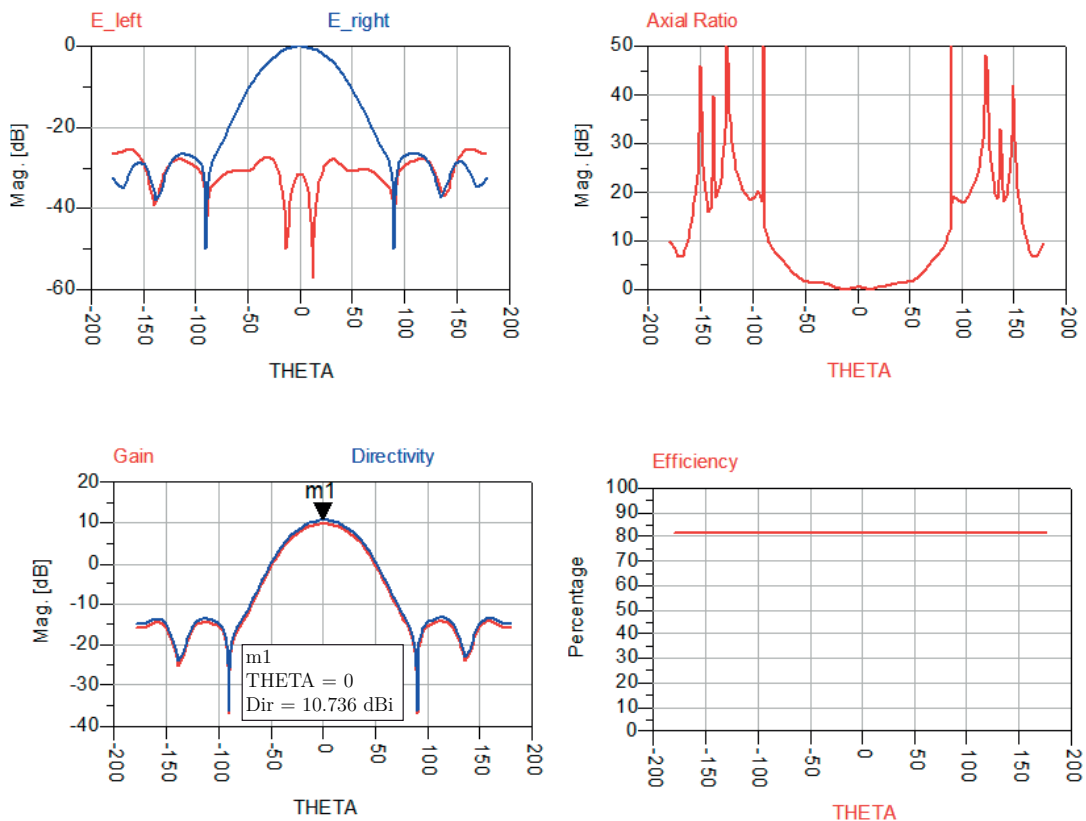


Figure 2.29.: Array of  $2 \times 2$  round CP patches, simulated radiation pattern, elevation plane.



In addition, due to the fact that the antenna sub-system occupies different positions on the satellite surface, further investigations on the robustness of the performances have been carried out. The  $2 \times 2$  elements array has been simulated on the most critical positions on the single face of the satellite, including corners and edges and, as anticipated in the fourth benchmark shown in Par. 2.3.3, all the simulations led to non-critical modifications on the basic radiation pattern performances and the impact of these variations, although existing, did not degrade significantly the characteristics of the array.

#### 2.4.4. Slot antennas designs

The first attempt of implementing the ideal radiation pattern revealed the necessity of using a sub-array, rather than a single radiator, to achieve the required Directivity; this made the surface occupation of patch antennas a major drawback of the solution. For these reasons, patch antennas were considered as a second level candidate, while the investigation was oriented towards slot antennas.

The main advantage of slot antennas as elementary radiators lies in the integration easiness and robustness. Fig. 2.30 shows a possible way of mounting the antenna behind the satellite wall, in which an aperture slightly larger than the radiating slot is performed, leaving the remaining satellite surface available for the allocation of other devices and functionalities.

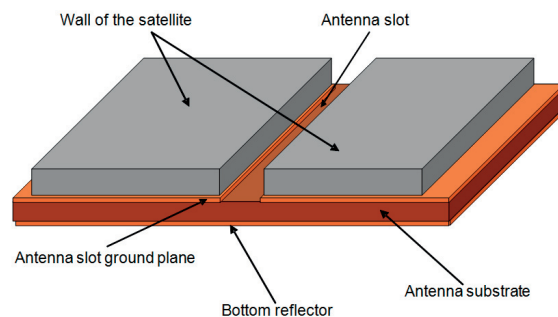


**Figure 2.30.:** Slot antenna mounted behind the wall of the satellite.

Slots on a Ground Plane (GP) can be used as efficient and quite broadband antennas, but the nature of the slot radiation is essentially bi-directional and typically a reflector must be used in order to suppress back radiation. However, when a metallic reflector is placed behind the radiating slot, the parasitic Transverse Electric Magnetic (TEM), Parallel Plate WaveGuide (PPWG) mode can propagate between the slot GP and the reflector. The power leakage through this mode may result in a severe decrease of the antenna Gain and/or in deterioration of the original radiation pattern due to the diffraction occurring at the end of the GPs, as well as in unwanted coupling between elements. An optimum distance of about one-quarter wavelength between the slot and reflector is generally recommended and

in our case is about 35 mm. Such an antenna thickness on a cubic spacecraft with faces of  $250 \times 250$  mm represents an unacceptable volume occupation. As a result, enhanced solutions must be sought after in order to make slot antennas viable candidates for the application. To that respect, a deep survey on reflector-backed slot antennas has been carried out with the aim of reducing their height while maintaining suitable radiation performances.

### Cross slot

A first slot-based solution is inspired by [42] and is composed of four apertures arranged as a cross. The element is depicted in Fig. 2.31a. Each cross arm is a folded linear slot: this produced a very small element while retaining most of the characteristics of a simpler cross slot. Each radiator is excited with a  $100\Omega$  line. The two horizontal slots are excited in phase and they have a phase shift of 90 deg with respect to the vertical ones. As depicted in Fig. 2.31b, the couples of slots oriented in the same direction are connected via  $100\Omega$  lines to a  $50\Omega$  microstrip line. The phase shift between the vertical and the horizontal slots is obtained by changing the length of the  $100\Omega$  line. Finally, the two  $50\Omega$  lines are joined together using a Wilkinson power divider. A back reflector is placed 30 mm behind the antenna in order to increase its directivity (Fig. 2.31a). This element is designed to work in S-band between 2200 MHz and 2290 MHz.

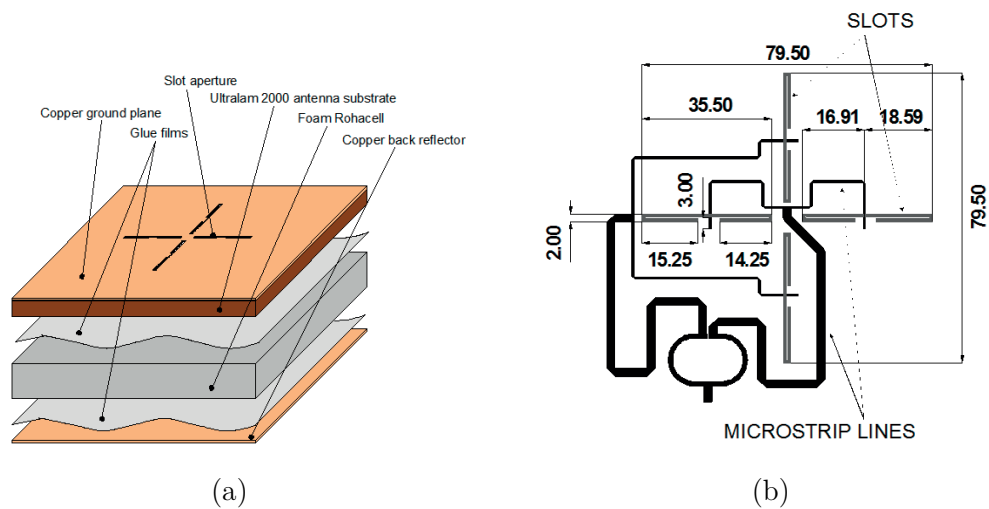


**Figure 2.31.:** Single cross slot: (a) exploded view of the element and (b) layout of the feeding network.

The cross slot element can be arranged in an array configuration in order to implement re-configurability and multi-beam functions and to improve the circular polarization performance. A possible solution envisages four elements disposed in a  $2 \times 2$  configuration, as depicted in Fig. 2.32a. Each element is turned 90 deg with respect to the other and is fed with a phase shift of 90 deg using the feeding network shown in Fig. 2.32b. The measured radiation pattern, depicted in Fig. 2.32c, presents a directive behavior with a

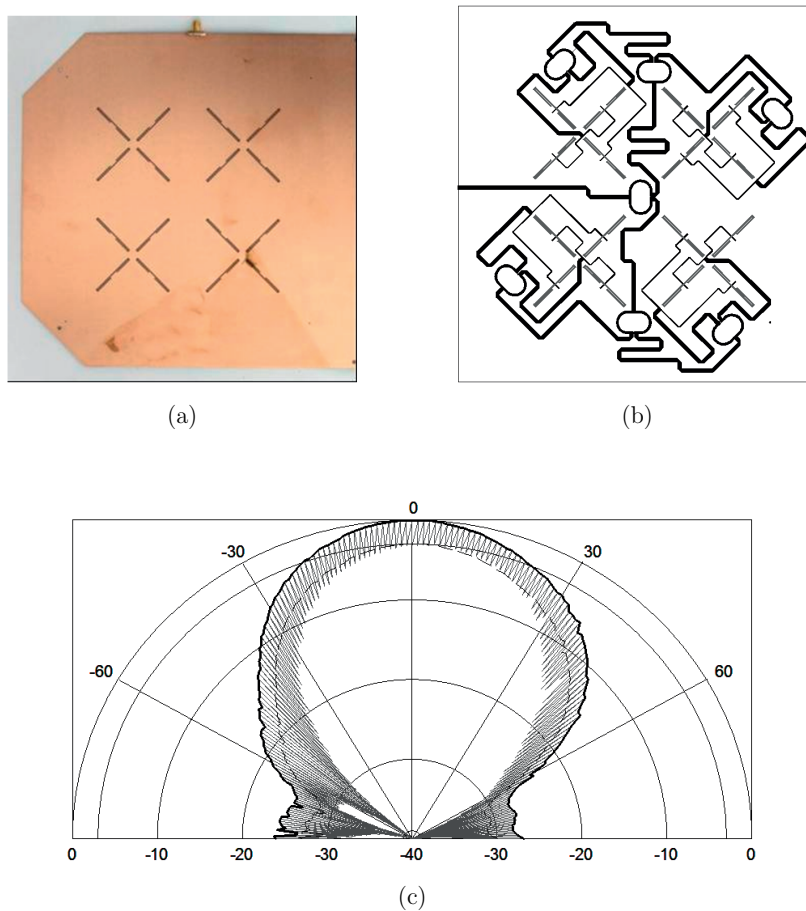


**Figure 2.32.:** Cross slot sub-array [42]: (a) layout, (b) feeding network and (c) radiation pattern on the elevation plane.

Gain of 10.3 dB; this value, slightly higher than the targeted 9.8 dB, can be controlled by acting on the amplitude and phases of the four elements. In the same way, by applying a multi-beam-forming network it is possible to generate four different beams with the required directivity necessary to fulfill the specifications for the TT&C mode (Mode C).

### Square array of slot antennas

An improved version of the previous configuration is shown in Fig. 2.33. In this case, the identical single slot element is used and the array is re-arranged for a simpler and smaller structure. At the same time, this configuration allows higher integration level by leaving most of the surface of each face available for the allocation of other components on the spacecraft. The elements are fed in such a way as to obtain a good polarization purity, while the distance between them is optimized targeting the requested Directivity and, at the same time, minimizing the grating lobes. The elevation cut (equivalently on the plane  $\varphi = 0, 90$ )

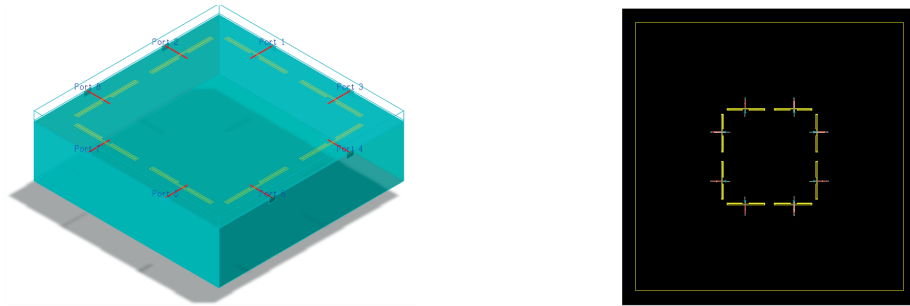


**Figure 2.33.:** 8 slot elements in square array configuration.

of the radiation pattern at the center frequency of the operative band is depicted in Fig. 2.34 (simulations performed with Agilent ADS): a good polarization purity is achieved and the Side Lobe Level is  $-10$  dB, while the maximum of the directivity is exactly 9.8 dB.

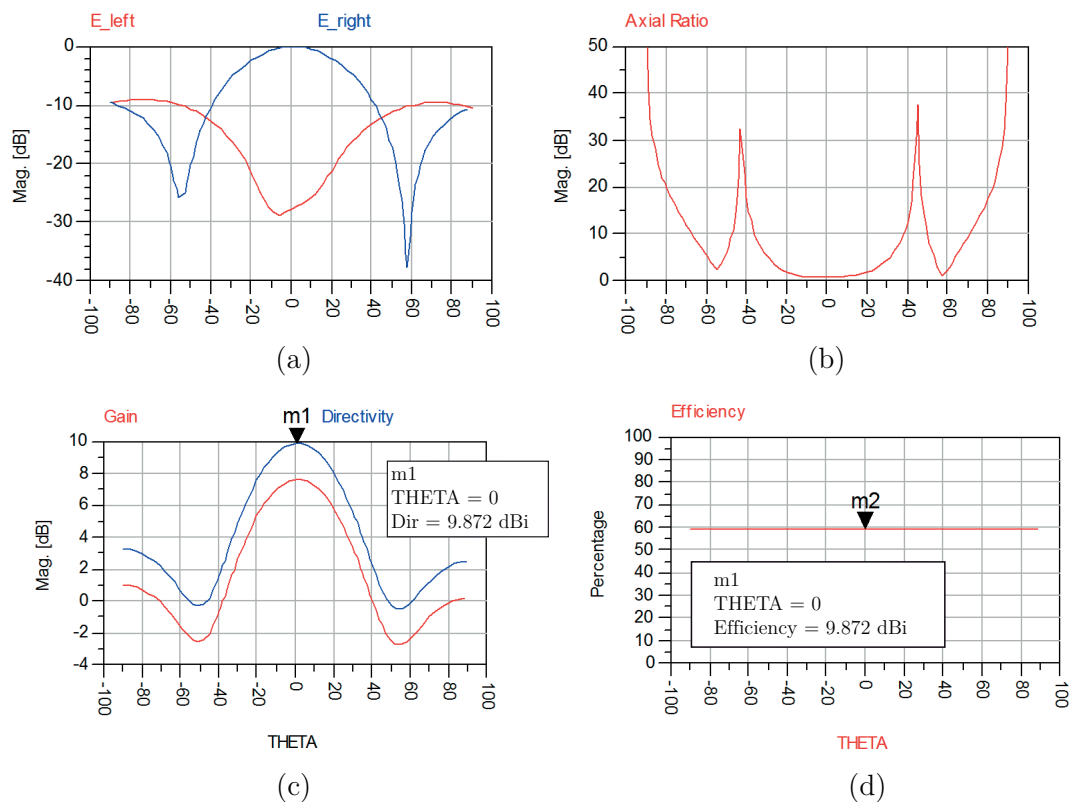


**Figure 2.34.:** Radiation pattern and power levels of the 8 slot square array at the frequency 2.5 GHz on one of the two main elevation planes.

If on one hand the presented configurations of slot antennas well satisfy the project specifications, they all suffer the problem of PPWG mode excitation: in fact, no solution

was found to prevent the PPWG mode excitation with a reasonably low thickness, while keeping a sufficiently large bandwidth. For this reason, we focused on the investigation of cavity-backed slot antennas.

### Cavity-backed slot antennas

A back-cavity naturally allows the total cancellation of the parasitic PPWG mode. Moreover, using specific cavity modes combined with the slot resonance allows to achieve efficient resonant antennas using much thinner structures (a few millimeters) than the classical reflector solution which requires a quarter-wavelength thickness (around 35 mm in S-band). However, this type of antennas suffer from a decreased bandwidth (a few percent) because they rely on strong resonances occurring in a small volume.

The investigation on cavity-backed slot antennas involved the design of three possible solutions. We describe here the final model; the complete illustration of all the designs can be found in App. A. The final antenna design is shown in Fig. 2.35.

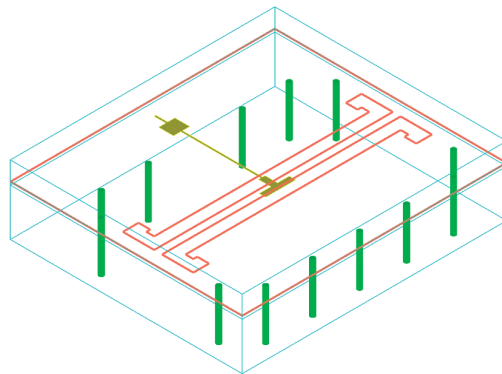


**Figure 2.35.:** Layout of the final slot single element.

It consists of two thin slots which have been bent to decrease the linear dimension. The radiator occupies a surface of  $60 \times 30$  mm, while the air gap which separates the ground plane from the reflector is 12 mm. The slot is fed by a  $50\Omega$  T-shaped microstrip line and surrounded by vias to avoid the propagation of the unwanted PPWG mode. The structure can be seen as some sort of cavity-backed slot antenna, but where the vertical walls of the cavity are not completely closed, which also appears more favorable in terms of bandwidth than completely closed cavities.

The substrate for the feed is the space qualified Rogers RO4350B (details in Tab. 2.7). The antenna has been simulated with Agilent ADS Momentum; in the simulation model, both ground planes are infinite. The relevant parameters of the antenna at the four frequencies which delimit the two bands of interest are reported in Tab. 2.8. The high efficiency observed confirm that the unwanted PPWG mode is effectively eliminated. Indeed, in the simulation

**Table 2.7.:** RO4350B substrate parameters.

<b>Rogers RO4350B</b>	
Relative permittivity	$\epsilon_r = 3.66$
Dielectric losses	$\tan \delta = 0.0037$

**Table 2.8.:** Performance of the final proposed antenna at the frequencies which delimit the bands of interest) ( $S_{11}$ : reflection coefficient,  $D$ : directivity,  $G$ : gain,  $\eta$ : efficiency,  $G_R$ : realized gain).

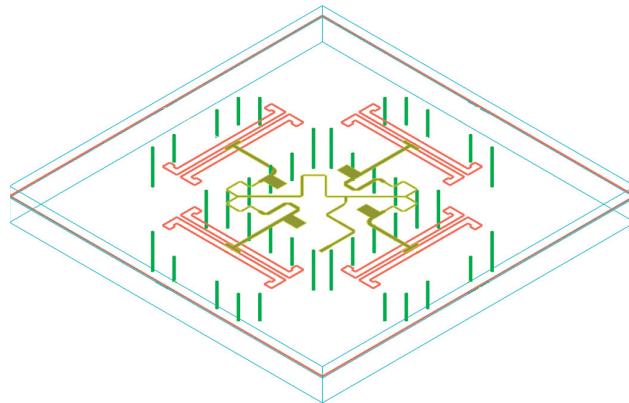
Freq [GHz]	$S_{11}$ [dB]	$D$ [dB]	$G$ [dB]	$\eta$ [%]	$G_R$ [dB]
2.025	-19.4	5.4	5.3	96	5.2
2.120	-15.5	5.5	5.4	99	5.3
2.200	-16.0	5.5	5.4	97	5.3
2.300	-18.4	5.6	5.4	94	5.3

any power leaked through this mode is not radiated since the two ground planes in the simulation model are infinite and would not contribute to the radiation.

### The final sub-array

As it was studied in Par. 2.4.1, the target pattern for one face for achieving Mode A, or omnidirectional mode, consists of a rather directional beam of 9.8 dB of maximum directivity. Major advantage of our strategy is the fact that this directive beam already meets the specifications of Mode B and can be re-used to generate the required directional beam. Therefore, the goal of the proposed solution is to arrange the basic radiating elements to achieve the target pattern.

The best performing solution is composed of 4 double slots arranged in a  $2 \times 2$  squared configuration, as depicted in Fig. 2.36; the 3D radiation pattern is shown in Fig. 2.37, while the radiation performance on the elevation cut is illustrated in Fig. 2.38.

**Figure 2.36.:** Layout of the complete sub-array.

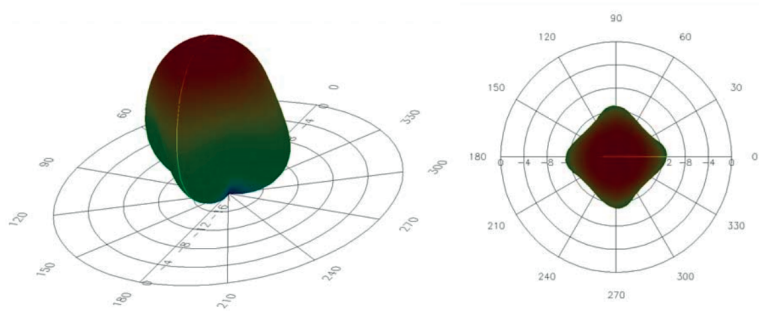


Figure 2.37.: 3D radiation pattern of the face sub-array designed for Mode A (reusable for Mode B).

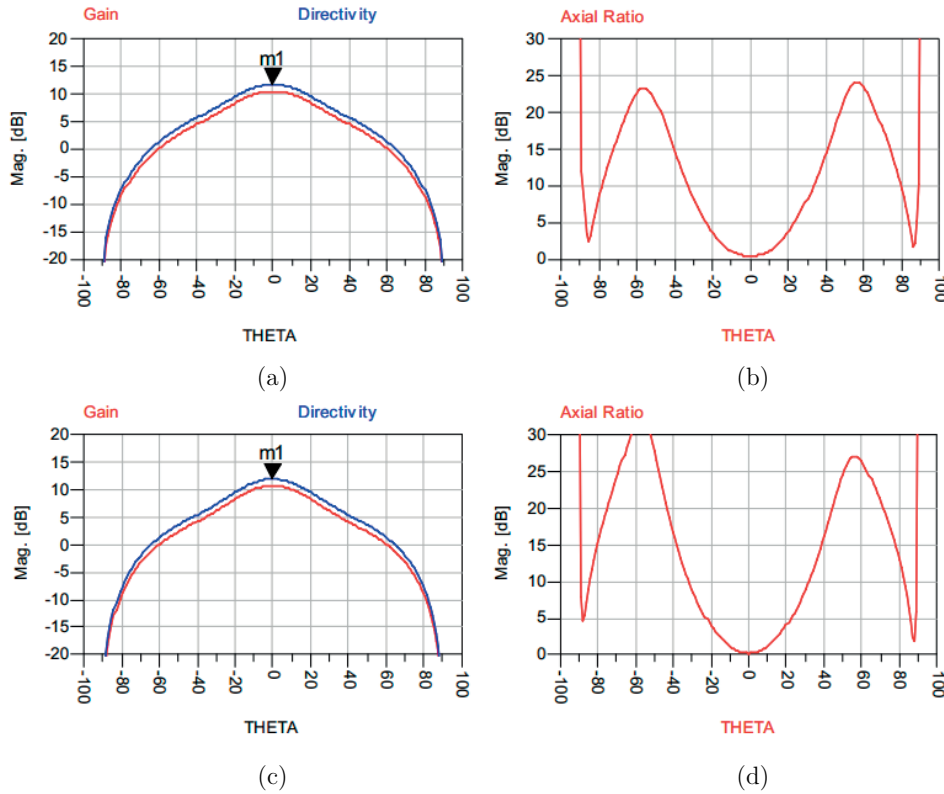
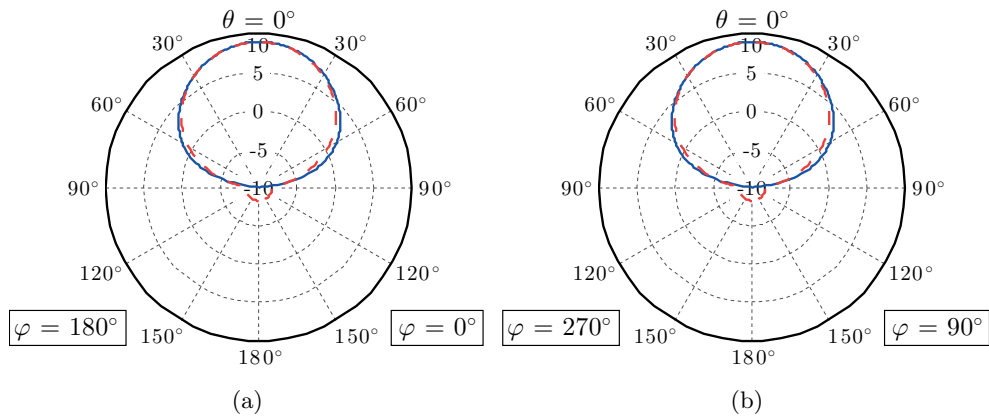


Figure 2.38.: 2D Gain and Axial Ratio cuts at (a,b) 2050 MHz and (c,d) 2250 MHz.

The detailed design and characterization of such sub-array is left to App. A which contains all the technological details of the adopted solution. Moreover, it is shown there that the final sub-array of Fig. 2.36 is also suitable for antenna Modes B and C. It was found that the best position which minimizes the radiation towards end-fire angles was obtained by spacing the elements 64 mm apart (almost  $\lambda/2$  in free space) and turning them to form a square. Furthermore, applying a sequential rotation to the linear elements provides the circularly polarized radiation pattern.

The comparison between the obtained face sub-array and the target pattern is shown in Fig. 2.39: the agreement is very good on both planes, anticipating a good preservation of the radiation performance obtained with the ideal antenna system.



**Figure 2.39.:** Radiation pattern comparison between the ideal and the designed radiator; (a)  $\varphi = 0$  plane and (b)  $\varphi = 90$

#### 2.4.5. The final antenna system and the measurement campaign

The sub-array of customized slot antennas described in the previous section has been manufactured and assembled to realize the Proof-Of-Concept architecture. Fig. 2.40 illustrates the exploded structure: the satellite walls and the six face elements. In Fig. 2.41(a) is visible the inside of the satellite, with four of the six face-elements connected to the power divider. Fig. 2.41(b) shows the final prototype.

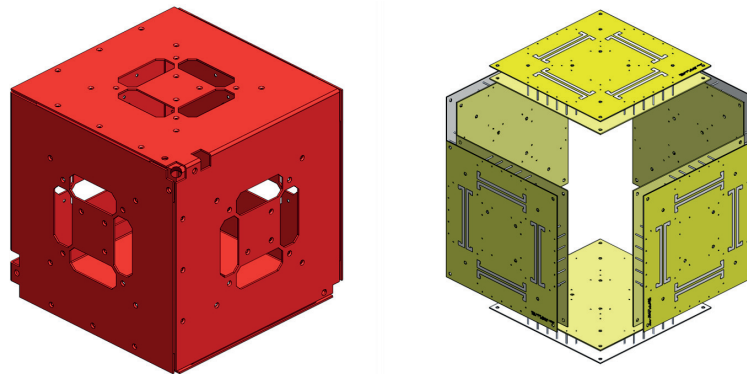


**Figure 2.40.:** The exploded view of the POC.



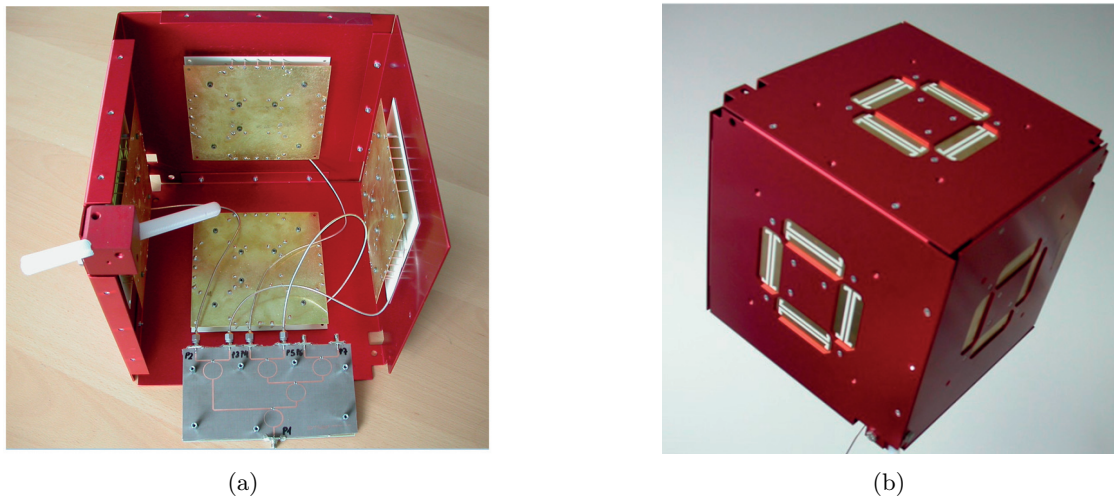


**Figure 2.41.:** The POC: (a) internal view of the POC and (b) the final assembly.

### The measurement campaign

The three antenna modes generated by the POC were measured in EPFL-LEMA anechoic chamber. A standard linearly polarised horn antenna was used for the Co- and Cross-Polarization measurements; though the polarization could not be directly identified with our measurement setup, it was easily inferable from the measures in the regions where one of the two polarization are predominant and known.

Measurements were performed within the operative frequency  $2025 \sim 2030$  MHz. Absolute Gain measures could not be obtained due to unavailability at the time of the campaign of a third antenna for the "three antennas method"; the curves in this section are therefore presented as Normalized Gain patterns [dBn]. Note that the normalized Gain is perfectly sufficient for the quantification of the Global Coverage (1.2), defined with respect to the maximum Gain.

The measurements of the Mode A (omnidirectional) radiation pattern were performed along two cuts:

- Plane "R": the satellite lies on a LHCP face (Fig. 2.42) and the face sub-arrays on the four lateral faces are RHCP. The cut is along the azimuth plane.
- Plane "RL": the satellite lies on a RHCP face (similar to Fig. 2.42) but the lateral faces sub-arrays are alternately R- and L-HCP polarized. The cut is along the azimuth plane.

The center frequency ( $f = 2.15$  GHz) radiation pattern are presented hereafter in Fig. 2.43 and Fig. 2.44. The diagrams on the left column show separately the normalized Gain for RHCP and LHCP components of the radiated fields, renamed CO- and X-POL. As the specifications require the *strongest* of the two circular polarizations to be within a range  $-6$  dB from the maximum gain, in the plot on the right it is shown for better readability the

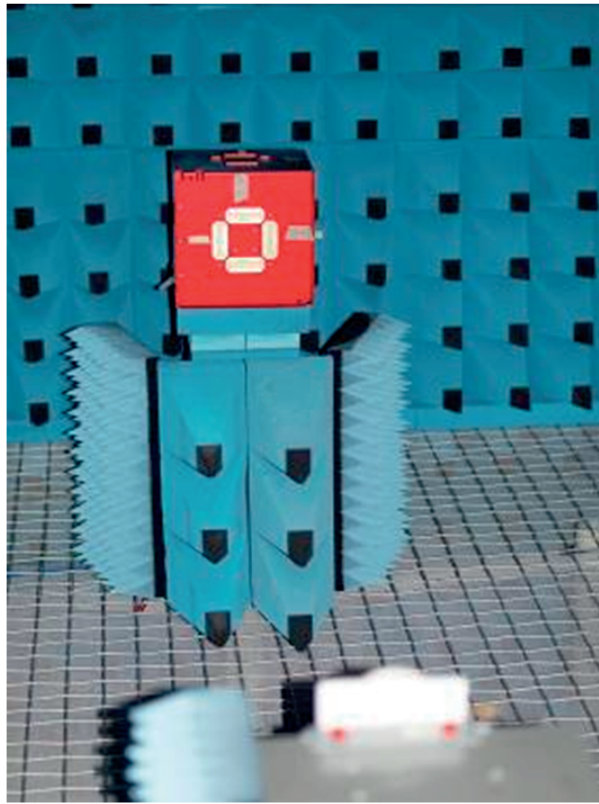


**Figure 2.42.:** Measurement setup for cuts R and RL (the POC is lying on a different face in the second case).

strongest of the two polarization and the range where patterns are within the specifications (light blue area).

A more exhaustive characterization of the antenna system radiation patterns for the three modes and within the whole operative bandwidth, together with the measurements of the Beam Feeding Network reflection losses, is documented in App. A.

Regarding performances, the Global Coverage ranges from 70% up to 90% in all the patterns shown and can be retained overall satisfying. This holds in particular not only at center frequency, but also in the adjacent frequencies within the operation bandwidth dictated by the antenna reflection coefficient.

## 2.5. MAST measurements compared with SatAF

The satisfying results of the measurement campaign are an important and necessary proof of the solidity of the work performed; more interesting than the very results is anyway the comparison of the measured radiation patterns with SatAF predictions, not only in

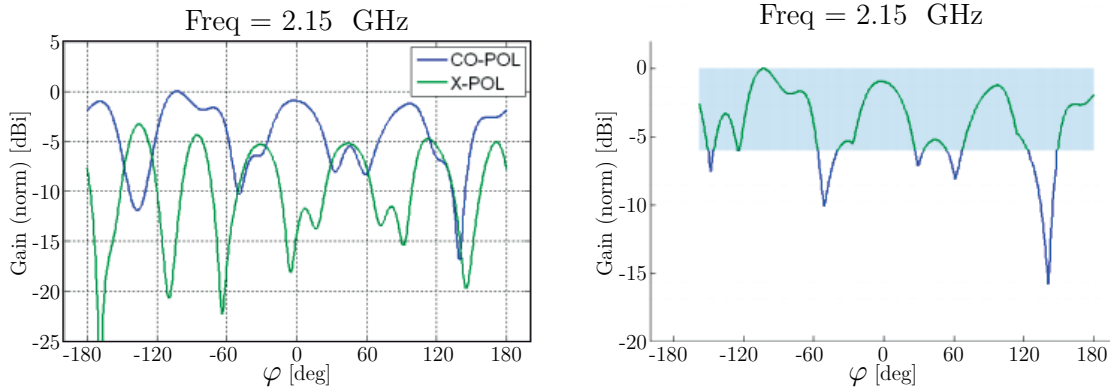


**Figure 2.43.:** Measured radiation pattern of Mode A in “R” setup: CO- and X-POL diagrams (left) and strongest R-/L-HCP component (right). The three frequencies correspond to lower bound, center and upper bound of the operative band.

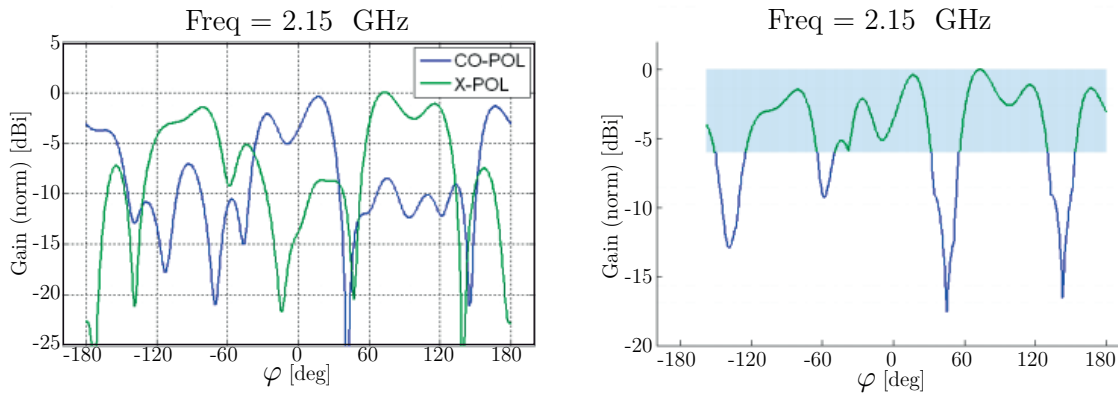


**Figure 2.44.:** Measured radiation pattern of Mode A in “RL” setup: CO- and X-POL diagrams (left) and strongest R-/L-HCP component (right). The three frequencies correspond to lower bound, center and upper bound of the operative band.

the context of this thesis but also due to the decision of manufacturing and measuring a Proof-of-Concept antenna system, similar but simpler than the architecture identified as best candidate (Par. 2.4.1), privileging the validation of the adopted design strategy to the maximization of performances. A reasonable agreement between predicted and measured radiation patterns was decided to constitute a sufficient proof of the reliability and quality of the actually proposed antenna system.

The measured patterns for Mode A are here compared with SatAF predictions. As the sub-array was re-adapted for the additional generation of Mode C, the slight modification in its radiation pattern, in the form of a narrowing of the main lobe, has been compensated by

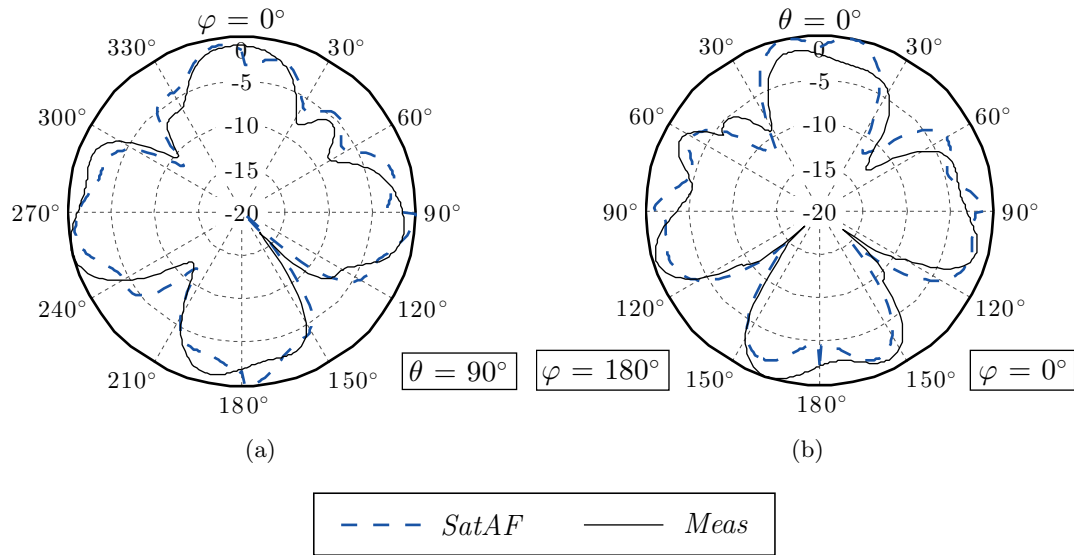


**Figure 2.45.:** Radiation pattern comparison between SatAF predictions and measurements: (a), RHCP component relative to the “R” setup; (b), strongest R-/L-HCP component relative to the “RL” setup

increasing the size of the virtual element (the circular patch described in Par. 2.4.1) used as input for SatAF, in order to make the comparison actually meaningful.

In Fig. 2.45 are shown the comparisons relative to the setups “R” and “RL”. In the first plot, the RHCP component of the field is shown, being the predominant in the considered cut; in the second, R- and L-HCP polarizations are mixed and the strongest component is drawn. The curves exhibit a good agreement: the overall pattern shape is correctly predicted and, despite the evident differences between the ideal element and the realized one, the deviation is almost everywhere lower than 1.5 dB.

## 2.6. SatAF final assessment and potential improvements

The MATLAB tool SatAF was designed for a first-approach analysis of the radiation performance of the antenna systems involved in the design process performed in the frame of the MAST project.

The strategy adopted for the design allowed the definition of a series of hypotheses and simplifications: basically, we assumed that the far fields generated by an array of sources allocated on a metallic platform is only determined by direct radiation, while the phenomena of edge diffraction and mutual coupling are assumed negligible. This concept has been implemented in SatAF obtaining a strong reduction of the antenna arrays simulation time.

The design of the antenna system, at level of radiation pattern and for the three requested antenna modes, was almost exclusively performed through SatAF. The reliability and usefulness of the software have been confirmed by benchmark campaign described in the previous sections.

It is anyway a fact that this basic version of SatAF suffers some non-negligible limitations. In first place, when slot antennas were selected as radiating element, an external software (Agilent ADS) was necessary to analyze apertures with non standard shape (such as C-slots or dog-bones), as the original SatAF does not offer any possibility in this direction. Secondly, it must be kept in mind that the hypotheses on which SatAF is based can be safely assumed only when working with directive elements, which represent only a restricted class of radiators. This fact actually limits the range of applicability of the software to a particular type of problems, whose most representative example is obviously MAST. The degradation of accuracy which occurs when any of the hypotheses is violated can include lobes misplacement and significative pattern discontinuities.

A strategic combination of SatAF with a full-wave analysis method could remove all the aforementioned limitations and significantly improve the accuracy of the software, without renouncing to computational speed, main advantage of the tool. Retaining the fundamental concept of identifying a “basic radiator” in an antenna array, computing and replicating its radiation pattern according to the different positions and orientations, a local full-wave simulation can be used to generate the “basic” radiation pattern (in place of the analytical formula used in the first version of the software) which is then imported in SatAF and treated according to 3D Array Theory.

Some preliminary test on simple geometries, inspired by the MAST design process, were performed and confirmed the expectations; the most significant one are illustrated hereafter. In the examples, we consider arrays of slot antennas lying either on finite size ground planes or on 3D platforms. In each case, we compare three methods:

- The array is solved using the basic version of SatAF, i.e. using analytical formulas to generate the basic element’s radiation pattern (SatAF + Math).
- The radiation pattern of a sub-set of elements is generated using the commercial full-wave software Ansoft HFSS and is imported in SatAF, which is used to generate the total radiation pattern (SatAF + HFSS).
- The simulation of the whole structure, performed with HFSS, is used as reference (Full HFSS).

For each case, we specify the sub-set used for point 2 (SatAF + HFSS) and we refer to it with “basic element”.

Let us consider in the first test case a pair of thin, rectangular apertures of size  $0.4 \times 7.6$  cm on a finite size ground plane (a square of 15 cm side) as shown in Fig. 2.46; the operating frequency is set to 2 GHz. As “basic element” we use a single slot lying in the center of the ground plane. The comparison on the two main cuts is shown in Fig. 2.47: the limits of using an analytical formula for the slot are evident, as well as the excellent agreement obtained combining SatAF and HFSS.

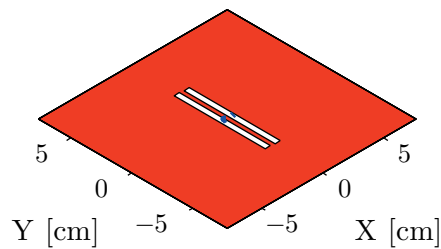


Figure 2.46.: Test case 1, layout.

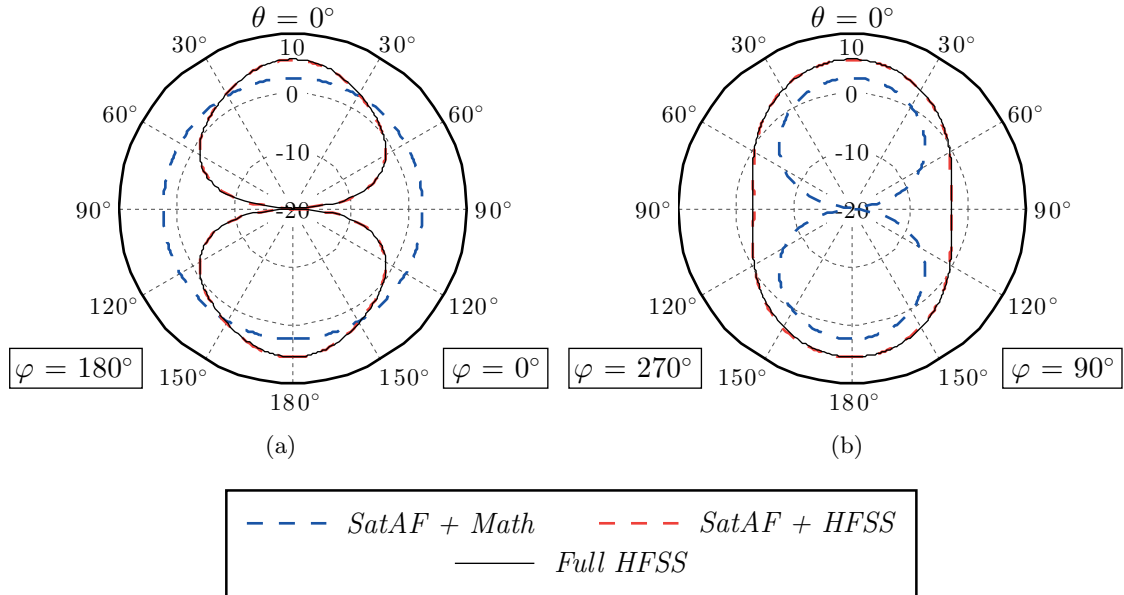
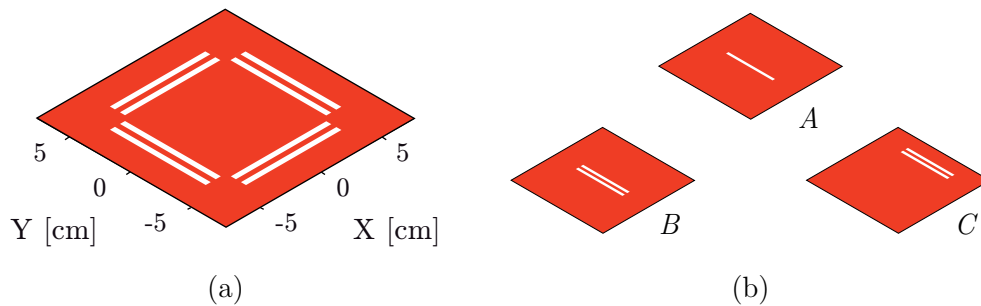


Figure 2.47.: Test case 1: radiation pattern comparison on (b)  $\varphi = 0$  deg and (c)  $\varphi = 90$  deg.

The second test case involves a 4 elements array of slot pairs (Fig. 2.48a). Three “basic elements” are used for SatAF:

- A single slot in the center of the ground plane (SatAF\_A + HFSS).
- A double slot in the center of the ground plane (SatAF\_B + HFSS).
- A double slot occupying on the ground plane the same position as in the array (SatAF\_C + HFSS).

The three basic elements are sketched in Fig. 2.48b. Now, we see that only in the third case an acceptable agreement is obtained (Fig. 2.49).



**Figure 2.48.:** Test case 2: (a) layout and (b) basic elements used.

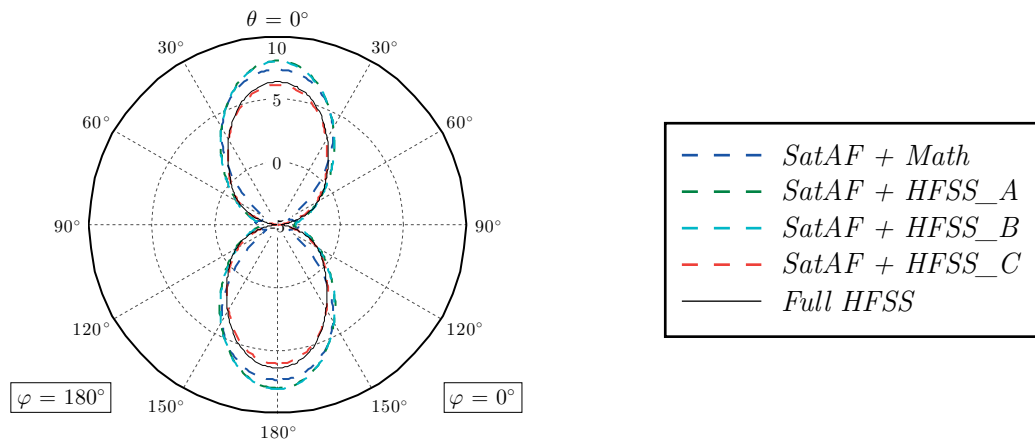


**Figure 2.49.:** Test case 2: radiation patterns on the  $\varphi = 0$  deg cut.

When considering a 3D geometry, the benefits of introducing a local full-wave analysis become more evident. We propose as last test case a cubic geometry similar to the MAST antenna system: six rings of four slot pairs are located in the center of the faces of a 25 cm cubic platform, as it is sketched in Fig. 2.50. A single pair of slots lying on a ground plane of the size of the face is used as input for SatAF (case “C” in Fig. 2.48b).

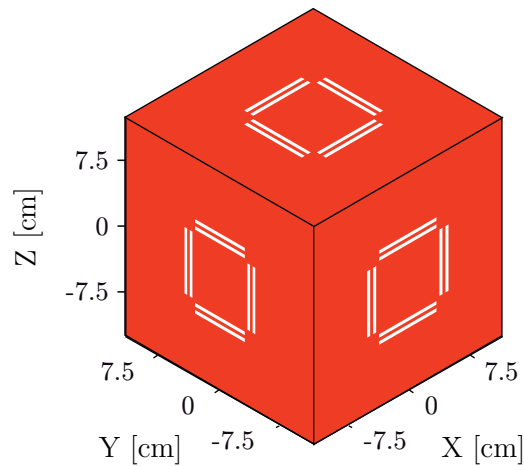


**Figure 2.50.:** Test case 3, layout.

The radiation pattern comparison is performed using two different excitation phase schemes for the array elements, simply named Feed Scheme 1 and Feed Scheme 2; results are shown respectively in the groups of figures Fig. 2.51, Fig. 2.52, Fig. 2.53 and Fig. 2.54, Fig. 2.55, Fig. 2.56 representing the main elevation and azimuth cuts.

The plots contain a twofold information: using a mathematical model, the position and amplitude of the radiation lobes and nulls can be fairly predicted but in some regions the deviation from the reference reaches high values. The accuracy improvement obtained with the local full-wave simulation is significant and makes the predictions in excellent agreement with the reference.



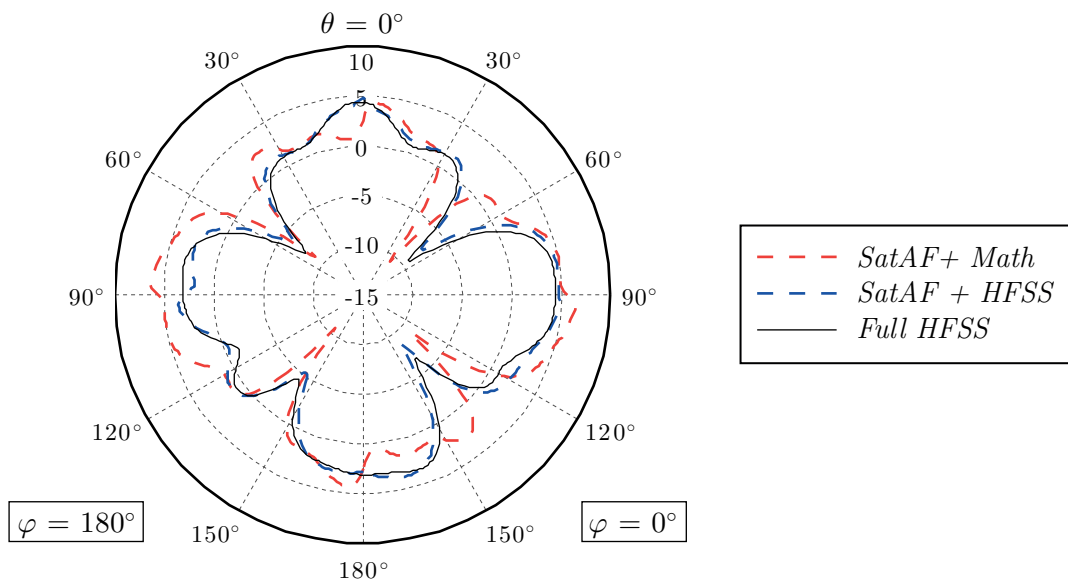


Figure 2.51.: Test case 3, Feed Scheme 1: radiation patterns on  $\varphi = 0$  deg cut.

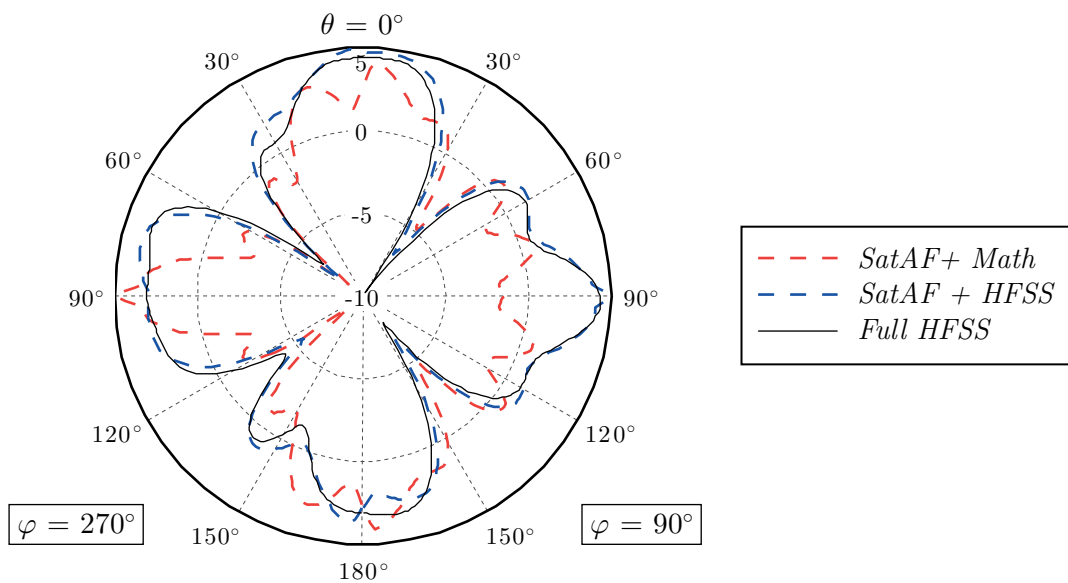
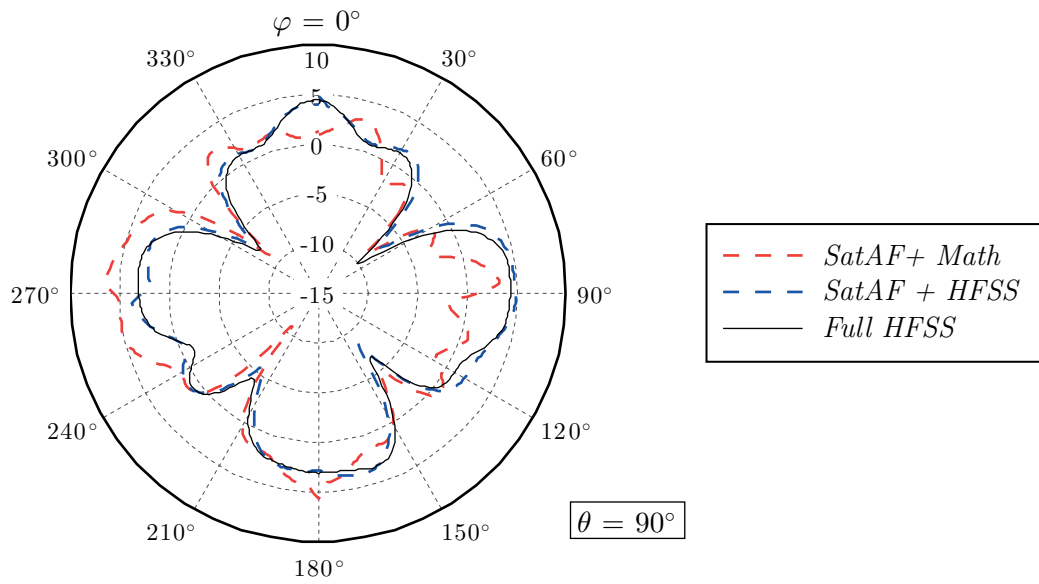
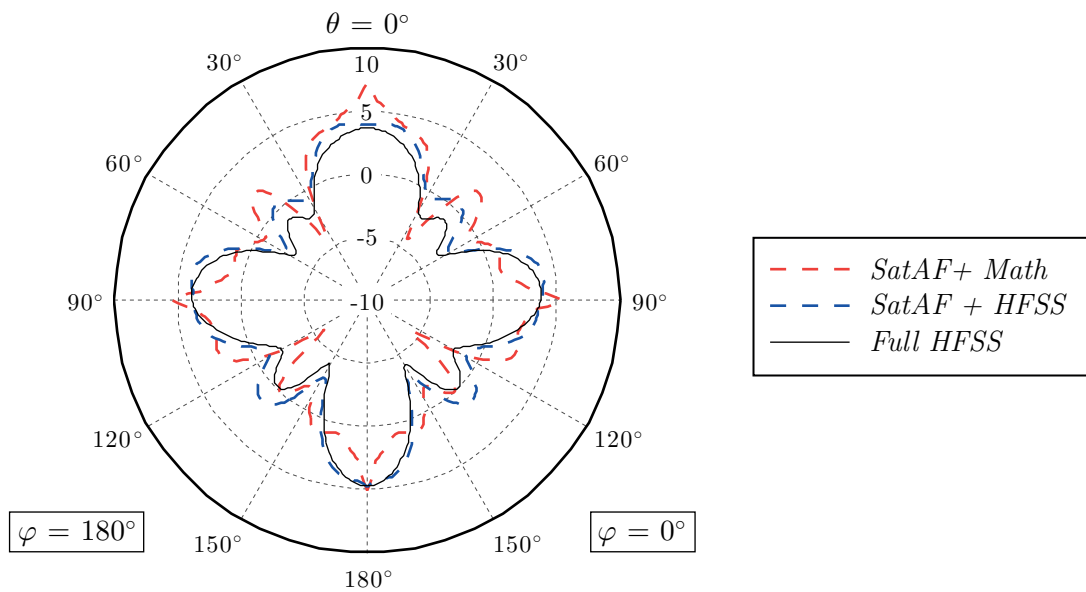


Figure 2.52.: Test case 3, Feed Scheme 1: radiation patterns on  $\varphi = 90$  deg cut.



**Figure 2.53.:** Test case 3, Feed Scheme 1: radiation patterns on  $\theta = 90$  deg cut.



**Figure 2.54.:** Test case 3, Feed Scheme 2: radiation patterns on  $\phi = 0$  deg cut.

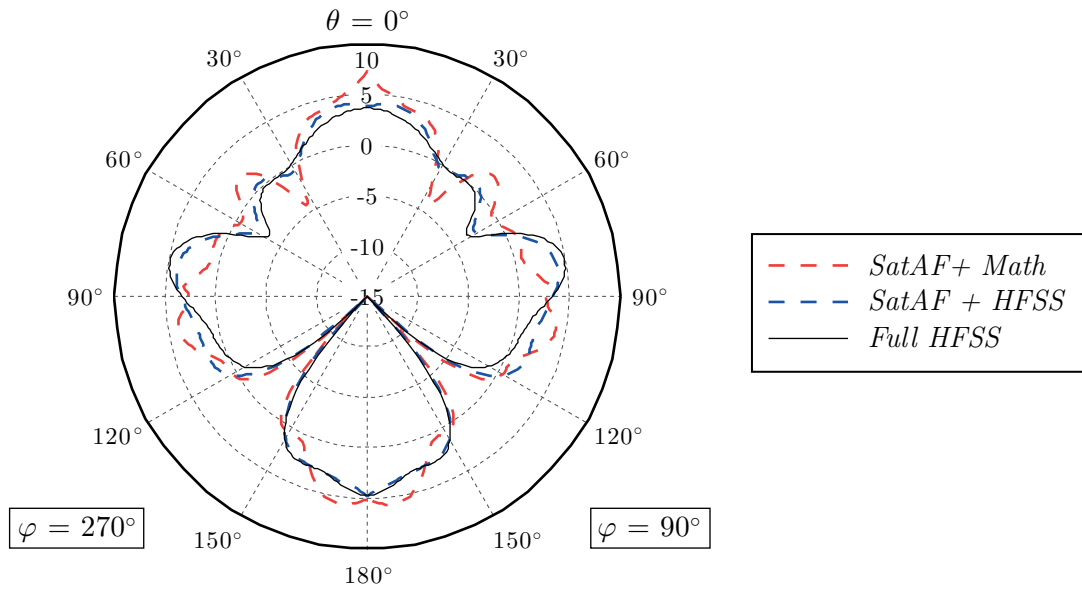


Figure 2.55.: Test case 3, Feed Scheme 2: radiation patterns on  $\varphi = 90$  deg cut.

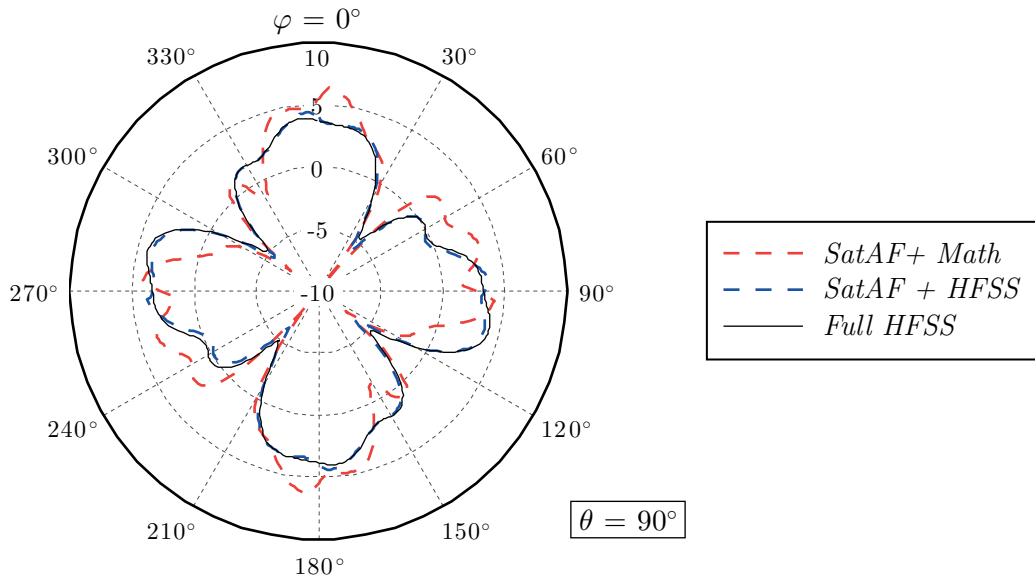


Figure 2.56.: Test case 3, Feed Scheme 2: radiation patterns on  $\theta = 90$  deg cut.

After this investigation, the most advantageous strategy for combining SatAF with full waves simulators can be summarized in the following statements:

- The basic version of SatAF, making use of analytical formulas to represent elements' radiation patterns, is inadequate for the analysis of complex arrays of slot antennas.
- Local full-wave simulations are absolutely necessary for the correct treatment of non-standard geometries, in particular offset-fed or customized shaped slot antennas.
- In two dimensional geometries, the radiation pattern of slot antenna arrays are accurately predicted only when the basic element occupies, on the ground plane, the same position as in the array.
- On a 3D platform, the analysis of the entire antenna system can be reduced to the simulation of a sub-array on a 2D geometry (a ground plane representing a platform face), once the basic element is identified. After the faces sub-array radiated fields are computed, they can be imported in SatAF for the generation of the total radiation pattern.
- The replacement of the sub-array ground plane with the 3D platform introduces a minimal improvement which does not justify the increase in complexity and computational time.

## 2.7. Conclusions

In this chapter we illustrated the multi-functional antenna system for micro/nano-satellites designed in the frame of the ESA project MAST. The proposed architecture consists of an array of customized slot antennas allocated on a micro-satellite (a platform of 25 cm side) and allows the generation of three antenna modes:

- Mode A - Omnidirectional
- Mode B - Directive beam
- Mode C - Tracking lobes

operating in circular polarization in S-band and according to the specifications provided in Sec. 1.4.

The omnidirectional mode was recognized as the real challenge of the design. The presence of the satellite (a metallic body of an electric size which could be considered neither small like in missions operating in V/UHF band, and thus be neglected, neither very large, like in classic spacecrafts and be assimilated to an indefinite metallic surface) prevents the use of independent elements producing by themselves omnidirectional patterns, as their radiation would be significantly affected by the platform, deteriorating in all likelihood the

performance.

Two opposite strategies were conceived to deal with the problem: on one hand, the use of simple emitters to excite currents on the satellite surface, which would generate the required radiation pattern; a second possibility envisaged the use of directive elements, less dependent on the specific characteristics of the platform, to generate by pattern superposition the omnidirectional field.

Simple electromagnetic consideration led us to adopt from the very beginning the second strategy. The idea of making use of the satellite as an antenna proved fascinating and yet misleading, due to the implicit and non realistic constraint of having the design of the entire spacecraft to be dictated exclusively according to electromagnetic issues. On the other hand, concentrating surface currents in limited regions of the platform allows a robust design, easily adaptable to different platforms, A feasibility study was undertaken and quickly confirmed the expectations.

A number of different architectures involving the radiating elements the most suitable for space applications were investigated and evaluated according to three parameters: performance (in terms of omnidirectional coverage), number of elements required and complexity of the satellite shape.

A key role in the phase of array designing was held by the in-house developed MATLAB software SatAF. The tool, essentially combining three-dimensional array theory with pattern interpolation and neglecting second-order radiation components such as diffraction or mutual coupling between sources, constitutes a good compromise between simulation speed and accuracy of results, other than offering a convenient interface for the quick control of the array elements, often present in a high number.

A sub-array of customized slot antennas was designed according to the outcomes of the array design phase. As an extra asset, the antenna system re-uses this very element to generate the two remaining antenna modes (Mode B or directive beam, Mode C or TT&C mode), via dedicated Beam Forming Networks, for a maximum degree of integration.

A set of best performing architectures was selected among the proposed designs while a simplified structure was selected as prototype, retaining an agreement between simulated results and measurements a proof of the performance of the other antenna systems. The Proof-of-Concept was realized and characterized through a measurement campaign. The outcome was that performance generally confirms simulations predictions, even though some aspects, typical of realization processes, have been identified as responsible for perturbations. The measurements validated the strategy adopted through the development of the project and highlighted the robustness of the software SatAF, its usefulness and its correct implementation.

The benchmark and measurement campaigns established the in-house software SatAF as a reliable simulation software and proved its usefulness, especially for the design of antenna systems for small platforms. Nevertheless, a successful use of the tool requires the knowledge and the respect of the hypotheses on which the implemented method is based; if on one hand this aspect did not prevent the application of SatAF for the design of MAST, it limited its use to a restricted class of configurations: when the design was oriented towards slot antennas, in particular with non-standard geometries, the use of an external software became necessary to support the design.

The combination of SatAF with *local* simulations of sub-sets of the elements constituting the antenna system appears as an interesting opportunity to extend SatAF beyond the restricted class of problems for which it was designed and to improve the accuracy of the predictions, without compromising its advantage in computational speed with respect to all-purpose simulation software.

In particular we showed that retaining the array theory concept, core of the tool, the solution of complex 3D architectures can be successfully decomposed into the analysis of two-dimensional geometries to be solved with a full-wave method and elaborated with SatAF to produce the total radiation pattern.

This perspective is investigated in the remaining part of this thesis work, with special attention dedicated to the treatment of aperture antennas, both for their relevancy as space-qualified radiator and for the weakness shown by SatAF towards them.

Starting with the choice as full-wave method of the Method of Moments (MoM) and the recall of the fundamental theoretical concepts necessary for the discussion (Chap. 3), the dissertation proceeds through Chap. 4 where a novel, simplified analysis model for the excitation of slot antennas is introduced, to the illustration in Chap. 5 of an original computational method which we call the “Magic Distance Inspired” method: derived from the classical formulation of MoM, it allows a strong reduction of the computational effort especially in its final combination with SatAF, whose description in Chap. 6 concludes this thesis work.







## 3. Integral Equations and Method of Moments

In the frame of the development of an improved version of the simulation tool SatAF, already used for the design of the MAST antenna system, we investigated the possibility of simplifying the classical formulation of one among the most popular and reliable analysis methods in Computational Electromagnetics: the Integral Equation (IE) formulation solved with the Method of Moments (MoM). Targeting the best compromise between speed and accuracy in the prediction of the radiation performance of an antenna system and concentrating on the type of structures relevant to MAST, we explored the MoM in all its aspects and we concentrated on the ones relevant for our purposes, in particular the replacement of the integral evaluations with point-to-point calculations.

In this chapter, we recall the analytical background elements necessary for the illustration of the methods studied in this work: the fundamental electromagnetic theory, the definition of Integral Equation and its solution via the Method of Moments. The concepts of this chapter can be found scattered among many textbooks and tutorial papers and are collected here with a uniform notation for the sake of completeness of the thesis.

### 3.1. Electromagnetics fundamentals

In this section we recall the mathematical elements necessary for the discussion of the numerical methods developed in the frame of this thesis work, in particular the Method of Moments. The treatment of the various topics is specialized to the class of problems involving metallic structures radiating in free space, in view of the application to the design of antenna systems treated in the previous chapter.

#### 3.1.1. Maxwell equations

Classical electromagnetic phenomena occurring within an arbitrary medium can be described by a consistent set of vector equations, the Maxwell Equations. When fields are characterized by a harmonic time dependence  $\exp(j\omega t)$ , the equations can be expressed in the frequency

domain in differential form [43]:

$$\nabla \times \mathbf{E} = -j\omega\mathbf{B} - \mathbf{M} \quad (3.1a)$$

$$\nabla \times \mathbf{H} = +j\omega\mathbf{D} + \mathbf{J} \quad (3.1b)$$

$$\nabla \cdot \mathbf{D} = \rho_e \quad (3.1c)$$

$$\nabla \cdot \mathbf{B} = \rho_m \quad (3.1d)$$

where  $\mathbf{E}$  and  $\mathbf{H}$  are the electric and magnetic field intensities,  $\mathbf{D}$  and  $\mathbf{B}$  are the electric and magnetic flux densities,  $\mathbf{J}$  and  $\mathbf{M}$  the electric and magnetic current densities and  $\rho_e$ ,  $\rho_m$  the electric and magnetic charge densities. Induced magnetic current and charges have been introduced to the classical Maxwell-Minkowski formulation [44] to balance the equations; even if not present in nature, they appear as equivalent quantities in many physical problems. In this formulation, (3.1a) is the (modified) Faraday's Law, (3.1b) is the Ampere's Law, (3.1c) and (3.1d) are respectively called the electric and (modified) magnetic Gauss Laws.

In addition to (3.1), a set of three equations relating the electromagnetic fields is introduced to account for the characteristics of the medium, the constitutive relations:

$$\mathbf{D} = \varepsilon\mathbf{E} \quad (3.2a)$$

$$\mathbf{B} = \mu\mathbf{H} \quad (3.2b)$$

$$\mathbf{J} = \sigma\mathbf{E} \quad (3.2c)$$

where  $\varepsilon$  is the complex permittivity of the medium,  $\mu$  the complex permeability and  $\sigma$  the complex conductivity.

These constitutive equations won't be much relevant in this thesis since we concentrate on free-space situations. On the other hand, the Continuity Equations relating current and charges are of particular interest in our formulations. Taking the divergence of (3.1b) and using (3.1c) we get the first of:

$$\nabla \cdot \mathbf{J} + j\omega\rho_e = 0 \quad (3.3a)$$

$$\nabla \cdot \mathbf{M} + j\omega\rho_m = 0 \quad (3.3b)$$

while the second equation can be obtained for the corresponding magnetic quantities.

This tells us that the current densities  $\mathbf{J}$  and  $\mathbf{M}$  can be considered as the sole sources in an electromagnetic problem, the charge densities being fully defined by the currents. However, in many strategies it is worth to consider charge densities as explicit sources. In that case, we need to represent the current densities with functions whose divergence is mathematically well-defined.

The validity of Maxwell Equations requires the field vectors to be single valued and bounded functions, continuous and with continuous derivative: these assumptions are generally satisfied as long as charge and current densities do not exhibit a singular behavior. Typically, discon-

tinuous distributions of charges and currents occur in correspondence of interfaces between media characterized by different electrical parameters  $\varepsilon$  and  $\mu$ . The behavior of electromagnetic fields across the interfaces is governed by the boundary conditions:

$$\hat{\mathbf{n}} \times (\mathbf{E}_2 - \mathbf{E}_1) = \mathbf{M}_s \quad (3.4a)$$

$$\hat{\mathbf{n}} \times (\mathbf{H}_2 - \mathbf{H}_1) = \mathbf{J}_s \quad (3.4b)$$

$$\hat{\mathbf{n}} \cdot (\varepsilon_2 \mathbf{E}_2 - \varepsilon_1 \mathbf{E}_1) = \rho_{es} \quad (3.4c)$$

$$\hat{\mathbf{n}} \cdot (\mu_2 \mathbf{H}_2 - \mu_1 \mathbf{H}_1) = \rho_{ms} \quad (3.4d)$$

$$(3.4e)$$

with the subscripts 1 and 2 indicating the two media along the interface  $S$  separating the two media. The quantities  $\mathbf{J}_s$  and  $\mathbf{M}_s$  are the electric and magnetic current linear densities ( $[A/m]$  and  $[V/m]$ ) while  $\rho_{es}$  and  $\rho_{ms}$  are the electric and magnetic charge surface densities ( $[C/m^2]$  and  $[Wb/m^2]$ ).

The particular case where one of the two media is a Perfect Electric Conductor, PEC, is specifically addressed in this work. Inside a PEC, fields vanish and (3.4) simplify into:

$$\hat{\mathbf{n}} \times \mathbf{E} = 0 \quad (3.5a)$$

$$\hat{\mathbf{n}} \times \mathbf{H} = \mathbf{J}_s \quad (3.5b)$$

$$\hat{\mathbf{n}} \cdot (\varepsilon \mathbf{E}) = \rho_{es} \quad (3.5c)$$

$$\hat{\mathbf{n}} \cdot (\mu \mathbf{H}) = 0 \quad (3.5d)$$

$$(3.5e)$$

valid in any point of the interface.

### 3.1.2. Potentials formulation

The solution of electromagnetic scattering problems is often simplified by the introduction of additional functions, the vector and scalar potentials  $\mathbf{A}$  and  $\phi_e$  (electric) and  $\mathbf{F}$  and  $\phi_m$  (magnetic). While electric and magnetic fields represent physical quantities, the potentials are strictly mathematical tools which are derived by manipulations of the Maxwell Equations (3.1).

We consider in this section the case of a homogeneous region. The linearity of the Maxwell Equations allows to separate a generic electromagnetic problem in two parts, one involving only electric sources, only magnetic sources the other. The fields present in the two cases are identified by the subscripts  $\mathbf{A}$  and  $\mathbf{F}$  respectively; following a parallel procedure, we derive the

necessary quantities which allow to express the total fields:

$$\mathbf{H} = \mathbf{H}_A + \mathbf{H}_F \quad (3.6a)$$

$$\mathbf{E} = \mathbf{E}_A + \mathbf{E}_F \quad (3.6b)$$

Due to the absence of electric or magnetic charge, the electric and magnetic flux densities  $\mathbf{D}_F$  and  $\mathbf{B}_A$  are solenoidal and can be expressed as the curl of another vector  $\mathbf{F}$  and  $\mathbf{A}$  respectively, the vector potentials. Through the constitutive relations (3.2), we can express the electric and magnetic fields as functions of the vector potentials:

$$\mathbf{H}_A = +\frac{1}{\mu} \nabla \times \mathbf{A} \quad (3.7a)$$

$$\mathbf{E}_F = -\frac{1}{\varepsilon} \nabla \times \mathbf{F} \quad (3.7b)$$

A manipulation of Maxwell Equations leads to the relations:

$$\nabla \times [\mathbf{E}_A + j\omega\mathbf{A}] = 0 \quad (3.8a)$$

$$\nabla \times [\mathbf{H}_F + j\omega\mathbf{F}] = 0 \quad (3.8b)$$

The quantities between brackets are irrotational and can be expressed as the gradient of another function  $\phi_e$  and  $\phi_m$  respectively, the scalar potentials. This choice allows to define the vectors:

$$\mathbf{E}_A = -j\omega\mathbf{A} - \nabla\phi_e \quad (3.9a)$$

$$\mathbf{H}_F = -j\omega\mathbf{F} - \nabla\phi_m \quad (3.9b)$$

By combining (3.7) and (3.9) with the Maxwell Equations (3.1) and applying the assumption of homogeneous medium ( $\varepsilon$  and  $\mu$  are independent on the position vector), further calculations yield the following equivalences:

$$\nabla^2 \mathbf{A} + k^2 \mathbf{A} = -\mu \mathbf{J} + \nabla(\nabla \cdot \mathbf{A} + j\omega\varepsilon\phi_e) \quad (3.10a)$$

$$\nabla^2 \mathbf{F} + k^2 \mathbf{F} = -\varepsilon \mathbf{M} + \nabla(\nabla \cdot \mathbf{F} + j\omega\mu\phi_m) \quad (3.10b)$$

with  $k = \omega\sqrt{\varepsilon\mu}$ .

In order to uniquely define  $\mathbf{A}$  and  $\mathbf{F}$ , both the divergence and the curl are required and can be defined independently one from the other. In (3.7) the curls were defined; one possible choice for the divergences is the *Lorentz Gauge*:

$$\nabla \cdot \mathbf{A} = -j\omega\mu\varepsilon\phi_e \quad (3.11a)$$

$$\nabla \cdot \mathbf{F} = -j\omega\mu\varepsilon\phi_m \quad (3.11b)$$

Thanks to this choice, (3.10) reduces to:

$$\nabla^2 \mathbf{A} + k^2 \mathbf{A} = -\mu \mathbf{J} \quad (3.12a)$$

$$\nabla^2 \mathbf{F} + k^2 \mathbf{F} = -\varepsilon \mathbf{M} \quad (3.12b)$$

while taking the divergence of (3.9) and combining the *Lorentz Gauge* (3.3) yields:

$$\nabla^2 \phi_e + k^2 \phi_e = -\frac{1}{\varepsilon} \rho_e \quad (3.13a)$$

$$\nabla^2 \phi_m + k^2 \phi_m = -\frac{1}{\mu} \rho_m \quad (3.13b)$$

When combined, (3.7) and (3.9) allow the expression of the fields in terms of the “mixed” potentials [45]:

$$\mathbf{E} = \mathbf{E}_A + \mathbf{E}_F = -j\omega \mathbf{A} - \nabla \phi_e - \frac{1}{\varepsilon} \nabla \times \mathbf{F} \quad (3.14a)$$

$$\mathbf{H} = \mathbf{H}_A + \mathbf{H}_F = -j\omega \mathbf{F} - \nabla \phi_m + \frac{1}{\mu} \nabla \times \mathbf{A} \quad (3.14b)$$

or, equivalently, through (3.11) as functions of the sole vector potentials:

$$\mathbf{E} = -j\omega \mathbf{A} + \frac{1}{j\omega\mu\varepsilon} \nabla(\nabla \cdot \mathbf{A}) - \frac{1}{\varepsilon} \nabla \times \mathbf{F} \quad (3.15a)$$

$$\mathbf{H} = -j\omega \mathbf{F} + \frac{1}{j\omega\mu\varepsilon} \nabla(\nabla \cdot \mathbf{F}) + \frac{1}{\mu} \nabla \times \mathbf{A} \quad (3.15b)$$

### 3.1.3. Green's Functions

The formulation of a wide range of electromagnetic problems involves second order partial differential equations derived from the Maxwell Equations, expressing electromagnetic fields as function of the impressed currents and charges. A technique typically used for the treatment of these problems consists in finding a solution to the differential equations using an impulsive source: the obtained solution is the Green's Function (GF).

Being linearity one of the salient properties of Maxwell Equations, the complete characterization of the problem is derived by superposition of the effects of the single Dirac Deltas constituting the actual source; this superposition is expressed by the *convolution* operator:

$$G(\mathbf{r}) \otimes f(\mathbf{r}) = \int_V dv' G(\mathbf{r} - \mathbf{r}') \cdot f(\mathbf{r}') \quad (3.16)$$

$f$  being a generic function defined within the domain  $V$ .

The notation  $G(\mathbf{r} | \mathbf{r}')$  is identically used to indicate  $G(\mathbf{r} - \mathbf{r}')$ .

In the particular case where the differential equation is in the form of a scalar Helmholtz

equation:

$$\nabla^2 G(\mathbf{r}) + k^2 G(\mathbf{r}) = -\delta(\mathbf{r}) \quad (3.17)$$

the Green's Function can be written:

$$G(\mathbf{r}) = \frac{\exp(jk|\mathbf{r}|)}{4\pi|\mathbf{r}|} \quad (3.18)$$

### 3.1.3.1. GF in homogeneous media

In general, different formulations of the GF are available for a given problem and their complexity depends primarily on the characteristics of the media involved. In the assumption of an homogeneous medium, where the sources are enclosed in a volume  $V$ , a manipulation of the Maxwell Equations (3.1) allows to write [46]:

$$\nabla^2 \mathbf{E} + k^2 \mathbf{E} = j\omega\mu \left[ \mathbf{J} - \frac{1}{j\omega\varepsilon} \nabla(\nabla \cdot \mathbf{J}) \right] \quad (3.19)$$

Due to the linearity of the differential operator, we can take the component in the  $x_i$  direction:

$$\nabla^2 E_{x_i} + k^2 E_{x_i} = j\omega\mu \left[ J_{x_i} + \frac{1}{k^2} \frac{\partial}{\partial x_i} (\nabla \cdot \mathbf{J}) \right] \quad (3.20)$$

Recalling the GF (3.18) solution of the Helmholtz equation (3.17), the electric field is obtained as:

$$\mathbf{E}(\mathbf{r}) = -j\omega\mu \int_V dV G(\mathbf{r}|\mathbf{r}') \left[ \mathbf{J}(\mathbf{r}') + \frac{1}{k^2} \nabla' \nabla' \cdot \mathbf{J}(\mathbf{r}') \right] \quad (3.21)$$

Using the identity:

$$\int_V dV G(\mathbf{r}|\mathbf{r}') [\nabla' \nabla' \cdot \mathbf{J}(\mathbf{r}')] = \int_V dV [\nabla \cdot \nabla G(\mathbf{r}|\mathbf{r}')] \mathbf{J}(\mathbf{r}') \quad (3.22)$$

the electric field can be expressed as explicit function of  $\mathbf{J}$ :

$$\mathbf{E}(\mathbf{r}) = -j\omega\mu \int_V dV \left[ \bar{\bar{\mathbf{I}}} + \frac{1}{k^2} \nabla \nabla \right] G(\mathbf{r}|\mathbf{r}') \cdot \mathbf{J}(\mathbf{r}') \quad (3.23)$$

where we identify as the Green's Function  $\bar{\bar{\mathbf{G}}}_{\mathbf{E},\mathbf{J}}$  the quantity:

$$\bar{\bar{\mathbf{G}}}_{\mathbf{E},\mathbf{J}}(\mathbf{r}) = -j\omega\mu \left( \bar{\bar{\mathbf{I}}} + \frac{\nabla \nabla}{k^2} \right) G(\mathbf{r}) \quad (3.24)$$

Similar manipulations of the Maxwell Equations lead to the expression of the electric field generated by an electric current

$$\nabla^2 \mathbf{E} + k^2 \mathbf{E} = j\nabla \times \mathbf{M} \quad (3.25)$$

and consequently to the derivation of the relative GF:

$$\bar{\bar{\mathbf{G}}}_{\mathbf{E},\mathbf{M}}(\mathbf{r}) = -\bar{\bar{\mathbf{I}}} \times \nabla G(\mathbf{r}) \quad (3.26)$$

A similar procedure leads to the derivation of the GFs for the magnetic field:

$$\bar{\bar{\mathbf{G}}}_{\mathbf{H},\mathbf{J}}(\mathbf{r}) = \bar{\bar{\mathbf{I}}} \times \nabla G(\mathbf{r}) \quad (3.27a)$$

$$\bar{\bar{\mathbf{G}}}_{\mathbf{H},\mathbf{M}}(\mathbf{r}) = -j\omega\varepsilon(\bar{\bar{\mathbf{I}}} + \frac{\nabla\nabla}{k^2})G(\mathbf{r}) \quad (3.27b)$$

The knowledge of the GFs allows the full characterization of the electromagnetic problem;

$$\mathbf{E} = \bar{\bar{\mathbf{G}}}_{\mathbf{E},\mathbf{J}} \otimes \mathbf{J} + \bar{\bar{\mathbf{G}}}_{\mathbf{E},\mathbf{M}} \otimes \mathbf{M} \quad (3.28a)$$

$$\mathbf{H} = \bar{\bar{\mathbf{G}}}_{\mathbf{H},\mathbf{J}} \otimes \mathbf{J} + \bar{\bar{\mathbf{G}}}_{\mathbf{H},\mathbf{M}} \otimes \mathbf{M} \quad (3.28b)$$

When fields are expressed through potentials (3.14), the associated GFs satisfying

$$\mathbf{A} = \mu \left[ \bar{\bar{\mathbf{G}}}_{\mathbf{A},\mathbf{J}} \otimes \mathbf{J} \right] \quad \phi_e = \frac{1}{\varepsilon} [G_{\phi_e,\rho_e} \otimes \rho_e] \quad (3.29a)$$

$$\mathbf{F} = \varepsilon \left[ \bar{\bar{\mathbf{G}}}_{\mathbf{F},\mathbf{M}} \otimes \mathbf{M} \right] \quad \phi_m = \frac{1}{\mu} [G_{\phi_m,\rho_m} \otimes \rho_m] \quad (3.29b)$$

are:

$$\bar{\bar{\mathbf{G}}}_{\mathbf{A},\mathbf{J}}(\mathbf{r}) = \bar{\bar{\mathbf{G}}}_{\mathbf{F},\mathbf{M}}(\mathbf{r}) = \bar{\bar{\mathbf{I}}}G(\mathbf{r}) \quad (3.30)$$

and

$$G_{\phi_e,\rho_e}(\mathbf{r}) = G_{\phi_m,\rho_m}(\mathbf{r}) = G(\mathbf{r}) \quad (3.31)$$

The two formulations of the GF here discussed are equivalent and lead to the same solution of the electromagnetic problem. On the other hand, one should remark that the double derivative appearing in  $\bar{\bar{\mathbf{G}}}_{\mathbf{E},\mathbf{J}}$  and  $\bar{\bar{\mathbf{G}}}_{\mathbf{H},\mathbf{M}}$  leads to a singularity of the type  $1/r^3$  which is known to show problems when numerically evaluated. The potential formulation instead does not involve any differentiation of the GFs  $\bar{\bar{\mathbf{G}}}_{\mathbf{A},\mathbf{J}}$  and  $G_{\phi_e,\rho_e}$ , offering therefore a milder  $1/r$  singularity. Also important is the fact that  $\bar{\bar{\mathbf{G}}}_{\mathbf{E},\mathbf{J}}$  and  $\bar{\bar{\mathbf{G}}}_{\mathbf{H},\mathbf{M}}$  express a direct relation between the electric field and the source, whereas  $\bar{\bar{\mathbf{G}}}_{\mathbf{A},\mathbf{J}}$  and  $G_{\phi_e,\rho_e}$  are partial solutions which require the definition of mathematical entities, the potentials, to be formulated and used for the derivation of the electric field.

### 3.1.3.2. Inhomogeneous and stratified media

The theoretical foundations for the computation of fields in layered media was already developed in [47, 48], where a double spatial Fourier transformation was used to reduce the Maxwell Equations to a one-dimensional differential equation solvable, for instance, using a transmission line approach; the transformation from the spectral domain to the space domain

is then performed via the well-known Sommerfeld integral [49]. Great effort has been directed both to the analytical treatment of the integral and its numerical evaluation [50–53].

The different approaches lead to formulation of the GFs which, though involving integrals and analytical series, maintain the same characteristics as the free-space ones in terms of singularity. A relevant difference concerns instead the potential formulation, which is often badly defined: the definition of the Lorentz Gauge is not evident and it is known for instance that already in case of a planar stratified medium the scalar potential depends on the orientation of the source. The situation becomes even worse with more complex media, such as meta-materials.

Even if this work does not involve explicitly the analysis of inhomogeneous structures, these remarks will be addressed during the illustration of one of the developed numerical method the Magic Distance Inspired method, (discussed in detail in Chap. 5), as it offers an interesting possibility of extension towards inhomogeneous structures.

### 3.1.4. The electrostatics problem

When the frequency approaches zero,  $\omega \rightarrow 0$ , the time-harmonic quantities involved in the problem become constants, currents vanish and the Maxwell Equations (3.1) reduce to:

$$\nabla \times \mathbf{E} = 0 \quad (3.32a)$$

$$\nabla \times \mathbf{H} = 0 \quad (3.32b)$$

$$\nabla \cdot \mathbf{D} = \rho_e \quad (3.32c)$$

$$\nabla \cdot \mathbf{B} = \rho_m \quad (3.32d)$$

Because the electric and magnetic fields are irrotational, they can be expressed as the gradient of a scalar function, the electrostatic potentials:

$$\mathbf{E} = -\nabla \phi_e^{ES} \quad (3.33a)$$

$$\mathbf{H} = -\nabla \phi_m^{ES} \quad (3.33b)$$

The boundary condition valid for a PEC, occupying a volume  $V$  with surface  $S = \partial V$  is also expressed in terms of the potential as:

$$\phi_e^{ES}|_S = U = \text{const} \quad (3.34)$$

Moreover, in a similar fashion as in the electrodynamic case, and assuming an homogeneous medium, a manipulation of the electrostatics Maxwell Equations allows to cast the differential equations, in the form of Laplace equations:

$$\nabla^2 \phi_e^{ES} = -\frac{1}{\epsilon} \rho_e \quad (3.35a)$$

$$\nabla^2 \phi_m^{ES} = -\frac{1}{\mu} \rho_m \quad (3.35b)$$



which can be used, introducing impulse sources, to derive the electrostatics Green's Functions:

$$\phi_e^{ES}(\mathbf{r}) = \frac{1}{\varepsilon} \int_V dv' G_{\phi_e, \rho_e}^{ES}(\mathbf{r} | \mathbf{r}') \cdot \rho_e(\mathbf{r}') \quad (3.36a)$$

$$\phi_m^{ES}(\mathbf{r}) = \frac{1}{\mu} \int_V dv' G_{\phi_m, \rho_m}^{ES}(\mathbf{r} | \mathbf{r}') \cdot \rho_m(\mathbf{r}') \quad (3.36b)$$

where the GFs are given by:

$$G_{\phi_e, \rho_e}^{ES}(\mathbf{r}) = G_{\phi_m, \rho_m}^{ES}(\mathbf{r}) = \frac{1}{4\pi |\mathbf{r}|} \quad (3.37)$$

## 3.2. Integral Equations

Scattering problems are a particular class of electromagnetic problems where currents are induced on an object by an external source and are not known a priori; the knowledge of those currents allows the derivation of the field re-radiated by the object and therefore the complete electromagnetic characterization of the problem. The analysis of the radiation characteristics of an antenna can be classified as a scattering problem, and its solution allows the derivation of all the parameters which characterize the antenna, such as far fields, input impedance, efficiency, etc.

Integral Equations (IE) [54, 55] can be used for the formulation of scattering problems involving finite extent geometries. In an IE, the unknown appears under the integral sign and the solution is typically obtained using numerical techniques, such as the Method of Moments (MoM). In electromagnetics, an IE can be cast by combining one of the expressions relating the fields and the currents with the Boundary Condition (BC) valid for the specific material constituting the scatterer. In this way, the scattered fields, which are function of the unknown currents (charges in electrostatics), are related to the impressed fields, which represent the known term in the equation.

Different formulations of IEs are available depending on the nature of the scatterer, the choice of the BC to enforce, or the formula relating the currents with the fields; among these, most popular are the Electric Field IE (EFIE), enforcing the BC on the tangential electric field, the Magnetic Field IE (MFIE), enforcing the BC on the tangential magnetic field, the Combined Fields IE (CFIE, [56, 57]), combination of EFIE and MFIE, and the Mixed Potential IE (MPIE, [58], [59, Chapter 3], [60–62]), a version of EFIE which involves vector and scalar potentials.

Another distinction can be made depending on the region where the currents exist. In the case of a penetrable scatterer, currents are distributed inside the object, the integrals are three-dimensional and we have a Volume IE (VIE, [63–65]); if the scatterer is made of a PEC, currents are distributed only on its surface and we have a Surface IE (SIE). As a remark, homogenous penetrable scatterers can be also solved via SIE, through the application of the Equivalence Principle. This formulation requires anyway the introduction of both equivalent

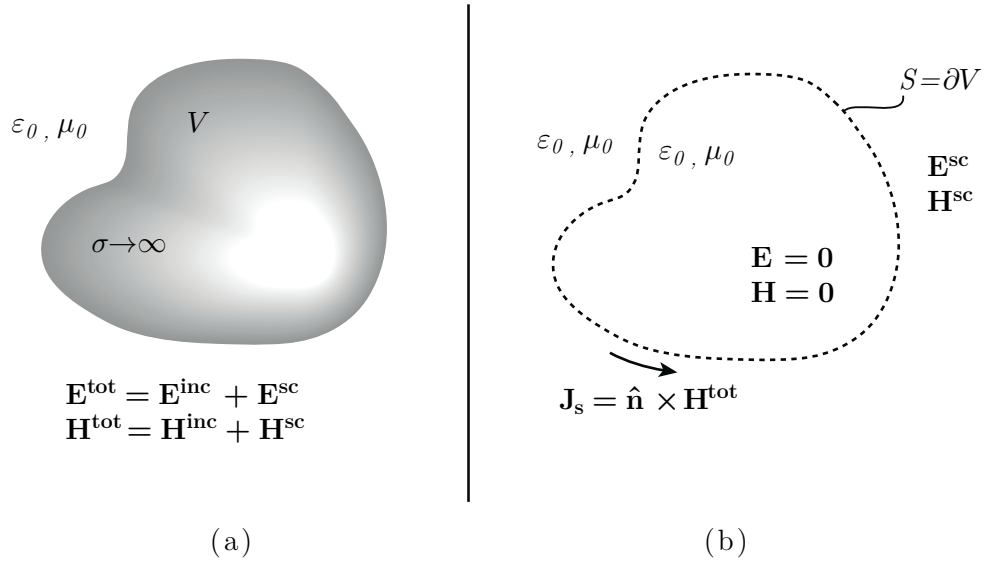


**Figure 3.1.:** The full wave problem: a metallic object in free space excited by an incident field. (a) Physical and (b) equivalent problems.

electric and magnetic surface currents, even for non-magnetic bodies, whereas only equivalent electric volume currents (polarization currents) appear in the VIE treatment of non-magnetic bodies.

Concerning electrostatics, the equivalent of MPIE is the Electrostatic Potential IE, EPIE.

### 3.2.1. SIE for conducting bodies in free space

Let us consider (Fig. 3.1) the problem of a Perfect Electric Conductor in a homogeneous medium, which we identify as free space, excited by an incident field  $\mathbf{E}^{\text{inc}}, \mathbf{H}^{\text{inc}}$ . The total fields  $\mathbf{E}^{\text{tot}}, \mathbf{H}^{\text{tot}}$  in any point of the space is the combination of the incident field and the fields  $\mathbf{E}^{\text{sc}}, \mathbf{H}^{\text{sc}}$  scattered by the object.

The scattered field is produced by the (unknown) currents induced on the object by the incident field; by means of the Huygens Principle [66], the metallic body can be removed and an equivalent problem can be constructed where equivalent electric and magnetic currents  $\mathbf{J}_s, \mathbf{M}_s$  are located on the surface of the scatterer and are radiating in free space:

$$\mathbf{J}_s = [\hat{\mathbf{n}} \times \mathbf{H}^{\text{tot}}]_S \quad (3.38a)$$

$$\mathbf{M}_s = [\mathbf{E}^{\text{tot}} \times \hat{\mathbf{n}}]_S = 0 \quad (3.38b)$$

as stated by the Boundary Conditions (3.4).

In the equivalent problem, the scattered field can be derived using the Green's Functions for homogeneous media introduced in Par. 3.1.3; in particular, all these GFs are formulated

in terms of the single Green's Function  $G(\mathbf{r})$ , defined as:

$$G(\mathbf{r}) = \frac{\exp(jk|\mathbf{r}|)}{4\pi|\mathbf{r}|} \quad (3.39)$$

As the surface currents depend on the total fields, which are unknown, it is necessary to enforce the Boundary Conditions on the PEC to cast an Integral Equation. Solving the IE for the surface currents allows a complete description of the electromagnetic problem.

The formulation of the problem as EFIE, MFIE or MPIE depends on the Boundary Condition enforced and on the Green's Function used. This work is essentially focused on the solution of full-wave scattering problems via special implementations of SIE in the form of EFIE and MPIE; the electrostatic problem (EPIE) is also partially involved in the illustration of the developed methods. The analytical details of the IEs required for the discussion are recalled in the present chapter.

### 3.2.2. The Electric Field Integral Equation (EFIE)

In an electromagnetic problem involving PEC objects, magnetic currents are absent and the EFIE is cast by enforcing the tangential component of the total electric field to vanish on the surface of the scatterer:

$$\hat{\mathbf{n}} \times \int_S ds' \bar{\bar{\mathbf{G}}}_{\mathbf{E},\mathbf{J}}(\mathbf{r}|\mathbf{r}') \cdot \mathbf{J}_s(\mathbf{r}) = -\hat{\mathbf{n}} \times \mathbf{E}^{\text{inc}}(\mathbf{r}) \quad (3.40)$$

The relation between the surface currents and the electric field is expressed by the dyadic Green's Function  $\bar{\bar{\mathbf{G}}}_{\mathbf{E},\mathbf{J}}$ , kernel of the integral equation:

$$\bar{\bar{\mathbf{G}}}_{\mathbf{E},\mathbf{J}}(\mathbf{r}) = -j\omega\mu \left( \bar{\bar{\mathbf{I}}} + \frac{\nabla\nabla}{k^2} \right) G(\mathbf{r}) \quad (3.41)$$

For the sake of convenience, we include the explicit formulation of the cartesian components of  $\bar{\bar{\mathbf{G}}}_{\mathbf{E},\mathbf{J}}$  in spherical coordinates. These formulas will be required later in Chap. 5. Defining the quantities:

$$G_0(r) = j\omega\mu \frac{\exp(-jkr)}{4\pi r} \quad (3.42)$$

and

$$G_r(r) = 1 + 3 \left[ \frac{1}{(kr)^2} - \frac{1}{jkr} \right] \quad (3.43)$$

the components of  $\bar{\bar{\mathbf{G}}}_{\mathbf{E},\mathbf{J}}$  are:

$$G^{xx} = G_0 \left[ G_r \left( \sin^2 \theta \cos^2 \varphi - \frac{1}{3} \right) - \frac{2}{3} \right] \quad (3.44a)$$

$$G^{xy} = G_0 G_r (\sin^2 \theta \sin \varphi \cos \varphi) \quad (3.44b)$$

$$G^{xz} = G_0 G_r (\sin \theta \cos \varphi \cos \varphi) \quad (3.44c)$$

$$G^{yx} = G_0 G_r (\sin^2 \theta \sin^2 \varphi \cos \varphi) \quad (3.44d)$$

$$G^{yy} = G_0 \left[ G_r \left( \sin^2 \theta \sin^2 \varphi - \frac{1}{3} \right) - \frac{2}{3} \right] \quad (3.44e)$$

$$G^{yz} = G_0 G_r (\sin \theta \cos \varphi \sin \varphi) \quad (3.44f)$$

$$G^{zx} = G_0 G_r (\sin \theta \cos \varphi \cos \varphi) \quad (3.44g)$$

$$G^{zy} = G_0 G_r (\sin \theta \cos \varphi \sin \varphi) \quad (3.44h)$$

$$G^{zz} = G_0 \left[ G_r \left( \cos^2 \theta - \frac{1}{3} \right) - \frac{2}{3} \right] \quad (3.44i)$$

It is obvious that Green's Functions for the electric field exhibit complex angular dependencies. This fact will be of paramount relevance in the development of Chap. 5.

### 3.2.3. The Magnetic Field Integral Equation (MFIE)

The MFIE [67] valid for a three-dimensional PEC in homogeneous unbounded media is derived by enforcing the Boundary Condition on a fictitious surface  $S^+$  at an infinitesimal distance from the surface of the object:

$$\left[ \hat{\mathbf{n}} \cdot (\mathbf{H}^{\text{inc}} + \mathbf{H}^{\text{sc}}) \right]_{S^+} = 0 \quad (3.45)$$

The scattered field is expressed in terms of the surface electric current through the Green's Function  $\bar{\bar{\mathbf{G}}}_{\mathbf{H},\mathbf{J}}$ :

$$\bar{\bar{\mathbf{G}}}_{\mathbf{H},\mathbf{J}}(\mathbf{r}) = \bar{\bar{\mathbf{I}}} \times \nabla G(\mathbf{r}) \quad (3.46)$$

and the MFIE is given by:

$$\hat{\mathbf{n}} \cdot \int_S ds' \bar{\bar{\mathbf{G}}}_{\mathbf{H},\mathbf{J}}(\mathbf{r} | \mathbf{r}') \cdot \mathbf{J}_s(\mathbf{r}') = -\hat{\mathbf{n}} \cdot \mathbf{H}^{\text{inc}}(\mathbf{r}) \quad (3.47)$$

The kernel of the integral  $\bar{\bar{\mathbf{G}}}_{\mathbf{H},\mathbf{J}}$  involves a derivation which results in a  $1/r^2$  singularity. On one hand, the MFIE offers advantages with respect to EFIE, one of the most remarkable being the fact that when discretized with the Method of Moments (Sec. 3.3) it produces a well-conditioned matrix, whereas the EFIE condition number grows larger reducing the mesh electrical size [46]. The major limitation of MFIE remains anyway its inadequacy for

the analysis of open structures or even thin sheets (Par. 3.2.6), an issue that prevents its application to the common slot antenna problems which are one of the main focuses of this work.

### 3.2.4. The Mixed Potential Integral Equation (MPIE)

The Electric Field Integral Equation can be transformed into the Mixed Potential IE by resorting to the relations introduced in Par. 3.1.2. The electric field is expressed in terms of potentials by:

$$\mathbf{E} = -j\omega\mathbf{A} - \nabla\phi_e \quad (3.48)$$

The vector and scalar potentials are expressed as functions of the surface current and charge by the respective Green's Functions (3.30) and (3.31); the Continuity Equation can eventually be used to obtain a formulation including either both the currents and the charges or the currents alone.

As no magnetic quantity is involved and currents and charges are distributed on surfaces, the formalism can be simplified as:

$$\begin{cases} \bar{\bar{\mathbf{G}}}_{\mathbf{A},\mathbf{J}} \rightarrow \bar{\bar{\mathbf{G}}}_{\mathbf{A}} = \bar{\bar{\mathbf{I}}}G \\ G_{\phi_e,\rho_e} \rightarrow G_V = G \end{cases} \quad (3.49)$$

$$\begin{cases} \mathbf{J} \rightarrow \mathbf{J}_s \\ \rho_e \rightarrow \rho_s \end{cases} \quad (3.50)$$

Applying the PEC Boundary Condition, the MPIE are derived as:

$$\hat{\mathbf{n}} \times \left[ \begin{array}{l} +j\omega\mu \int_S ds' \bar{\bar{\mathbf{G}}}_{\mathbf{A}}(\mathbf{r}|\mathbf{r}') \cdot \mathbf{J}_s(\mathbf{r}') + \\ -\frac{1}{j\omega\varepsilon} \nabla \int_S ds' G_V(\mathbf{r}|\mathbf{r}') \cdot [\nabla' \cdot \mathbf{J}_s(\mathbf{r}')] \end{array} \right]_{\mathbf{r} \in S} = \hat{\mathbf{n}} \times \mathbf{E}^{\text{inc}}(\mathbf{r})|_{\mathbf{r} \in S} \quad (3.51)$$

or equivalently showing explicitly the charge density:

$$\hat{\mathbf{n}} \times \left[ \begin{array}{l} +j\omega\mu \int_S ds' \bar{\bar{\mathbf{G}}}_{\mathbf{A}}(\mathbf{r}|\mathbf{r}') \cdot \mathbf{J}_s(\mathbf{r}') + \\ +\frac{1}{\varepsilon} \nabla \int_S ds' G_V(\mathbf{r}|\mathbf{r}') \cdot \rho_s(\mathbf{r}') \end{array} \right]_{\mathbf{r} \in S} = \hat{\mathbf{n}} \times \mathbf{E}^{\text{inc}}(\mathbf{r})|_{\mathbf{r} \in S} \quad (3.52)$$

### 3.2.5. The Electrostatic Potential Integral Equation (EPIE)

In the electrostatic problem, the objective of the IE method is the derivation of the unknown surface charge density lying on the scatterer.

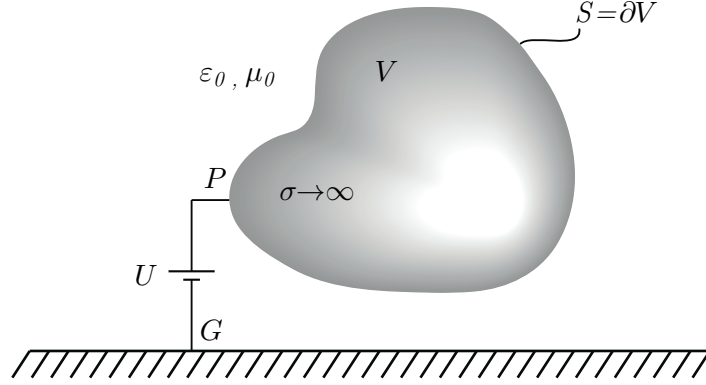


**Figure 3.2.:** The electrostatics problem: a metallic object in free space with an impressed voltage  $U$ .

The problem of a metallic object with surface  $S = \partial V$  lying in free space is reformulated for electrostatics as sketched in Fig. 3.2, where the PEC is set to a potential  $U$ .

The Electrostatic Potential IE can be formulated starting from the MPIE:

$$\hat{\mathbf{n}} \times \left[ j\omega\mu \bar{\bar{\mathbf{G}}}_{\mathbf{A}} \otimes \mathbf{J}_{\mathbf{s}} + \frac{1}{\epsilon} \nabla (G_V \otimes \rho_s) \right]_S = \hat{\mathbf{n}} \times \mathbf{E}^{\text{inc}} \Big|_S \quad (3.53)$$

When the MPIE is integrated along an arbitrary path  $\ell$  connecting the ground  $G$  with a generic point  $P$  on the surface of the PEC, it becomes:

$$j\omega\mu \int_G^P d\ell \bar{\bar{\mathbf{G}}}_{\mathbf{A}} \otimes \mathbf{J}_{\mathbf{s}} + \frac{1}{\epsilon} [G_V \otimes \rho_s - 0] = U \quad (3.54)$$

Letting the frequency tend to zero,  $\omega \rightarrow 0$  and the EPIE finally writes:

$$\frac{1}{\epsilon} G^{ES} \otimes \rho_s = U \quad (3.55)$$

where the electrostatic Green's Function  $G^{ES}$ , expressing the potential in  $\mathbf{r}$  generated by an infinitesimal charge in  $\mathbf{r}'$  is defined as:

$$G^{ES}(\mathbf{r}) = \frac{1}{4\pi |\mathbf{r}|} \quad (3.56)$$



Figure 3.3.: Degeneration of a thin volume to a 2D geometry.

### 3.2.6. Open surfaces and slots

The IE formulated in the previous sections are valid for closed, three-dimensional metallic bodies. Of particular interest in this work is the treatment of indefinitely thin structures, such as sheets or shells, which are typically used to model the ground plane where slots are etched.

The transformation from 3D to 2D does not require any modification of the EFIE as it has been formulated: the condition (3.5a) remains valid as the volume collapses into the zero-thickness sheet and the currents  $\mathbf{J}_1$  and  $\mathbf{J}_2$  are superimposed on the strip itself, as in Fig. 3.3. Therefore, it can be safely written:

$$\begin{aligned} \oint_{\partial V} dS \bar{\bar{\mathbf{G}}}_{\mathbf{E},\mathbf{J}}(\mathbf{r}|\mathbf{r}') \cdot \mathbf{J}_s(\mathbf{r}') &= \\ \int_{S_1} dS \bar{\bar{\mathbf{G}}}_{\mathbf{E},\mathbf{J}}(\mathbf{r}|\mathbf{r}') \cdot \mathbf{J}_1(\mathbf{r}') + \int_{S_2} dS \bar{\bar{\mathbf{G}}}_{\mathbf{E},\mathbf{J}}(\mathbf{r}|\mathbf{r}') \cdot \mathbf{J}_2(\mathbf{r}') &= \\ \int_S dS \bar{\bar{\mathbf{G}}}_{\mathbf{E},\mathbf{J}}(\mathbf{r}|\mathbf{r}') \cdot [\mathbf{J}_1(\mathbf{r}') + \mathbf{J}_2(\mathbf{r}')] & \end{aligned} \quad (3.57)$$

The MFIE on the other hand is based on (3.5b) which is not valid for infinitely thin geometries: derived from the general (3.4b), the condition holds only when the magnetic field vanishes on one side of the surface (which is the case of PEC volumes). A possible solution [46] consists in excluding from the integration the surface portion  $\delta S$  surrounding the observation point; the MFIE is then formulated as:

$$\hat{\mathbf{n}}(\mathbf{r}) \times \mathbf{H}^{\text{inc}}(\mathbf{r}) = \frac{\mathbf{J}_s(\mathbf{r})}{2} - \hat{\mathbf{n}} \times \int_{S-\delta S} dS \bar{\bar{\mathbf{G}}}_{\mathbf{H},\mathbf{J}}(\mathbf{r}|\mathbf{r}') \cdot \mathbf{J}_s(\mathbf{r}') \quad (3.58)$$

With this choice, treatment [68] is also required when the surface is not planar.

An aperture on a infinite size metallic sheet can be formulated as an equivalent problem where the sole magnetic equivalent currents are radiating in the free space [37]. On the other hand, if the aperture is on a reasonably small metallic surface (like the MAST project satellite platforms) it is frequently advantageous to keep the aperture as a mathematical hole and model it with the electric currents circulating around it. The slight increase in the number of unknowns is more than compensated by the simplicity of the formulation which requires only a single type of GFs.

### 3.3. The Method of Moments

As recalled in the previous sections, many electromagnetic problems can be described with an Integral Equation (IE) derived by the Boundary Conditions (BC) valid for the specific geometry and material. When the integration limits are fixed, the unknown appears only inside the integral and the known term is not identically zero, the IE is classified as “inhomogeneous Fredholm equation of the first kind” [69]. A generic IE of this type would be:

$$I [\mathbf{v}(\mathbf{r}')] = \int d\mathbf{r}' \bar{\bar{\mathbf{G}}}(\mathbf{r}|\mathbf{r}') \cdot \mathbf{v}(\mathbf{r}') = \mathbf{f}(\mathbf{r}) \quad (3.59)$$

Particular formulations of IE generally used for the solution of electromagnetic problems were discussed in Sec. 3.2; the following treatment applies indistinctly to any of the formulation.

When a closed form solution is not available, the Method of Moments (MoM) can be applied to solve numerically the IE. The procedure requires the expansion of the unknown  $\mathbf{v}(\mathbf{r}')$  using a suitable set of  $N$  Basis Functions (BFs)  $\mathbf{b}_j$  defined over a generic domain  $B_j$ :

$$\mathbf{v}(\mathbf{r}') = \sum_{j=1}^N v_j \mathbf{b}_j(\mathbf{r}') \quad (3.60)$$

The expansion leads to an equation containing  $N$  unknowns in the form:

$$\sum_{j=1}^N v_j \mathbf{I} [\mathbf{b}_j(\mathbf{r}')] = \mathbf{f}(\mathbf{r}) \quad (3.61)$$

The required linear independent equations are constructed by defining an inner product:

$$\langle \mathbf{t}(\mathbf{r}), \mathbf{f}(\mathbf{r}) \rangle = \int_T d\mathbf{r} \mathbf{t}^*(\mathbf{r}) \cdot \mathbf{f}(\mathbf{r}) \quad (3.62)$$

and a set of  $M$  (typically  $M = N$ ) Test Functions (TFs)  $\mathbf{t}$ , defined over a domain  $T_i$ . Forming the inner product between (3.59) and each test function yields the conditions necessary to solve the linear system:

$$[Z^{MoM}] [v] = [f] \Rightarrow [v] = [Z^{MoM}]^{-1} [f] \quad (3.63)$$

The generic entry  $z_{ij}$  of the matrix  $Z^{MoM}$  can be written as:

$$z_{ij} = \langle \mathbf{t}_i, \mathbf{I} [\mathbf{b}_j] \rangle = \int_{T_i} d\mathbf{r} \int_{B_j} d\mathbf{r}' \mathbf{t}_i^*(\mathbf{r}) \cdot \left[ \bar{\bar{\mathbf{G}}}(\mathbf{r}|\mathbf{r}') \cdot \mathbf{b}_j(\mathbf{r}') \right] \quad (3.64)$$



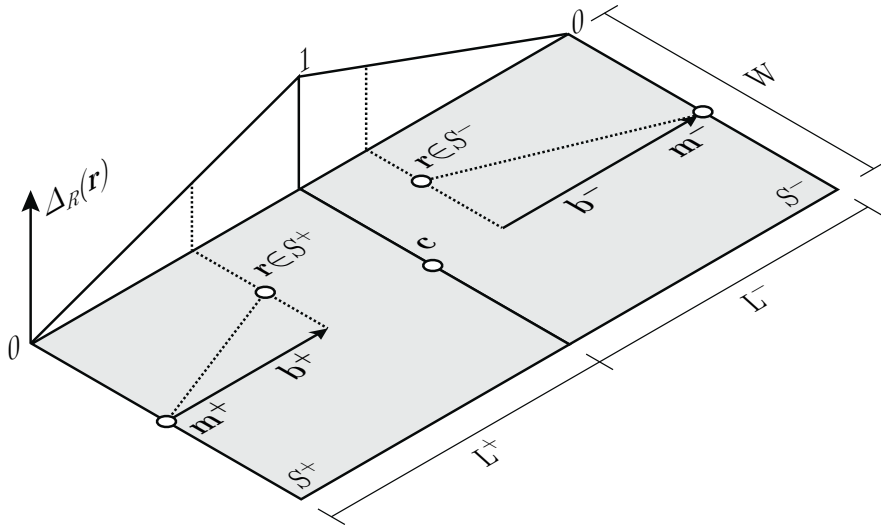


**Figure 3.4.:** The rectangular domain rooftop. The two cells  $S^+$  and  $S^-$  of dimensions  $L^\pm \times W$  share an edge with mid-point  $\mathbf{c}$ ; the opposite edges have midpoints  $\mathbf{m}^\pm$ , which in turn are respectively the root and the endpoint of the vectors  $\mathbf{b}^+$  and  $\mathbf{b}^-$  representing the basis functions.

### 3.3.1. Basis functions

The criterium which determines the choice of a basis function is its capability of representing the unknown function within its domain. A benefit of a correct choice of the basis function is also the mitigation of the singularities appearing in the kernel of the IE.

Typical basis functions are the pulse and the rooftop.

#### 3.3.1.1. Pulse function

A pulse function with support  $A$  is written:

$$\square(\mathbf{r}) = \begin{cases} 1 & \text{if } \mathbf{r} \in A \\ 0 & \text{otherwise} \end{cases} \quad (3.65)$$

#### 3.3.1.2. Rectangular domain rooftop

The rectangular domain rooftop, is illustrated in Fig. 3.4. In general, the BF is not planar and the orientation unit vector is defined as:

$$\begin{cases} \hat{\mathbf{b}}^+ = \frac{\mathbf{c} - \mathbf{m}^+}{L^+}, & \mathbf{r} \in S^+ \\ \hat{\mathbf{b}}^- = \frac{\mathbf{m}^- - \mathbf{c}}{L^-}, & \mathbf{r} \in S^- \end{cases} \quad (3.66)$$

The basis function is expressed as:

$$\Delta_{\mathbf{R}}(\mathbf{r}) = \begin{cases} \frac{(\mathbf{r} - \mathbf{m}^+) \cdot \hat{\mathbf{b}}^+}{L^+} \hat{\mathbf{b}}^+, & \mathbf{r} \in S^+ \\ \frac{(\mathbf{m}^- - \mathbf{r}) \cdot \hat{\mathbf{b}}^-}{L^-} \hat{\mathbf{b}}^-, & \mathbf{r} \in S^- \end{cases} \quad (3.67)$$

In the case where the BF is oriented along two generic reference system axis  $\pm \hat{\mathbf{u}}$  and  $\pm \hat{\mathbf{v}}$ , (3.67) simplifies into:

$$\Delta_{\mathbf{R}}(\mathbf{r}) = \begin{cases} \frac{u - m_u^+}{L^+} \hat{\mathbf{u}}, & \mathbf{r} \in S^+ \\ \frac{m_v^- - v}{L^-} \hat{\mathbf{v}}, & \mathbf{r} \in S^- \end{cases} \quad (3.68)$$

The divergence of the rectangular domain BF, which will be required for the computation of the MoM elements when solving the MPIE, is given in this last hypothesis by:

$$\nabla \cdot \Delta_{\mathbf{R}}(\mathbf{r}) = \begin{cases} +\frac{1}{L^+}, & \mathbf{r} \in S^+ \\ -\frac{1}{L^-}, & \mathbf{r} \in S^- \end{cases} \quad (3.69)$$

The formulation provided for the rooftop function, even more complicated than the functions appearing in some textbook, has the advantage of being valid for generic oriented cell pairs, a feature of particular relevance in the implementation of the MoM for 3D bodies.

### 3.3.1.3. Triangular domain rooftop

For the sake of completeness, we include the formulation of triangular domain rooftop functions, also known as RWG [70], illustrated in (Fig. 3.5). Defining the vectors:

$$\mathbf{b}^+(\mathbf{r}) = \mathbf{v}^+ - \mathbf{r} \quad \mathbf{r} \in S^+ \quad (3.70a)$$

$$\mathbf{b}^-(\mathbf{r}) = \mathbf{r} - \mathbf{v}^- \quad \mathbf{r} \in S^- \quad (3.70b)$$

the expression of the RWG function is written:

$$\Delta_{\mathbf{T}}(\mathbf{r}) = \frac{W}{2A^\pm} \mathbf{b}^\pm(\mathbf{r}) \quad \mathbf{r} \in S^\pm \quad (3.71)$$

$A^\pm$  being the area of the surface  $S^\pm$ . The divergence of the triangular domain rooftop is:

$$\nabla \cdot \Delta_{\mathbf{T}}(\mathbf{r}) = \pm \frac{W}{A^\pm} \quad \mathbf{r} \in S^\pm \quad (3.72)$$

Rooftops defined in rectangular and triangular domains can be advantageously simplified by replacing them by dipoles having the same momentum.

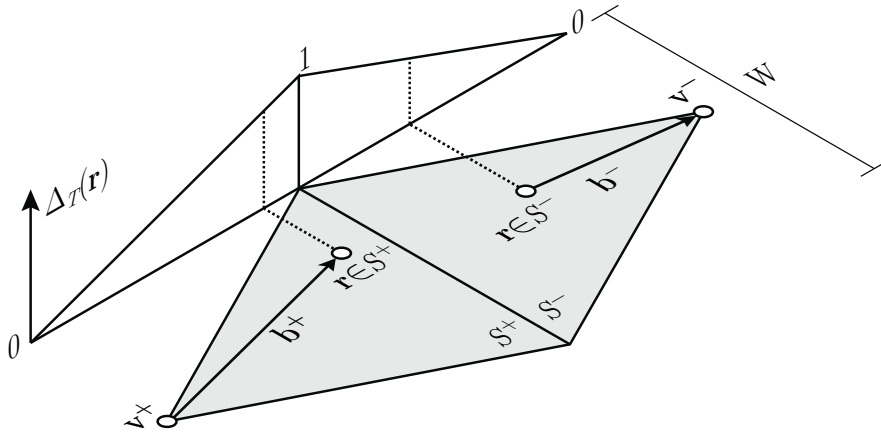


**Figure 3.5.:** The triangular domain rooftop. The two cells  $S^+$  and  $S^-$  share a common edge of length  $W$ . The opposite corners  $\mathbf{v}^\pm$  are respectively the root and the endpoint of the vectors  $\mathbf{b}^+$  and  $\mathbf{b}^-$  representing the basis functions.

### 3.3.2. The test function

The choice of the TF determines where the BC is *exactly* satisfied and is therefore crucial for an accurate approximation of the solution of the IE.

#### 3.3.2.1. The Galerkin method

One of the most popular choices for the TF is the *Galerkin method*, [44, 71] which consists in using the Basis Functions themselves as Test Functions:

$$\mathbf{t}_j(\mathbf{r}) = \mathbf{b}_j(\mathbf{r}') \quad (3.73)$$

With this technique, the BC is actually enforced throughout the whole solution domain (except the case when the BF is a Dirac Delta) and the highest accuracy for the solution is achieved.

#### 3.3.2.2. Point matching

The *Point Matching* or *Collocation* method consists in using as TF the simplest function, the Dirac's Delta:

$$\mathbf{t}_i(\mathbf{r}) = \hat{\mathbf{t}}_i \delta(\mathbf{r} - \mathbf{r}_i) \quad (3.74)$$

With this choice, the BC is actually enforced only in the point  $\mathbf{r}_i \in T_i$ , rather than averaging it on the entire domain  $T_i$ , and no control is directly wielded on the other points. Major advantage of this technique lies in the computational effort, which is strongly reduced due to the substitution of a 2D integral with a one-point calculation. Similarly, the Dirac Delta can be used as BF, thus approximating the current with its value in the point  $\mathbf{r}'_j \in B_j$ .

### 3.3.2.3. Razor test

With the razor test technique, the function  $\mathbf{f}(\mathbf{r})$  is multiplied by:

$$\hat{\mathbf{n}} \times \mathbf{d}\ell \quad (3.75)$$

where  $\mathbf{d}\ell$  is a path on the domain  $T_m$  with endpoints  $P, Q$ .

The razor test function is particularly interesting when applied to the MPIE. Since

$$(\hat{\mathbf{n}} \times \mathbf{f}) \cdot (\hat{\mathbf{n}} \times \mathbf{d}\ell) = (\hat{\mathbf{n}} \times \mathbf{d}\ell \times \hat{\mathbf{n}}) \cdot \mathbf{f} = \mathbf{f} \cdot \mathbf{d}\ell \quad (3.76)$$

we have for metallic surfaces:

$$\int_P^Q \mathbf{E}^{\text{inc}} \cdot \mathbf{d}\ell = - \int_P^Q \mathbf{E}^{\text{sc}} \cdot \mathbf{d}\ell \quad (3.77)$$

When the scattered field is separated into its vector and scalar potential components,  $\mathbf{E}^{\text{sc}} = -j\omega\mathbf{A} - \nabla\phi_e$ , (Par. 3.1.2), the previous equation reduces to:

$$\int_P^Q \mathbf{E}^{\text{inc}} \cdot \mathbf{d}\ell = j\omega \int_P^Q \mathbf{A} \cdot \mathbf{d}\ell + \int_P^Q \nabla\phi_e \cdot \mathbf{d}\ell = j\omega \int_P^Q \mathbf{A} \cdot \mathbf{d}\ell + [\phi_e(Q) - \phi_e(P)] \quad (3.78)$$

If in addition the right- and left-hand side integrals are evaluated using the trapezoidal rule

$$\int_a^b f(x)dx \approx \frac{f(a) + f(b)}{2}(b - a) \quad (3.79)$$

then the whole computation reduces to the evaluation of  $\mathbf{A}$  and  $\phi_e$  in the endpoints  $P, Q$ .

An eventual problem arises if the path  $\mathbf{d}\ell$  changes direction within  $\overline{PQ}$  (bent paths). In the classical case where  $\overline{PQ}$  can be split into two straight segments  $\overline{PR}$  and  $\overline{RQ}$ , we obtain:

$$\int_P^Q \mathbf{E}^{\text{inc}} \cdot \mathbf{d}\ell = j\omega [\mathbf{A}(P) \cdot \overline{PR} + \mathbf{A}(Q) \cdot \overline{RQ}] + [\phi_e(Q) - \phi_e(P)] \quad (3.80)$$

Again, to implement this TF we only need the integral of the excitation electric field along the path  $\overline{PQ}$  and the discrete values of  $\mathbf{A}$  and  $\phi_e$  at both the endpoints  $P$  and  $Q$ .

### 3.3.2.4. Surface test

When using the surface test, we define a unit vector  $\mathbf{d}\ell$  along the rim of the test surface  $T_m$  and we test the function  $\mathbf{f}(\mathbf{r})$  on the whole surface by multiplying it by a vectorial function  $\mathbf{t}$ , tangential to  $T_m$  in each internal point and additionally orthogonal to  $\mathbf{d}\ell$  on the rim.

Like the razor test, the surface test becomes interesting when applied to the solution of the

MPIE. In this particular case, we obtain:

$$\int_S ds \mathbf{E}^{\text{inc}} \cdot \mathbf{t} = j\omega \int_S ds \mathbf{A} \cdot \mathbf{t} + \int_S ds \nabla \phi_e \cdot \mathbf{t} \quad (3.81)$$

Since

$$\nabla \phi_e \cdot \mathbf{t} = \nabla \cdot (\phi_e \mathbf{t}) - (\nabla \cdot \mathbf{t}) \phi_e \quad (3.82)$$

then

$$\int_S ds \nabla \cdot (\phi_e \mathbf{t}) = \oint_{\partial S} \phi_e \mathbf{t} d\ell = 0 \quad (3.83)$$

because of properties we imposed on  $\mathbf{t}$ . Therefore

$$\int_S ds \mathbf{E}^{\text{inc}} \cdot \mathbf{t} = j\omega \int_S ds \mathbf{A} \cdot \mathbf{t} + \int_S ds \phi_e (\nabla \cdot \mathbf{t}) \quad (3.84)$$

If  $T_m$  is the combination of two rectangles  $T_p$  and  $T_q$ , having centers  $P$  and  $Q$  and with a generic orientation, and  $\mathbf{t}$  is the classical RWG function (which satisfies the hypothesis we made on  $\mathbf{t}$ ), then the implementation of surface testing using the most approximate values for the integral (the mean theorem) gives a similar result as the razor test:

$$\int_S ds \mathbf{E}^{\text{inc}} \cdot \mathbf{t} = j\omega [S_p A_t(P) + S_q A_t(Q)] + [\phi_e(Q) - \phi_e(P)] \quad (3.85)$$

### 3.3.2.5. The Nyström Method

In its original and rigorous formulation, the Nyström Method [72] allows the approximation of integral equations of the *second* kind:

$$\varphi(\mathbf{x}) - I[\varphi(\mathbf{x})] = f(\mathbf{x}) \quad (3.86)$$

where the unknown function  $\varphi$  appears also outside the integral and  $I$  is an integral function with continuous kernel, which can be any of the convolution products appearing in the IE previously illustrated:

$$I[\varphi(\mathbf{x})] = \int_D d\mathbf{y} G(\mathbf{x}|\mathbf{y}) \varphi(\mathbf{y}) \quad (3.87)$$

We introduce now a quadrature rule which allows to write the approximated integral as:

$$I_N[\varphi(\mathbf{x})] = \sum_{n=1}^N w_n G(\mathbf{x}|\mathbf{y}_n) \varphi(\mathbf{y}_n) \quad (3.88)$$

Then,  $\varphi(\mathbf{x})$  solution of (3.86) is approximated by  $\varphi_N(\mathbf{x})$ , solution of the linear system:

$$\varphi_N(\mathbf{x}) - I_N[\varphi_N(\mathbf{x})] = f(\mathbf{x}) \quad (3.89)$$

The Nyström theorem [73] states that if the values  $\varphi_N(\mathbf{x}_m), m = 1 \dots N$  satisfy the linear system:

$$\varphi_N(\mathbf{x}_m) - \sum_{n=1}^N w_n G(\mathbf{x}_m | \mathbf{y}_n) \varphi_N(\mathbf{y}_n) = f(\mathbf{x}_m), \quad m = 1 \dots N \quad (3.90)$$

then the equation

$$\varphi_N(\mathbf{x}) = f(\mathbf{x}) + \sum_{n=1}^N w_n G(\mathbf{x} | \mathbf{y}_n) \varphi_N(\mathbf{y}_n) \quad (3.91)$$

is a solution of (3.89), approximating  $\varphi(\mathbf{x})$ .

The application of quadrature methods such as Nyström is limited in principle to *second-kind* IEs; we know anyway that the Boundary Condition for PEC (3.5) leads to an IE of the *first* kind. These equations are known to violate one or more of the postulates of existence, uniqueness and continuous dependence of the solution on the enforced quantities, which identifies them as ill-posed problems.

The extension of the analysis so far illustrated to the electromagnetic problems formulated via EFIE, MFIE or MPIE requires the introduction of a *projection method*, an operator which basically consists in sampling the function  $\varphi$ , defined over the domain  $\mathbb{D}$ , in a collection of points internal to the domain, enabling an approximate solution of the equations.

Interpolation operators or even the simple collocation method previously discussed belong to the class of projection methods.

Using the collocation method, we can formulate the following expression for the application of the Nyström method to the MoM-SIE problems for the computation of the generic entry of the interaction matrix:

$$\begin{aligned} z_{ij} &= \int_{T_i} ds \int_{B_j} ds' \mathbf{t}_i(\mathbf{r}) \cdot \left[ \bar{\bar{\mathbf{G}}}(\mathbf{r} | \mathbf{r}') \cdot \mathbf{b}_j(\mathbf{r}') \right] \\ &\approx \sum_{m=1}^M \sum_{n=1}^N w_m w_n \hat{\mathbf{t}}_i(\mathbf{r}_m) \cdot \left[ \bar{\bar{\mathbf{G}}}(\mathbf{r}_m | \mathbf{r}'_n) \cdot \hat{\mathbf{b}}_j(\mathbf{r}'_n) \right] \end{aligned} \quad (3.92)$$

Note that the weights have been distributed into the two sets  $w_m$  and  $w_n$ . The beauty of this formulation lies in the intuitive association of the Nyström with the use of weighted impulse basis and test functions in the MoM:

$$\mathbf{t}_i = \sum_{m=1}^M w_m \delta(\mathbf{r} - \mathbf{r}_m) \hat{\mathbf{t}}_i \quad (3.93a)$$

$$\mathbf{b}_j = \sum_{n=1}^N w_n \delta(\mathbf{r}' - \mathbf{r}'_n) \hat{\mathbf{b}}_j \quad (3.93b)$$

The choice of quadrature points and weights is the key aspect of the method and inspired a number of different formulations; a driving condition in that sense is the necessity of treating

the eventual kernel singularities and led for instance to the so-called Local Corrected Nyström (LCN) [74, 75], where singular terms are separately evaluated using a modified algorithm. In this thesis, we have developed a novel MoM formulation, derived from the Nyström strategy, which allows the simultaneous computation of singular and non-singular terms with an universal quadrature rule: the “Magic Distance Inspired” method, described in Chap. 5.

### 3.3.2.6. Resume

The different combinations of basis and test functions illustrated in this section are summarized in Tab. 3.1. In the next chapters, when a MoM procedure is used to check the results obtained with other strategies, the Galerkin formulation is always used. Also when new simpler MoM versions needed to be calibrated in terms of complexity and accuracy, the Galerkin MoM formulation is always used as benchmark with the choice of basis / test functions shown in Tab. 3.2.

**Table 3.1.:** Method of Moments formulations

Basis	Test	Formulation
$\mathbf{b}_j$	$\mathbf{t}_i$	Generic MoM
$\mathbf{b}_j$	$\mathbf{t}_j = \mathbf{b}_j$	Galerkin
$\mathbf{b}_j$	$\delta(\mathbf{r} - \mathbf{r}_i)$	Point Matching
$\mathbf{b}_j$	$\int \mathbf{d}\ell \cdot \square$	Razor test
$\mathbf{b}_j$	$\int_{S_i} ds \square \cdot \mathbf{t}_i$	Surface test
$\sum_{n=1}^N w_n \delta(\mathbf{r}' - \mathbf{r}'_n) \hat{\mathbf{b}}_j$	$\sum_{m=1}^M w_m \delta(\mathbf{r} - \mathbf{r}_m) \hat{\mathbf{t}}_i$	Nyström method

**Table 3.2.:** Choice of functions for Galerkin formulation

IE		Basis	Test
EFIE	$\mathbf{J}$	Rooftop	Rooftop
MPIE	$\mathbf{J}$	Rooftop	Rooftop
	$\rho$	Pulse	Pulse
EPIE	$\rho$	Pulse	Pulse

### 3.3.3. Galerkin-MoM formulation of IEs

The MoM in the Galerkin formulation can be used for the discretization of the Integral Equations EPIE (3.55), EFIE (3.40) and MPIE, (3.51) or (3.52).

#### 3.3.3.1. The EPIE

As the Green's Function (3.56) does not include any derivative, finite domain zero-order (pulse) functions  $\square(\mathbf{r})$  (3.65) can be safely used as basis / test functions. The generic entry  $z_{ij}$  of the MoM matrix can be expressed as:

$$z_{ij} = \frac{1}{\varepsilon} \int_{S_i} ds \square_i(\mathbf{r}) \int_{S_j} ds' \square_j(\mathbf{r}') G^{ES}(\mathbf{r} | \mathbf{r}') \quad (3.94)$$

$$= \frac{1}{\varepsilon} \int_{S_i} ds \int_{S_j} ds' G^{ES}(\mathbf{r} | \mathbf{r}') \quad (3.95)$$

#### 3.3.3.2. The EFIE

The kernel of the integral is the Green's Function  $\bar{\bar{\mathbf{G}}}_{\mathbf{E},\mathbf{J}}$  (3.41) which exhibits a  $r^{-3}$  singularity. The discretization of the EFIE (3.40) results in matrices whose elements are given by double surface (and hence 4D) integrals, where - at least in theory - singularity can be integrated. Using as basis/test functions the rectangular domain RWG  $\Delta_R(\mathbf{r})$  (3.67) we obtain:

$$z_{ij} = \int_{S_i} ds \int_{S_j} ds' \Delta_{\mathbf{R}_i}(\mathbf{r}) \cdot \left[ \bar{\bar{\mathbf{G}}}_{\mathbf{E},\mathbf{J}}(\mathbf{r} | \mathbf{r}') \cdot \Delta_{\mathbf{R}_j}(\mathbf{r}') \right] \quad (3.96)$$

#### 3.3.3.3. The MPIE

When applying the MoM to the MPIE (3.51) in a homogeneous environment, the differential operator outside the second integral can be redistributed to the test function (with a change of sign). Following this procedure, the generic entries of the MoM matrix, separated into their vector and scalar potential components  $a_{ij}$  and  $v_{ij}$ , can be expressed as:

$$a_{ij} = \frac{j\omega\mu}{4\pi} \int_{S_i} ds \Delta_{\mathbf{R}_i}(\mathbf{r}) \int_{S_j} ds' \Delta_{\mathbf{R}_j}(\mathbf{r}') \frac{\exp(-jkR)}{R} \quad (3.97a)$$

$$v_{ij} = \frac{(j\omega\varepsilon)^{-1}}{4\pi} [\nabla \cdot \Delta_{\mathbf{R}_i}(\mathbf{r})] [\nabla' \cdot \Delta_{\mathbf{R}_j}(\mathbf{r}')] \int_{S_i} ds \int_{S_j} ds' \frac{\exp(-jkR)}{R} \quad (3.97b)$$

with  $R = |\mathbf{r} - \mathbf{r}'|$ .

The  $z_{ij}$  term of the MoM matrix becomes then sum of four integrals  $I_{\pm i, \pm j}$  associated to the interaction between the  $S^+/S^-$  parts of the  $i$ -th and  $j$ -th  $\Delta$ . If the support of the rooftop



is a rectangle, we can use (3.66) and (3.67) to derive the partial integral:

$$I_{\pm i, \pm j} = (-1)^{i+j} \frac{1}{L_i^\pm} \frac{1}{L_j^\pm} \int_{T_i^\pm} ds \int_{B_j^\pm} ds' \left[ (u - m_{i,u}^\pm) (v - m_{i,v}^\pm) \hat{\mathbf{u}} \cdot \hat{\mathbf{v}} - \frac{1}{k_0^2} \right] \frac{\exp(-jkR)}{R} \quad (3.98)$$

whereas with triangular domain rooftops, we have:

$$I_{\pm i, \pm j} = \frac{L_i}{A_i} \frac{L_j}{A_j} \int_{T_i^\pm} ds \int_{B_j^\pm} ds' \frac{1}{4} \left\{ t^\pm(\mathbf{r}) b^\pm(\mathbf{r}') (\hat{\mathbf{t}} \cdot \hat{\mathbf{b}}) - \frac{1}{k_0^2} \left[ \frac{1}{L_t^\pm} \right] \left[ \frac{1}{L_b^\pm} \right] \right\} \frac{\exp(-jkR)}{R} \quad (3.99)$$

### 3.4. Implementation of MoM

The investigation of new original MoM formulations required at first having at our disposal a robust home-made MoM implementation. This was the Galerkin strategy described in Tab. 3.2. This reference tool allows the control and manipulation of all the quantities involved in the computation, that is, the entries of the reaction matrix in their vector and scalar parts (MPIE) and the algorithm used for the numerical evaluation of the integrals. The generation of typical outputs such as surface currents and radiated fields was also implemented, in order to use the software, once validated, as reference against the simplified versions we formulated.

Three of the formulations of IE illustrated in this chapter have been implemented: EPIE for the electrostatic problem, MPIE and EFIE for the full-wave case. Special attention has been paid to the evaluation of the self term: while the electrostatic GF allows a closed form solution of the integral, in the electrodynamic case the presence of the exponential term  $\exp(-jkr)$  in  $\bar{\bar{\mathbf{G}}}_{\mathbf{A}, G_V}$  (MPIE, (3.49)) or  $\bar{\bar{\mathbf{G}}}_{\mathbf{E}, \mathbf{J}}$  (EFIE, (3.41)) requires either an approximated solution or numerical integration. In the first case, assuming the size of the cells to be small in terms of wavelength, the exponential can be expanded in Taylor series: the first term of the expansion is exactly the electrostatic term and, like the higher-order terms, allows a closed form solution. The numerical computation of the self term on the other hand cannot be directly performed, as the singularity appearing in the GF leads to a divergent result or, in the best case, to a rather inaccurate one. A standard technique [66] was successfully used to tackle this problem for the MPIE GF: the singularity extraction

$$\frac{\exp(-jkr)}{4\pi r} = \frac{\exp(-jkr) - 1}{4\pi r} + \frac{1}{4\pi r} \quad (3.100)$$

The first term on the right hand side is not singular and can be (numerically) evaluated; the second term is the static GF and is computed analytically, for instance [76].

Our MoM-Galerkin software was intended to cover the specific range of application related to the design of the MAST antenna system. This class of electromagnetic problems involves the scattering of PEC objects in free space (the satellite), hence the formulation discussed in Par. 3.3.3 constitutes the core of the algorithm. A peculiar characteristic is also the exclusive presence of rectangular geometries: the cuboidal platform, rectangular (bent) slots, eventually rectangular patches and PIFAs; this suggests that rectangular domain rooftops Par. 3.3.1.2 (or rectangular pulses Par. 3.3.1.1 in electrostatics) can be used as basis functions.

### MPIE self term

We consider a couple  $S$  of rectangular cells  $S_+, S_-$  with endpoints:

$$S_+ = [u_a, u_b] \times [v_a, v_b] \quad (3.101a)$$

$$S_- = [u_b, u_c] \times [v_a, v_b] \quad (3.101b)$$

which is associated to an  $\hat{\mathbf{u}}$  oriented basis/test function of amplitude:

$$b(u) = \begin{cases} \frac{u - u_a}{u_b - u_a} & u \in [u_a, u_b] \\ \frac{u_c - u}{u_c - u_b} & u \in [u_b, u_c] \end{cases} \quad (3.102a)$$

$$db(u) = \nabla \cdot b(u) = \begin{cases} +\frac{1}{u_b - u_a} & u \in [u_a, u_b] \\ -\frac{1}{u_c - u_b} & u \in [u_b, u_c] \end{cases} \quad (3.102b)$$

Applying the singularity extraction, the vector potential integral is given by:

$$\begin{aligned} \int_S du dv \int_S du' dv' b(u) b(u') \frac{\exp(-jkR)}{R} = \\ \int_S du dv \int_S du' dv' b(u) b(u') \frac{\exp(-jkR) - 1}{R} + \\ \int_S du dv b(u) \left\{ \left[ b(u) \int_S du' dv' \frac{1}{R} \right] + \left[ db(u') \int_S du' dv' \frac{u - u'}{R} \right] \right\} \end{aligned} \quad (3.103)$$

and the scalar potential integral is:

$$\begin{aligned} \int_S du dv \int_S du' dv' db(u) db(u') \frac{\exp(-jkR)}{R} = \\ \int_S du dv db(u) \int_S du' dv' db(u') \frac{\exp(-jkR) - 1}{R} + \\ \int_S dudv db(u) \int_S du' dv' db(u') \frac{1}{R} \end{aligned} \quad (3.104)$$

Analytical formulas [76] are available for the evaluation of the integrals with kernel  $1/R$  and  $(u - u')/R$ ; note anyway that with this formulation a numerical evaluation is required for each term [76].

The basis function can also be approximated in order to simplify the computation and the analytical treatment of the self term. A possibility is replacing the rooftop of amplitude 1 with a pulse of amplitude 1/2: as a result, an equation in the form of (3.104) can be used indistinctively for the vector and the scalar potential parts. The same procedure can be applied to the EFIE self-term with the difference that the  $1/R^3$  singularity is only mitigated by the extraction; the accuracy of the computation is anyway not satisfying and is therefore necessary to revert to the MPIE formulation.

The numerical evaluation of the integrals is performed using the Gauss-Legendre quadrature rule. We found that when the structure is meshed with cells of size in the order of  $\lambda/10$ ,  $10 \times 10$  points grids are required for near terms (cells sharing an edge) and  $5 \times 5$  points grids for the generic off-diagonal terms; with this choice,  $5^4 = 625$  computations are required for each term ( $10^4$  for the near terms). When evaluating the self term, the same point grid cannot be used for the inner and outer integral, as they produce overlapping points which cause a division by zero in the first right-hand side of (3.103) and (3.104). Grids of  $20 \times 20 \times 21 \times 21$  points are therefore used for the computation of the self terms, for a total of  $\sim 1.8 \text{ E}04$  calculations.

### 3.5. Comparison of the different IE formulations

After recalling the fundamental aspects of the most well-known formulations of IE and MoM, we resume here those characteristics which, though not constituting any original conclusion, have driven the choices about the strategy adopted in the following chapters.

In fact, in the frame of the improvement of the developed software SatAF, main objective of this thesis, a number of well-known, useful considerations concerning the Green's Function associated with the different formulations of IE were fundamental for the choice of the full-wave method to be combined with SatAF, according to the strategy adopted at the end of Chap. 2. These considerations are resumed hereafter.

A comparison between the two formulations of the IE in electrodynamics, the EFIE and MPIE, highlights the advantages and the weaknesses of the two.

The dyadic Green's Function  $\bar{\mathbf{G}}_{\mathbf{E},\mathbf{J}}$ , kernel of the EFIE, can or cannot include the effect of the material environment surrounding our metallic sheets. Therefore, the complexity of the dyadic GF goes from the closed-form analytical formulation for free space recalled in (3.41) to quite involved expressions, like the combinations of Sommerfeld integrals and analytical series found in the treatment of planar, cylindrical and spherical layered dielectric media. In all cases, it is known that the double derivative contained in the EFIE GF produces a singularity in the computation of the self term of order  $1/r^3$  (hypersingularity). This means that when discretizing the EFIE with a classical MoM procedure, a special treatment must

be used for the computation of the self-term and a simple scheme like Point-matching, as reminded in Par. 3.3.2.2, cannot be used. The strong singularity also prevents the use of otherwise promising approaches like the Nyström method, resumed in Par. 3.3.2.5. It is true that the space singularity problem can be avoided by solving the EFIE in the spectral domain [49]; however, spectral approaches are inefficient for arbitrary or non-canonical geometries. In practice, all commercially successful implementations of EFIE (FEKO [40], WIPL-D [77]) remain in space domain and resort to the use of two-dimensional basis [70] and a MoM-Galerkin approach.

In this context, a well-known successful strategy is to transform the EFIE into the MPIE. The GF appearing in (3.52) exhibits only a mild source-observer singularity of  $1/r$  type; this simplifies the numerical evaluation of the self term and allows the use of simple point-matching discretization (Par. 3.3.2.2).

### Possible applications to SatAF

When analyzing antenna arrays allocated on small platforms, the electromagnetic problem can be reduced to metallic surfaces in free space. In this environment, MPIE, or even EFIE, appear as the most suitable formulations of the IE and can be combined with SatAF for the local analysis of sub-sets of sources constituting the complete antenna system. If on one hand the Galerkin formulation is well established as reliable, the demand of reduced computational speed leads to the investigation of an alternative formulation where the bottle neck of the algorithm, the computation of 4D integrals, is removed. An eventual price paid in terms of accuracy of the solution (the surface currents) can be tolerated as long as it does not degrade the quality of the predictions of the radiated fields, which is the primary target of the analysis method under investigation.

It is a clear outcome of the well-known concepts reviewed in the present chapter that the correct treatment of the singularity associated with the self term is the key aspect that determines the possibility of simplifying (or avoiding) the evaluation of 4D integrals appearing in the Galerkin formulation of MoM and therefore easing the computational effort required by the algorithm.

## 3.6. Conclusions

In this chapter we have recalled, for the sake of completeness, the fundamental elements of electromagnetism pertinent to the discussion of Integral Equation formulations and their Method of Moments implementations.

After defining the vector and scalar potential, we derived the different Integral Equations: the MFIE and the EFIE, its alternative formulation, the MPIE, and the electrostatic version the EPIE. A review of the most popular choices for the MoM basis and test functions was performed, with special attention paid to the Nyström method which will be used s

inspiration for the MoM original formulation described in Chap. 5.

The uniformed notation used in this chapter will be used throughout all the mathematical formulations performed in the next chapters.



## 4. Towards an improved version of SatAF

### 4.1. Introduction

The combination of Array Theory with elementary sources' radiation patterns, implemented in the software SatAF, is useful for a first-approach evaluation of the radiation characteristics of an array of antennas allocated onboard small satellites. Even if the fundamental concept of taking advantage of the Array Theory is valid for a first approach, the main weakness lies in the fact that it considers the antenna elements as ideal sources and neglects the true influence of the currents induced on the platform regions close to the antenna elements, which can largely modify the radiation pattern. These assumptions are valid and lead to reliable results only for a restricted class of problems; in particular, it was observed that slot antennas in particular are a critical element causing the breakdown of the software. In order to extend the range of applicability of SatAF, it is therefore required an evolution of the analysis method.

The improvement of the method primarily requires the treatment of platform scattering; in this direction, two different strategies can be adopted. On one side are the methods that approximate the phenomenon itself: to this category belong the methods based on ray tracing, which span in increased complexity from the Physical Optics to the more sophisticated Geometrical Theory of Diffraction and Uniform Theory of Diffraction. Another approach consists in the use of classical, solid full-wave methods which completely represent the scattering phenomenon, introducing at the same time approximations in the formulation that relax the computational effort.

In this work, we selected the Electric Field Integral Equation (EFIE) (or its analogous, the Mixed Potential IE, MPIE) for the formulation of the electromagnetic problem and the Method of Moments (MoM) for the solution of the IE.

A first implementation of MoM in the canonical Galerkin formulation, based on the theoretical concepts recalled in the previous section, is first developed as reference and baseline for the investigation on a simplified, alternative formulation, which will be illustrated in depth in the following chapter, Chap. 5.

This chapter is dedicated to the illustration of an original, simplified method for the analysis and design of slot antenna arrays, based on a Mixed Potential Integral Equation formulation solved by Method of Moments (MoM-MPIE). Two aspects are addressed in particular: the simplification of the model used for the excitation of the single slot antenna and the exploitation of Array Theory, which is now improved by the inclusion of the induced

currents allowed by the MoM, for the generation of the total radiation pattern.

Capitalizing the experience of SatAF, we investigate the actual possibility of replacing the full-wave simulation of the entire antenna system, which (as discussed in Chap. 2), usually consists of an array of replicas of a simple radiator in different positions and orientations, with the combination of 3D Array Theory and a simplified Method of Moments.

Analyzing the simple radiator with MoM enables to control the accuracy in the representation of the second-order radiation mechanisms through the choice of the elements to be included in the simulation model. As an example, in the case of a slot lying on a metallic platform, the simulation can be performed including in the model either the whole structure or parts of it, for instance a finite ground plane representing one of the faces which being a 2D geometry reduces the complexity of the model. In particular, we are interested in establishing the limit of applicability of this concept and finding the most useful and significant compromise between simplification of the model and accuracy of the results.

## 4.2. Dealing with slots: the excitation problem

Low weight and low profile are key requirements for allocation of devices on satellites and radiators such as patches, PIFAs and in particular slot antennas are often preferred. The antenna system developed in the frame of the MAST project itself consists of an array of slot antennas. In this section we introduce a novel model for the slot excitation, fully compatible with the well-known Mixed Potential Integral Equation (MPIE) formulation of the problem solved with Method of Moments (MoM).

An investigation on some of the most well-established excitation techniques for slot antennas (among others: microstrip feed, coaxial feed) highlights a common phenomenon: fields are coupled from the feeding network to the radiating element through a charge accumulation located in proximity of the slot edges. Including in the model the charge accumulation alone as source is expected to excite the same field as if the entire feeding structure were present.

The choice of MPIE allows a simple representation of this phenomenon, fully compatible with the MoM framework: the excitation field is assumed to be produced by two constant (and opposite) charge distributions located in two cells on the two sides of the slot. An intuitive justification for this choice is given hereafter.

The most obvious (although not the most sophisticated) way of exciting a slot antenna is to connect the metallic areas near the long edges of the aperture and facing each other to the extremities of a transmission line. Imagining that the slot ground plane is meshed with rectangular cells, the opposite currents excited by the transmission line conductors spread across the two cells where the conductors are connected and can be expanded with rooftops (as defined in Par. 3.3.1.2). Taking the divergence of those currents on the respective cells



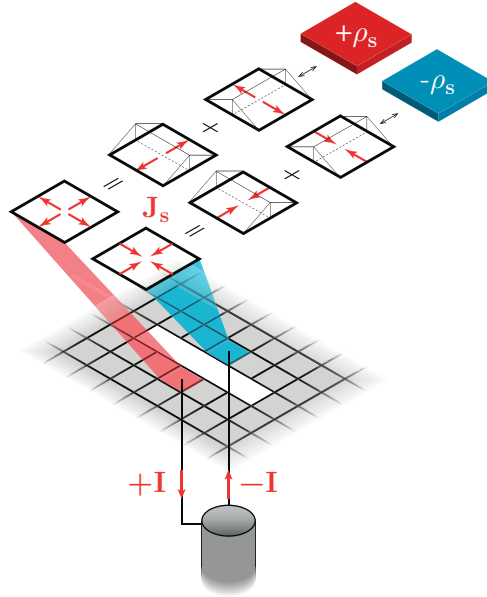


**Figure 4.1.:** Current and charge model for the slot excitation.

yields two constant positive/negative charges associated with the cells themselves. The concept is illustrated in Fig. 4.1, where the transmission line is represented by a coaxial cable.

The opposite current densities are located very close, have opposite direction and similar, if not identical, magnitude; therefore, they can be considered to cancel reciprocally and the incident field, to be used as known value in the right-hand side of the Integral Equation (3.52), is obtained using the scalar potential part of (3.97). Note that other formulations of the Integral Equation different from MPIE (such as Electric Field Integral Equation, EFIE) do not offer the same possibility as they don't explicitly contain the contribution of charge densities to the scattered electric field.

It is worth stressing the fact that with this model, the excitation is given by a part of a generic entry of the MoM matrix and no extra coding is necessary in addition to the basic MoM implementation.

As a further simplification, the charge densities do not contribute to far field radiation, which is therefore produced by the sole surface currents induced on the scatter, which are just the solution of the MoM. In fact, when the electric field generated by a current  $\mathbf{J}(\mathbf{r})$  in free space is decomposed into its vector and scalar potential components according to (3.14), using the GFs in (3.49) we have for the vector potential:

$$\begin{aligned} \mathbf{E}_A(\mathbf{r}) &= -j\omega\mu G(\mathbf{r}) \otimes \mathbf{J}(\mathbf{r}) \\ &= -j\omega\mu \frac{\exp(-jkr)}{4\pi r} \otimes \mathbf{J}(\mathbf{r}) \end{aligned} \quad (4.1)$$

while the scalar potential part can be expanded as:

$$\begin{aligned} \mathbf{E}_V(\mathbf{r}) &= +\frac{1}{j\omega\epsilon} (\nabla\nabla G(\mathbf{r})) \otimes \mathbf{J}(\mathbf{r}) \\ &= -\frac{1}{j\omega\epsilon} \left\{ -k^2 \left[ \left( 1 - \frac{3}{k^2 r^2} + \frac{3j}{kr} \right) \hat{\mathbf{r}}\hat{\mathbf{r}} + \left( \frac{1}{k^2 r^2} + \frac{j}{kr} \right) \bar{\bar{\mathbf{I}}} \right] \frac{\exp(-jkr)}{4\pi r} \right\} \otimes \mathbf{J}(\mathbf{r}) \end{aligned} \quad (4.2)$$

In the far field region  $k|\mathbf{r} - \mathbf{r}'| \gg 1$ ,  $\mathbf{r}' \in S$  (the metallic plate), the terms  $1/r$ ,  $1/r^2$  are neglected and the scalar potential contribution becomes:

$$\begin{aligned} \mathbf{E}_V(\mathbf{r}) &= +j\omega\mu \left( \frac{\exp(-jkr)}{4\pi r} \hat{\mathbf{r}}\hat{\mathbf{r}} \right) \otimes \mathbf{J}(\mathbf{r}) \\ &= -[\mathbf{E}_A(\mathbf{r}) \cdot \hat{\mathbf{r}}] \hat{\mathbf{r}} \end{aligned} \quad (4.3)$$

The far field produced by the charge has therefore the only effect of cancelling the radial component of the field produced by the current. In our model the excitation consists exactly of sole charges and does not require to be included in the computation of the far field.

Moreover the major benefit of the proposed method, we can highlight the extreme simplification of the model, which does not require the design of any additional structure to excite the slot and reduces the geometry to the very platform itself.

The excitation model has been integrated into an in-house implementation of MPIE - MoM in the classical Galerkin formulation. The consistency of the model is proved in the next section by comparing its predictions with the commercial software HFSS in a series of test cases inspired by the actual design process followed in the MAST project.

#### 4.2.1. Validation

The slot excitation model has been integrated into our MoM algorithm (Sec. 3.4) for the solution of the MPIE in the Galerkin formulation. The consistency of the model has been validated through the computation of the surface current  $\mathbf{J}_s$  and the far field in different test cases and the comparison with the converged values obtained with the commercial software HFSS.

For a complete benchmark of the model, different shapes of the slot have been explored, starting from the canonical thin, rectangular slot to bent geometries, like the dog-bone or the "C-shaped" slot, which are actually used for practical antenna design. The slots are first radiating on a ground plane, then on a metallic platform; also for the sake of completeness, a configuration involving an array of four slots has been included in the benchmark. A working frequency  $f = 2$  GHz (corresponding to a free space wavelength  $\lambda = 15$  cm) has been used through the campaign.

### Center-fed slot on ground plane

A canonical half-wavelength slot of  $7.5 \times 0.4$  cm lies on a small ground plane of 10 cm side and the excitation is located in the center of the slot. The current distribution, illustrated in Fig. 4.2, is characterized by an accumulation of current around the tips of the slot and can be recognized to be the typical distribution produced by a thin aperture of length  $\lambda/2$ . The far field on the two orthogonal elevation planes is compared with the reference in Fig. 4.3 and shows an excellent agreement with the reference.

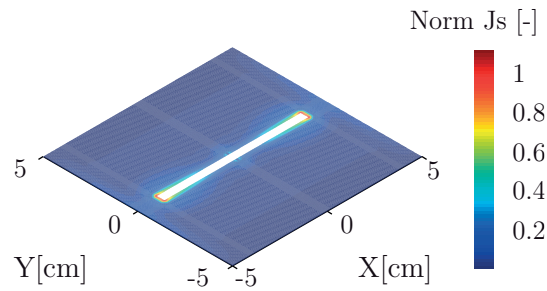


**Figure 4.2.:** Center-fed slot, surface current on the ground plane (results generated with the in-house MoM).

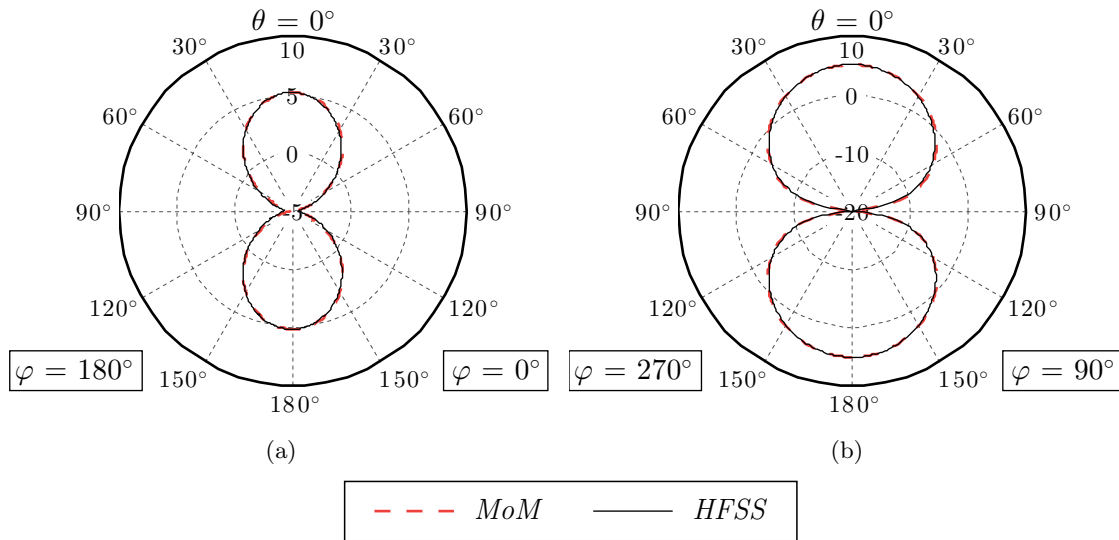


**Figure 4.3.:** Center fed slot, radiation patterns: (a)  $\varphi = 0$  deg and (b)  $\varphi = 90$  deg.

### Offset-fed slot on ground plane

In a more realistic design, the feed is located with an offset of 2.1 cm from the center of the slot, in order to match the antenna. The predictions of the surface current Fig. 4.4a describes correctly the tip behavior at both ends of the slot. Radiated fields exhibit a degree of accuracy almost identical to the center-fed case, Fig. 4.4b.

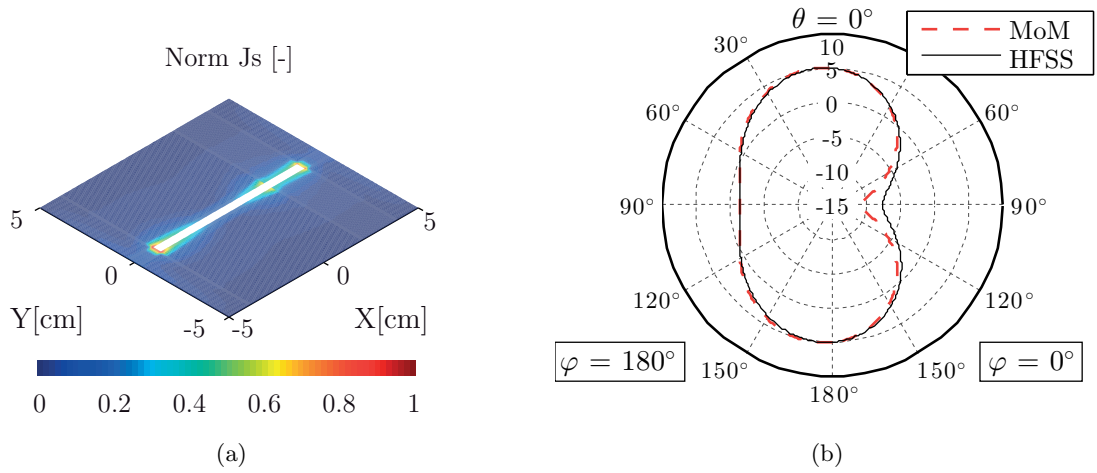


**Figure 4.4.:** Offset-fed slot. (a) Current distribution (in-house MoM) and (b) radiation pattern on  $\varphi = 0$  deg.

#### Dog-bone and C-shaped slots on ground plane

The excitation model was tested with the more complex slot shapes actually used during the design of the MAST antenna system. Two examples of relevant interest, similar to the final design, are the "dog-bone" and the C-shaped slot. The feed and the characteristic dimensions of the slots are adjusted in order to achieve a proper input matching. In all the cases, the current distribution cannot be easily figured out and the predictions obtained with our method are compared with HFSS, as illustrated in Fig. 4.5 and Fig. 4.6. The comparison of the radiation patterns on the two main elevation planes are shown in Fig. 4.7 for the dog-bone and Fig. 4.8 for the C-shaped slot and exhibit again an excellent accuracy.

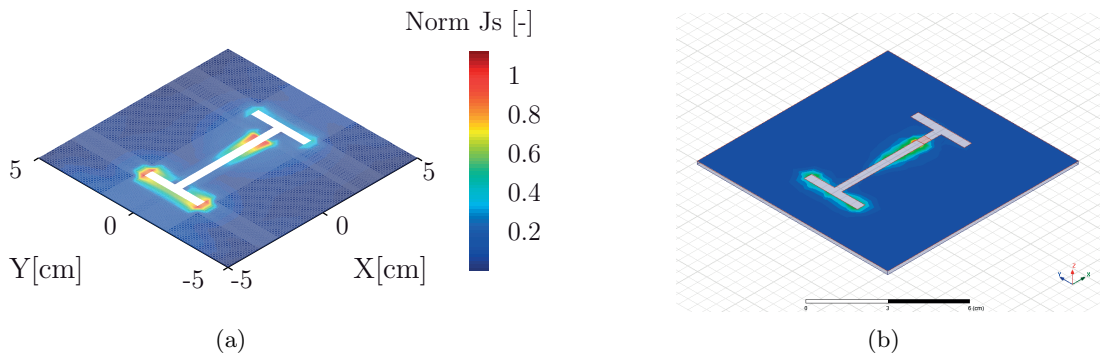


**Figure 4.5.:** Dog-bone slot, surface current on the slot ground plane. (a) MoM and (b) HFSS.

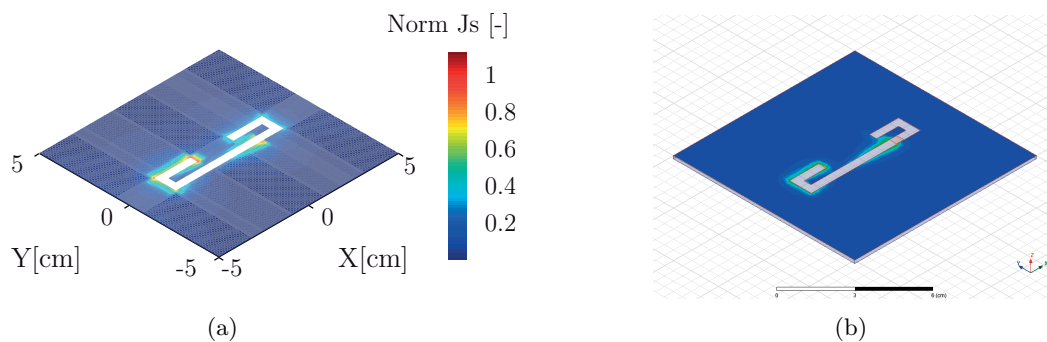


Figure 4.6.: C-shaped slot, surface current on the slot ground plane. (a) MoM and (b) HFSS.

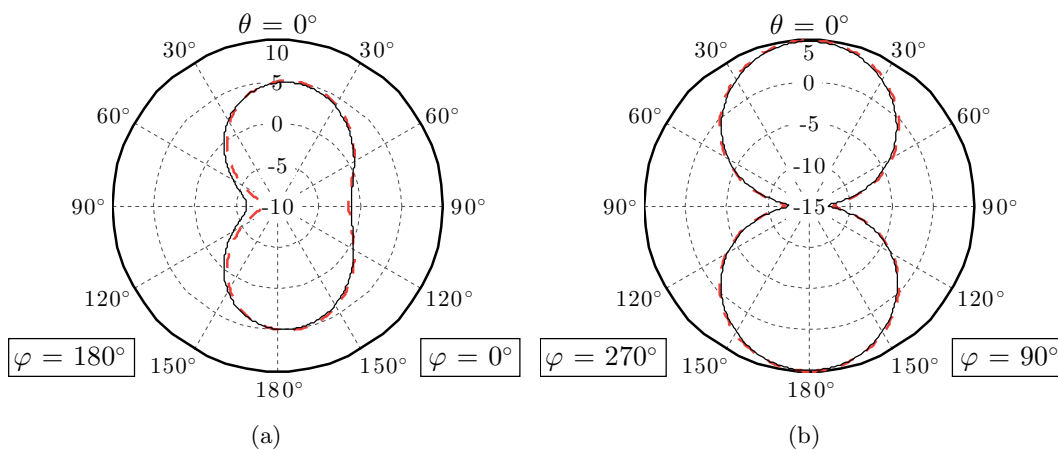


Figure 4.7.: Dog-bone slot, radiation patterns: (a)  $\varphi = 0$  deg and (b)  $\varphi = 90$  deg.

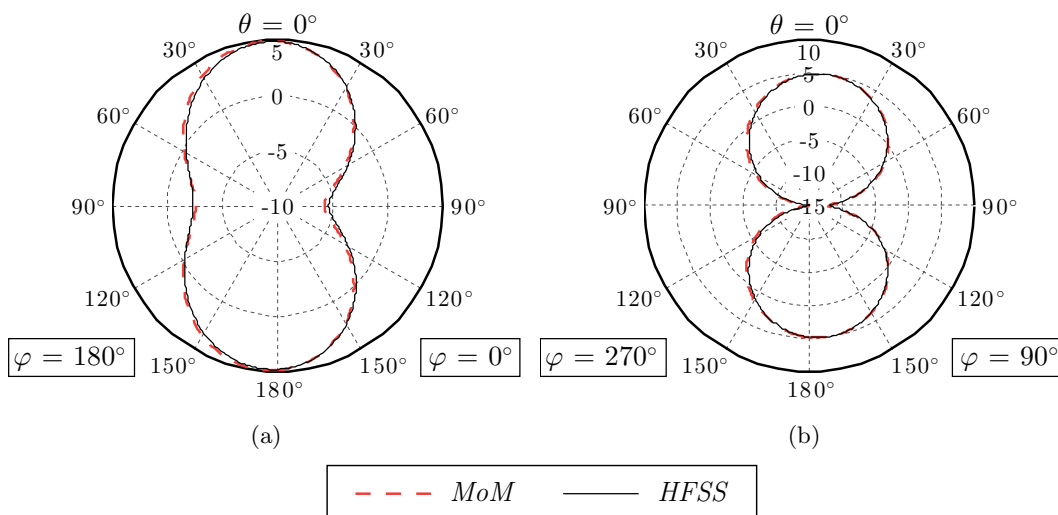
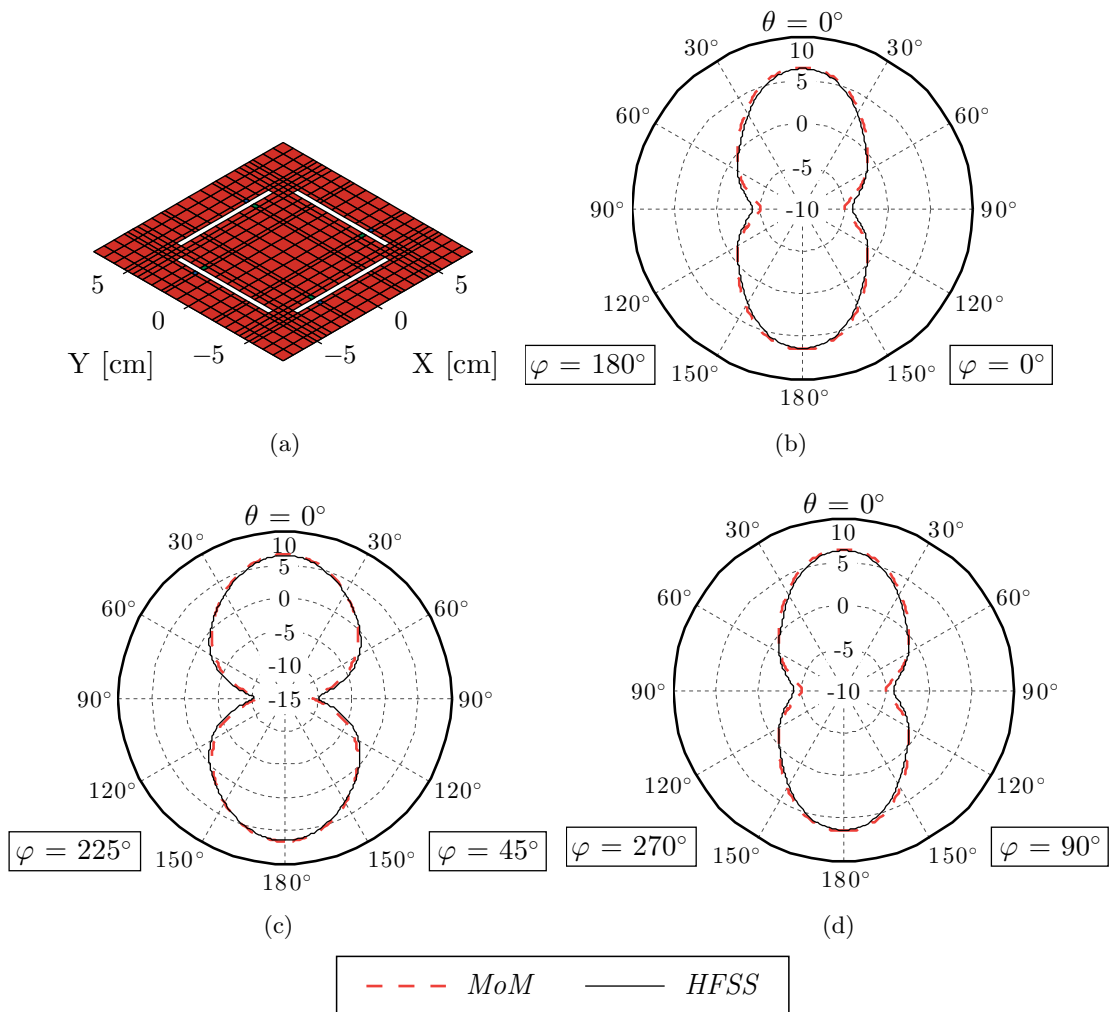


Figure 4.8.: C-shaped slot, radiation patterns: (a)  $\varphi = 0$  deg and (b)  $\varphi = 90$  deg.

### Slot array in sequential rotation on ground plane

This configuration is conceptually similar to the radiating element located on each face of the satellite: four single-slots are arranged as a ring on a groundplane of size  $\lambda = 15$  cm (Fig. 4.9a) and are fed with sequential rotation in order to generate a RHCP polarization. The double dog-bone slots have been replaced by the simplified canonical slot just for the purpose of reducing the mesh complexity and avoid an excessive computational load.

The radiation patterns on the main elevation cuts  $\varphi = 0, 45, 90$  are shown in Fig. 4.9b-d; again, a very high degree of accuracy is obtained.



**Figure 4.9.:** Four slots in sequential rotation, (a) layout and surface currents, (b-d) radiation patterns on  $\varphi = 0, 45, 90$  deg planes.

### 4.3. Combination with Array Theory

After having introduced the slot excitation model, which simplifies the computation of the radiation pattern of a single element, we focus on the problem of an array of slots allocated on a metallic platform.

In the last of the test configurations shown in Sec. 2.6, involving an array of slot pairs allocated on a cubic platform, we investigated the potentialities of the combination of SatAF and HFSS. In particular, the results of the HFSS simulation of *one* slot pair lying on a ground plane representing the platform face was imported in SatAF as “basic element” and manipulated to generate the total radiation pattern. This latter was finally compared against the full-wave simulation of the entire structure.

Results were promising (Fig. 2.51 to Fig. 2.56) and motivated the attempt of developing an analysis method tailored for space platform problems.

In this section we validate the first advance made in the direction of the improvement of SatAF, showing that retaining the same approach used in Sec. 2.6 and just recalled, HFSS can be seamlessly replaced with our implementation of MoM, which features in particular the simplified slot excitation model illustrated in this chapter.

To demonstrate the validity of the solution “SatAF + MoM”, we refer to the aforementioned test configuration, also recalled here in Fig. 4.10; as it was the case in Sec. 2.6, we use again two different feeding schemes for the elements, named “Feed Scheme 1” and “Feed Scheme 2”.

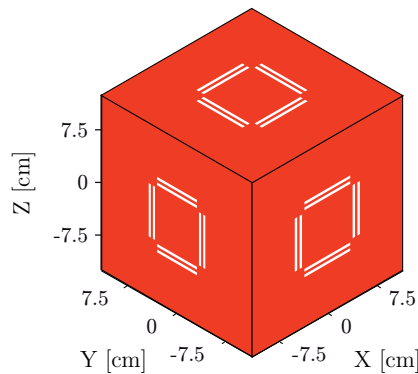


**Figure 4.10.:** The test case, layout.

The predictions of the new solution (SatAF + MoM) are compared in Fig. 4.11 through Fig. 4.16 with the other previously generated curves representing:

- The combination of SatAF with HFSS (SatAF + HFSS).
- The combination of SatAF with MoM, with the slot excitation model (SatAF + MoM).
- The full-wave simulation of the entire structure, taken as reference (Full HFSS).

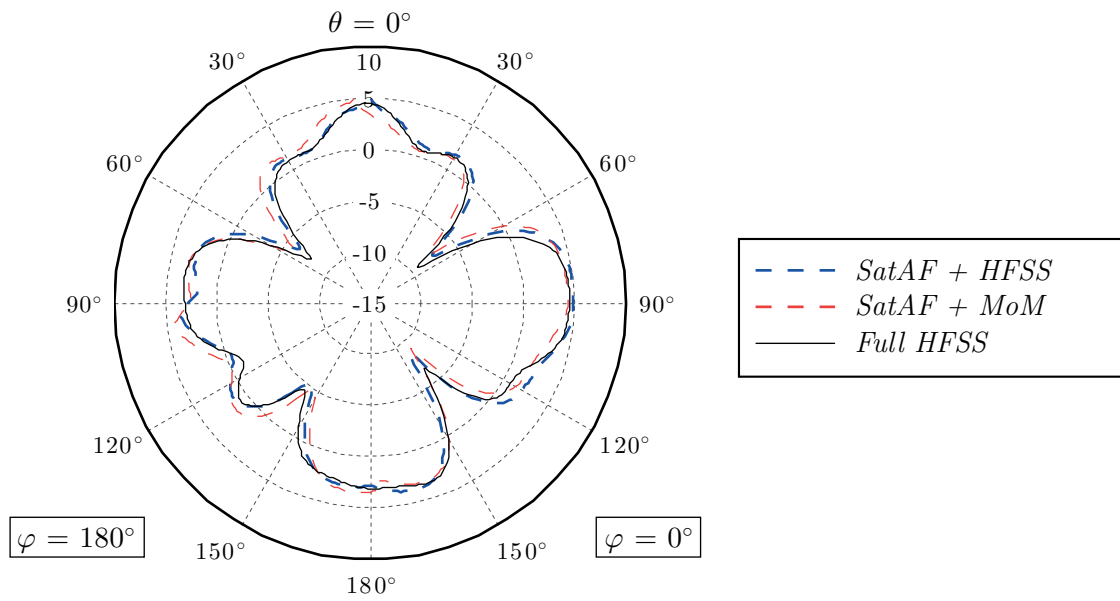


**Figure 4.11.:** Feed Scheme 1: radiation patterns on  $\varphi = 0$  deg cut.

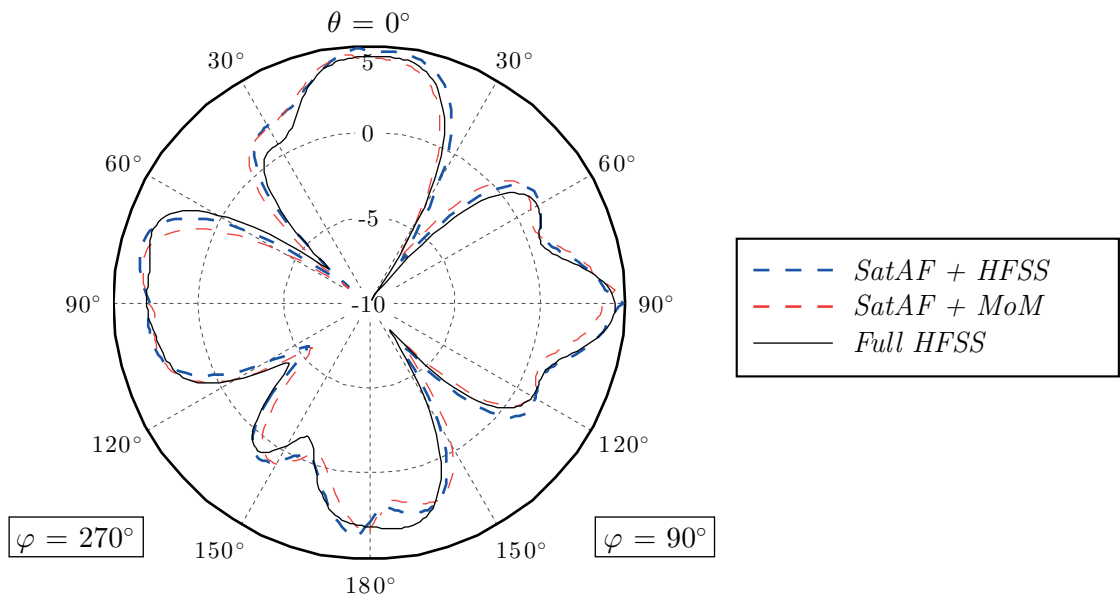


**Figure 4.12.:** Feed Scheme 1: radiation patterns on  $\varphi = 90$  deg cut.



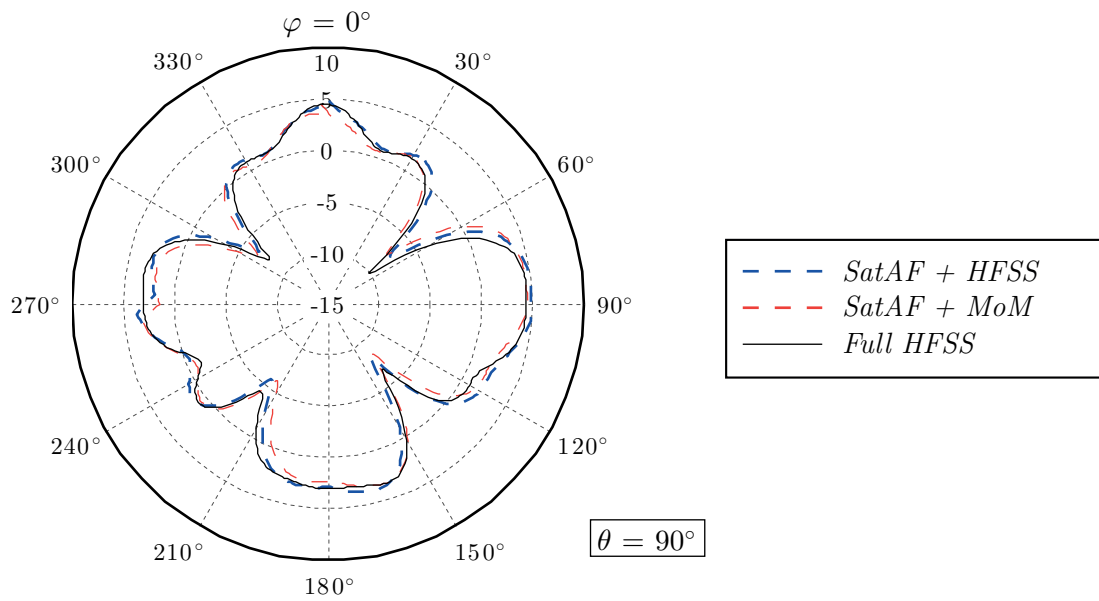


Figure 4.13.: Feed Scheme 1: radiation patterns on  $\theta = 90$  deg cut.

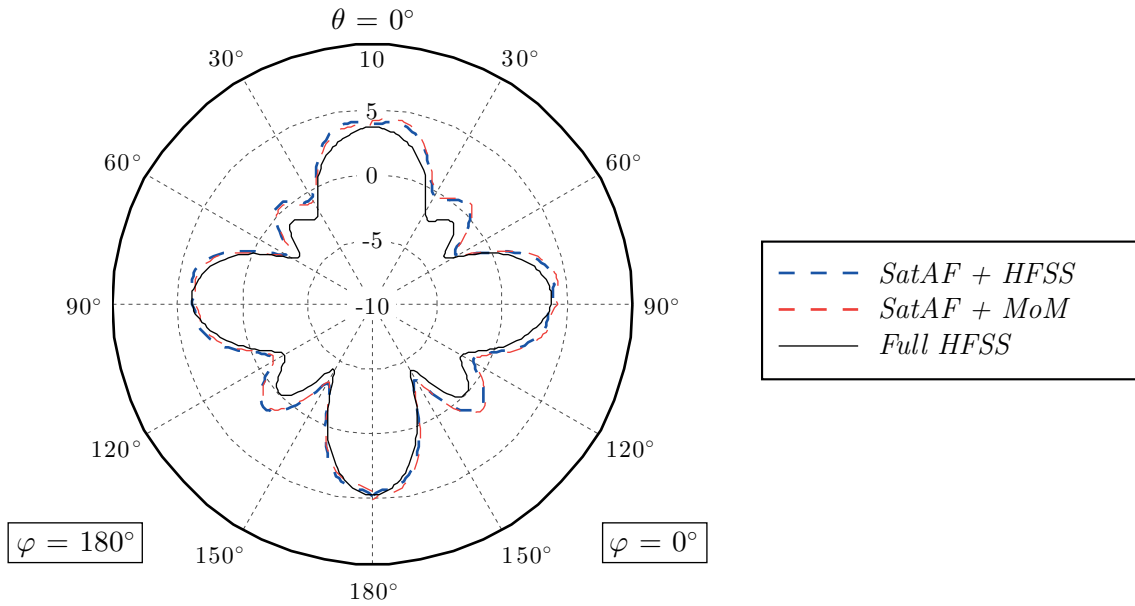
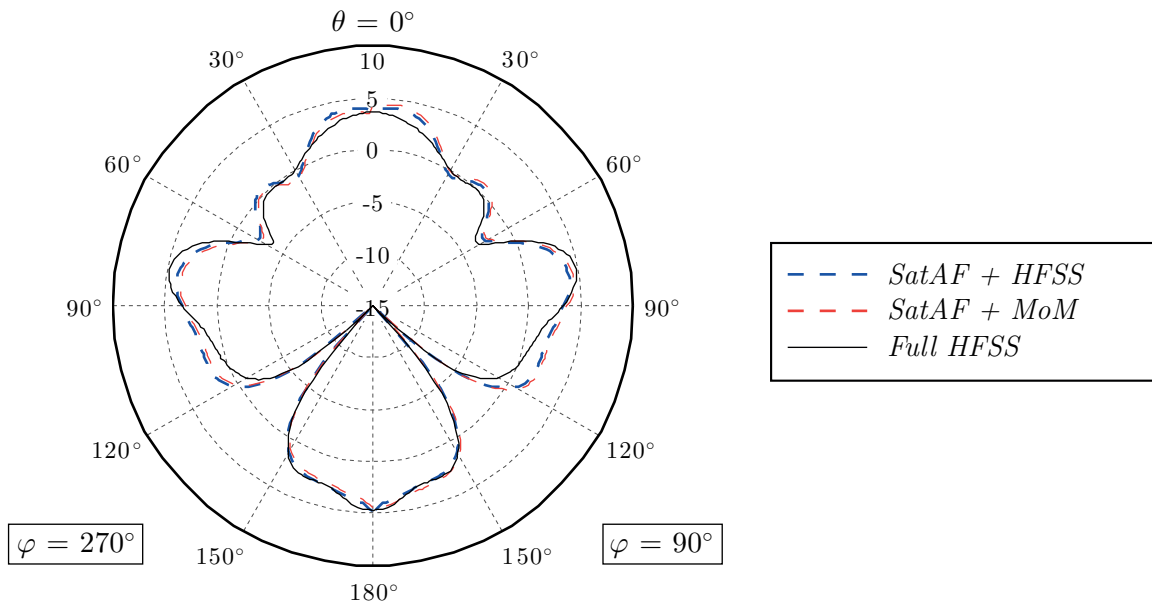
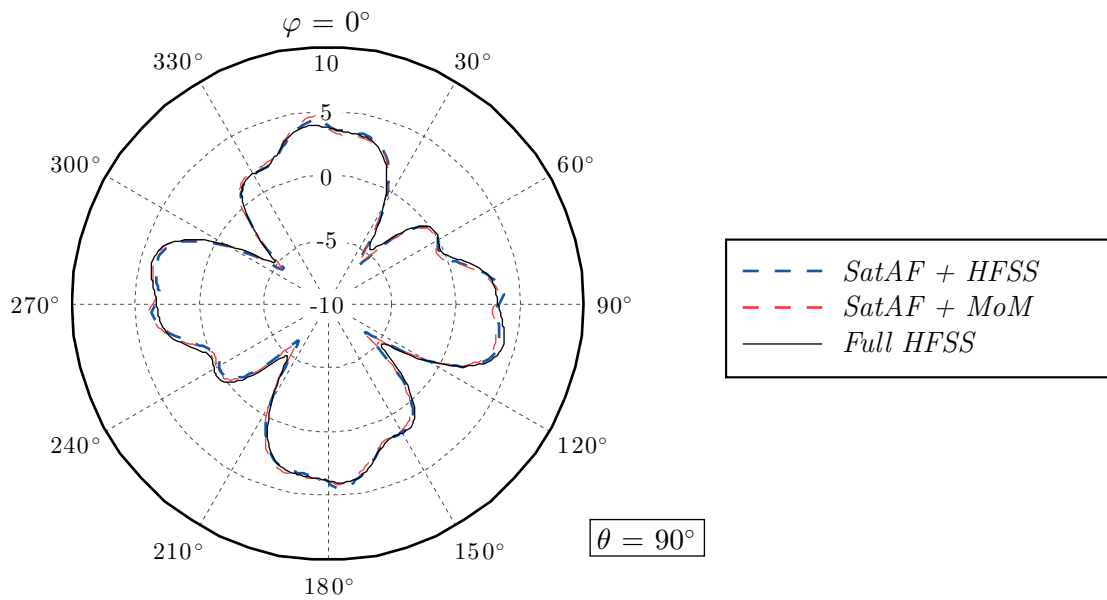


Figure 4.14.: Feed Scheme 2: radiation patterns on  $\varphi = 0$  deg cut.



**Figure 4.15.:** Feed Scheme 2: radiation patterns on  $\varphi = 90$  deg cut.



**Figure 4.16.:** Feed Scheme 2: radiation patterns on  $\theta = 90$  deg cut.

The agreement is very good for all the curves shown; this result is a logical consequence of the almost perfect agreement observed for the single slots in the previous section.

Also important is to evaluate the accuracy achieved with respect to the measurements of the POC satellite realized. As usual, the “basic element” which is in this case the customized slot, is solved with MoM and imported in SatAF, where first the face-element and then the complete array are built. The measurements available (Par. 2.4.5) are taken along the two cut-planes “R” (Fig. 4.17) and “RL” (Fig. 4.18), involving the four RHCP faces of the satellite the former, two R- and two L-HCP the latter: consequently, the quantities depicted are respectively the RHCP and “BestRL” (strongest of the two CP components).

The scope of this comparison is first to demonstrate the capability of the combination of SatAF and MoM to provide significant results when complex geometries and slot shapes are involved. In both cases the objective is well reached and even a substantial accuracy improvement is observed in the RL measurement.

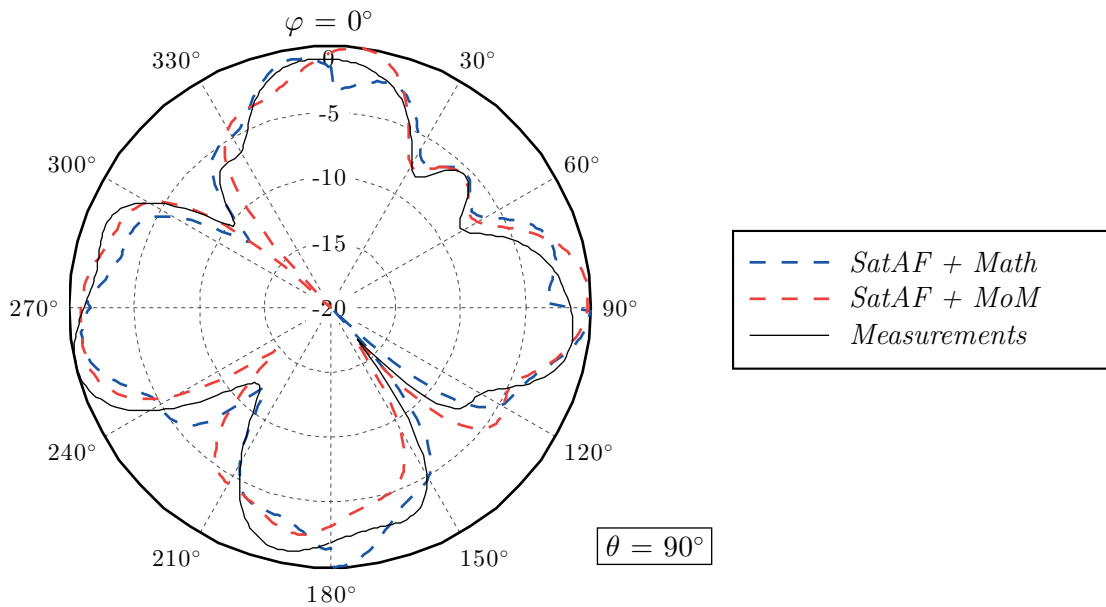


**Figure 4.17.:** Feed Scheme 2: radiation patterns on  $\theta = 90$  deg cut.

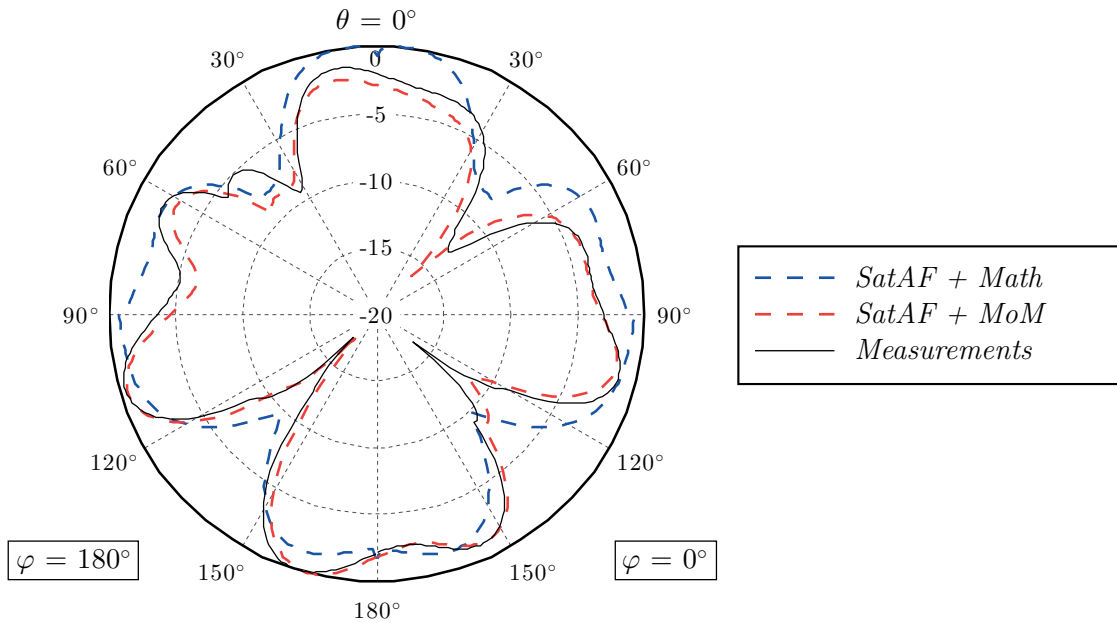


Figure 4.18.: Feed Scheme 2: radiation patterns on  $\theta = 90$  deg cut.

#### 4.4. Conclusions

In this chapter we investigated the possibility of combining the basic version of the in-house developed MATLAB software SatAF (implementing a particular formulation of 3D Array Theory for the solution of platform distributed antenna arrays) with the canonical implementation of the Mixed Potential Integral Equation, solved via Method of Moments (MPIE-MoM) in the Galerkin formulation.

The analysis of slot antennas, by themselves of paramount interest in the context of space application, was identified as one limitations of the original version of SatAF, because of the impossibility of modeling non-canonical aperture shapes and of the inaccurate predictions obtained.

Targeting in particular the analysis of slot antennas, we developed a novel, simplified excitation model, perfectly compatible with the MPIE-MoM framework, which allows the correct representation of the coupling mechanism (as it is typically performed via microstrip line or coaxial cable) with the advantage of not requiring the inclusion in the simulation model of any structure other than the very slot support (ground plane or metallic platform), for a significant reduction of the model complexity and computational effort.

The excitation model has been validated first with single slots of different shapes of

---

practical interest in antenna design (dog-bone or C-shaped slots). Secondly, the reliability of the combination SatAF-MoM in the analysis of complex antenna systems has been proved with the application of the method to the most significant test case proposed in Sec. 2.6 and, most important, to the actual architecture realized in the frame of the MAST project. In all the cases, the results have met the expectations.

In the following chapter, we perform a further advance in the reduction of the computational effort. The canonical Galerkin-MoM formulation will be replaced by a novel, simplified MoM formulation called the “Magic Distance Inspired” method. This method is easily implemented in MATLAB and can be therefore be directly integrated with the original SatAF version, for a stand-alone, compact and efficient software.



# 5. The Magic Distance Inspired method

## 5.1. Introduction

A very large class of useful antennas and electromagnetic scatterers can be reduced to open metallic surfaces (metallic sheets) embedded in layered or stratified media. When dealing with such geometries, the simplest integral equation that can be used for a full-wave treatment is the Electric Field Integral Equation (EFIE, Par. 3.2.2). The EFIE only involves tangential electric fields, which are always mathematically well-defined quantities, thanks to the obvious physical meaning. On the other hand, it is known that a hyper-singularity of  $1/r^3$  kind is present in all the formulations of  $\bar{\bar{\mathbf{G}}}_{\mathbf{E},\mathbf{J}}$  (3.41) [78, 79], from the closed-form analytical formulation valid for free-space to very involved expressions, like the combinations of Sommerfeld integrals and analytical series found in the treatment of planar, cylindrical and spherical layered dielectric media [61, 80–84]. Even though the space singularity problem can be avoided by solving the EFIE in the spectral domain [49], these approaches are inefficient for arbitrary or non-canonical geometries and a more successful strategy is to transform the EFIE into a Mixed Potential Integral Equation (MPIE, Par. 3.2.4), where the GFs  $\bar{\bar{\mathbf{G}}}_{\mathbf{A}}$  and  $G_V$  exhibit a much milder  $1/r$  singularity [85].

Potentials are however somewhat artificial quantities that can be defined in several ways and connected through different gauge equations (Coulomb, Lorentz...). The situation is even worse for the GF associated to these potentials. While in free space, a quite well defined approach is possible, relatively simple media like isotropic or stratified media already result in a scalar potential GF whose value can depend on the orientation of the original dipole source, a strange situation for a potential which is supposed to be created by a point charge. Moreover, potentials are badly defined (or even impossible to define) in complex media (anisotropic, gyromagnetic, chiral...) while, due to its physical meaning, the electric field cannot be affected by any mathematical indetermination.

The obvious conclusion of the above reasoning is that an ideal IE implementation should be based on fields rather than potentials, but avoiding the strong singularities associated to the fields.

According with the general IE-MoM developments recalled in Chap. 3, a Galerkin formulation using well behaving basis and test functions is required to compensate the strong singularity of the fields.

Then, the diagonal elements (or self-terms) in the MoM matrix, where the singularity problem

appears, are given by (3.92) with  $j = i$ :

$$z_{ii} = \int_{S_i} ds \int_{S_i} ds' \mathbf{t}_i(\mathbf{r}) \cdot \left[ \bar{\bar{\mathbf{G}}}(\mathbf{r}|\mathbf{r}') \cdot \mathbf{b}_i(\mathbf{r}') \right] \quad (5.1)$$

Here,  $\bar{\bar{\mathbf{G}}}$  is a generic GF, defined within a specific environment (homogeneous, stratified, complex media, a combination of the precedent, etc.) since the singularity problem is universal for all media. It is obvious that a four-fold integral should be able (at least in theory) to compensate the  $1/R^3$  field singularity [86, 87]. However, dealing with the singularity needs quite sophisticated procedures that aims either to the extraction [88–90] or the cancellation [91–95] of the strong singularity.

This makes the MoM implementation rather cumbersome and far away from the goals targeted in this thesis.

At the other extremity of the complexity scale, we should consider Nyström methods (introduced and discussed in Par. 3.3.2.5, which essentially consists in the application of a generic quadrature rule for the numerical approximation of an integral. With this approach a generic MoM element is simply given by:

$$z_{ij} = \sum_{m=1}^M \sum_{n=1}^N w_m w_n \bar{\bar{\mathbf{G}}}(\mathbf{r}_{i,m}|\mathbf{r}'_{j,n}) \quad (5.2)$$

As it was pointed out in Chap. 3, the Nyström family includes point-matching (Par. 3.3.2.2) which can be considered for all practical aspects as a Nyström method, where a quadrature of order  $M = 1$  (the Mean Theorem of Calculus) is applied to the test domain.

The original Nyström scheme was introduced [72] for the case  $M = N = 1$ , which implies point sources whose values are tested by point-matching. If the same point grid is used, the equation (5.2) would obviously lead to infinite values for the self-terms when filling the diagonal of the MoM matrix:

$$z_{ii} = S_i S_i \hat{\mathbf{t}}_i \cdot \bar{\bar{\mathbf{G}}}(\mathbf{r}_{i,m}|\mathbf{r}'_{i,n}) \cdot \hat{\mathbf{b}}_i \quad (5.3)$$

since  $\mathbf{r}_{i,m} \equiv \mathbf{r}'_{i,n}$ .

A possibility to avoid singular situations in the self-terms is to use different quadrature orders to perform the integrations in the basis and test functions. As it will be shown later in this chapter with the Gauss-Legendre quadrature, a direct approach can lead to erratic results.

Another bold idea is to stick to the most simple case  $M = N = 1$  but select different localisations for the point-wise basis and test functions. This is the concept of “**Magic Distance**”. When computing diagonal terms, the distance between the source and test points

$$R_{MD} = |\mathbf{r}_{i,m} - \mathbf{r}'_{i,n}| \quad (5.4)$$



is selected in such a way that it provides the exact value that could be obtained with a precise evaluation of the four fold Galerkin integral:

$$\begin{aligned}
 z_{ii} &= \int_{S_i} ds \int_{S_i} ds' \mathbf{t}_i(\mathbf{r}) \cdot \left[ \bar{\bar{\mathbf{G}}}(\mathbf{r}|\mathbf{r}') \cdot \mathbf{b}_i(\mathbf{r}') \right] \\
 &= S_i S_i \hat{\mathbf{t}}_i \cdot \bar{\bar{\mathbf{G}}}(\mathbf{r}_{i,m}|\mathbf{r}'_{i,n}) \cdot \hat{\mathbf{b}}_i \\
 &= S_i S_i \hat{\mathbf{t}}_i \cdot \bar{\bar{\mathbf{G}}}(R_{MD}) \cdot \hat{\mathbf{b}}_i
 \end{aligned} \tag{5.5}$$

Also, all our numerical experiments will be performed assuming a free space environment and therefore using free space Green's Functions. However, this choice does not limit in any sense the range of applicability of the method. In fact, the concept of magic distance depends essentially on the singularity of the involved GFs and this singularity remains the same with or without dielectrics.

The concept of "Magic Distance" is a very fruitful one, especially when combined with the strategies underlying the multi-point implementations of the Nyström method. Together, they provide novel MoM implementations which combine the simplicity of point-matching with the accuracy of Galerkin. We call them "**Magic Distance Inspired (MDI)**" methods and they are the subject of the present chapter.

## 5.2. On mesh and discretization

Two-dimensional metallic objects (metallic surfaces or sheets) are usually discretized using flat triangles [70] or quadrangles/trapezoids [96, 97]. Curvilinear cells-domains and the use of higher-order basis functions on them are obvious improvements in the path to further sophistication.

As stated in the first chapters, the keyword in this thesis is simplicity. Therefore, the Magic Distance concept will be introduced in the context of a rectangular mesh and most numerical tests will be performed on the simplest rectangle, the square. Cartesian orthogonal meshes are not only the ideal benchmark to test a proof-of-concept implementation: additionally, they have interest "per se" in many practical geometries, as those proposed by the European Space Agency in the frame of the project MAST.

The generalization of the concepts developed in this thesis to quadrangular (trapezoidal) or triangular meshes is quite straightforward by using homothetic and affine transformations that mimic the well known transformation used in numerical integration when any quadrangular shape (including the particular case of a triangle considered as a quadrangle with a zero-length side) is reduced to a canonical unit square, where quadrature rules are easily applied. For instance, the concept of Magic Distance on a square cell can be easily transposed to N-sided polygons by generalizing the definition of the configuration in terms of apothem and radius (Fig. 5.1) or, alternatively, by using homothetic changes of variables, exactly as done when

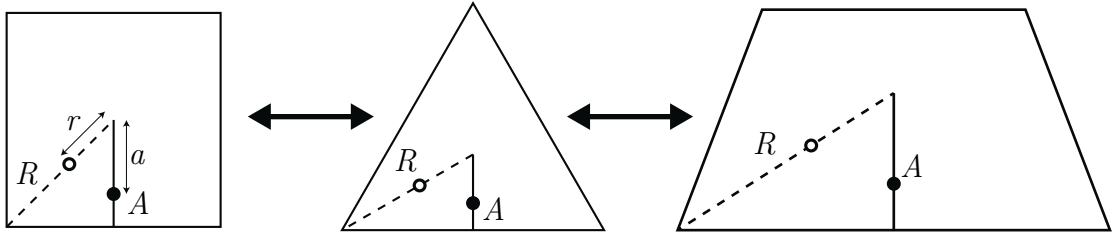


**Figure 5.1.:** Example of transposition of the Magic Distance from rectangular to triangular mesh. The vales of the normalized Magic Distance  $a/A$ ,  $r/R$  can be related in the three figures by simple geometrical considerations.

defining two-dimensional quadrature over non-canonical surfaces.

### 5.3. General formulation

The characteristic parameters which identify an implementation of the Nyström Method are the sampling points and the weights. The objective of this work is to define two different point grids and sets of weights (for the inner and outer integrals) which allow the most accurate approximation of the MoM matrix in the EFIE formulation. The point grids and therefore the formulation of the method shall be universal, in the sense that once the point grid is fixed, it must allow the computation of *all* the terms of the matrix, including and especially the self-term, which is the dominant element in the matrix. Key feature of the method shall be an improved simplicity and computational speed with respect to the classic implementation of MoM combined with typical integration rules.

In fact, when using quadrature rules like Gauss-Legendre (GL) [98], the computation of the self term  $z_{ii}$  involving a singularity of any type  $1/r^n$  cannot be performed using the same number of points  $M = N$  for the inner and outer integrals, as they produce identical grids and therefore  $z_{ii} \rightarrow \infty$ . Even using different number of points, the result is only fairly accurate and only if a high number of points is used, making extremely cumbersome the definition of a universal interaction grid to be used for all the elements (diagonal and off-diagonal) of the MoM matrix.

Tab. 5.1 shows an example of the number of significant digits obtained when solving the vector potential self-term integral (3.97) derived in Par. 3.3.3:

$$I = \int_S ds \Delta_{\mathbf{R}}(\mathbf{r}) \int_S ds' \Delta_{\mathbf{R}}(\mathbf{r}') \frac{1}{|\mathbf{r} - \mathbf{r}'|} \quad (5.6)$$

where the kernel is the first-order Taylor approximation of the Green's Function  $G$  (for which an analytical solution is available, see Par. 5.3.1) and the integration domain is the unitary surface  $S = 1 \times 1$  m.

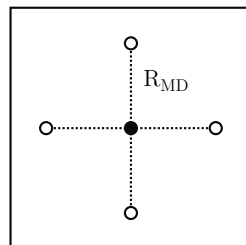
The general structure of the Magic Distance algorithm starts with the choice of two particular

**Table 5.1.:** Significant digits obtained using the GL algorithm for the self-term (5.6).

Number of points		Method (*)	Operations	Result	Significant digits
$M$	$N$		$4\times$		
20	21	Dir	176,400	7.02417...	2
30	31	Dir	864,900	7.02813...	2
40	41	Dir	2,689,600	7.02984...	2
5	6	SE	900	7.03486...	3
10	11	SE	12,100	7.03427...	3
20	21	SE	176,400	7.03397...	4
40	41	SE	2,689,600	7.03388...	5
Analytical				7.03384...	-

(\*) Dir = Direct evaluation, SE = Singularity Extraction (Par. 5.3.1)

point-schemes, one for the inner/source integral and one for the outer/observation one. The different point-schemes are identified by two aspects: the number of points, which directly determines the numerical complexity and influences the accuracy of the method, and the distribution of the points on the cell. In order to preserve the symmetrical properties of the problem, the point arrangements have to maintain a geometrical regularity; this suggest to ideally collect the points into symmetrical sub-sets associated with one or more parameters, typically the distance from the center, which locate the position of all the points of the sub-set. An example of sub-set is the Cross (+) shown in Fig. 5.2, which involves 4 points where the only parameter is the distance from the center. Point-schemes are therefore reduced to small numbers of collections of points and are uniquely identified by the parameters associated to these collections. The choice of the configuration is then completed with the definition of the weights  $w_m$  and  $w_n$  associated to the points or, more specifically, to collections of points (it is logical that in sub-grids like the cross, all the points must be associated with the same weight).

**Figure 5.2.:** The Cross point-scheme.

The 4D MoM integral is therefore replaced by:

$$\begin{aligned} z_{ij} &= \int_{S_i} ds \int_{S_j} ds' \mathbf{t}_i(\mathbf{r}) \cdot \left[ \bar{\bar{\mathbf{G}}}_{\mathbf{E},\mathbf{J}}(\mathbf{r}|\mathbf{r}') \cdot \mathbf{b}_j(\mathbf{r}') \right] \\ &\approx \sum_{m=1}^M \sum_{n=1}^N w_m w_n \hat{\mathbf{t}}_i \cdot \left[ \bar{\bar{\mathbf{G}}}_{\mathbf{E},\mathbf{J}}(\mathbf{r}_{i,m}|\mathbf{r}_{j,n}) \cdot \hat{\mathbf{b}}_j \right] \end{aligned} \quad (5.7)$$

Remark that with this particular choice, the basis/test function appear explicitly only as unit vectors, while their magnitude contribution is included in the weights.

The core of the method is the accurate approximation of the most influential terms in the MoM matrix. In view of this, the parameters defining a point scheme and its weights become the degrees of freedom which are used to match first the matrix self-term ( $z_{ST}$ ) and secondly, for improved accuracy, the other terms of the matrix:

- The near terms  $z_{NT}$ , which indicate cell pairs sharing a portion of their domain.
- The adjacent terms  $z_{AT}$ , which indicate cell pairs only sharing an edge.

$$\sum_{m=1}^M \sum_{n=1}^N w_m w_n \hat{\mathbf{t}}_i \cdot \left[ \bar{\bar{\mathbf{G}}}_{\mathbf{E},\mathbf{J}}(\mathbf{r}_{i,m}|\mathbf{r}_{j,n}) \cdot \hat{\mathbf{b}}_j \right] = \begin{cases} z_{ST} \\ z_{NT} \\ \dots \\ z_{AT} \\ \dots \end{cases} \quad (5.8)$$

The point scheme which better fits the desired conditions can be obtained, except for a few trivial cases, using an optimization algorithm. The cost function is built using weights to prioritize the matching of the elements which influence the MoM matrix most. As a remark, an attempt of directly optimizing a point grid to match the MoM matrix (or even its inverse) with the smallest error does not succeed, probably due to the low correlation between the optimization variables and the cost function, which makes a gradient-based algorithm fail in finding the right direction to generate the forthcoming point.

It is important to highlight at this point the most relevant differences between the MDI method and a generic quadrature rule. In fact, the definition of sample points and weights in the MDI algorithm is performed with the specific intent of matching the self-term (and eventually the near- or adjacent terms) using a *reduced* number of points, in the limit a single source scheme; with such a coarse sampling the GL algorithm would be rather inaccurate or even unable to perform the integration. On the other hand, no control is granted on those terms of the MoM matrix where no condition (5.8) is imposed and which are anyway assumed to have a minor influence on the solution of the system. In order to ensure the physical meaningfulness of the method, special attention is paid to far-field terms, whose

correct evaluation is not granted per-se as with GL, as discussed in Par. 5.3.3.

A second remark concerns reciprocity. The Lorentz Reciprocity Theorem [56] states that in a linear and isotropic (not necessarily homogeneous) medium, source and observation points can be interchanged when calculating the electric (or magnetic) field. While most implementations of MoM satisfy reciprocity and show a symmetric matrix, this is not necessarily valid for the MDI method, due to the limited number of points used for replacing the 4D integrals. A significative example is the case of two cells arranged as an "L", as shown in Fig. 5.3: when computing the interaction with MoM, the value is identical regardless which cell is the source or the observer; this is not the case with MDI method, as the relative position of observation points (empty circles in Fig. 5.3) with respect to sources (full circles) is clearly different depending which cell is the source and which is the observer.

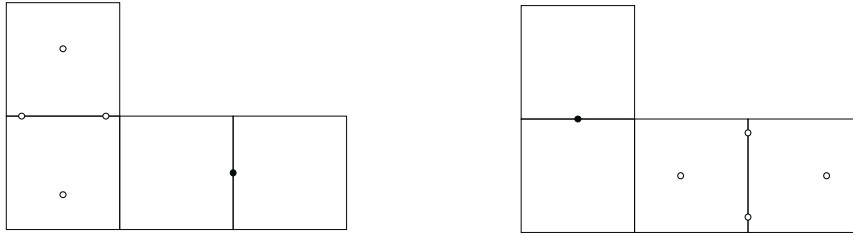


**Figure 5.3.:** Source and observation roles are not interchangeable in the Magic Distance method.

Before entering in the details of the application of the method to particular problems, it is worth to delve into the treatment of the self term, the definition of the weights and to introduce the concept of asymptotic convergence.

### 5.3.1. The self term

The MDI method is based on the most accurate approximation of the self-term of the MoM matrix  $z_{ii}$  and the precision this value is computed with is crucial for a correct result. Since our problem allows the definition of potentials, it is preferable to compute the self-term in the MPIE formulation, where the kernels of the vector (A) and scalar (V) potential integrals are the Green's Functions:

$$\begin{aligned} \bar{\bar{\mathbf{G}}}_A &= \bar{\bar{\mathbf{I}}} G & G_V &= G \\ G &= \frac{\exp(-jkr)}{4\pi r} \end{aligned} \quad (5.9)$$

The electrostatic problem (Electric Potential IE, EPIE) allows a closed form solution; the calculation of the EFIE integral can be reduced to the static part using different strategies:

- **Taylor expansion:** the exponential term in the GF is linearized assuming a small distance source-observer:

$$\exp(-jkr) = 1 - jkr - \frac{1}{2}k^2r^2 + j\frac{1}{6}k^3r^3 + \frac{1}{24}k^4r^4 + \dots \quad (5.10)$$

This choice is valid when the electric size of the cell is significantly small. Closed form solution is possible for each term of the series; in particular, when the expansion is limited to the zero-order, the EFIE GF reduces to the EPIE one.

- **Singularity Extraction (SE):** the exponential function is re-written as:

$$\frac{\exp(-jkr)}{r} = \frac{\exp(-jkr) - 1}{r} + \frac{1}{r} = G_{EXT}(r) + G_0(r) \quad (5.11)$$

Note that the term  $4\pi$  do *not* appear in the denominator.

This formulation is general applies to any type of source/observer cell.

With SE, the self term is decomposed into a non-singular part which is evaluated numerically, while the remaining expression is identical to the EPIE and can be solved analytically. Recalling the expressions of the MoM matrix terms (3.97), we introduce for consistency the following symbolism:

$$a_{i,i} = \frac{j\omega\mu}{4\pi} I_A^{ST} = \frac{j\omega\mu}{4\pi} (I_{A,EXT}^{ST} + I_{A,0}^{ST}) \quad (5.12a)$$

$$v_{i,i} = \frac{(j\omega\varepsilon)^{-1}}{4\pi} I_V^{ST} = \frac{(j\omega\varepsilon)^{-1}}{4\pi} (I_{V,EXT}^{ST} + I_{V,0}^{ST}) \quad (5.12b)$$

$$z_{i,i} = I_{EXT}^{ST} + I_0^{ST} = \frac{j\omega\mu}{4\pi} I_{A,EXT}^{ST} + \frac{(j\omega\varepsilon)^{-1}}{4\pi} I_{V,EXT}^{ST} + \frac{j\omega\mu}{4\pi} I_{A,0}^{ST} + \frac{(j\omega\varepsilon)^{-1}}{4\pi} I_{V,0}^{ST} \quad (5.12c)$$

and the same association is made for the near terms and it is indicated by  $\square^{NT}$ . The static parts of the A and V integrals differ in the form of the basis/test function, which remains a rooftop for A and becomes a pulse in V (due to the derivations). The analytical treatment can be further simplified by approximating the rooftop in the vector potential integral with a pulse function, allowing the solution of the A integral using the result of the V integral.

In this work, we provide the closed form expression of the integrals of type:

$$I_0^{ST} = \int_{S_i} ds t_i \int_{S_i} ds' b_i \frac{1}{|\mathbf{r} - \mathbf{r}'|} \quad (5.13a)$$

$$I_0^{NT} = \int_{S_i} ds t_i \int_{S_j} ds' b_j \frac{1}{|\mathbf{r} - \mathbf{r}'|} \quad (5.13b)$$

when the basis/test functions are pulses (3.65),  $S_i, S_j$  are overlapping (self term) or adjacent cells; when the basis/test functions are rooftops (3.67)  $S_i, S_j$  are completely overlapping cell pairs (self term) or cell pairs sharing one cell.

Cells are supposed rectangular (single cell for pulse BF, a couple for RWG) with sides  $D_x, D_y$ ; we also define the dimension  $D_t = 2D_x$  and the diagonals  $D_\rho = \sqrt{D_x^2 + D_y^2}$  and  $D_{\rho t} = \sqrt{(2D_x)^2 + D_y^2}$  as depicted in (Fig. 5.4).

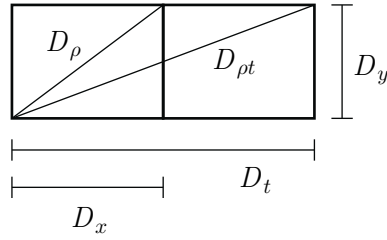


Figure 5.4.: Cell pair: quantities used for the computation of the self-term.

### 5.3.1.1. Pulse functions

The analytical solution of (5.13) with pulse basis and test function is the exact value of the self/near terms of the electrostatic MoM matrix; moreover, it is necessary for the computation of the MPIE self term (the scalar potential part  $I_{V,0}$ , or even for the vector potential part when the rooftop is approximated with a pulse). The near term is not singular, yet its closed form solution combined with the same techniques used for the self term is convenient for an improved accuracy.

$$I_0^{ST} = 2D_x D_y \left[ D_x \ln \frac{D_\rho + D_y}{D_x} + D_y \ln \frac{D_\rho + D_x}{D_y} \right] - \frac{2}{3} (D_\rho^3 - D_x^3 - D_y^3) \quad (5.14a)$$

$$I_0^{NT} = D_t D_y \left[ D_t \log \left( \frac{1}{2} \frac{D_{\rho t} + D_y}{D_\rho + D_y} \right) + D_x \log \left( \frac{D_\rho + D_y}{D_x} \right) + D_y \log \left( \frac{D_{\rho t} + D_t}{D_\rho + D_x} \right) \right] - \frac{1}{3} D_{\rho t}^3 + \frac{2}{3} D_\rho^3 + 2D_x^3 - \frac{1}{3} D_y^3 \quad (5.14b)$$

### 5.3.1.2. Rooftop functions

The analytical solution of (5.13a) when basis / test functions are rooftops is required for the vector potential component  $I_{A,0}$  of the MPIE MoM matrix self term; also, the solution of (5.13b) can be useful for improved accuracy in the computation of the near terms:

$$I_0^{ST} = D_x^2 D_y \left[ \frac{1}{2} D_x \ln \left( \frac{D_\rho + D_y}{D_x} \right) + \frac{2}{3} D_y \ln \left( \frac{D_\rho + D_x}{D_y} \right) \right] - \frac{2}{15} D_x^2 (D_\rho - D_x) + \\ - \frac{1}{3} \left( D_y^2 + \frac{1}{15} \frac{D_y^4}{D_x^2} \right) (D_\rho - D_y) + \frac{1}{90} D_\rho D_y^2 \quad (5.15a)$$

$$I_0^{NT} = \frac{1}{6} D_x^2 D_y \left[ 8 \ln \left( \frac{D_{\rho t} + D_y}{D_x} \right) + 5 \ln \left( \frac{D_\rho - D_y}{D_x} \right) \right] + \frac{4}{3} D_x D_y^2 \ln \left( \frac{D_{\rho t} + D_t}{D_\rho + D_x} \right) + \\ - \frac{1}{12} \frac{D_y^4}{D_x} \left[ \ln \left( \frac{D_{\rho t} + D_t}{D_y} \right) + 2 \ln \left( \frac{D_\rho - D_x}{D_y} \right) \right] + \\ \left[ \frac{D_x^3 - D_y^3}{3} + \frac{D_x^2 + 4D_y^2}{5} D_\rho - \frac{4}{15} (D_x^2 + 2D_y^2) D_{\rho t} \right] + \\ + \frac{1}{90} \frac{D_y^2}{D_x^2} [D_{\rho t} D_\rho (D_{\rho t} + D_\rho) - 3D_\rho D_y^2 + D_y^3] \quad (5.15b)$$

Numerical tests show that the most accurate result is provided by extracting the singularity, computing numerically the non-singular integral  $I_{A/V,EXT}^{ST}$  and using the exact formula for the static part  $I_{A/V,0}^{ST}$ . Significant degradation is instead introduced by any other approximation, including the reduction of the rooftop to a pulse function for the vector potential integral. The computational cost of the numerical integration is anyway affordable, since the calculation of the self term is a preliminary step of the MDI algorithm to be executed once and does not occur in the iterative part where the matrix is filled.

It is interesting to highlight some properties of the solution of the static part integral  $I_0^{ST}$ , which will be addressed in the next sections. Once the exponential term is removed, the integrands of  $I_{A,0}$  and  $I_{V,0}$  are pure real functions and so are their solutions. The total integral  $I_0$  is instead a pure imaginary number (see (3.15)) whose sign depends on the values of the A,V components which are opposite sign and differently weighted.

It turns out that for the self term the integral  $I_0$  is always purely imaginary and positive; moreover, the same applies to the complete integral  $I^{ST}$ .

In fact, if the static part is associated to the first term of the Taylor expansion of the exponential, one recognizes that since the higher order terms are alternated in sign and decreasing in magnitude, the total sign is determined by the zero-order term.



### 5.3.2. The weights

The Nyström method envisages the use of weights associated to the sampling points. These weights can either be fixed, or left as a degree of freedom in the optimization process. If weights are fixed, a possibility is dividing the cell into sectors  $\sigma_m, \sigma_n$  associated to each observation / source point respectively and integrating the TF/BF on that sector:

$$\begin{aligned} w_m &= \int_{\sigma_m} ds t(\mathbf{r}) \\ w_n &= \int_{\sigma_n} ds b(\mathbf{r}) \end{aligned} \quad (5.16)$$

The choice of the sector rule, or any fixed values for the weights, proves to be meaningful for the computation of the self term. When more matching conditions are requested, the method actually deviates from the association with a quadrature rule and follows different laws better intercepted through optimization.

### 5.3.3. Asymptotic condition

The weights used with any generic quadrature rule are subject to a condition which is necessary to ensure the correct evaluation of the integral in a trivial case. Typical example is the 1D quadrature rule used to approximate the integral:

$$\int_a^b f(x) dx \approx \sum_{n=1}^N w_n f(x_n) \quad (5.17)$$

The quadrature rule must apply to any function and in particular to the simplest one  $f(x) = 1$ , for which the quadrature rule becomes an exact approximation. Applying (5.17) we obtain that, according to the constraint, the weights must be subject to:

$$\left. \begin{aligned} \int_a^b 1 dx &= (b - a) \\ \sum_{n=1}^N w_n f(x_n) &= \sum_{n=1}^N w_n \end{aligned} \right\} \Rightarrow \sum_{n=1}^N w_n = (b - a) \quad (5.18)$$

Since in the formulation of MDI the terms not included in the optimization are not controlled, it is important to enforce a constraint on the weights when analyzing the interaction between two cells in the far field.

We consider the interaction between two generic rectangular cells  $S_i, S_j \in S$  of dimension  $a_i \times b_i, a_j \times b_j$  and whose centers are  $\mathbf{r}_{i0}$  and  $\mathbf{r}_{j0}$ . When  $|\mathbf{r}_i - \mathbf{r}_j| \gg \max\{a_i, b_i, a_j, b_j\}$ , the observation point  $\mathbf{r}_i$  is far from the source point  $\mathbf{r}_j$  and the corresponding entry in the MoM

matrix  $z_{i,j}$  can be approximated as:

$$z_{i,j}^{MoM} \approx \frac{S_i}{2} \frac{S_j}{2} \hat{\mathbf{t}}_i \cdot \left[ \bar{\bar{\mathbf{G}}}_{\mathbf{E},\mathbf{J}}(\mathbf{r}_{i0}|\mathbf{r}_{j0}) \cdot \hat{\mathbf{b}}_j \right] \quad (5.19)$$

Following the same reasoning, the same term  $C_{i,j}$  computed using the Nyström Method is approximated as:

$$z_{i,j}^{MDI} \approx \hat{\mathbf{t}}_i(\mathbf{r}_{i0}) \cdot \left[ \bar{\bar{\mathbf{G}}}_{\mathbf{E},\mathbf{J}}(\mathbf{r}_{i0}|\mathbf{r}_{j0}) \cdot \hat{\mathbf{b}}_j(\mathbf{r}_{j0}) \right] \sum_{m=1}^M \sum_{n=1}^N w_m w_n \quad (5.20)$$

By comparing (5.19) and (5.20), it follows immediately the condition the weights must satisfy:

$$\sum_{m=1}^M \sum_{n=1}^N w_m w_n = \frac{S_i}{2} \frac{S_j}{2} \quad (5.21)$$

### 5.3.4. Phase Correction

The Asymptotic Condition is used to ensure that the particular choice of points and weights produces a physically meaningful result when the cells are widely spaced and the condition is obtained through (5.19); anyway, when structures electrically large are analyzed, it is worth to introduce a more accurate far-field approximation and thus an improved Asymptotic Condition.

In order to verify first the validity of (5.19), we investigate the degree of accuracy obtained when the 4D integral with kernel  $\bar{\bar{\mathbf{G}}}_{\mathbf{E},\mathbf{J}}$ , computed using the Gauss-Legendre method with  $(M \times M) \times (N \times N)$  points, is replaced first by a 2D integral, associated to  $N = 1$  source points (or equivalently  $M = 1$  observation points) and secondly with the  $M = N = 1$  point-to-point (P2P) calculation of  $\bar{\bar{\mathbf{G}}}_{\mathbf{E},\mathbf{J}}$ , which is actually representing the Asymptotic Condition as it is formulated in (5.19). Since the integrand is only dependent on the distance, we expect that collapsing the cell into its center introduces an error on the two approximations which is asymptotically decreasing with the distance between the cells.

As test case we consider two cells constituted by pairs of squares of size  $\lambda/10$ , located at increasing distances (Fig. 5.5). Even when the spacing between the cells becomes very large, in the order of the dozen of wavelengths, the error does not decrease below the threshold of 3% (2D) and 7% (P2P). The error reduces when cells are smaller, but still tends to a limit value greater than zero.

We identified the reason for this behaviour in the effect of the phase delay associated to the exponential  $\exp(-jkr)$ : similarly to Array Theory, where the path difference must be accounted for, in this case the distance between the points into the cells can be averaged by the distance between the centers everywhere in  $\bar{\bar{\mathbf{G}}}_{\mathbf{E},\mathbf{J}}$  with the exception of  $\exp(-jkr)$ . If

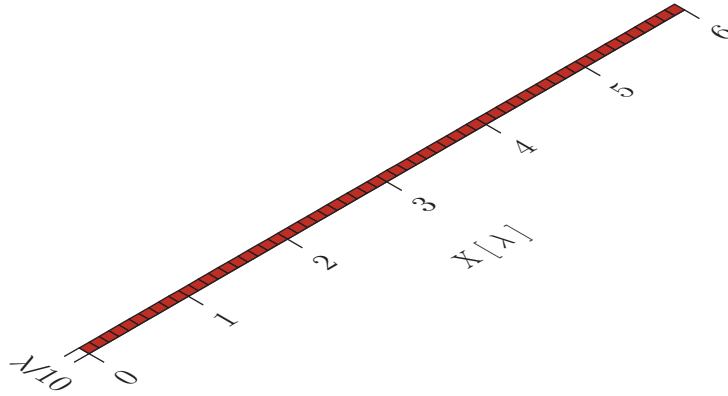


Figure 5.5.: The test case used for the Phase Correction.

$\bar{\bar{\mathbf{G}}}_{\mathbf{E},\mathbf{J}} = \bar{\bar{\mathbf{G}}}_{\mathbf{E},\mathbf{J}}^0 \exp(-jkR)$ , it is:

$$\begin{aligned} & \int_{S_o} ds \int_{S_s} ds' \mathbf{t}(\mathbf{r}) \cdot \left[ \bar{\bar{\mathbf{G}}}_{\mathbf{E},\mathbf{J}}(\mathbf{r} | \mathbf{r}') \cdot \mathbf{b}(\mathbf{r}') \right] \\ &= \int_{S_o} ds \int_{S_s} ds' \mathbf{t}(\mathbf{r}) \cdot \left[ \bar{\bar{\mathbf{G}}}_{\mathbf{E},\mathbf{J}}^0(\mathbf{r} | \mathbf{r}') \cdot \mathbf{b}(\mathbf{r}') \right] \exp(-jk|\mathbf{r} - \mathbf{r}'|) \\ &\approx \int_{S_o} ds \mathbf{t}(\mathbf{r}) \cdot \left[ \bar{\bar{\mathbf{G}}}_{\mathbf{E},\mathbf{J}}^0(\mathbf{r}, \mathbf{r}'_s) \cdot \hat{\mathbf{b}} \right] \int_{S_s} ds' b(\mathbf{r}') \exp(-jkR) \quad (2D) \quad (5.22) \end{aligned}$$

$$\approx \hat{\mathbf{t}} \cdot \left[ \bar{\bar{\mathbf{G}}}_{\mathbf{E},\mathbf{J}}^0(\mathbf{r}_o, \mathbf{r}'_s) \cdot \hat{\mathbf{b}} \right] \int_{S_o} ds \int_{S_s} ds' t(\mathbf{r}) b(\mathbf{r}') \exp(-jkR) \quad (\text{P2P}) \quad (5.23)$$

with  $R$  representing the projection of the vector  $(\mathbf{r} - \mathbf{r}')$  on the unit vector  $\hat{\mathbf{r}}_{os}$  which links the center of the source and observation cells. The 2D and P2P approximations can be improved by evaluating the terms:

$$I_{2D}(\mathbf{r}) = \int_{S_o} ds b(\mathbf{r}') \exp(-jkR) \quad (5.24)$$

$$I_{P2P} = \int_{S_o} ds \int_{S_s} ds' t(\mathbf{r}) b(\mathbf{r}') \exp(-jkR) \quad (5.25)$$

The integrals can be solved analytically. With reference to Fig. 5.6, we define the unit vector  $\hat{\mathbf{r}}_{os}$  as:

$$\hat{\mathbf{r}}_{os} = \frac{(x_o - x_s) \hat{\mathbf{x}} + (y_o - y_s) \hat{\mathbf{y}}}{\sqrt{(x_o - x_s)^2 + (y_o - y_s)^2}} = \cos \phi \hat{\mathbf{x}} + \sin \phi \hat{\mathbf{y}} = \alpha \hat{\mathbf{x}} + \beta \hat{\mathbf{y}} \quad (5.26)$$

and the distance between the centers of the cells:

$$R_{os} = \alpha(x_o - x_s) + \beta(y_o - y_s) \quad (5.27)$$

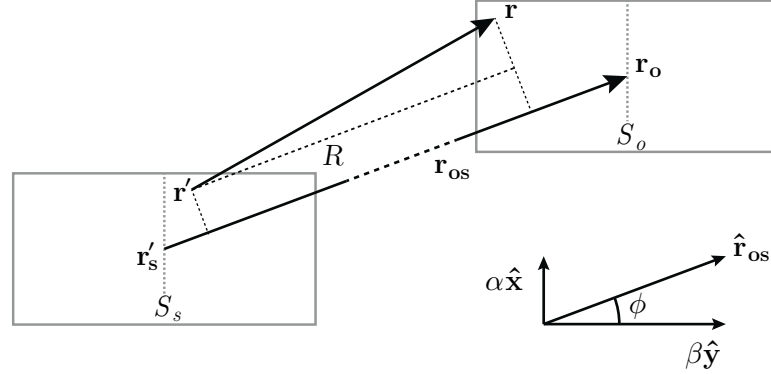


**Figure 5.6.:** Formalism used for the derivation of the Phase Correction.

The solutions of the two integrals are in the form:

$$\Psi_{2D}(\mathbf{r}) = \Psi_{2D}^0 \exp[-jk(\alpha x + \beta y)] \exp(-jkR_{os}) \quad (5.28)$$

$$\Psi_{P2P} = \Psi_{P2P}^0 \exp(-jkR_{os}) \quad (5.29)$$

and the terms  $\Psi_{2D}^0$ , and  $\Psi_{P2P}^0$  in the two cases valid when the segments associated with the cell pairs are parallel ( $\parallel$ ) or orthogonal ( $\perp$ ):

$$\Psi_{2D}^0 = D_x D_y \frac{1 - \cos(\alpha k D_x)}{\alpha^2 k^2 D_x^2 / 2} \frac{\sin(\beta k D_y / 2)}{\beta k D_y / 2} \quad (5.30)$$

$$\Psi_{P2P}^0 = \begin{cases} (D_x D_y)^2 \frac{[1 - \cos(\alpha k D_x)]^2}{\alpha^4 k^4 D_x^4 / 4} \frac{1 - \cos(\beta k D_y)}{\beta^2 k^2 D_y^2 / 2} & (\parallel) \\ (D_x D_y)^2 \frac{\sin^3(\alpha k D_x / 2)}{\alpha^3 k^3 D_x^3 / 8} \frac{\sin^3(\beta k D_y / 2)}{\beta^3 k^3 D_y^3 / 8} & (\perp) \end{cases} \quad (5.31)$$

Note the dependency of  $\Psi_{2D}$  on  $\mathbf{r}$ .

The benefit of the introduction of the Phase Correction is demonstrated by the curves in Figs. 5.7 and 5.8 showing the relative error for increasing distances between the cells at different values of  $\phi$  (as defined in Fig. 5.6). All the cases highlight that without Phase Correction the error on the integrals tends to a limit value in the order of a few percents, around twice as much in  $I_{P2P}$  than in  $I_{2D}$ , whereas with the introduction of the corrective terms (5.28) it approaches zero within a few wavelengths.

Therefore, this original treatment of Phase Correction is a simple but essential operation to be implemented in all our operations.

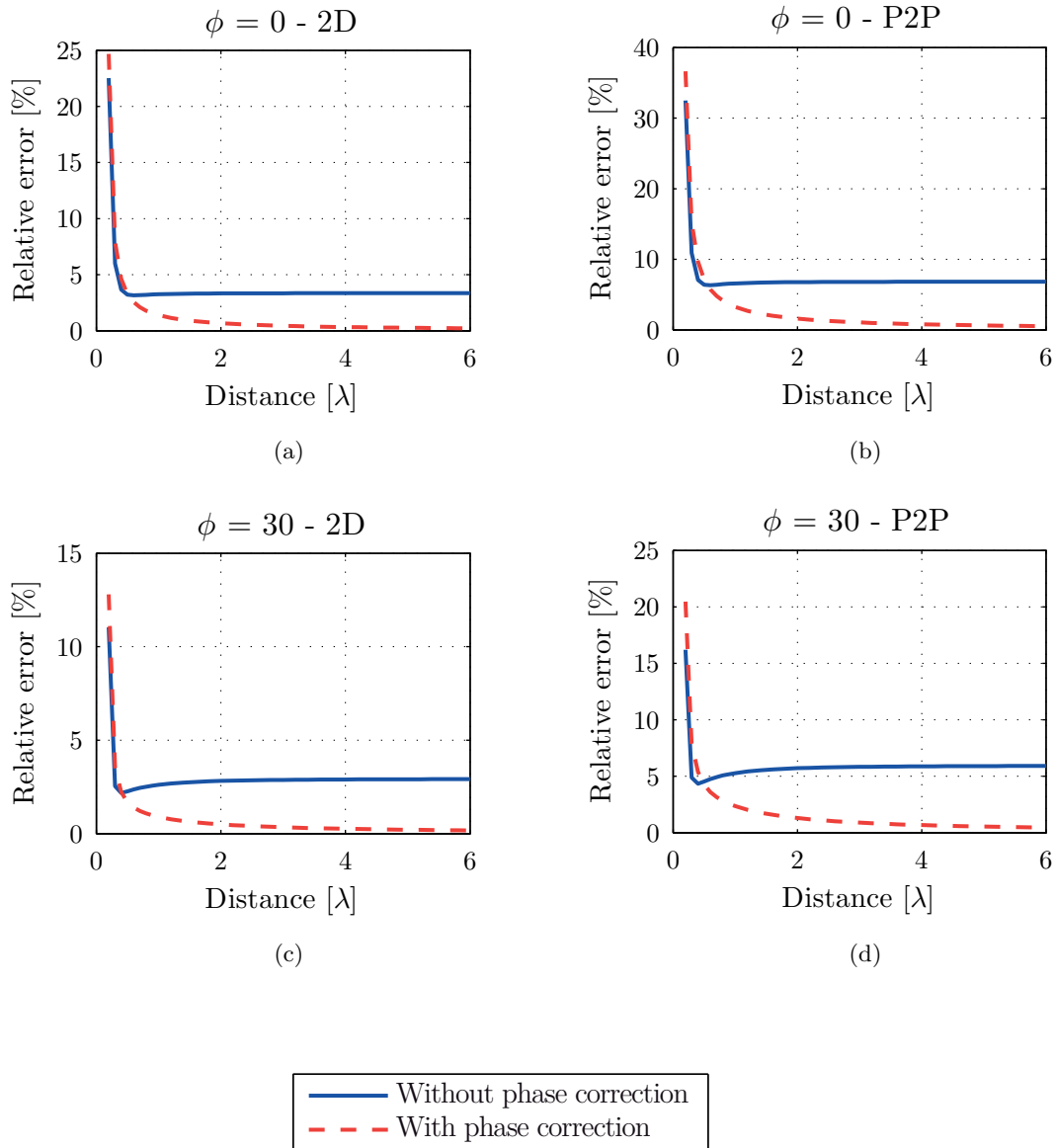


**Figure 5.7.:** Improvement in the computation of far-field terms given by the introduction of the Phase Correction:  $\phi = 0, 30$  cases.

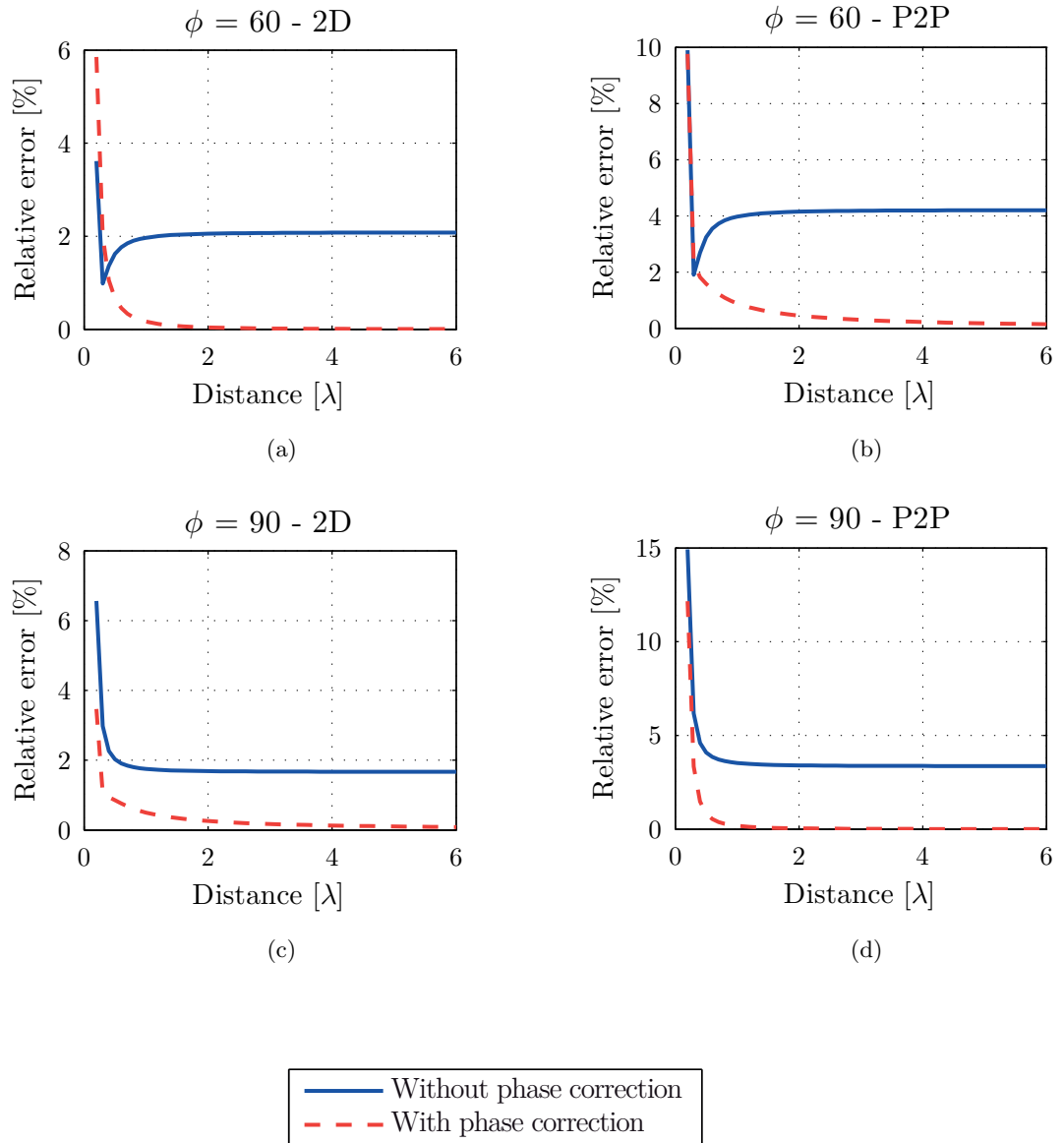


**Figure 5.8.:** Improvement in the computation of far-field terms given by the introduction of the Phase Correction:  $\phi = 60, 90$  cases.

## 5.4. The electrostatic case: the EPIE

The primary objective of the MDI method is the analysis of full-wave problems; yet, for the sake of clarity in the illustration of the method we prefer to discuss first the details of the algorithm when this is applied to an electrostatic problem.

In electrostatics, the sources used in the MDI method are infinitesimal charges  $\rho_s$  which produce in the observation points the potential  $V$ , which is a scalar quantity. When rectangular domain pulses are used as basis/test functions (Par. 3.2.5), the expression of the generic entry of the MoM matrix is:

$$z_{ij} = \frac{1}{\varepsilon_0} \int_{S_i} ds \int_{S_j} ds' G^{ES}(\mathbf{r} | \mathbf{r}') \quad (5.32)$$

with  $G^{ES}$  being the Green's Function:

$$G^{ES}(\mathbf{r} | \mathbf{r}') = \frac{1}{4\pi |\mathbf{r} - \mathbf{r}'|} \quad (5.33)$$

The first step of the method consists in the most accurate computation of the self-, near- and adjacent terms (and any other term one desires to include in the optimization). The integral (5.32) can be solved analytically and the closed-form expression for the self term and the near term were given in (5.14).

Secondly, the expressions of the same terms are formulated in the shape of MDI entries (5.8), leaving the position of the points and eventually the weights dependent on the set of variables  $\nu$  used for the optimization:  $\nu_{wo}$  and  $\nu_{ws}$  for the observer / source weights and  $\nu_{po}$  and  $\nu_{ps}$  for the position of the observer / source points:

$$z^{MDI}(\nu) = \frac{1}{\varepsilon_0} \sum_{m=1}^M \sum_{n=1}^N w_m(\nu_{wo}) w_n(\nu_{ws}) G^{ES}[\mathbf{r}_{i,m}(\nu_{po}) | \mathbf{r}_{j,n}(\nu_{ps})] \quad (5.34)$$

By taking the appropriate i,j cells we obtain the terms  $z_{ST}^{MDI}$ ,  $z_{NT}^{MDI}$ ,  $z_{AT}^{MDI}$  ..., respectively the self-, near- and adjacent terms. By equating these terms to the analytical solutions (5.14) we generate the linear system:

$$\begin{cases} z_{ST}^{MDI}(\nu) = \frac{1}{\varepsilon_0} I_0^{ST} \\ z_{NT}^{MDI}(\nu) = \frac{1}{\varepsilon_0} I_0^{NT} \\ z_{AT}^{MDI}(\nu) = \frac{1}{\varepsilon_0} I_0^{AT} \\ \dots \end{cases} \quad (5.35)$$

The linear system is then solved using classical optimization algorithms whose cost function  $C(\nu)$  is derived from the linear system and can include weight  $\Omega$  to prioritize the matching

condition on specific terms:

$$C(\nu) = \sqrt{\frac{\Omega_{ST} (z_{ST}^{MDI}(\nu) - I_0^{ST}/\varepsilon_0)^2 + \Omega_{NT} (z_{NT}^{MDI}(\nu) - I_0^{NT}/\varepsilon_0)^2 + \dots}{\Omega_{ST} + \Omega_{NT} + \dots}} \quad (5.36)$$

Care should be taken in constraining the variables  $\nu$  within the cell domain; in fact, this is not necessarily a strict requirement but preserves the consistency of a physical insight.

The discussion proceeds in the following section with the study of the most basic configurations and their application to a real electrostatic problem. A preliminary evaluation of the performance of the method is then assessed on the basis of the obtained results.

#### 5.4.1. Configurations for the electrostatic problem

In this section, we illustrate the logical reasoning which leads to the identification of the simplest and most accurate point schemes for a typical electrostatic problem. We begin the discussion by focusing on the self term in an abstract environment, with the only assumption of a regular mesh for the metallic object using rectangular cells of size  $D_x \cdot D_y$ , the center of the  $i$ -th cell being  $\mathbf{r}_{i0}$ . Then, we proceed to the complete explanation of the algorithm by introducing a realistic benchmark case, whose analysis with MDI is performed and compared with the classical MoM. The obtained results are finally shown and discussed as preliminary assessment on the validity of the method, which will then be extended to the full-wave problem in Sec. 5.6.

Targeting simplicity, we try initially a  $N = 1$  source scheme, placing the source point in the middle of the cell. In this case, the single weight associated to the source-inner integral is  $w_1 = ab$ . We have then:

$$z_{ij}^{MDI} \approx \frac{D_x D_y}{\varepsilon_0} \sum_{m=1}^M w_m G^{ES}(\mathbf{r}_{im} | \mathbf{r}_{j0}) \quad (5.37)$$

The weights associated to the observation points are constrained by the Asymptotic Condition reformulated for electrostatics:

$$\sum_{m=1}^M w_m = D_x D_y \quad (5.38)$$

In principle, it is possible to select also  $M = 1$  observation point, placed in a generic point  $\mathbf{r}_{i*} \in S_i$  excluding the center of the cell to avoid the singularity. This choice produces for the



generic term and the self-term respectively:

$$z_{ij} \approx \frac{(D_x D_y)^2}{\varepsilon_0} G^{ES}(\mathbf{r}_{i*} | \mathbf{r}_{j0}) \quad (5.39)$$

$$z_{ii} \approx \frac{(D_x D_y)^2}{\varepsilon_0} G^{ES}(\mathbf{r}_{i*} | \mathbf{r}_{i0}) \quad (5.40)$$

Focusing on the self term, one can recognize that the only parameter determining its value is  $R = |\mathbf{r}_{i*} - \mathbf{r}_{i0}|$ , which corresponds to the distance of the observation point from the center of the cell. If properly adjusted, this distance can produce an exact value for the self-term:

$$z_{ST}^{MDI} = \frac{(D_x D_y)^2}{4\pi\varepsilon_0} \cdot \frac{1}{R} = \frac{1}{4\pi\varepsilon_0} I_0^{ST} \quad (5.41)$$

$$\Rightarrow R = \frac{1}{I_{ST}} \cdot (D_x D_y)^2 \quad (5.42)$$

The integral  $I_{ST}$  has been analytically computed in Par. 5.3.1. By inserting the first value of the (5.14), one obtains the  $R$  which exactly matches the self-term. If the case of a square cell of unitary size  $D_x = D_y = 1$  m, the distance is

$$R_{MD} = 0.336336866593418... \approx 1/3 \quad (5.43)$$

value which we call the “Magic Distance”.

If using  $M = 1$  observation point is enough for an accurate computation of the self-term, the same cannot be expected for the off-diagonal terms of the MoM matrix. In fact, a grid with a single point placed outside the center of the cell, is evidently asymmetric. With respect to the rectangular mesh adopted, symmetrical grids can be generated using at least 4 observation points which can be arranged as a “Cross” (+) or “Star” (x), as it is shown in Fig. 5.9.

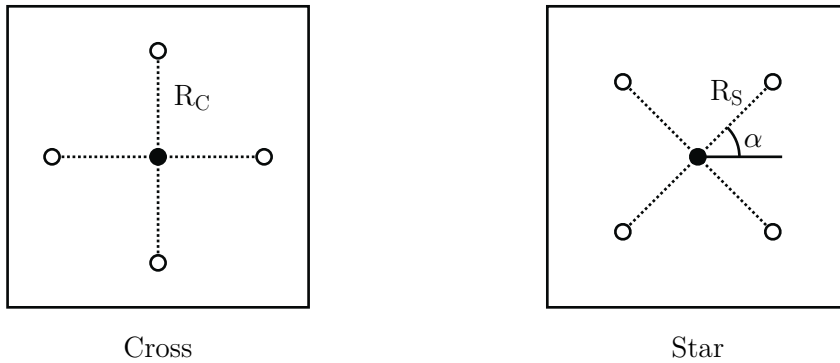


**Figure 5.9.:** The “Cross” (+) and “Star” (x) configurations

The expression for the  $z_{ij}$  entry of the MoM matrix becomes then:

$$z_{ij}^{MDI} = \frac{D_x D_y}{4\pi\epsilon_0} \sum_{m=1}^4 \frac{D_x D_y}{4} \frac{1}{|\mathbf{r}_{im} - \mathbf{r}_{j0}|} \quad (5.44)$$

where  $\mathbf{r}_{mi}$  is defined in a different way depending on the grid used:

$$\mathbf{r}_{im} = \begin{cases} \mathbf{r}_{i0} \begin{cases} \pm d \hat{\mathbf{x}} \\ \pm d \hat{\mathbf{y}} \end{cases} & (+) \\ \mathbf{r}_{i0} \pm d \cos \alpha \hat{\mathbf{x}} \pm d \sin \alpha \hat{\mathbf{y}} & (\times) \end{cases} \quad (5.45)$$

The value of  $z_{ST}^{MDI}$  only depends on the distance source-observation, therefore both grids produce an identical representation of the self-term; the choice between the grids depends then on the accuracy achieved on the other entries of the MoM matrix.

The problem used as benchmark in the following sections consists of a square metallic plate of size  $1 \text{ m} \times 1 \text{ m}$ , lying on an infinite groundplane and set to a voltage  $U = 1 \text{ V}$ . The plate is meshed with  $10 \times 10$  cells (Fig. 5.10), numbered following the x-oriented rows. The ordering of the cells influences the shape of the MDI matrix; with this choice, cells 2 and 11 are near-terms for cell 1 while cell 12 represents the diagonal term. The surface charge density  $\rho_s$ , as well as the capacity  $C = Q/U$ ,  $Q$  being the total charge on the plate, are computed and compared with the implementation of the canonical MoM.

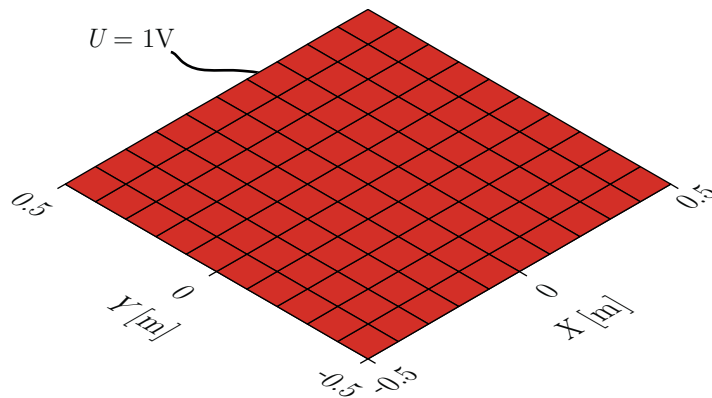


**Figure 5.10.:** The test configuration used for MDI applied to the electrostatic problem.

### 5.4.1.1. The cross configuration

The Magic Distance algorithm is run first with the only goal of matching the self term. The approximated matrix computed using the method is compared with the classic MoM one and the relative error on each term is shown in Fig. 5.11. The error on the self term is practically zero while the peak, which falls on the first near-term corresponding to the interaction between two adjacent cells, is around 6.5%. The Root Mean Square (RMS) error on the matrix is around 1.5%, which propagates to 3.5% on the surface charge and is finally reduced to 1.7% on the capacitance confirming the expectations. It is also interesting to observe how the error decreases with the distance between the interacting cells, in agreement with what discussed in Par. 5.3.3.

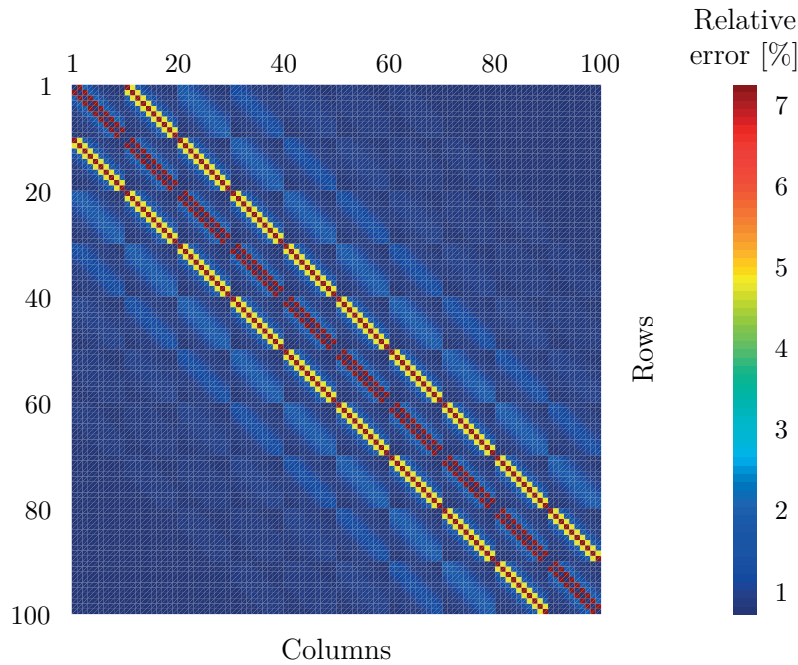


**Figure 5.11.:** Cross configuration, relative error on the MoM matrix.

When the near-term is included in the optimization,  $0 < \Omega_{NT} < \Omega_{ST}$  in (5.36), only a minor improvement is observed. On the other hand, if one tries to sacrifice accuracy on the self-term for the near-term, no satisfying compromise is found and the reduced error on  $z_{NT}^{MDI}$  is paid with a major degradation on  $z_{ST}^{MDI}$ ; also remarkable is that the optimal location of the points moves towards the borders of the cell, even if no constraint is set on their position. The conclusion is that a second set of points is necessary for a further improvement of the method's performance.

The configuration “Star” (×) shows characteristics similar to “Cross” with only a slightly

higher error on the near-term and having no peculiar aspects is not further discussed to avoid redundancies.

#### 5.4.1.2. The Cross-Star configuration

It can be seen that already using a 4 points grid the accuracy in the computed surface charge density is already satisfying. Anyway, in view of the application of the method to the electrostatics case we illustrate here the principle which allows a better approximation of the first adjacent term, which here is the one affected by the highest error.

The idea consists in introducing beside the “Cross” a second set points, for instance the “Star”, for a total of 8 observation points characterized by the distance from the center  $R_C$  (+) and  $R_S$  ( $\times$ ), Fig. 5.9. These two degrees of freedom can now be optimized to produce a configuration which minimizes the error on both the self- and the first near-term simultaneously; further extending the reasoning, the diagonal near-term (DT, the one sharing only one corner) can be also optimized. The  $z^{MDI}$  terms are therefore expressed, assuming square cells of side  $D_x = D_y = L$ , by the following:

$$z_{ST}^{MDI} = \frac{(D_x D_y)^2}{4\pi\epsilon_0} \cdot \frac{1}{8} \left( \frac{4}{R_C} + \frac{4}{R_S} \right) \quad (5.46a)$$

$$z_{NT}^{MDI} = \frac{(D_x D_y)^2}{4\pi\epsilon_0} \cdot \frac{1}{8} \left( \frac{1}{L + R_C} + \frac{1}{L - R_C} + \frac{2}{\sqrt{L + R_C^2}} + \right. \\ \left. \frac{2}{\sqrt{(L + R_S/\sqrt{2})^2 + R_S^2/2}} + \frac{2}{\sqrt{(L - R_S/\sqrt{2})^2 + R_S^2/2}} \right) \quad (5.46b)$$

$$z_{DT}^{MDI} = \frac{(D_x D_y)^2}{4\pi\epsilon_0} \cdot \frac{1}{8} \left( \frac{2}{\sqrt{L^2 + (L + R_C)^2}} + \frac{2}{\sqrt{L^2 + (L - R_C)^2}} + \right. \\ \left. \frac{1}{(\sqrt{2}L + R_S)} + \frac{1}{(\sqrt{2}L - R_S)} + \frac{2}{\sqrt{(L + R_S/\sqrt{2})^2 + (L - R_S/\sqrt{2})^2}} \right) \quad (5.46c)$$

The weights associated with the two sets of points can be fixed or used as a third (one weight is actually free, the other is forced by the Asymptotic Condition) optimization variable. In the first case, they can either be set equal,  $w_C = w_S = L^2/8$ , or defined by the sector rule:

$$w_C = \frac{L^2}{4} \tan \frac{\pi}{8} \quad (5.47a)$$

$$w_S = \frac{L^2}{4} \left( 1 - \tan \frac{\pi}{8} \right) \quad (5.47b)$$

In all the cases, a slight improvement is observed, with the errors on the near and diagonal terms,  $E_{NT}$  and  $E_{DT}$ , reduced to a value around 4%. If the constraint on the position is

removed and points are allowed to lie outside their cell, then a better agreement is obtained (peak error 3% on the diagonal term). Both error matrices are shown in Fig. 5.12.

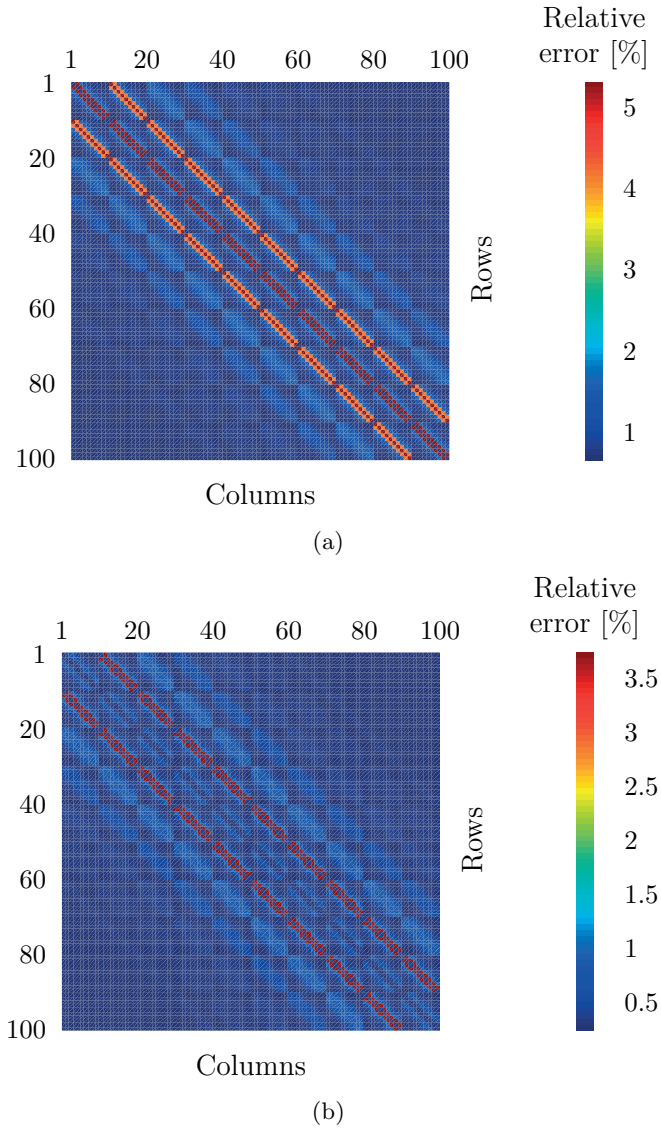


**Figure 5.12.:** Relative error on the MDI matrix for the Cross-Star configuration with fixed weights: (a) with position constraint and (b) with the constraint removed.

When the weight is included in the optimization, an interesting result is obtained. When trying to match all the conditions with the sole “Cross” configuration, points were located on the border of the cell, an average accuracy was achieved for the NT and DT, but the error on the ST was elevated. When the “Star” is added, the optimal location for the “Cross” set remains close to the border, while the “Star” points are concentrated near the source with a

very little weight (around 1% of “Cross”). This way, the accuracy on the near- and diagonal terms is preserved and the self term is corrected by the new set of points.

The error of the matrix generated using an optimized solution is shown in Fig. 5.13: as expected, the error on the near term is clearly minimized below 1% and the peak falls on the diagonal term. The RMS error on the matrix is also below 1%. The accuracy of the surface charge density is determined by comparison with MoM and is shown in Fig. 5.14: an excellent degree of matching is achieved, with RMS error halved (1.5%) and capacitance practically exact (error smaller than 0.3% on a value of 45 pF).

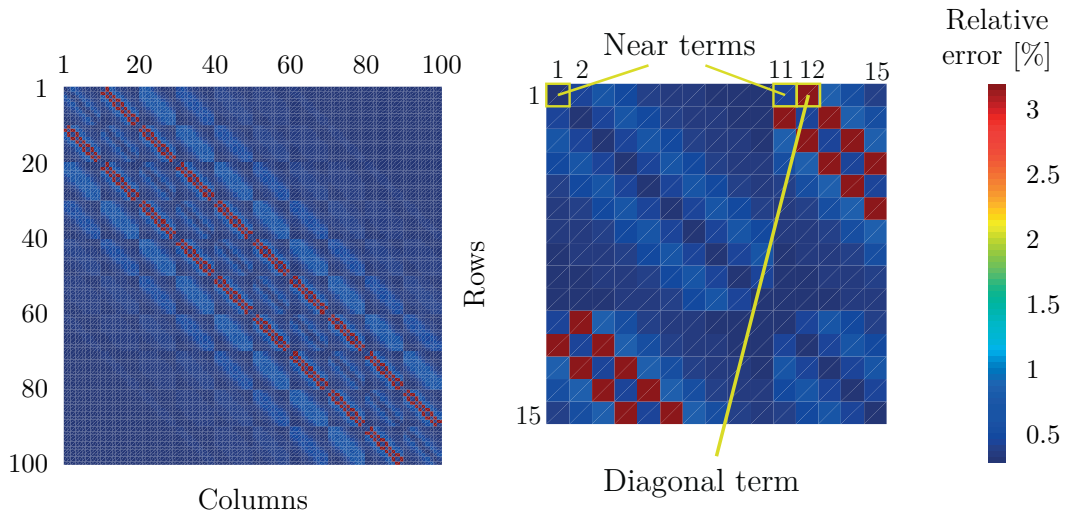


**Figure 5.13.:** Relative error on the MDI matrix for the Cross-Star configuration with optimized weights, full matrix and particular.

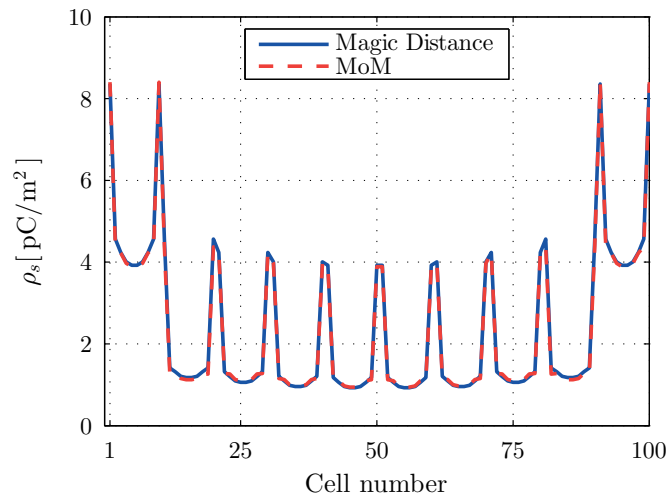


**Figure 5.14.:** Surface charge: comparison with MoM.

## 5.5. Infinite Ground Plane

The original formulation of the Magic Distance Inspired method is open for application to different formulations of Integral Equations; moreover, its capability of completely handling the EFIE kernel and its hypersingularity without resorting to the definition of potentials makes it a versatile solution for problems involving complex media, such as stratified layers; in this environments, the formulation of the IE remains the same while the characteristics of the stratification are included in the Green's Function.

For the sake of simplicity, in the previous chapter we applied the MDI algorithm to the electrostatic problem of a metallic surface in the free-space. In order to demonstrate that the method is also suitable for more complex GFs, we introduce in the patch problem an Infinite Ground Plane (IGP, Fig. 5.15).

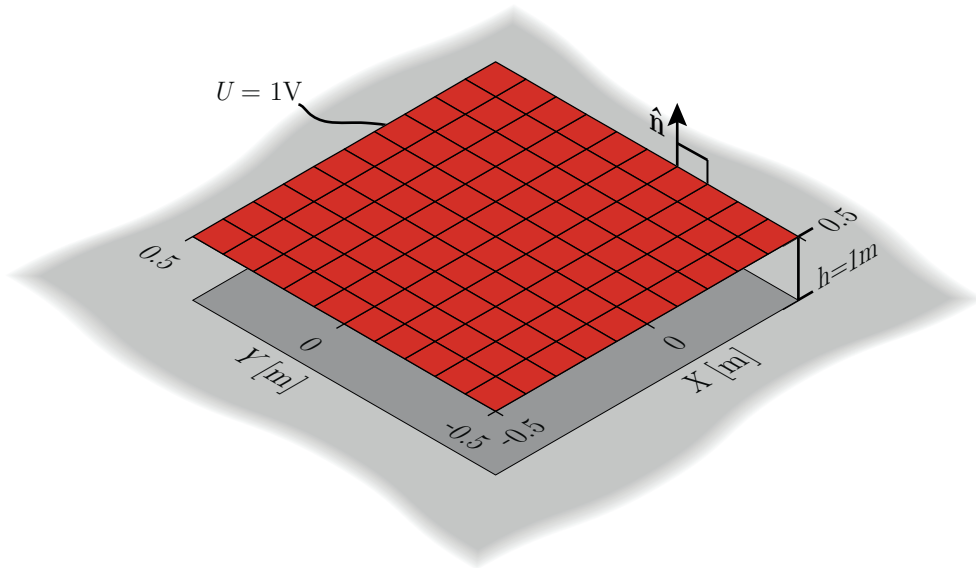


**Figure 5.15.:** The test configuration including an Infinite Ground Plane.

The GF, formulated in the spatial domain, depends on the distance  $h$  of the source from the ground plane:

$$G^{ES}(\mathbf{r} | \mathbf{r}') = \frac{1}{4\pi} \left[ \frac{1}{|\mathbf{r} - \mathbf{r}'|} - \frac{1}{|\mathbf{r} - \mathbf{r}' + 2h\hat{\mathbf{n}}|} \right] \quad (5.48)$$

The Method of Moments is used as reference for the results of MDI. In the MoM, the ground plane is substituted by means of the image theorem with a second patch in  $z = -h$ ; the GF remains therefore the free-space one, two patches are included in the simulation model and the number of unknowns is doubled. Despite the different formulation of the GFs, the accuracy of the approximation is again very good (Fig. 5.16), even improved with respect to the free-space problem, as well as the precision on the surface charge and the capacity (159 pF).

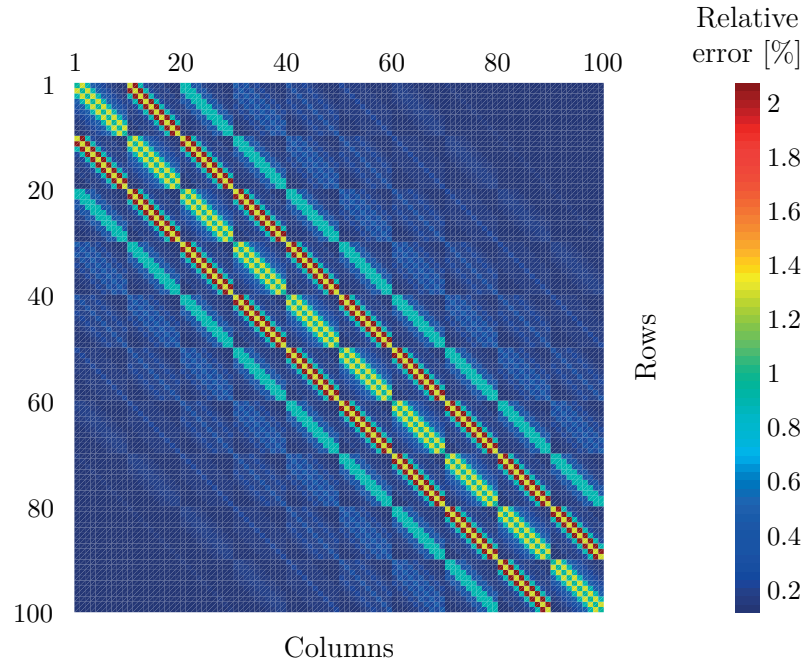


**Figure 5.16.:** Error on the MDI with Cross-Star point grid for the electrostatic case with infinite ground plane.

### 5.5.1. Application to rectangular cells

The MDI algorithm has been applied in the previous section to square cells. In view of an extension of the method to other types of mesh, we investigated the stability of the value of the MD  $R_{MD}$  found in (5.43) for square cells when the cell becomes a rectangle. As the dependency of  $R_{MD}$  on the cell aspect ratio is expressed by the quantity  $I_0^{ST}$  (5.14), we reformulate  $I_0^{ST}(Dx, Dy)$  as  $I_0^{ST}(\eta, \sigma)$  with the variables  $\eta$  (cell aspect ration) and  $\sigma$  (cell surface) are defined as:

$$\begin{cases} \eta = \frac{Dy}{Dx} \\ \sigma = Dx \cdot Dy \end{cases} \iff \begin{cases} Dx = \sqrt{\frac{\sigma}{\eta}} \\ Dy = \sqrt{\eta \cdot \sigma} \end{cases} \quad (5.49)$$

We obtain:

$$I_0^{ST}(\eta, \sigma) = 2 \left( \frac{\sigma}{\eta} \right)^{3/2} \left[ \eta \ln \left( \sqrt{1 + \eta^2} + \eta^2 \right) + \eta^2 \ln \left( \frac{\sqrt{1 + \eta^2} + 1}{\eta^2} \right) \right] - \frac{1}{3} \left[ (1 + \eta^2)^{3/2} - \eta^3 - 1 \right] \quad (5.50)$$



We consider cells with a fixed surface  $\sigma = 1$  and we compute (5.50) for different cell aspect ratios, i.e.  $I_0^{ST}(\eta, 1)$ . Normalizing with respect to the value for square cells  $I_0^{ST}(1, 1)$  we derive the curve illustrated in Fig. 5.17.

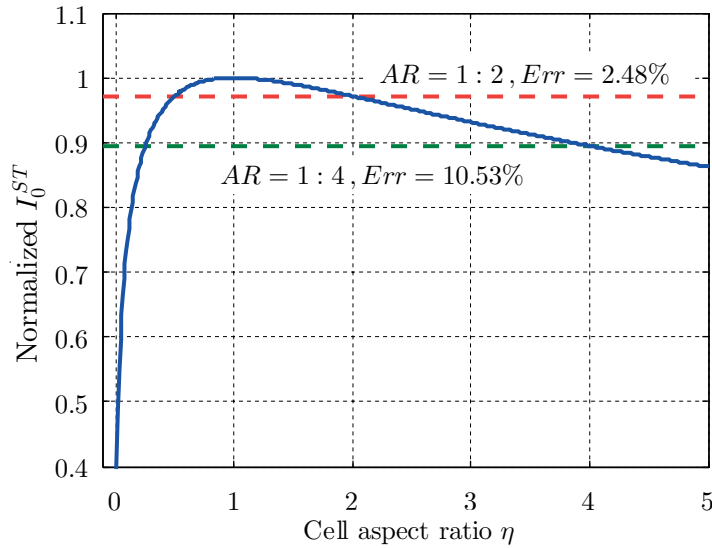


**Figure 5.17.:** Variation of the normalized four fold, self-term integral  $I_0^{ST}$  for different cell aspect ratios.

The variation within a range of aspect ratios of 1 : 2 is negligible ( $Err < 2.5\%$ ), while an acceptable stability is observed up to aspect ratios in the order of 1 : 4.

We saw in (5.41) that  $R_{MD}$  is directly and uniquely related to  $I_0^{ST}$ : therefore the stability of the integral immediately translates into the validity of the Magic Distance for non-square cells. The MDI method based on the value of  $R_{MD}$  found for the square cell can be applied to rectangular cells with moderate values of aspect ratios; the case of extreme values of aspect ratio can be considered as an unusual mesh which is anyway often avoided also in canonical MoM implementations.

### 5.5.2. Resume

The performance of the different point-schemes employed for the generation of the MDI reaction matrix associated with the electrostatic problem are resumed in Tab. 5.2.

**Table 5.2.:** Performance of the different point-schemes used in the electrostatic problem.

Scheme	Weights	Points	Peak Error %	RMS Error %	Acceleration (*)
Cross	Fixed	4	6.5	1.5	> 150
Star	Fixed	4	7	1.7	> 150
Cross + Star	Fixed	8	4	1	~ 80
Cross + Star	Opt	8	< 1	< 1	~ 80

(\*) Acceleration represents the ratio between the number of evaluation points required when solving the 4D integral with a 5 points GL quadrature ( $5^4 = 625$ ) and the number of points used in MDI.

## 5.6. The full-wave problem: the EFIE

In the previous section we have demonstrated that the “Magic Distance Inspired” method can be successfully employed to fill the MoM matrix associated to a generic electrostatic problem involving a metallic object in a homogeneous medium, also in presence of an infinite ground plane. In this section we apply the same methodology to the full-wave problem.

Different possible formulations are available for the Integral Equation: among these, we focus our interest in the Electric Field Integral Equation (EFIE) and the Mixed Potential Integral Equation (MPIE). A detailed mathematical treatment of the two was described in Par. 3.2.2 and Par. 3.2.4.

We show in the following sections that a straightforward application of MDI to the MPIE is possible, while the characteristics of the EFIE Green’s Function only allow a less intuitive insight of the method. Nevertheless, a successful implementation of MDI for full wave problems is obtained featuring a very good accuracy with a strongly reduced number of computations.

The full-wave problem presents several aspects that differ from the static case and need to be treated additionally. The Green’s Function is now the dyadic  $\bar{\bar{\mathbf{G}}}_{\mathbf{E},\mathbf{J}}$  (3.41) which contains terms in the order of  $1/r^2$  and  $1/r^3$  other than the  $1/r$  present in electrostatics; the stronger interaction between source and observation point is expected to make more difficult the definition of a point grid which produces high accuracy on the self- term and on the adjacent terms. Secondly, in the integral equation (3.40), the unknown and the known terms are now vectorial quantities,  $\mathbf{J}_{\mathbf{s}}$  and  $\mathbf{E}^{\text{inc}}$ ; consequently, the source will be identified with an infinitesimal dipole, in replacement of the charge used in electrostatics. Moreover, the entries

of the MDI matrix depend not only on the distance source/observer but also on their relative position. Finally, the use of the standard Galerkin method (Par. 3.3.2) and the choice of RWG functions (3.67) makes the basis / test functions segment-associated: this introduces a whole new set of relative orientation of source/observation cell pairs, which can generate quasi-singularities or even singularities also for off-diagonal terms.

All the elements necessary to build the MDI algorithm were introduced in the previous section: the computation of the self term (5.15), the possibilities for the choice of the weights (5.16), the enforcement of the Asymptotic Condition (5.21) eventually including the Phase Correction (5.68).

In the following sections, the optimal point schemes for the electrodynamic case are derived and discussed. The investigation starts with an overview of the analytical properties of the algorithm adapted to the full-wave problem; subsequently a benchmark case is introduced to evaluate the performance of the specific configuration. In order to clarify the formalism used in the following sections, we illustrate here extensively the benchmark model and the format in which the results will be presented.

### 5.6.1. The benchmark model

The investigation on the different point schemes to be used by the Magic Distance method requires after the treatment of the self- and near- terms, which can be conducted with an analytical approach and is mainly oriented to the approximation of the MoM matrix, a realistic test case to determine the overall performance of the method, its capability of producing the most important electromagnetic quantities, such as currents and radiated fields, and its accuracy on the predictions.

The MoM in its Galerkin formulation is known to be among the most solid and best performing simulation tools; consequently, a method based on its approximation is expected to be reliable as long as the approximation is accurate. The core of the MoM (and identically of MDI) lies in the computation of the entries of the interaction matrix and those values are dependent on the relative position of the cells. Once the basis/test functions are fixed (rectangular domain rooftops in this work), then the same amount of information can be extracted by simple geometries as well as complex ones; yet, being the solution of the method based on the inverse of the interaction matrix, on which we have no direct control, it is necessary to define an excitation, anyone, to generate the results. Also, as already discussed (Sec. 5.3), the method will be tested using the free-space Green's Function.

Based on these considerations, a perfectly meaningful and yet simple geometry to be used as benchmark is a square metallic patch of one wavelength size. The patch is normal to  $\hat{\mathbf{z}}$  and is meshed with a grid of  $10 \times 10$  cells of size  $\lambda/10$ , resulting in 180 internal segments, 90 aligned along  $\hat{\mathbf{x}}$  and 90 along  $\hat{\mathbf{y}}$ . The patch is illuminated by a plane wave with normal

angle of incidence and the electric field is parallel to one of the patch edges (here  $\hat{\mathbf{x}}$ ). The benchmark structure is depicted in Fig. 5.18.

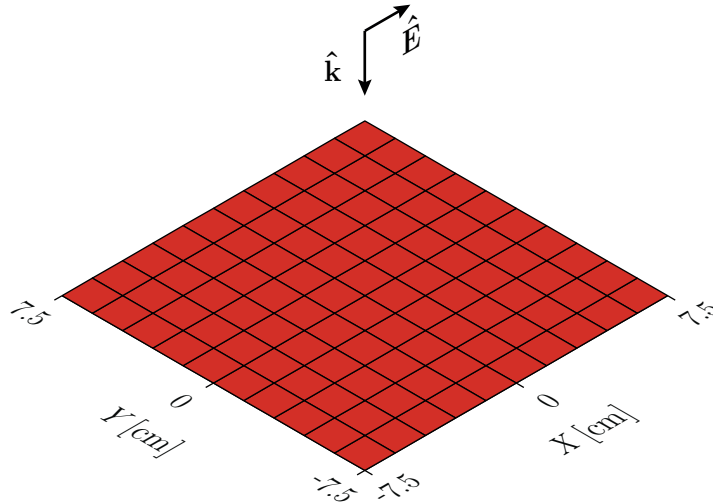


**Figure 5.18.:** The benchmark structure for the full-wave problem.

The current distribution induced by the plane wave on the patch is known to tend to infinite when approaching the patch edges which are parallel to the impinging electric field; this makes the solution of the problem already challenging with this simple geometry.

The results will be presented in different formats: the error on the entries of the Z matrix will be presented as a rectangular plot showing the first row of the matrix; this will ease the reading and the comparison with other curves (also due to the size of the matrix itself,  $180 \times 180$  and will contain all the necessary information (all the possible combination of position source/observer). The values of the surface current will be shown as a 3D color-plot and, for a better comparison with MoM, as a segment-by-segment rectangular plot. The format of the rectangular plots basically depends on the fact that the basis/test functions are segment-associated and on the numbering rule used for the segments; these are ordered first by orientation ( $\hat{\mathbf{x}}$ ,  $\hat{\mathbf{y}}$  then  $\hat{\mathbf{z}}$ ) then by position, spanning consecutively the x, y and z coordinate. An example of the correspondence between mesh and rectangular plot is shown in Fig. 5.19.

### 5.6.2. Full-wave implementation of the MDI method

The application of the MDI method to the Electric Field Integral Equation follows quite straightforwardly from the formulation for the electrostatic problem.

In view of this, we need to consider the Mixed Potential version combined with the Galerkin-MoM formulation in the case of rectangular mesh and typical RWG basis/test functions, Par. 3.3.1. The four fold integral is separated into its vector and scalar potential parts, according

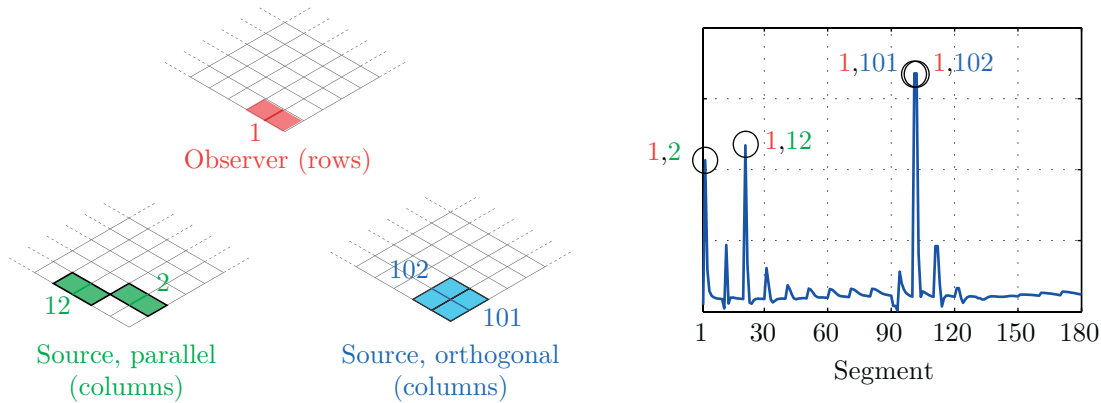


**Figure 5.19.:** Correspondence between cell couples and rectangular plots.

to (3.97), both with kernel  $\exp(-jkr)/r$  and weighted the former by a rooftop function, by pulse functions (due to the derivatives) the latter. In the hypothesis of electrically small cells, the exponential can be approximated with the first-order term of its Taylor expansion (5.10). As sketched in Fig. 5.20, the scalar potential integral is exactly the combination of two static self-term integrals (5.14a) plus two static near-term integrals (5.14b), taken with the proper sign. The vector potential can also be reduced to a contribution in the form (5.14a) with the further approximation of replacing the rooftop with a pulse (Fig. 5.20).

Summarizing, the procedure involves the computation of the electrostatic self-term for both potentials, plus the near-term for the scalar potential. It was found in Par. 5.4.1 that a 8 points grid (a “Cross” and a “Star”) was necessary to achieve a good degree of accuracy for both terms. It is therefore expected that the same condition holds for the electrodynamic case in the MPIE formulation. On the other hand, the results of the next section, where the electrostatic configurations are used to find the MD which approximates the 4D integral with kernel  $\bar{\mathbf{G}}_{\mathbf{E},\mathbf{J}}$  show that no physically meaningful value can be obtained, confirming the expected increase in complexity associated with the EFIE.

### 5.6.3. Electrostatics configurations

The first logical step consists in applying to the EFIE the same point schemes successfully used for the EPIE in Par. 3.2.5. These configurations, readapted to the segment-associated rooftops, are illustrated in Fig. 5.21. Some important conclusions about these configurations can be drawn from the mathematical analysis of the source-field interaction. The source is an infinitesimal electric dipole parallel to the cell’s BF and, in the observation point, the TF-oriented E-field component is taken. Let us also suppose the weights to be fixed according to the Sector Rule (5.16). As previously stated, the matrix entry which is important to approximate with the highest precision is the self term: in analogy with electrostatic, we first attempt to derive analytically the optimal position of the points (the Magic Distance) which

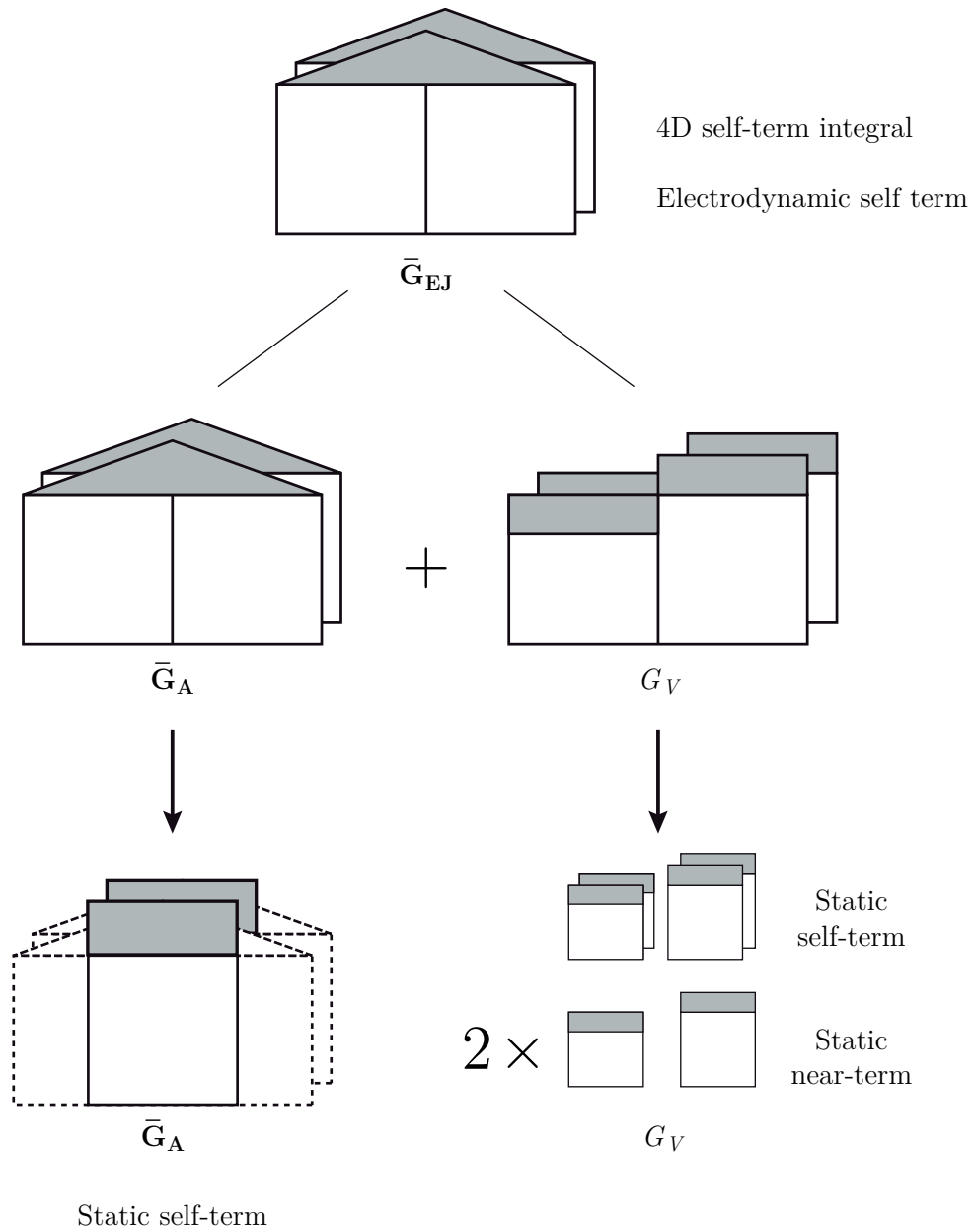


**Figure 5.20.:** Intuitive adaptation of the electrostatic MDI to full-wave.

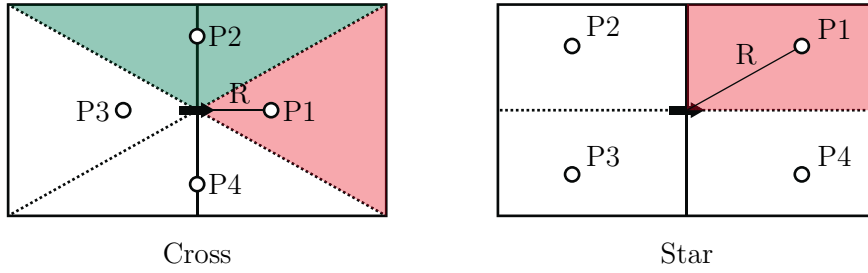


**Figure 5.21.:** Cross and Star configurations for segment-associated BF.

produce an exact value (with exact we refer to the most accurate computation available). Considering an  $\hat{\mathbf{x}}$  oriented BF/dipole, its  $\hat{\mathbf{x}}$  oriented component of the electric field was given in Par. 3.2.2, (3.44):

$$E_{TF}^{XX} = \frac{j\omega\mu}{4\pi} \frac{\exp(-jkr)}{r} \left\{ \left[ 1 - 3 \left( \frac{1}{(kr)^2} - \frac{1}{jkr} \right) \right] \left( \sin^2 \theta \cos^2 \phi - \frac{1}{3} \right) - \frac{2}{3} \right\} \quad (5.51)$$

$$(5.52)$$

In the hypothesis, generally verified, of electrically small cells, we can use the near-field formula to compute the MDI value at the four points relative to the two configurations at the generic distance  $R : kR \ll 1$ .

$$E_{NF}^{XX} = \frac{j\omega\mu}{4\pi} \frac{1}{r^3} (1 - 3 \sin^2 \theta \cos^2 \phi) \quad (5.53)$$

For the ‘‘Cross’’ configuration (Fig. 5.21) we have:

$$E_{TF}^{XX} = \frac{j\omega\mu}{4\pi} \frac{1}{r^3} \begin{cases} (-2) & (\text{P1,P3}) \\ (+1) & (\text{P2,P4}) \end{cases} \quad (5.54)$$

Applying the Sector Rule (5.16) for the weights we also obtain:

$$w_n = A/2 \quad n = 1 \quad (5.55)$$

$$w_m = \begin{cases} A/6 & (\text{P1,P3}) \\ A/3 & (\text{P2,P4}) \end{cases} \quad m = 1..4 \quad (5.56)$$

with  $A$  representing the cell surface. Combining weights and field values, we obtain the result:

$$z_{ST}^{MDI} = \frac{j\omega\mu}{4\pi} \frac{1}{r^3} \frac{A}{2} \left[ \frac{A}{6} (-2) + \frac{A}{3} (+1) + \frac{A}{6} (-2) + \frac{A}{3} (+1) \right] = 0 \quad (5.57)$$

Thus, the resulting approximation of the MoM self term is identically zero!

The case of “Star” configuration (Fig. 5.21) can be treated in the same way and leads to the expression of the near field:

$$E_{TF}^{XX} = \frac{j\omega\mu}{4\pi} \frac{1}{r^3} \left(-\frac{1}{2}\right) \quad (P1..P4) \quad (5.58)$$

while the weights are:

$$w_n = A/2 \quad n = 1 \quad (5.59)$$

$$w_m = A/8 \quad m = 1..4 \quad (5.60)$$

The MDI term is then:

$$z_{ST}^{MDI} = \frac{j\omega\mu}{4\pi} \frac{1}{r^3} \frac{A}{2} \left[4 \left(-\frac{1}{2}\right)\right] = -\frac{j\omega\mu}{4\pi} \frac{A^2}{32} \frac{1}{r^3} = -jC \frac{1}{r^3} \quad (5.61)$$

Due to the near-field approximation, the  $z$  term is purely imaginary and negative ( $C > 0$  is the coefficient collecting all the other constants). Following the procedure, in order to derive the Magic Distance we equal (5.61) to (5.15), again in the hypothesis that the cell is small enough that the exponential term can be neglected and the 4D integral can be replaced by  $I_0^{ST}$ :

$$R_{MD} = \sqrt[3]{-j \frac{1}{\omega\epsilon} \frac{A^2}{32\pi} \frac{1}{I_0^{ST}}} \quad (5.62)$$

Now, being  $\text{Re}\{I_0^{ST}\} = 0$  and  $\text{Im}\{I_0^{ST}\} > 0$  (see Par. 5.3.1), the value of  $R_{MD}$  is the cubic root of a negative number meaning  $R_{MD}$  is a *negative* distance!

It appears therefore impossible to use a single degree of freedom (and therefore a unique Magic Distance value) for the EFIE. So, more involved configurations will be explored in the following sections.

#### 5.6.4. Single-source configurations

In the previous section we demonstrated that simple point schemes like those used for electrostatics, the “Cross” and “Star” configurations, cannot be directly applied to the full-wave problem, as they result in identically zero fields or yield negative, nonphysical Magic Distances. Targeting simplicity and computational speed as key features of the method, we decided to take advantage of the results of the study conducted in the previous section and investigate reduced point schemes, before trying configurations with increased number of points. The idea of deriving of the Magic Distance only on the basis of geometrical or physical considerations, rather than through an optimization is indeed attracting and deserves special attention, provided it turns out to be capable to approximate the MoM matrix at least with fair accuracy.

The performed study consists in an extensive investigation on the possible choices concerning



the MDI method, which can be fixed using specific rules or left for optimization, and the choice of the weights, again definable by a rule or used as optimization variable. Moreover, in electrodynamics a correct approximation of the self-term is a necessary but definitely not sufficient condition for the accurate representation of the MoM matrix, due to the different cell superposition and orientation possibilities.

#### 5.6.4.1. Two and four points configurations

We consider a pair of adjacent cells of size  $(D_x, D_y)$ . Three possibilities were tried for the computation of the MDs:

- fixed, in the barycenter of the sector associated with the point
- fixed, derived by enforcing the matching condition on the self term
- left for optimization

and for the weights:

- fixed, determined by the sector-rule
- included as variables in the optimization (still enforcing the Asymptotic Condition)

We also selected two point schemes for the study:

- a  $N = 1$  source,  $M = 2$  observation points placed along the segment associated to the TF
- a  $N = 1$  source,  $M = 4$  observation points placed as “Cross” but with different distances  $d1$  and  $d2$  along the axes

With  $N = 2$  points, weights are automatically determined by symmetry considerations.

#### Barycenter and Sector rule

In the case of  $N = 2$  points, sectors are the rectangles of sides  $(2D_x, D_y/2)$  and the MD is immediately  $R_{MD} = D_y/4$ . With four points, the sectors are triangles: since the barycenter of a generic triangle with endpoints  $(x_a, y_a), (x_b, y_b), (x_c, y_c)$  is:

$$P_b = \left( \frac{x_a + x_b + x_c}{3}, \frac{y_a + y_b + y_c}{3} \right) \quad (5.63)$$

we find the values of  $R_{MD}$  associated with points  $P1...P4$  as in Fig. 5.21:

$$R_{MD} = \begin{cases} 2D_x/3 & (P1, P3) \\ D_y/3 & (P2, P4) \end{cases} \quad (5.64)$$

In both cases, the accuracy of this naive attempt is quite poor, but shows that also in the full-wave problem the error asymptotically decreases with the distance.

### Self-term matching and Sector rule

While the technique applied to the “Cross” configuration yields a negative distance, with the simpler 2 points configuration it is possible to derive a physically meaningful value for the MD when enforcing the matching condition on the self term. The procedure is the same as discussed in Par. 5.6.3 for “Cross” and “Star” configurations and leads to the value for the MD:

$$R_{MD} = \sqrt[3]{+j \frac{1}{\omega \epsilon} \frac{A^2}{16\pi} \frac{1}{I_0^{ST}}} \quad (5.65)$$

which, having  $I_0^{ST}$  only a positive imaginary part, yields a valid value for  $R_{MD}$ . In fact, generating the MDI matrix and comparing with MoM in the case of very small cells ( $\lambda/40$ ), confirms that the error on the self term is safely below 1%. It is then interesting to explore up to which limit holds the hypothesis of near-field approximation made for the infinitesimal dipole field and for the exponential term  $\exp(-jkr)$ . We observed that the error remains acceptable for  $\lambda/20$  cells ( $\sim 3\%$ ), then deviates reaching 16% for  $\lambda/10$  cells. As a result, a more accurate model for the self-term, either involving higher order Taylor expansion or the numerical evaluation of the integral is definitely required.

A last remark is necessary on the value of the MD: when square cells are used, the observation point falls *outside* the cell, regardless the frequency or the electric size of the cell. While from a purely mathematical insight this does not create any conflict with the validity of the solution, from an engineering point of view testing a quantity relative to a domain outside the domain itself sounds inconsistent. When correcting the aspect ratio of the cell  $D_y/D_x$  to 2 or more, the observation point comes back within the cell; anyway this artifice is to no avail as the aspect ratio becomes the reciprocal for orthogonal segments.

### Optimization and Sector rule

Concerning the 2 points case, the optimization algorithm confirms the expectations: when cells are square, the optimal observation point lies on the border of the cell (inside which it is constrained) and the error is relevant; when the cell aspect ratio is 2:1, the optimization succeeds in minimizing the cost function and the error falls below 1%.

In agreement with expectations is also the output of the optimization algorithm for the 4 points case. If the point distance is fixed to a single variable  $d_1 = d_2 = d$ , then the cost function cannot be minimized, meaning the self term cannot be matched with this configuration. This result confirms the analysis discussed in Par. 5.6.3.

If two independent variables are used, the self term can be matched but still the off-diagonal terms need improved accuracy.

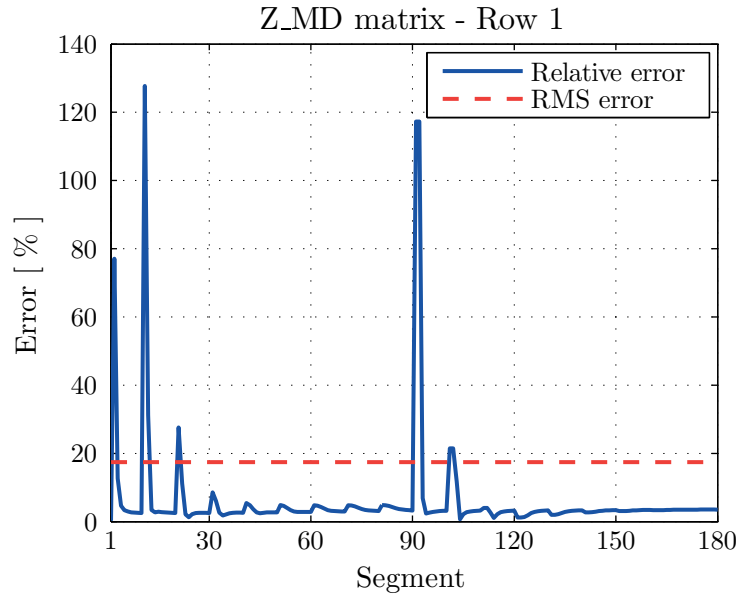


**Figure 5.22.:** Relative error associated to the “Cross” configuration with position and weights values optimized.

### Full optimization

As final attempt to reach a satisfactory precision with a 4 points scheme, we optimize the position of the points and the weights (subject to the Asymptotic Condition), for a total of three independent variables. A significant improvement in the overall accuracy is observed (Fig. 5.22), with an error on the two near-terms reduced below 15%. Yet, other terms still show a major deviation which requires more complex configurations to be suppressed. As a remark, the optimization outputs a value for the weights which is near one for the points P2 and P4 and consequently close to zero for P1 and P3. This result actually seems to tend exactly to the 2-point configuration; yet, removing the quasi-zero weighted points leaves the error practically unchanged, with the exception of the self term which now is affected by an error higher than 400%. As a conclusion, the points added have the only function of correcting the self term, while they do not affect the off-diagonal terms. A similar behaviour was also observed when using the 8 points configuration in electrostatics, Par. 5.4.1.

#### 5.6.4.2. Six, eight and twelve points configurations

The four-points configurations were interesting cases of study, yet their performance cannot be considered satisfying for an all-purpose simulation method. In this section, we perform an investigation on point schemes featuring an increasing number of points, with the aim of finding the best compromise between accuracy and computational requirements. The performance of a point grid is evaluated by referring to the error on the MDI matrix with respect to the MoM one; both the peak error on single terms and the RMS error are

accounted for in the evaluation.

Once a significant accuracy on the matrix is achieved, the focus is moved to the inverse matrix and the solution of the system, the surface current.

### A 6 point configuration

A significant improvement in the accuracy is obtained by combining a “Star” configuration with an additional couple of points lying along the segment joining the cell pair, for a total of 6 points and 4 optimization variables. The optimized point grid and the error on the MDI matrix are shown in Fig. 5.23 and Fig. 5.24 respectively.

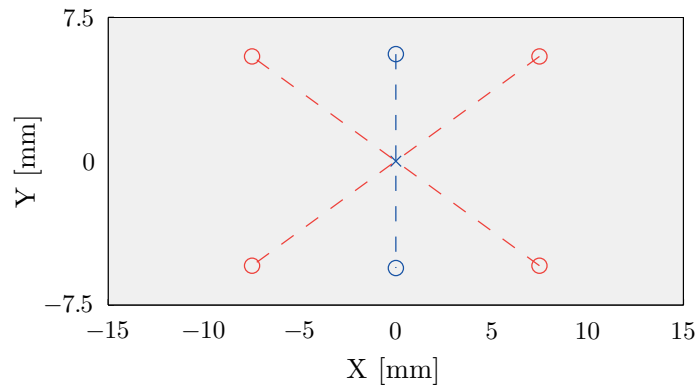


**Figure 5.23.:** Point scheme featuring 6 points.

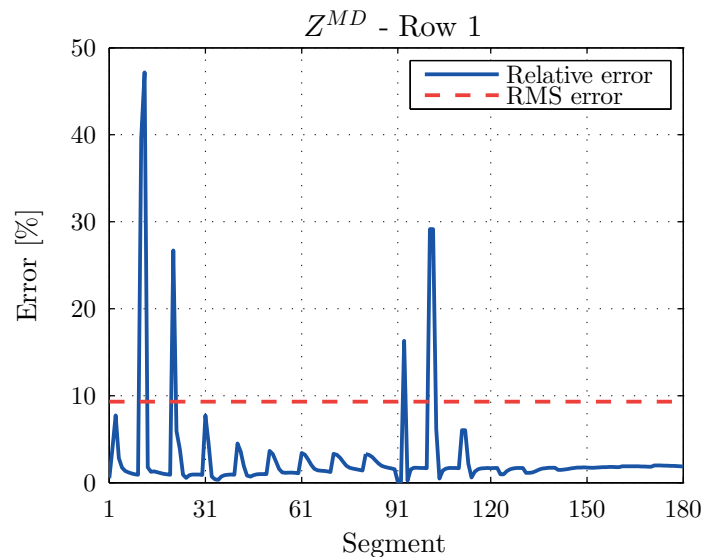


**Figure 5.24.:** Error on the MDI matrix obtained with a 6 points grid.

The RMS value is halved (10 % against the 19% of the 4 points configuration); when used to solve scattering problems like the benchmark (Par. 5.6.1) this is solution a good option at least for a first-approach analysis.

**An 8 point configuration**

The accuracy in the representation of the MoM matrix can be increased by adding observation points, avoiding on the other hand to compromise the effort of obtaining a fast and simple method.

The configuration, illustrated in Fig. 5.25, consists of 2 sets of 4 points; each of them is a “Star” and the positions of the points, spanning across the whole cell, are defined by  $d_{1x}$  and  $d_{1y}$  and  $d_{2x}$  and  $d_{2y}$ . A further improvement is observed with this point grid: the RMS error is again halved (5%) and the peak error, limited below 35%, affects only terms with a minor influence on the matrix, as shown in Fig. 5.26.

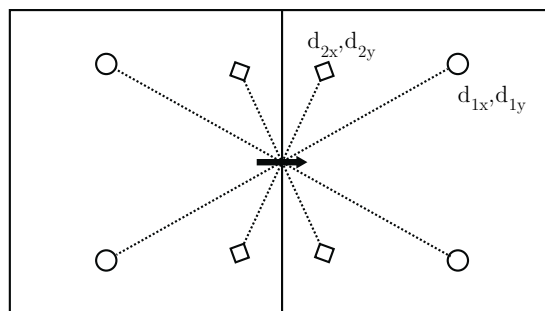


Figure 5.25.: Point scheme featuring 2 sets of 4 points.

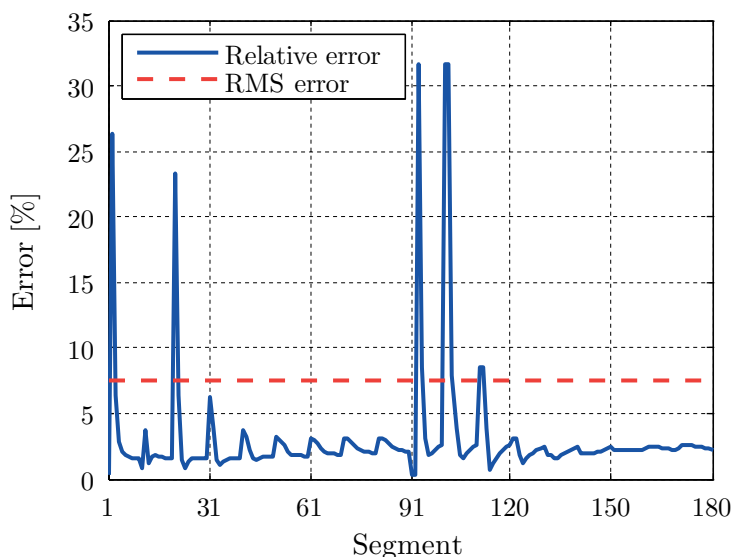


Figure 5.26.: Double Star configuration, relative error.

As a remark, the optimization outputs a particular position for one of the stars: points are located very close to the diagonals of the double-cell. Anyway, if they are forced to lie *on* the diagonal, thus removing a degree of freedom, the error critically increases.

Further reduction of the peak error, falling on the "L" adjacent term (Fig. 5.19 in Par. 5.6.1) can be obtained by including the weights in the optimization. Anyway, the accuracy on the MDI matrix obtained with the 8 points grid represents the limit above which the reduction of the error is not worth the increase of points (at least for a cell size in the order of  $\lambda/10$ , see Par. 5.6.7); moreover, even doubling the number of points, the error is redistributed among the matrix entries, rather than decreased. On the other hand, the error on the inverse matrix is closely related to the accuracy of the solution and, even though it cannot be directly manipulated, can be taken as figure of merit; if correctly interpreted it provides in fact an evaluation of the performance independent on the excitation but also closely related to the solution.

The MoM matrix and its inverse have a similar shape: they are characterized by strong diagonal elements and a dispersion of second-order terms associated (at least in the non inverted matrix) to interaction between orthogonal, nearby elements. While in the direct matrix the matching of the lesser order entries is ensured by the Asymptotic Condition (even without Phase Correction), in the inverse matrix these entries play the role of a "background noise". In fact, they do not contribute significantly to the solution, but affect strongly the RMS error; therefore, the evaluation of the latter is more meaningful if lesser magnitude elements are "filtered" and not considered. In particular, setting to threshold 3% of the maximum value generally provides a certain correlation between the RMS error on the inverse matrix and on the current.

Concerning the previously illustrated configurations, the optimized 4 points grid produces a RMS error exceeding 100%, the 6 points one  $\sim 72\%$  and the 8 points one 52%.

### A 12 point configuration

The highest degree of accuracy in the inverse matrix and in the surface current, still with a limited number of calculations, is obtained using 12 observation points. The configuration is an evolution of those already discussed; it consists of three "Star" as is shown in Fig. 5.27 where the points and the respective sectors are highlighted. In this configuration, the weights are associated to their sectors:

$$\begin{aligned}
 w_1 &= \frac{D_x^2}{6} \tan\left(\frac{\pi}{8}\right) \\
 w_2 &= \frac{D_x D_y}{4} - \frac{D_x^2}{6} \tan\left(\frac{\pi}{8}\right) + \frac{D_y^3}{48 D_x} \cot^2\left(\frac{3\pi}{8}\right) - \frac{D_y^2}{8} \cot\left(\frac{3\pi}{8}\right) \\
 w_3 &= -\frac{D_y^3}{48 D_x} \cot^2\left(\frac{3\pi}{8}\right) + \frac{D_y^2}{8} \cot\left(\frac{3\pi}{8}\right)
 \end{aligned} \tag{5.66}$$

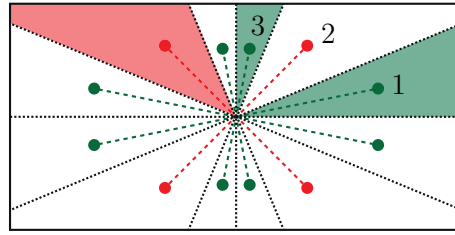


**Figure 5.27.:** The 12 point scheme consisting of three “Star” sets of points.

The error on the MDI matrix is shown in Fig. 5.28. Using fixed weights, the RMS error on the inverse of  $Z^{MDI}$  can be reduced around 25%; this result is almost not improved by including the weights in the optimization (unlike for the previous configurations); on the other hand, the cost function is minimized with more difficulty. This suggests that when the number of variables increases the optimization algorithm loses efficiency; in these cases, a choice based on physical insight could be preferred, even if at least in principle is not the optimal solution.

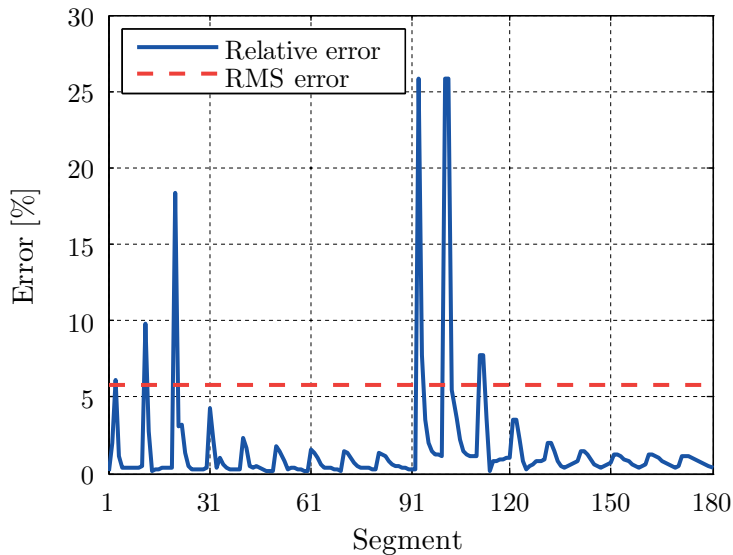


**Figure 5.28.:** Triple Star configuration, relative error.

This point scheme is suitable to show the accuracy of the predictions of the surface current achievable with the Magic Distance method. The benchmark problem has been introduced in details in Par. 5.6.1 and involves a metallic patch illuminated by a plane wave. The solution is compared with the canonical implementation of MoM-MPIE (Galerkin formulation) in Fig. 5.29 (segment-wise comparison) and Fig. 5.30 (surface plots): the degree of accuracy is very good, with an RMS error lower than 6%.

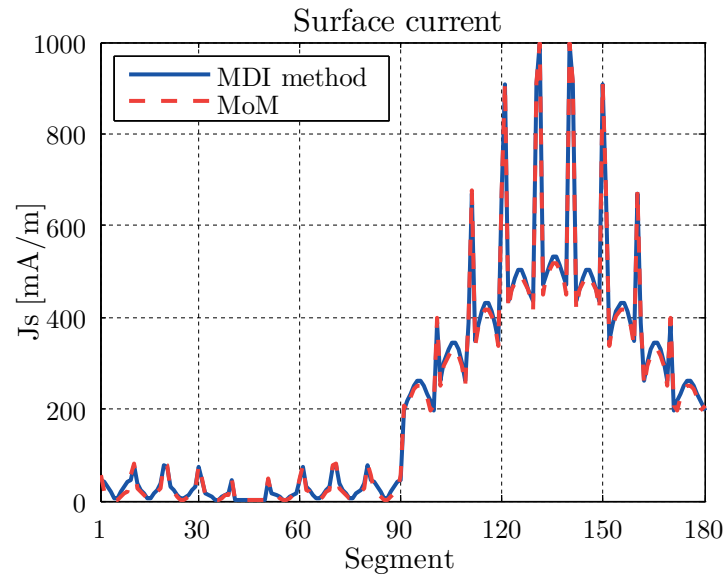


**Figure 5.29.:** Comparison of the surface current predictions between the Magic Distance Inspired method (Triple Star point grid) and the canonical MoM.

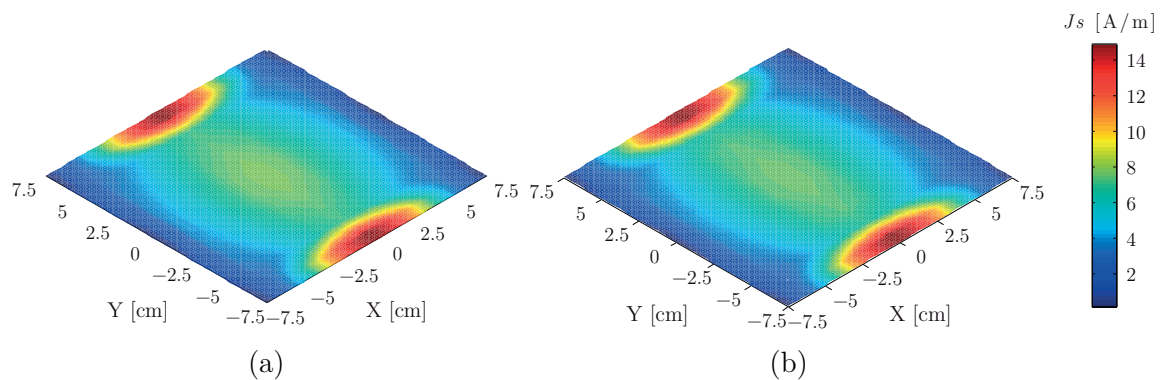


**Figure 5.30.:** Surface currents on the metallic patch computed with (a) Magic Distance Inspired method and (b) MoM.



### 5.6.5. Multi-source configurations

The configurations so far illustrated, consisting of a single point for the inner integral, produce very good results with 8 or 12 observation points. Replacing a 2D integral by a single point may however seem an unsafe approximation, as all the information about the basis function is practically lost. Moreover, in the case of non-planar cell couples, the direction of the basis / test function is not well defined; therefore, in view of an extension of the MDI algorithm to 3D problems, it is mandatory to remove points from the segments.

The driving strategy adopted for the study is similar to the one previously illustrated for single-source configurations, with the additional constraint of completely separating the source and observation associated sectors, in order to avoid singularities which make the optimization algorithm fail. We identified different interesting point grids based on combinations of subsets of points; the result can be summarized in the configuration that represents the best trade-off between accuracy and number of points employed.

The configuration is composed by 4 sources and 4 observation points and is sketched in Fig. 5.31.

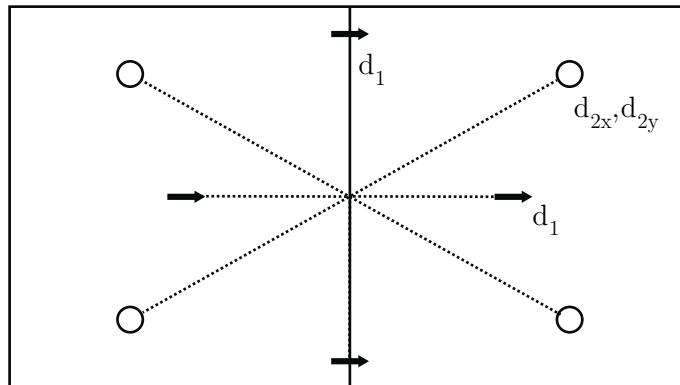
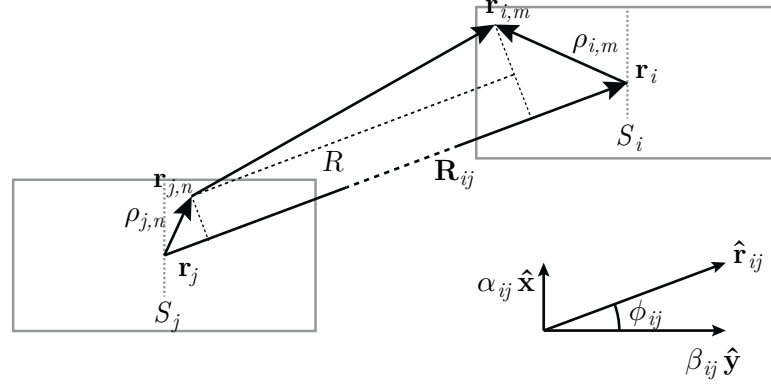


Figure 5.31.: The configuration with 4 source points and 4 observation points.

### 5.6.6. The impact of phase correction

In Par. 5.3.4 we discussed the opportunity of introducing a phase correction term in the numerical evaluation of the MoM entries, when one point is used for the inner integral. The result was an improvement in the asymptotic behaviour of the error, decreasing from a steady value of 3% to zero.

The Magic Distance Inspired algorithm cannot be classified as a generic quadrature rule: in fact, while with algorithms like Gauss-Legendre the correct evaluation of far field terms is intrinsically ensured, MDI requires the enforcement of the Asymptotic Condition to compute



**Figure 5.32.:** Formalism used for the derivation of the Phase Correction for the MDI algorithm.

the far field terms.

The Phase Correction must be introduced in the frame of the Magic Distance method by operating on the Asymptotic Condition, in particular on the approximation (5.19). The correction is necessary not only if a single point is used as source or observation (equivalently to the 2D cases) but with *any*  $M \times N$  grid (while the 4D GL integration does not require any correction).

In order to derive the corrected version of the Asymptotic Condition for the term  $z_{ij}$ , with reference to Fig. 5.32 we introduce the following quantities:

- $\mathbf{R}_{i,j}$  is the vector connecting the centers of the  $i$ -th and  $j$ -th cells.
- $\mathbf{r}_{i,m} \in S_i$  and  $\mathbf{r}_{j,n} \in S_j$  are the absolute positions of the  $m$ -th observation and  $n$ -th source point.
- $\rho_{i,m}$  and  $\rho_{j,n}$  are the positions of  $\mathbf{r}_{i,m}$  and  $\mathbf{r}_{j,n}$  with respect to the center of their cells.
- $R$  is the distance between  $\mathbf{r}_{i,m}$  and  $\mathbf{r}_{j,n}$ , projected on  $\mathbf{R}_{i,j}$ :

$$R = R_{i,j} + \rho_{i,m} \cdot \hat{\mathbf{R}}_{i,j} - \rho_{j,n} \cdot \hat{\mathbf{R}}_{i,j} = R_{i,j} + R_{m,n} \quad (5.67)$$

- The Phase Correction  $\Psi_{P2P}$ , which is defined in (5.28) and (5.30):  $\Psi_{P2P} = \Psi_{i,j}^0 \exp(-jkR_{i,j})$ , and depends (through  $\alpha_{i,j}$  and  $\beta_{i,j}$ ) only on the relative position of the cells.

Using such formalism, the Asymptotic Condition (5.21) becomes:

$$\sum_{m=1}^M \sum_{n=1}^N w_m w_n \exp(-jkR_{m,n}) = \Psi_{i,j}^0 \quad (5.68)$$

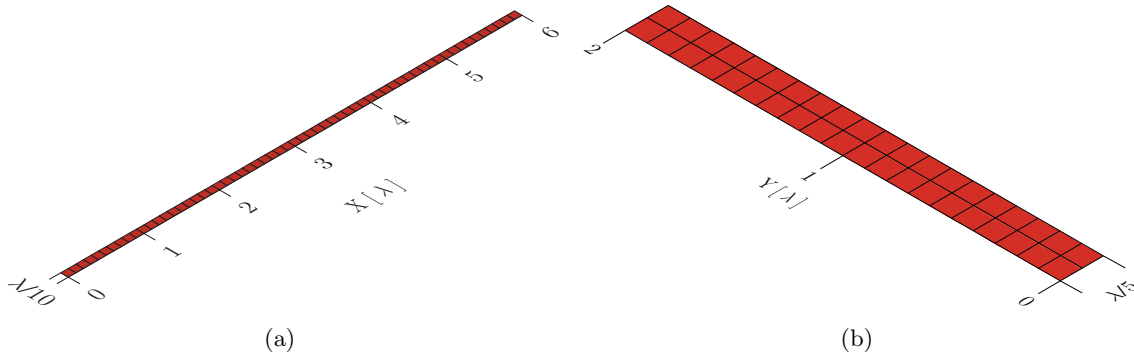


**Figure 5.33.:** Layout of the test cases used for Phase Correction.

The last weight can be obtained as:

$$w_M = \left[ \Psi_{i,j}^0 - \sum_{m=1}^{M-1} \sum_{n=1}^N w_m w_n \exp(-jkR_{m,n}) \right] \cdot \left[ \sum_{n=1}^N w_n \exp(-jkR_{M,n}) \right]^{-1} \quad (5.69)$$

The phase correction term is obtained by applying the far field approximation of the exponential part of the GF, that is assuming parallel rays, condition which is hardly valid for near terms. The MDI algorithm on the other hand is based on the computation of near (self) terms, which are used to derive the optimal distances of the points. The correct way of implementing this feature is therefore running the original MDI algorithm and correcting the matrix terms relative to cells spaced more than a certain threshold distance.

In order to estimate the distance after which the Phase Correction actually improves the approximation of the MoM matrix elements, we introduce two test cases: a long, thin strip in the x- and y-direction. In analogy with Par. 5.3.4, these two geometries allow the observation of the effect of the increased distance for different relative orientation between cells. The layout of the two cases is shown in Fig. 5.33; while the x-oriented strip is clearly associated with the  $\phi = 0$  case, note that in the y-oriented strip only the values associated to y-oriented segments are considered, as they represent cell couples with increasing spacing in the  $\phi = 90$  case. The results will be presented as the error curves (with respect to MoM) relative to the row of the MDI matrix associated to the first y-oriented segment (joining the first cell couple).

Three point schemes, discussed in Par. 5.6.4, have been used in the comparison, all including a single source point and the following observation grids:

- 4 points “Cross”
- 8 points “Double Star”
- 12 points “Triple Star”

Also, in all the configurations the weights have been included in the optimization.

### Cross

The “Cross” configuration is known to be affected by a significant error (Fig. 5.22), especially on the adjacent term in the  $\phi = 90$  direction. The comparison of the curves obtained when including or not the Phase Correction are shown in Fig. 5.34.

In agreement with the expectation, the Phase Correction improves the far field accuracy with an error asymptotically decreasing to zero. In the case of the x-oriented strip, the benefits of the Phase Correction appear when the distance is around  $\lambda/2$ ; more interesting, for the y-oriented strip the improvement takes place in all the terms not included in the optimization.

### Double Star

The best compromise between accuracy and number of points, the “Double Cross” is affected only by a modest error (Fig. 5.26), making this comparison the most significant for a practical implementation of the Magic Distance Inspired method. The comparison of the curves obtained when including or not the Phase Correction are shown in Fig. 5.35.

Expectations are again confirmed: the good performance of the MDI method is improved with Phase Correction starting from a distance of  $0.8\lambda$  in the  $\phi = 0$  case and  $0.3\lambda$  in the  $\phi = 90$  case.

### Triple Star

The accuracy of the MDI method with Phase Correction is almost independent on the specific point grid employed; on the other hand, the *improvement* introduced with respect to the basic MDI algorithm is related to the point scheme. To illustrate this behavior, we apply here the Phase Correction to the most accurate (and expensive) scheme developed, the “Triple Star”. The comparison of the curves obtained when including or not the Phase Correction are shown in Fig. 5.36. Note that the length of the strips have been increased for a more complete illustration of the comparison.

While the curves relative to the Phase Correction version are practically unchanged, now the basic algorithm exhibits an accuracy which is practically comparable with the corrected version, with an asymptotic error well below 1%.

After the discussed results, we can conclude that Phase Correction is mandatory for grids with reduced number of points; it is also recommended for an all-purpose implementation (8 points scheme) especially with geometries larger than one wavelength. When high accuracy is requested, the basic version of the MDI algorithm with at least a 12 point grid can be successfully employed.

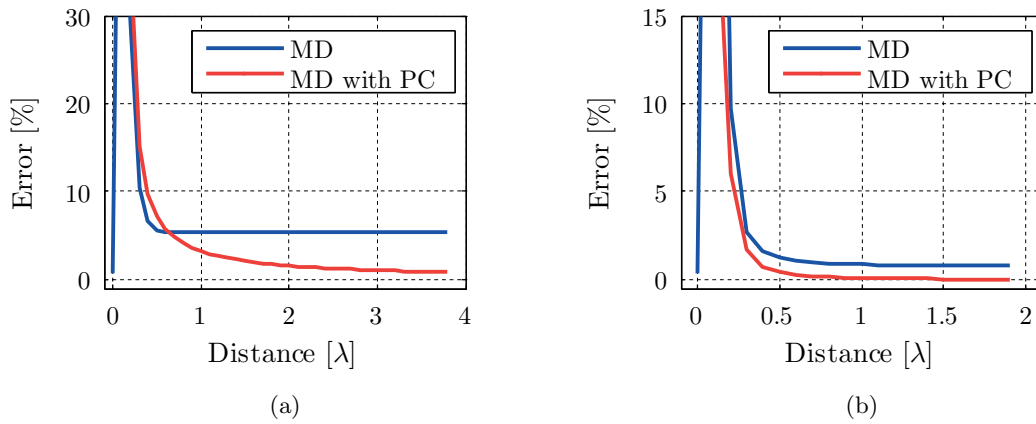


**Figure 5.34.:** Cross configuration: error on the MDI matrix, with and without Phase Correction: (a), x-oriented strip and (b), y-oriented strip.

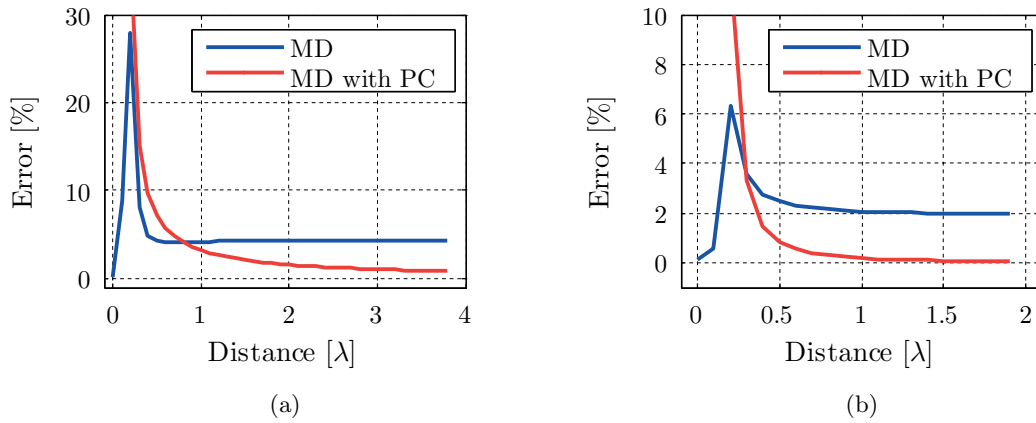


**Figure 5.35.:** Double Star configuration: error on the MDI matrix, with and without Phase Correction: (a), x-oriented strip and (b), y-oriented strip.

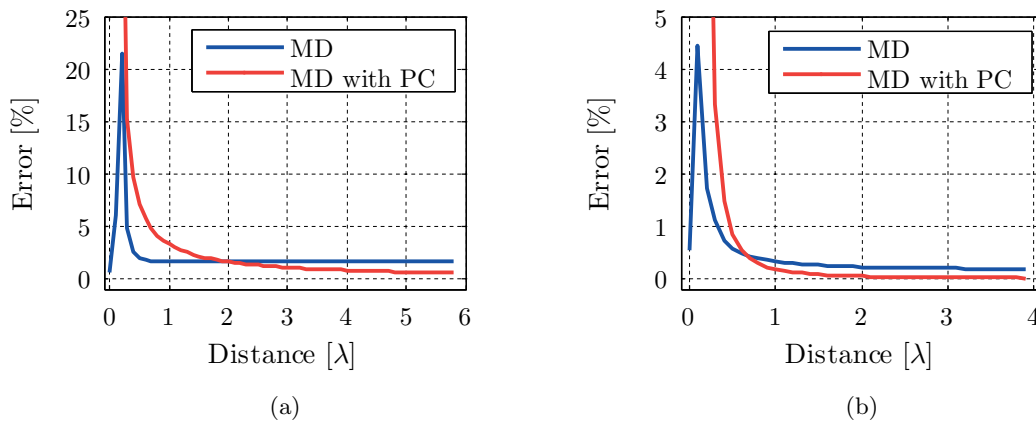


**Figure 5.36.:** Triple Star configuration: error on the MDI matrix, with and without Phase Correction: (a), x-oriented strip and (b), y-oriented strip.

### 5.6.7. Application to small cells

The Magic Distance Inspired method was applied in the previous sections to benchmark geometries which were meshed with cells of size in the order of  $\lambda/10$ , which is a standard value in most discretizations. With regards to such a mesh, it was shown which point scheme offered the best compromise between accuracy and computational speed. The obtained results hold in general for a wide range of cell sizes, but a special remark must be made when particularly small cells are used to mesh the geometry.

When the size of the cells drops below  $\lambda/20$ , the accuracy achieved even with the point scheme which was indicated as the best performing (Star-observation, Cross-source configuration,  $4 \times 4$  points, Fig. 5.31) suffers a significant degradation.

All the theoretical discussion on which the Magic Distance Inspired method is based is not invalidated, and in fact not even affected, by the electrical size of the integration domain and remains perfectly effective for any mesh used. On the contrary, the reason of this phenomenon lies in the fact that when cells are smaller, the interaction between them is stronger and the weights of the associated entries in the MoM matrix is higher. Those entries, which in the case of a regular mesh were not included in the cost function as their influence on the MoM matrix was negligible (and thus the error committed on them was affordable), assume with a finer mesh a major computational role and require to be treated together with the near and adjacent terms. Not controlling those terms results in general in a strong degradation of the accuracy of the solution.

The increase of the number of influent entries translates in a higher number of conditions to be satisfied through the minimization of the cost function; this calls immediately for a higher number of degrees of freedom, introduced using grids with an increased number of points. Also, from another point of view, the degree of accuracy achieved with previous point schemes is not high enough to produce correct results for small cells.

An interesting solution, which we found to produce very accurate results up to mesh cells of size  $\lambda/40$ , and also maintaining a reasonable precision up to cells one half of that size, envisages the use of the triple star configuration, shown in Fig. 5.27, for the observation points and the “Cross” for the source points.

The accuracy improvement can be observed by solving a problem similar to the benchmark used so far, where the size of the square plate is reduced to  $5 \times 5$  cm for a cell size of  $0.5$  cm =  $\lambda/30$ . When employing the Triple Star point-grid introduced in Par. 5.6.4, an error level which was shown to produce good results generates instead a meaningless solution. The new point grid produces on the other hand a highly accurate matrix, as shown in Fig. 5.37, with a peak error below 5%; the surface current is now correctly predicted, as shown in Fig. 5.38. Even if the increased accuracy comes at the price of a higher number of calculations ( $12 \times 4 = 48$  computations per term) the comparison with the Gauss-Legendre algorithm is still in favor of MDI: using 5 points in GL requires a much higher number ( $5^4 = 625$ ) of computations and yet produces rather inaccurate results.

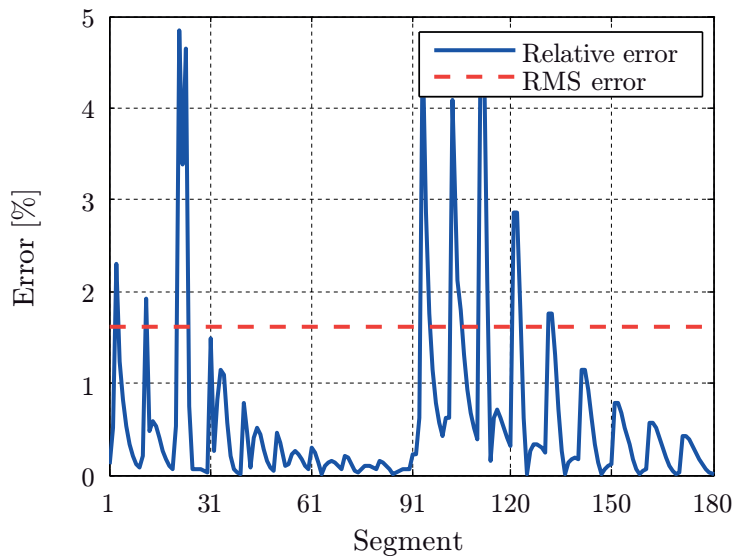


**Figure 5.37.:** Error on the MoM matrix obtained with the  $12 \times 4$  point grid.

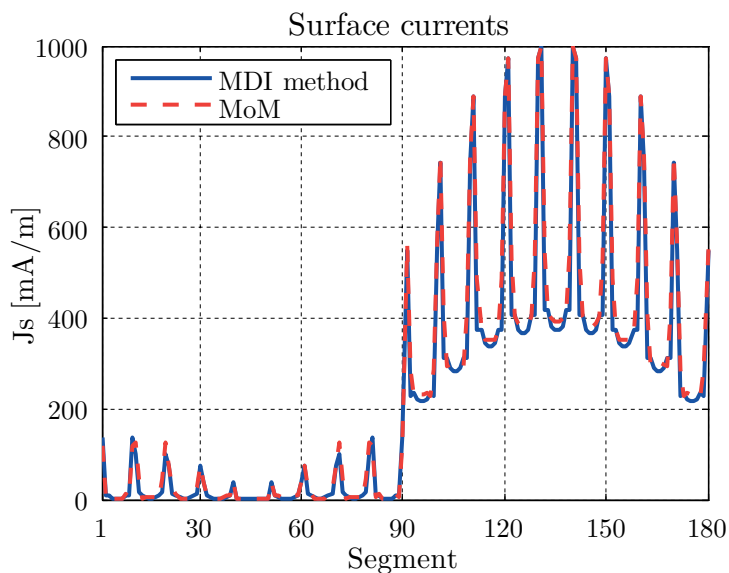


**Figure 5.38.:** Solution of the benchmark problem (surface current on the patch) when the cell size is  $\lambda/20$ . Results obtained with the  $12 \times 4$  point grid.

## 5.7. Summary of the full-wave benchmarks

The performance of the different point-schemes illustrated in this section are resumed in Tab. 5.3.

**Table 5.3.:** Performance of the different MDI point schemes when solving the benchmark problem.

Scheme	Weights	Points	Peak	RMS Error %		Acceleration (*)
			Error %	Direct	Inverse	
Cross	Opt	4	> 120	20	> 100	> 150
Line + Star	Fixed	6	> 45	10	~ 70	> 100
Double Star	Fixed	8	< 40	8	~ 50	~ 80
Double Star	Opt	8	< 35	7.5	~ 40	~ 80
Triple Star	Opt	12	< 30	< 6	~ 25	~ 50
Cross/Star	Fixed	4/4	< 15	< 5	~ 20	~ 40
Triple Star/Cross	Opt	12/4	< 5	< 2	~ 12	~ 13

(\*) Acceleration represents the ratio between the number of evaluation points required when solving the 4D integral with a 5 points GL quadrature ( $5^4 = 625$ ) and the number of points used in MDI.

## 5.8. Conclusions

In this chapter, the concept of “Magic Distance” has been introduced, with the goal of providing a fast and simplified MoM implementation that can be used as improved input for the SatAF software.

The Magic Distance concept bridges the gap between two strategies currently used to discretize integrals equations: point-matching and Nyström . In its simplified form, the magic distance is just the source-observer distance producing, for the self (diagonal) term, the same result as the full Galerkin interaction between a basis and a test function. Therefore, the use of Magic Distance guarantees to obtain an exact value for the self-terms in the diagonal of the MoM matrix. Of course, due to evident physical arguments, replacing basis and test functions by single source and observer points should provide also results that are asymptotically exact when the distance between basis and test functions increase. Therefore, good results should be expected from a crude and simple application of Magic Distance concept and this is the case in electrostatic problems. Although precisions will ultimately



depend on shapes and geometries, some representative benchmark cases show that an average accuracy above 93 % for the surface charge density is possible in electrostatic problems.

For even better results, it is necessary to control also the accuracy obtained when computing the near-diagonal MoM matrix elements. This is easily generalized by introducing multi-point schemes with points arranged in crosses, stars and weights attributed to each point. This leads to the so-called Magic Distance Inspired (MDI) algorithms where the involved source-observer distances are fine-tuned by numerical optimization. For instance an electrostatic MDI algorithm can provide a mean error in the charge distribution lower than 1% with only 8 points.

The situation is more critical in full-wave formulations, due to a series of factors mentioned during the chapter:

- stronger singularities,
- vectorial character of sources and fields,
- need to use sources like dipoles whose fields have an angular dependency,
- worse condition number in MoM matrix.

However, it has been possible through extensive optimization and testing to end up with some very efficient schemas like “Triple Star”, using 12 points and providing an average error of 6% in the RMS values of the surface currents.

This is reasonable when these currents must be used to compute near field quantities like input impedances and surely more than enough to compute the far field quantities which are the goal of this thesis.



## 6. Improved SatAF-MDI results

In the previous chapters, we have illustrated different methods to accelerate the generation of the MoM interaction matrix for the solution of electromagnetic scattering problems. As the main theme of this thesis work is the analysis of radiating structures like those involved in the MAST project, special attention has been paid to the class of problems involving metallic bodies in free space excited by arrays of slot antennas.

The original contributions of this thesis work, i.e. the MATLAB tool SatAF, the excitation model for slot antennas and the Magic Distance Inspired method can be finally combined into a complete, stand-alone simulation software for the efficient analysis of antenna systems allocated on small platforms.

In this chapter, we first resume in a final comparison the performance of the different methods which were discussed as approximation of the canonical MoM, showing that MDI actually offers the best compromise between acceleration, accuracy and range of applicability.

Secondly, the consistency of the proposed method will finally be proved by analyzing a realistic antenna system inspired by the slot array allocated on the cubic platform designed for MAST.

### 6.1. Final comparison of accelerated formulations of the MoM

In this section we compare the performance of the different numerical methods discussed in the previous chapters:

- EFIE solved with MoM, Galerkin formulation (EFIE 4D)
- EFIE solved with MoM, Surface Test (EFIE 2D)
- MPIE solved with MoM, Surface Test (MPIE 2D)
- Magic Distance Inspired method (MDI)
- Magic Distance Inspired method with Phase Correction (MDIpc)

For the MD method, the 8 point grid “Double Star” has been used, with weights included in the optimization process. More details about this point scheme can be found in Par. 5.6.4. The accuracy in the representation of the MoM interaction matrix is adopted as figure of

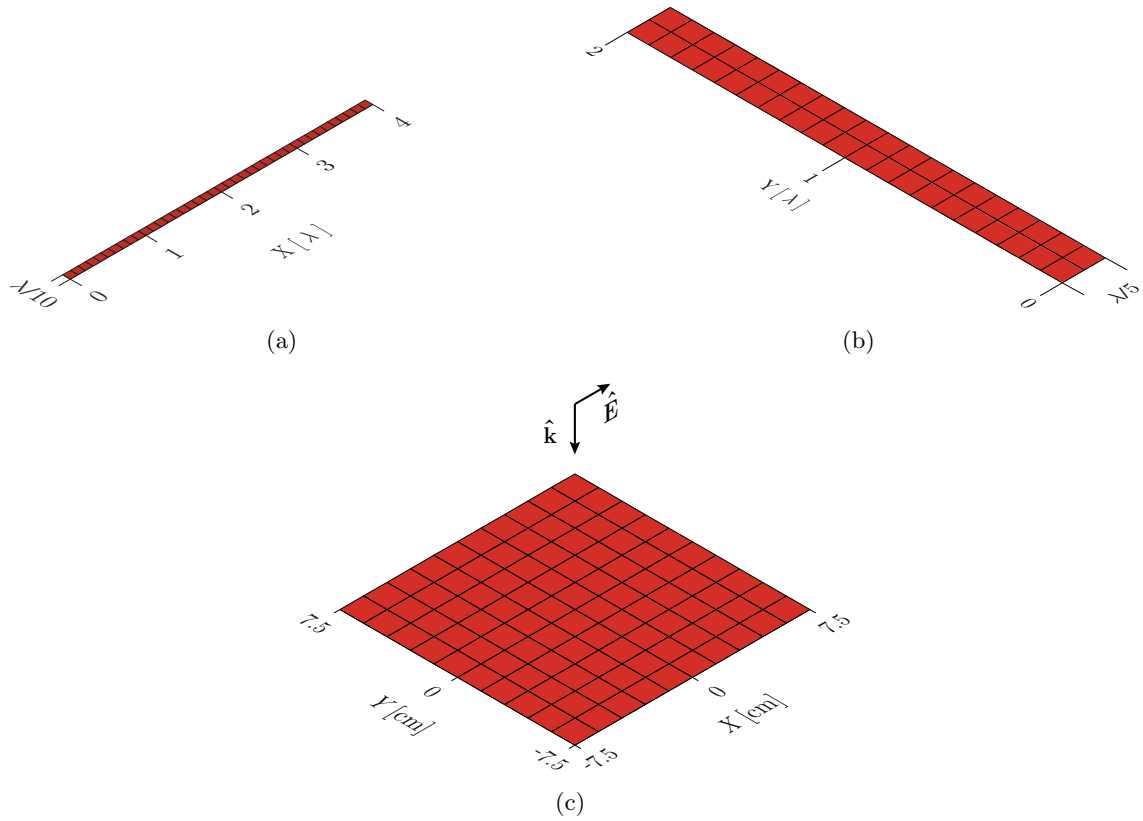


**Figure 6.1.:** Layout of the test cases: (a) y-oriented strip, (b) x-oriented strip, (c) square patch.

merit; the canonical implementation of MPIE with 4D integration of each reaction term of the matrix (Galerkin formulation) is taken as reference. For a comprehensive comparison between the methods, three geometries have been used as test cases:

- A two wavelengths long y-oriented strip, meshed with  $40 \times 1$  cells
- A four wavelengths long x-oriented strip, meshed with  $2 \times 40$  cells
- A square patch of size  $1.5 \times 1.5\lambda$  meshed with  $15 \times 15$  cells

The geometries are sketched in Fig. 6.1.

### **$2\lambda$ y-oriented strip**

The result of the comparison is illustrated in Fig. 6.2. The 4D EFIE is in perfect agreement with the reference, but comes at the price of the cumbersome 4D integration. The situation is mitigated in the case of EFIE with surface test; anyway, none of the two formulations allow the computation of self- and near-terms, a limitation restated several times in this thesis. Similar considerations hold for the EFIE formulated with Surface Test: if the loss in

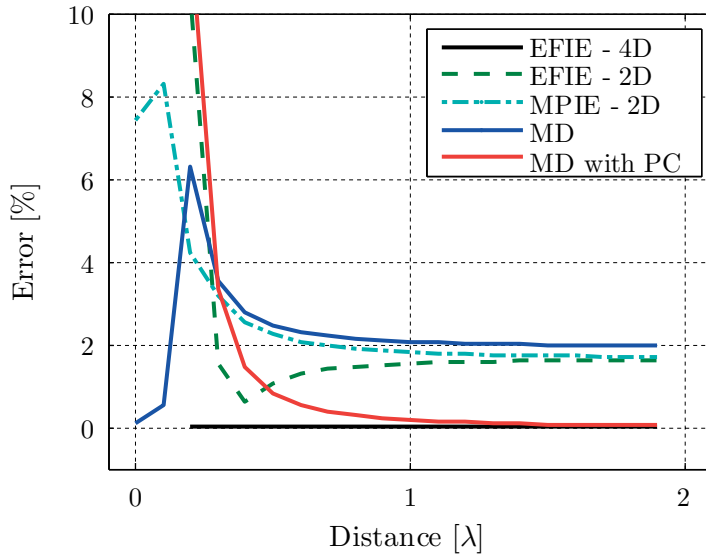


**Figure 6.2.:** The y-oriented strip, error with respect to the MoM matrix.

accuracy is definitely convenient thanks to the reduction of the computational cost, the issue concerning the computation of singular terms (and the significant error affecting quasi-singular terms) weight negatively on the overall performance.

The 2D implementation of MPIE appears as an interesting solution. It allows the computation of all the matrix entries, it introduces only moderate error which, at least on the far-field terms, could be strongly reduced by introducing the Phase Correction. On the other hand, it is true that the same reduction could not be operated on the self term.

The Magic Distance Inspired method offers a very good accuracy, especially in the computation of the self- and near-terms, allows the computation of the whole matrix and outperforms the other methods in terms of computational time. When combined with the Phase Correction for the computation of far field terms, its accuracy is excellent.

#### $4\lambda$ x-oriented strip

A non-trivial example, this second test case highlights unexpected behaviors of the methods (Fig. 6.3). Concerning the two EFIE version, the same considerations made for the y-strip are valid.

The 2D MPIE on the other hand exhibits a very strong divergence from the reference when terms become widely spaced. This surprisingly behavior is motivated by the following observation: the reduction of the source integral to one point does not introduces a dramatic error in the vector and scalar components of a matrix entry, on the contrary the accuracy is

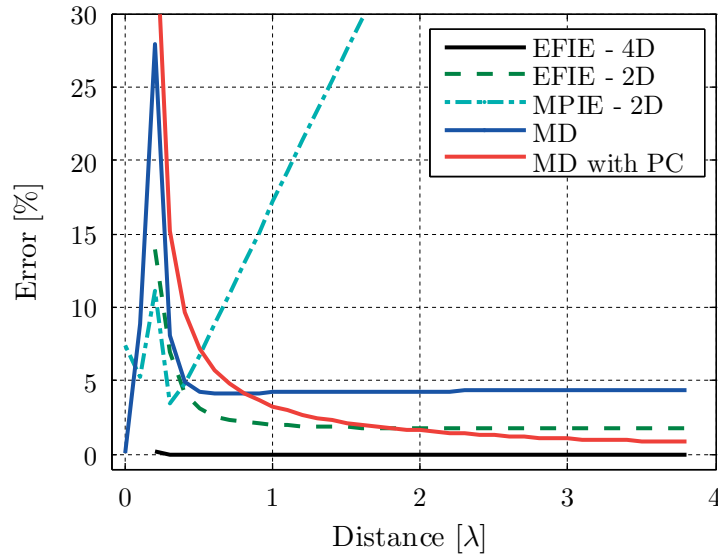


**Figure 6.3.:** The x-oriented strip, error with respect to the MoM matrix.

quite good (error in the order of 5%, as in the y-strip case). Unfortunately, when combining the two components, in the cases where these have similar magnitude (which happens when the cells are in the far field) and opposite phase the result suffers a strong inaccuracy. This phenomenon is well highlighted in the case of the long, x-oriented strip; in the y-oriented one, the particular geometry makes the scalar potential contribution to be identically zero by symmetry and therefore the final error is the one of the vector potential part, which is actually low. It is clear that such an erratic behavior prevents the use of this technique for generic problems.

The Magic Distance Inspired method confirms instead the expectations; the peak error was proved to be acceptable for a good accuracy in the solution and again the Phase Correction rectifies the far field terms for an asymptotically zero error.

### The square patch

In this last example we compare the two most interesting methods, the 2D MPIE and the MDI with Phase Correction, in the more realistic case of a metallic patch. Fig. 6.4 illustrates the result of the comparison. The Magic Distance method outperforms the MoM in almost every matrix entry: when cells are parallel, the 2D MPIE suffers the divergence highlighted in the x-strip case; on the other hand, the only flaw affecting MD concerns the few entries already identified as minor contributors to the accuracy of the solution. MD establishes itself as most performing solution specially with regard to the computational time, with 12 computation per integral against the 100 required for the 2D MoM (Gauss-Legendre algorithm with 10 points).

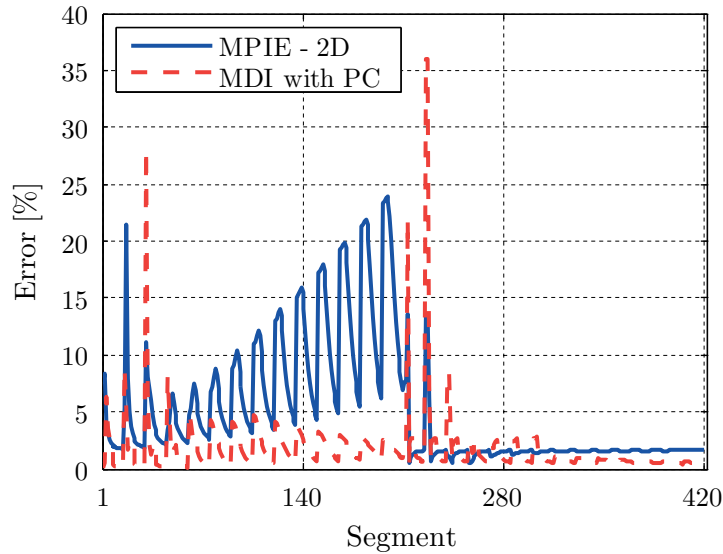


**Figure 6.4.:** The square patch, error with respect to the MoM matrix.

## 6.2. The MDI method applied to MAST

The canonical Galerkin implementation of the Method of Moments was used in Sec. 4.2.1 to solve a series of test configurations involving non-canonical shaped aperture antennas, either in stand-alone geometries or forming antenna systems on small metallic platforms. In particular, one of the tests concerned an array of 48 slot antennas arranged in a configuration similar to the MAST antenna system, while the final comparison was made directly on the measurements of the MAST architecture.

When the benchmark campaign involved an array, the MoM was used to solve a single element of the array in a localized region, often a ground plane representing a face of the platform. The computed radiated fields were then imported in SatAF which performed the necessary treatment to generate, through Array Theory, the complete radiation pattern. The slots were excited in all the cases using the original model introduced in Sec. 4.2.

The combination of SatAF and MoM proved to generate accurate and reliable results through all the benchmark campaign in Sec. 4.2.1, offering an increased computational speed thanks to the reduction of the model used for the full-wave simulation.

As final development of the SatAF based method and for a further reduction of the computational effort, we replace the calculation of the 4D integrals of the MoM interaction matrix with the Magic Distance Inspired method, according to the considerations discussed in Chap. 5.

With the validation illustrated in this section, we demonstrate the solidity of the combination of SatAF and MDI.

### Double-C slot

Following the same thread as in the validation of the classical MoM, we address at first a problem involving a single slot of non standard geometry: the first slot model designed for MAST. The slot lies on a small ground plane of 10 cm side and the excitation is located in the center of the aperture. Note that the excitation, originally a microstrip with a “T” shaped termination, has been modeled using the charge accumulation method described in Sec. 4.2. The current distribution is compared as usual with a complete full-wave software (here HFSS) and is illustrated in Fig. 6.5: the current accumulation around the slot curves suggests a correct representation of the electromagnetic phenomenon. The consistency of the predictions is also endorsed by the comparison of the radiation patterns in the three principal planes  $\varphi = 0, 45, 90$  degrees, as in Fig. 6.6. Even if a slightly higher deviation is observed with respect to the predictions produced with MoM, the agreement is very good, with a maximum deviation of 1.07 dB observed on the plane  $\varphi = 0$  and an average deviation below 0.5 dB.

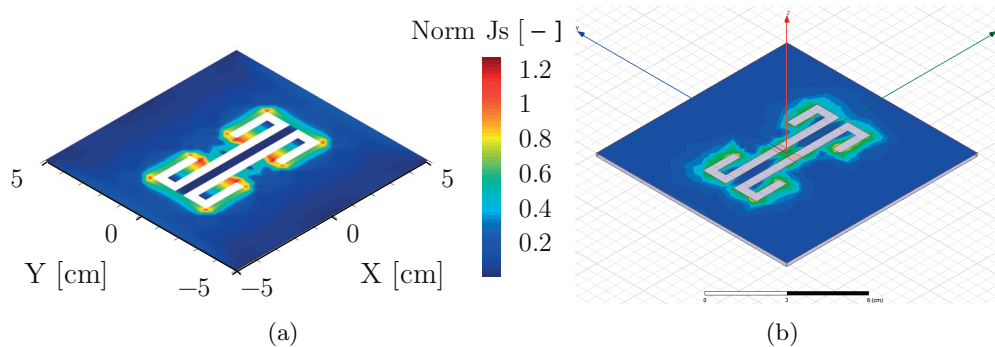


**Figure 6.5.:** Double-C slot, surface current on the ground plane: (a) MDI, (b) HFSS.

### MAST antenna system

The final benchmark is the realized MAST antenna system. The single MAST slot antenna was first solved with MDI and the computed radiated fields were imported in SatAF to generate the radiation pattern of the MAST array. In order to model the aperture with its real dimensions, the mesh has been refined to cells of size 2 mm. Such a small cell size required the use of the most accurate MDI point grid (Par. 5.6.7).

The radiation pattern computed with SatAF (*SatAF + MDI*) is shown in comparison with the field already computed in Sec. 4.2.1 with the *SatAF + MoM* combination and with the measurements performed on the MAST POC in Fig. 6.7 and Fig. 6.8 for the “R” and “RL” measurement cuts. A RMS error of 2.03 dB has been estimated on the “SatAF + MDI” predictions, only a few fractions of dB higher than the value of 1.95 dB one observed for the “SatAF + MoM” case.



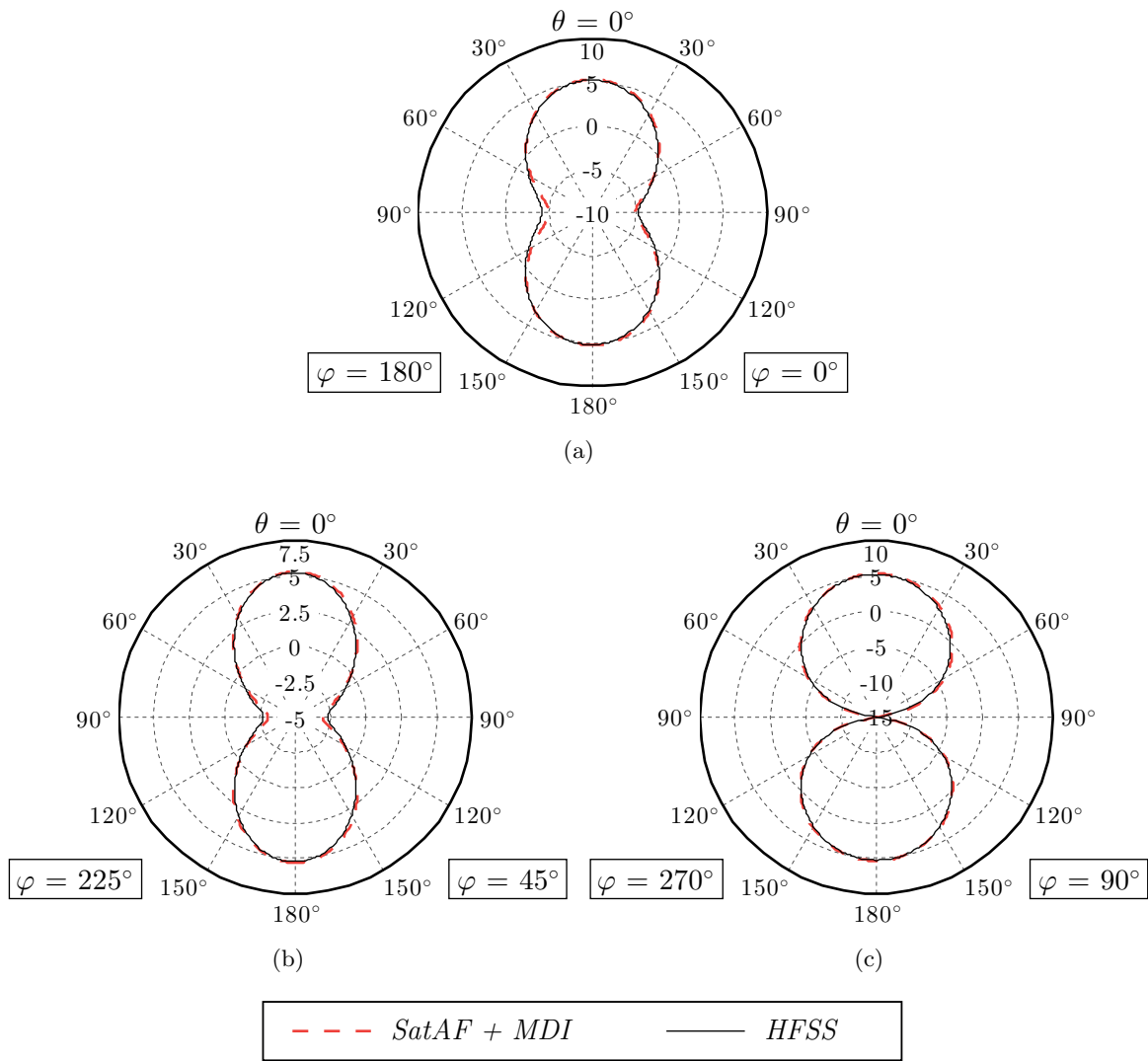


**Figure 6.6.:** Double-C slot, radiation patterns: (a)  $\varphi = 0^\circ$ , (b)  $\varphi = 45^\circ$  and (c)  $\varphi = 90^\circ$

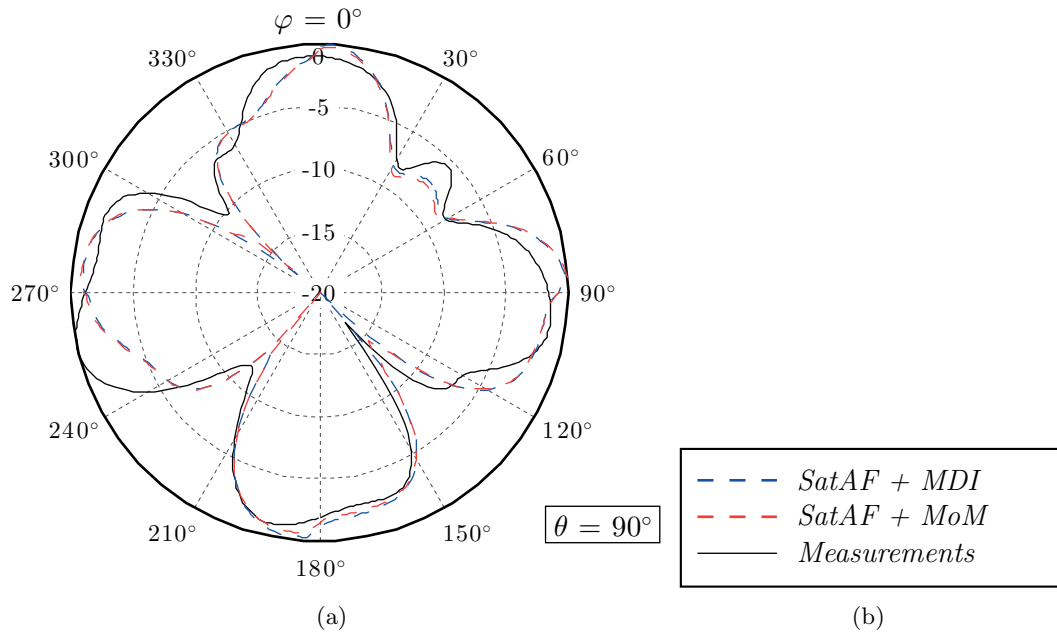


**Figure 6.7.:** MAST antenna system radiation pattern, comparison of MD with MoM and measurements on “R” plane.

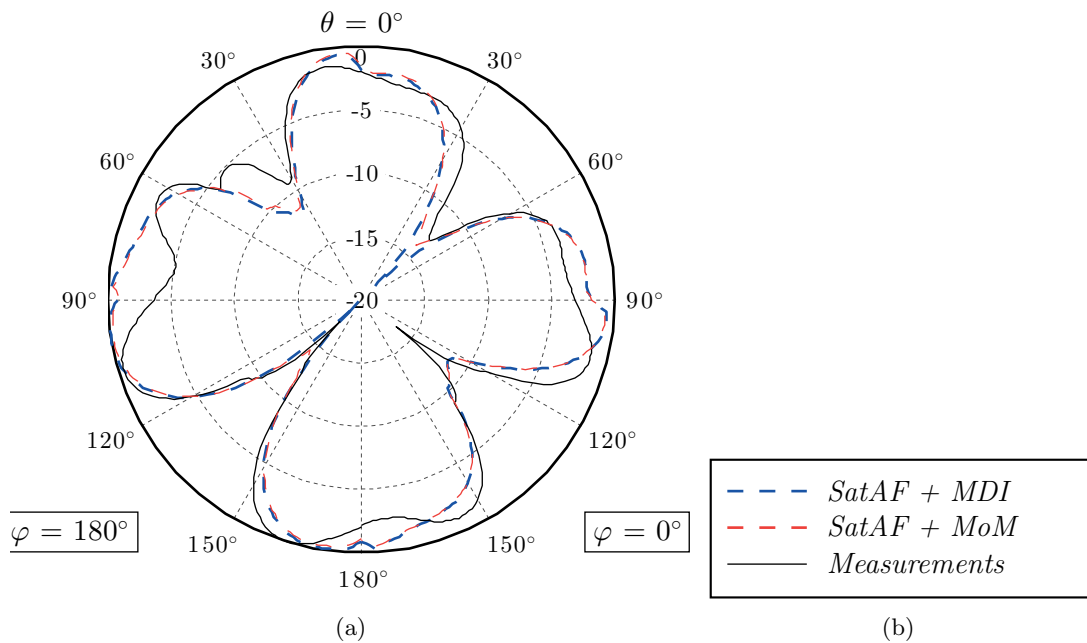


**Figure 6.8.:** MAST antenna system radiation pattern, comparison of MD with MoM and measurements on “RL” plane.





## 7. Conclusions and Perspectives

The last decade has been characterized by a growing interest on small spacecrafts. Constellations of micro/nano satellites are recognized as an efficient solution for short missions involving image acquisition, support and survey of maritime or automotive traffic (AIS and GPS) and telecommunication. In typical scenarios, multi-functional antenna systems composed by arrays of elementary sources are employed for data transmission and inter-satellite communication. The integration of radiators with the satellite platform is a critical issue critically affecting the performance of the antenna system and in particular its radiation pattern. Further challenges are posed by the stringent accommodation requirements and by the size of the spacecraft; when this size becomes comparable with the wavelength, the coupling of the platform with the radiated fields becomes severe and cannot be ignored.

Despite the great academic and industrial interest of this subject, no systematic methodology has been developed and the design of satellite antenna systems producing specific radiation patterns remains a challenge and a subject of intense research and study.

The ESA project MAST, requiring the design of an antenna system generating three different radiation modes (omnidirectional, directive beam and TT&C mode) on a two-wavelengths platform, represents a typical example of design of an antenna system for a micro-satellite. Hence, it offered to our laboratory the possibility to develop a specific design strategy, which led to the implementation of an in-house design software.

Inspired by MAST, we have developed the MATLAB simulation software SatAF, tailored for the analysis and design of antenna systems allocated on small spacecrafts. Targeting the accurate prediction of the radiation performance with reduced computational requirements with respect to all-purpose commercial software, SatAF allows a modular approach to the problem of arrays of identical radiators spatially distributed on (or around) the satellite body. According to the characteristics of a specific design, the user can set the trade-off between accuracy and speed first by identifying a subset of radiators and a part of the geometry to include in the simulation model, then by selecting the model used to solve the structure. Three options are considered for this model:

- A **mathematical approximation** of the radiating element, based on neglecting the effects of the interaction between radiators and the platform. This solution allows the maximum reduction of the simulation time and proved to be useful at least for a first approach to the problem.

- A canonical implementation of the **Method of Moments** in the MPIE - Galerkin formulation. This solution allows the highest accuracy, comparable with any existing commercial software, but with no advantage in terms of speed.
- The **Magic Distance Inspired (MDI)** method. In this original formulation of the EFIE MoM, the evaluation of the four fold integrals required to fill the interaction matrix is replaced with a point-to-point computation between reduced dimensions point grids, with a reduction in terms of performed calculations of at least one order of magnitude, only with a little price paid on the accuracy of the predictions.

The analysis of complex arrays constituted by replicas of the same element, typical of the design of antenna systems of small spacecrafts, can therefore be reduced to localized simulations involving a very reduced number of elements performed with any of the aforementioned methods.

The developed software has been extensively used during the design process of the MAST antenna system and its solidity has been demonstrated by the successful design and realization of a prototype showing a good agreement between the measures and the predictions. In addition, an exhaustive benchmark campaign, oriented to the validation of the implementation of the method and the hypotheses it is based on, has been accomplished.

## 7.1. Thesis assessment

The main achievements of this thesis can be identified in the following topics:

- The successful design of the MAST antenna system and the development of the simulation software SatAF
- The formulation of a novel, simplified excitation model for slot antennas integrated in a canonical implementation of MPIE Galerkin MoM
- The implementation of a set of original formulations of the Method of Moments, inspired by the Nyström method and called the “Magic Distance Inspired” methods. These original achievements are now summarized here below.

### **The MAST antenna system and the SatAF software**

The work performed in the frame of MAST produced a two-fold achievement.

On the side of technological design and realization, an antenna system capable of generating three antenna modes was designed, built and measured, with a positive result in terms of fulfillment of ESA specifications. In particular, the most challenging omnidirectional mode has been obtained, tackling the problem of platform interference thanks to the successful strategy adopted. The final antenna system is composed of an array of customized double dog-bone slot antennas.

In parallel, we implemented in the MATLAB tool SatAF the adopted design strategy,

consisting in the simplification of the antennas radiation mechanism to an equivalent source. The result, basically an implementation of a weighted 3D Array Factor, was a valuable tool for the fast prediction of the array radiation pattern, extensively used throughout the design and finally validated by the comparison with measurements.

### **The slot excitation model**

An implementation of SatAF with the Method of Moments was readily identified as a convenient possibility to extend the scope of the basic version of the software, remove its limitations and improve the accuracy.

Retaining the fundamental 3D array theory concept to reduce the simulation time, we introduced in SatAF the possibility of interfacing it with external software, used to analyze subsets of elements in a simplified geometry (replacing for instance the 3D platform with a finite size ground plane). The computed radiated fields can be finally imported in SatAF which provides the necessary manipulation to obtain the complete radiation pattern.

Targeting in particular the analysis of slot antennas, we developed a novel, simplified excitation model, fully compatible with the developed MoM framework, which allows through a charge accumulation mechanism the correct representation of typical feeding structures, e.g. coaxial cable or microstrip.

The solidity of the combination of SatAF with the MoM, using the developed slot excitation has been applied to the analysis of arrays of slot antennas and successfully validated against commercial software.

### **The Magic Distance Inspired (MDI) method**

EFIE works with physical quantities (currents, fields) and does not require the definition of potentials or charges. MPIE exhibits a milder ( $1/r$ ) singularity than EFIE ( $1/r^3$ ) and the evaluation of the self term is straightforward.

The MDI approach conciliates the two advantages, targeting the computation of the EFIE reaction matrix by replacing the computation of four fold integrals with an original formulation of the Nyström method, where the choice of point grids and weights aims to the approximation of the MoM self-terms.

A preliminary application of the method to electrostatic problems yields promising results, with accelerations of at least one order of magnitude (depending on the point grid used). A formal extension of MDI to the full-wave problem was found by analogy, using the concepts behind the calculation of self terms with a MPIE strategy.

MDI was successfully applied to the EFIE, one of the most remarkable results being a  $12 \times 1$  point grid which produces a very good accuracy reducing the number of computations by a factor of 50. A further enhancement of the method, the Phase Correction (PC) reduces the error on the entries of the MoM matrix related to cell couples spaced more than  $\lambda/2$ .

Together with PC, MDI is shown to perform better than other MoM formulations and is an excellent alternative to Galerkin.

The reliability of the method in its combination with SatAF has been finally assessed through the comparison of predictions relative to the MAST antenna system with the measurements of the satellite mock-up itself.

## 7.2. Perspectives

This thesis has shown the potentialities of an approach like the combination SatAF-MDI to replace brute force full-wave softwares. However, the developed MATLAB-based stand-alone software remains at a proof-of-concept level and has been tested essentially with the specific simple satellite platforms provided in the ESA project MAST.

So the obvious perspectives of this thesis should essentially aim at generalizing the SatAF-MDI, enlarging both its theoretical and practical scopes.

On the theoretical side, potential improvements in the full-wave problems call for a more rigorous treatment of the Magic Distance concept in EFIE formulations. The stronger singularities and the intrinsic angular dependence of the dyadic Green's function for the field require a more in-depth treatment, possibly leading to the replacement of the Magic Distance by an equivalent Magic Circle or contour. The various point-wise implementations, empirically demonstrated in this thesis would then be justified as discretizations of a theoretical result.

By the same token the applicability of the MDI algorithms to other meshes than rectangular or square (triangular, trapezoidal, curvilinear) should be rigorously proved, eventually computing theoretical values for the correction or shape factors to be introduced.

Finally, MDI has proven successful in approximating the fundamental EFIE unknown, which is the surface current density. Therefore no particular problem is expected when applying MDI schemes to the prediction of other near-field quantities like input impedances. However, an thorough and exhaustive benchmark campaign, eventually leading to further fine-tuning of the existing MDI algorithms would be needed.

From a more practical point of view, a proof of the applicability of SatAF-MDI to more complex antenna systems should be given. MDI should be tested in more complex environments like stratified media and with more complex radiators. The current benchmark (slot antennas in a all-metallic platform) should be generalized to more involved structures both in Space and ground applications. This would confirm the validity of the strategy developed in this thesis beyond a specific small satellite configuration and would pave the way to a complete new class of applications for SatAF-MDI.







# A. MAST antenna system technical details

In this appendix pre provide the exhaustive technical documentation about the design of the antenna system performed in the frame of the MAST project.

## A.1. Slot antennas designs

### Cavity-backed slot antennas

A back-cavity naturally allows canceling totally the problem of parasitic PPWG mode. Moreover, using specific cavity modes combined with the slot resonance allowed to achieve efficient resonant antennas using much thinner structures (a few millimeters), compared to the classical reflector solution which requires a quarter-wavelength thickness (around 35 mm in S-band). However, this type of antennas suffers from very limited bandwidth (a few percents) because they rely on strong resonances occurring in a small volume.

Further efforts were focused on designing an efficient, robust and well-performing radiating structure based on the slot aperture principle which reaches the target radiation properties with a reduced thickness. After many investigations on various configurations, we arrived at two potential candidates with slightly different properties which are described hereafter.

The first antenna design is shown in Fig. A.1. It consists of a slot antenna fed by a  $50\Omega$  T-shaped microstrip line and surrounded by vias to avoid the propagation of the unwanted PPWG mode. The structure can be seen as some sort of cavity-backed slot antenna, but where the vertical walls of the cavity are not completely closed, which seems to be more favorable in terms of bandwidth than completely closed cavities.

Except for the substrate used for the feed, the cavity is filled with air. The considered substrate for the feed is the space qualified Rogers RO4350B (details in Tab. A.1). The same substrate has been used in all the illustrated structures.

**Table A.1.:** RO4350B substrate parameters.

<b>Rogers RO4350B</b>	
Relative permittivity	$\varepsilon_r = 3.66$
Dielectric losses	$\tan \delta = 0.0037$

An open stub in parallel has been added in the feed line for matching purpose. The surface

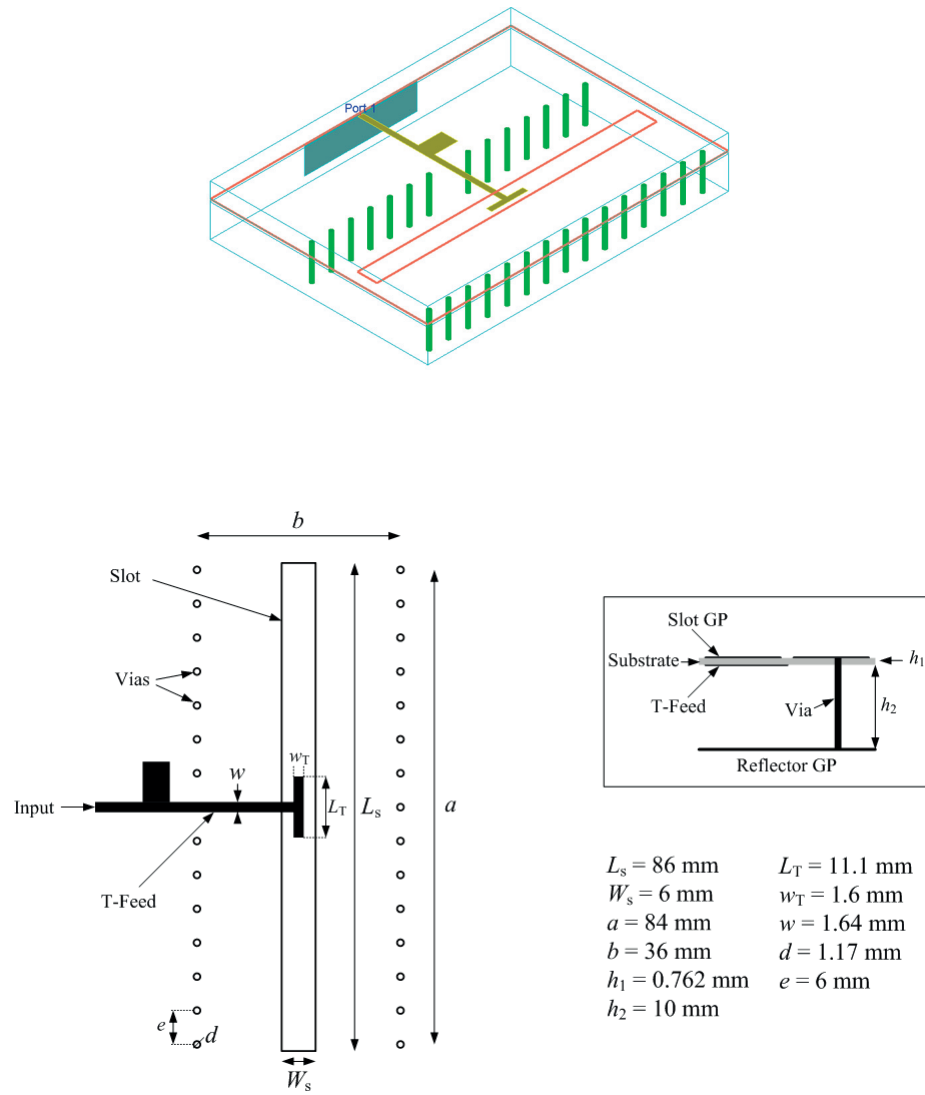
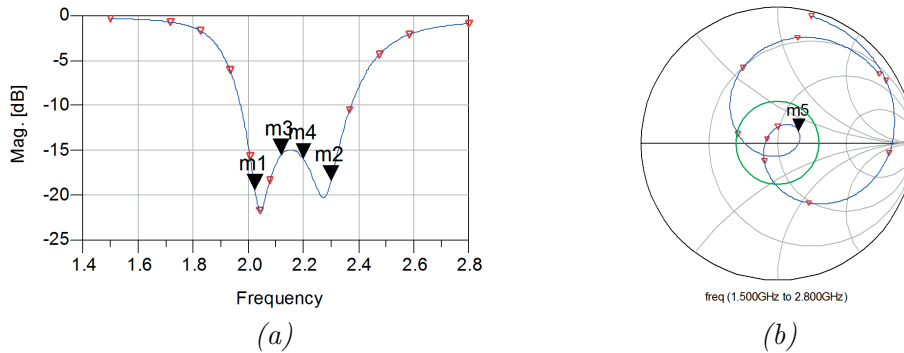


Figure A.1.: Description of the first antenna design.



**Figure A.2.:** Input reflection coefficient of the first antenna design. The markers m1 to m4 correspond to the limits of the two bands of interest. The marker m5 is at 2.16 GHz. The  $-10$  dB circle is shown in green in the Smith Chart.

occupied on the external side of the satellite wall is only the size of the slot, i.e.,  $86 \times 86$  mm. With the chosen feeding configuration, BFNs can be implemented on the same substrate in a seamless manner. After several fine tuning iterations, a trade-off could be achieved between the total thickness (around 10 mm), the efficiency, and the bandwidth.

The antenna has been simulated with Agilent ADS Momentum. In the simulation model, both ground planes are infinite. The radiation pattern is a typical slot pattern. The input reflection coefficient  $S_{11}$  of the antenna is shown in Fig. A.2. The antenna exhibits a 10 dB return loss bandwidth of 18%, and a 15 dB return loss bandwidth of 15%. Although two local minima can be seen on the  $S_{11}$  plot, the antenna supports a single resonance in this band, as confirmed by the inspection of the input impedance just at the slot edge (without the stub). This double minima behavior, which is beneficial for return loss bandwidth, is a matching effect introduced by the stub and the TL section between the latter and the slot.

The high efficiency observed confirm that the unwanted PPWG mode is efficiently eliminated. Indeed, in the simulation any power leakage through this mode is never radiated since the two ground planes are infinite, and would therefore contribute to decrease the radiation efficiency. It must be mentioned that the reported values of efficiency are rather optimistic because conductor losses cannot be taken into account around the slot, since the latter is represented in the simulation model by magnetic currents in an infinite perfect conductor. Nevertheless, a verification performed with the 3D full-wave software CST Microwave Studio gave an efficiency always higher than 85% while validating the general behavior of the proposed antenna.

This antenna presents very satisfactory performance, with a single drawback coming from its rather long size ( $L_s = 86$  mm), which can be a problem in an array configuration. In fact, the slot sees an effective permittivity of around 1.2, which means that its first half-wavelength resonance should occur at 1.6 GHz. However, it is known from the literature that a back-cavity, or equivalently vias with a reflector, tends to increase the resonance frequency of a slot antenna. This explains why the observed (half-wavelength) resonance is around 2.16 GHz.

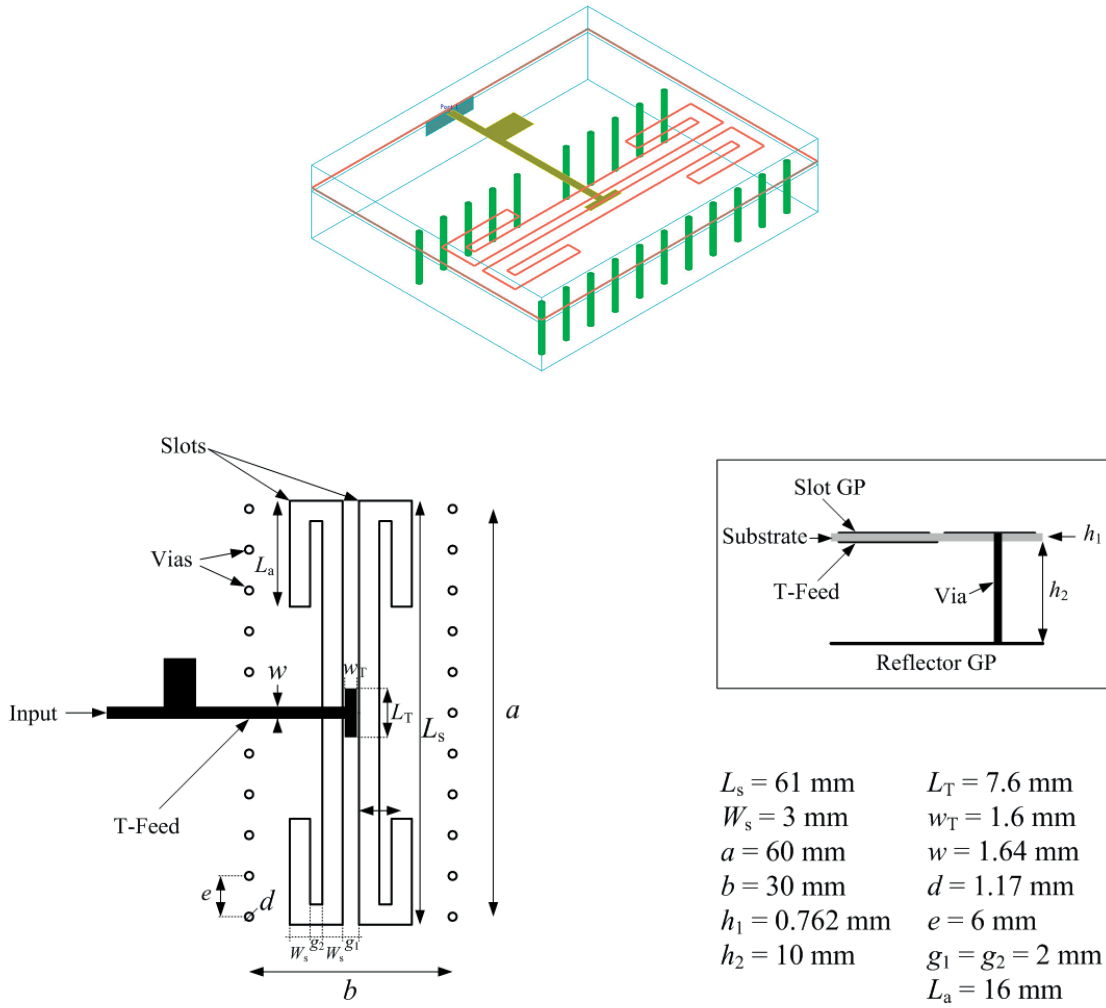


**Figure A.3.:** Description of the second antenna design.

A second slot antenna was designed with the goal of obtaining a more compact version of the first example and is shown in Fig. A.3. Compared with the first model, the slot has been separated in two thinner slots, and bent to decrease the occupied length. Now, the surface occupied on the external side of the satellite wall is  $18 \times 61 \text{ mm}$ . The dimensions of the via-cavity ( $a \times b$ ) has also been reduced in order to facilitate the combination of these elements to form arrays. The dimensions of the proposed antenna have been obtained after fine tuning of the geometry.

The antenna has been simulated in the same environment as the first example. Its input reflection coefficient  $S_{11}$  is shown in Fig. A.4. The antenna exhibits a 10 dB return loss bandwidth of 14%. The radiation pattern is a typical slot pattern. Some relevant parameters of the antenna at the four frequencies which delimit the two bands of interest are reported in

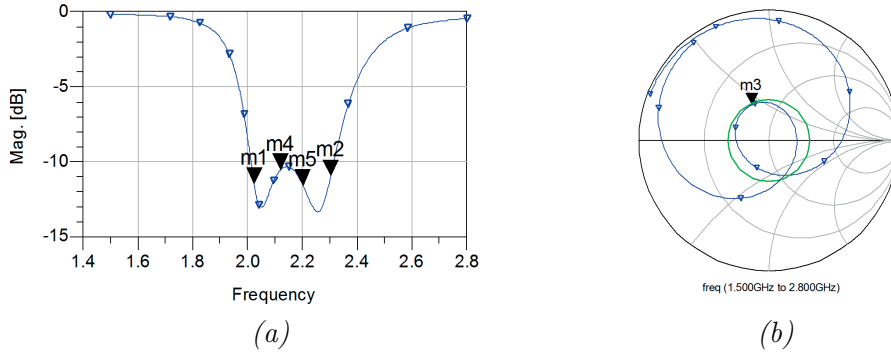


**Figure A.4.:** Input reflection coefficient of the first antenna design. The markers m1 to m4 correspond to the limits of the two bands of interest. The marker m5 is at 2.14 GHz. The  $-10$  dB circle is shown in green in the Smith Chart.

Tab. A.2. The comments made on the efficiency for the first antenna model also apply here. The return loss matching of this second antenna is not as good as for the first one, but its

**Table A.2.:** Performance of the first proposed antenna at the frequencies which delimit the bands of interest (markers m1 to m4 in Fig. A.2) ( $S_{11}$ : reflection coefficient,  $D$ : directivity,  $G$ : gain,  $\eta$ : efficiency,  $G_R$ : realized gain).

Freq [GHz]	$S_{11}$ [dB]	$D$ [dB]	$G$ [dB]	$\eta$ [%]	$G_R$ [dB]
2.025	-11.5	5.4	4.8	89	4.5
2.120	-10.5	5.3	5.3	100	4.9
2.200	-11.6	5.3	5.3	98	5.0
2.300	-10.9	5.4	5.1	94	4.7

total length is significantly lower (60 mm compared to 86 mm), which is more favorable for array configurations. For this reason, the second antenna was chosen for further investigations and, by introducing some small variations and by fine tuning, it was possible to re-design the element to achieve a better reflection loss results.

The layout of the final element is shown in Fig. A.5, while the measured input matching parameter is depicted in Fig. A.6. The structure of the new optimized element is the same as the previous one, with the differences that the number of vias has been halved, the air gap to the reflector has increased from 10 mm to 12 mm and the feeding line is matched at  $100\Omega$ , instead of  $50\Omega$ . On the other hand, the improvement on the performances of the measured element is rather satisfactory; keeping the  $S_{11}$  parameter practically below  $-14$  dB within the whole band of interest.

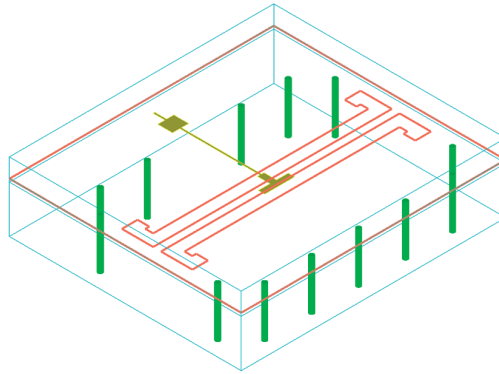


**Figure A.5.:** Layout of the final slot single element.

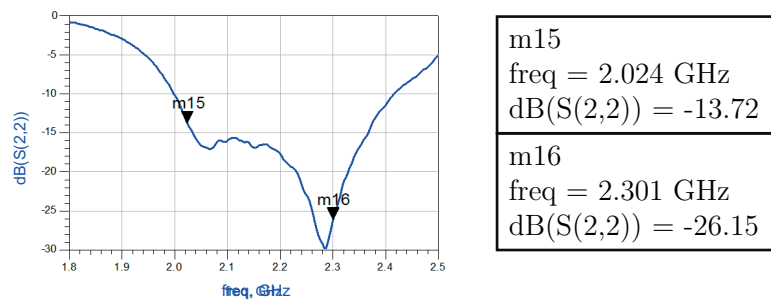


**Figure A.6.:** Input matching of the final slot single element.



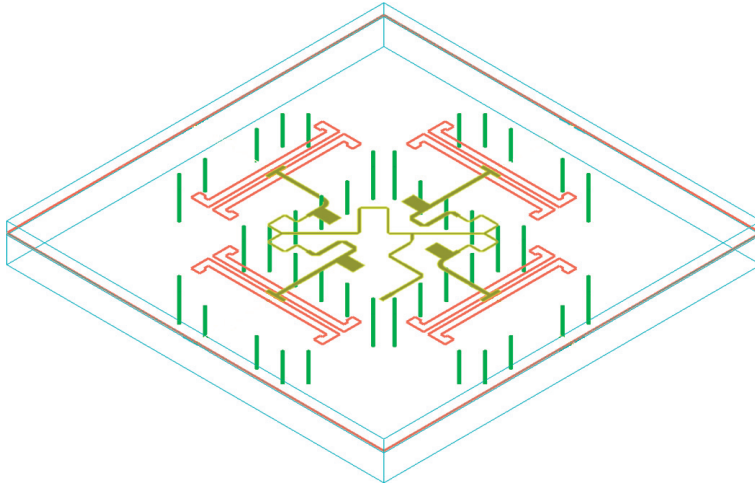


Figure A.7.: Layout of the face sub-array of four elements.

## A.2. Array design

The best performing solution is composed of only 4 of these radiating elements arranged in a  $2 \times 2$  squared configuration. It was found that the position which minimizes the low elevation radiation was obtained by spacing the elements 64 mm apart (almost  $\lambda/2$  in free space) and turning them on themselves such that they form a square. Furthermore, applying a sequential rotation to the linear elements provides the circularly polarized radiation pattern. When the sub-array is allocated on the face of a generic satellite wall of 250 mm by 250 mm (the smallest proposed size of a generic satellite), the toll taken is only 7% of the total surface of the satellite face, leaving significant free room for any other instrumental devices and/or solar panels.

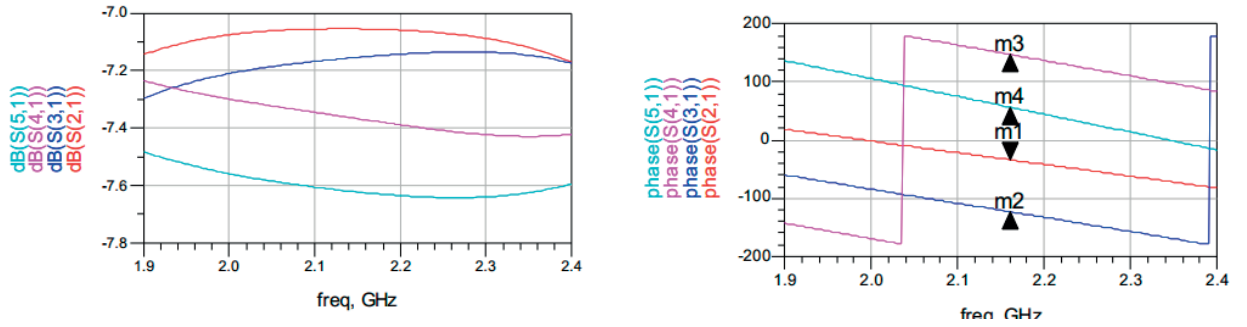
### The Beam Feeding Network

Since the elements of a given face need to be fed in a sequential rotation phase sequence, it was necessary to design a Beam Forming Network (BFN) to implement these phase delays. The layout of the sub-array, including the BFN, is shown in Fig. A.7.

The simulated insertion losses and phase shifts of the sole BFN are shown in Fig. A.8.

It can be observed that the input reflection coefficient  $S_{11}$  is below  $-30$  dB on the whole band of frequencies. On the other hand, the insertion losses associated with the feeding network are estimated around 1.5 dB. It can also be seen that the required phase shifts for sequential rotation feeding have been achieved.

It is remarkable that the whole BFN remains within the internal space between the radiating elements; thus, there is no need to make the antenna Printed Circuit Board (PCB) below the elements bigger than the size taken by the elements themselves. The input reflection coefficient for the face sub-array with its BFN is shown in Fig. A.9. Both frequency bands are covered with a maximum value of  $-12.3$  dB.



m1 freq = 2.160 GHz phase(S(2,1)) = -34.065	m2 ind Delta = 0.000 dep Delta = -89.476 Delta Mode ON	m3 ind Delta = 0.000 dep Delta = 270.798 Delta Mode ON	m4 ind Delta = 0.000 dep Delta = -90.916 Delta Mode ON
---	---	---	---

Figure A.8.: Insertion losses and phase shifts of the Mode A sub-array BFN.

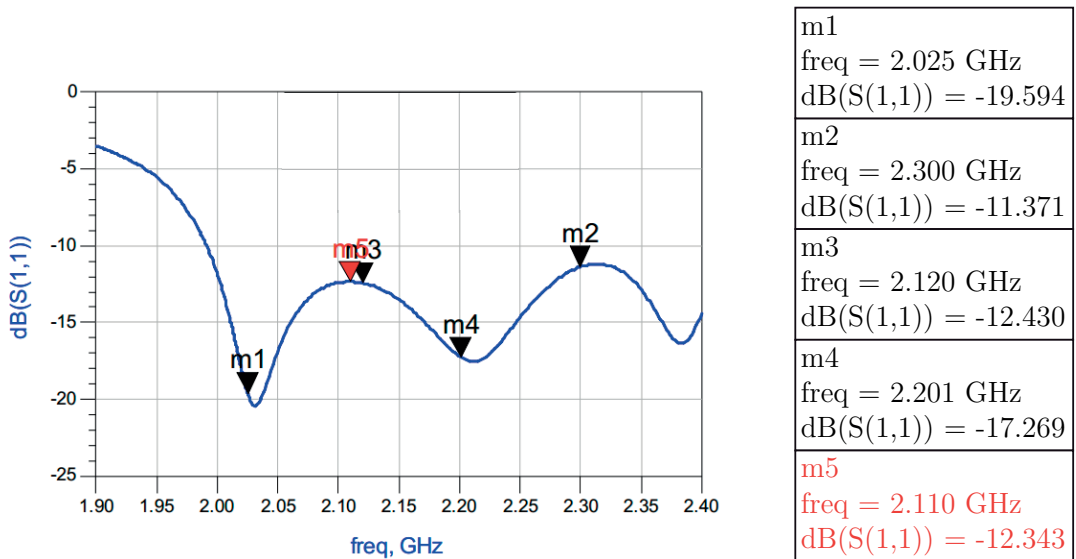
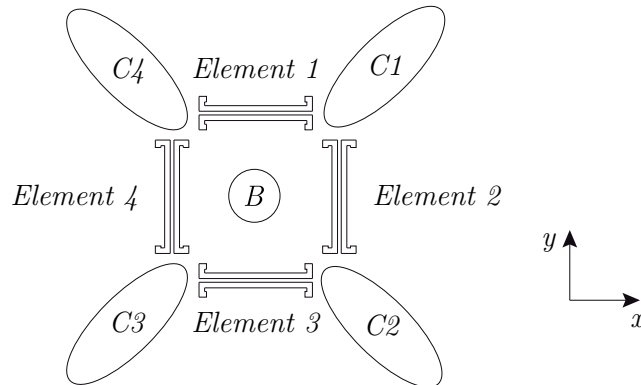


Figure A.9.: Reflection coefficient of the 4-elements sub-array including the BFN.



**Figure A.10.:** Sub-array used for Mode C: formalism used in Tab. A.3.

### A.3. Directive and TT&C modes

Mode B (directive beam) and C (TT&C lobes) specifications require respectively a single beam of 10 dBi minimum directivity and four lobes within a 60 deg cone. Circular polarization is also requested.

According to the design strategy discussed in Sec. 2.1, we succeeded in generating the Modes B and C simply re-using the same sub-array (face-element) designed for Mode A, for a maximum reduction of the occupation of the satellite surface.

The phase shifts required to generate the desired lobe in Right-Hand Circular Polarization were obtained using SatAF and are illustrated in Tab. A.3 (elements are named as in Fig. A.10).

The directivity for Beam 1 and Beam 3 on a 2D azimuthal cut at  $\phi = 45$  deg is shown in Fig.

**Table A.3.:** Input signal delay required for the lobes of Modes B and C.

	B	C1	C2	C3	C4
Element 1	0 deg	315 deg	45 deg	45 deg	315 deg
Element 2	90 deg	45 deg	45 deg	135 deg	135 deg
Element 3	180 deg	225 deg	135 deg	135 deg	225 deg
Element 4	270 deg	315 deg	315 deg	225 deg	225 deg

A.11. Both beams are within a 60 deg cone with their maximums pointing at  $\theta = \pm 15$  deg, respectively. Thus, the  $-3$  dB beam-width of each lobe is 30 deg as required. Moreover, the CP axial ratio is below 3 dB within the mentioned 60 deg cone. While Mode B feeding network is identical to the one used for Mode A, a dedicated BFN, implementing the phase delays necessary to tilt the beams, has been designed for Mode C. Two possibilities are

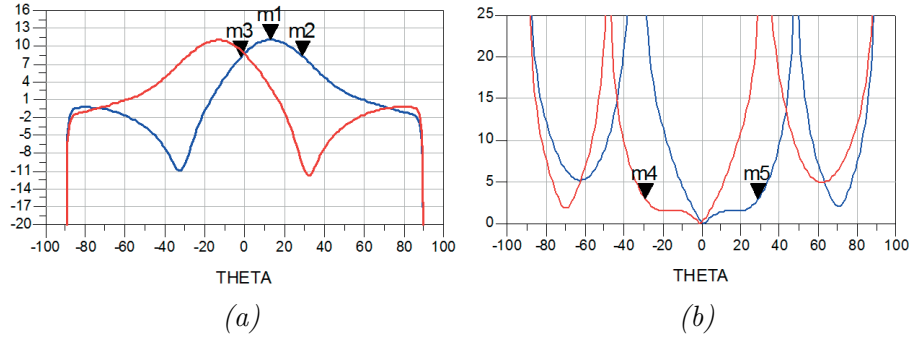


**Figure A.11.:** Mode C: (a) Directivity and (b) Axial Ratio of Beam 1 and Beam 3 ( $\phi = 45$  deg). Markers:  $m1, \theta = 13$  deg,  $D = 11.05$  dBi;  $m2, \theta = 30$  deg,  $D = 7.99$  dBi;  $m3, \theta = -1$  deg,  $D = 8.12$  dBi;  $m4, \theta = -30$  deg,  $AR_{cp} = 2.94$  dB;  $m5, \theta = 30$  deg,  $AR_{cp} = 2.98$  dB.

available for the design. The first consists in using four distinct BFNs, one for each beam. These four BFNs would be the same except for a mechanical rotation of 90 deg, and would be stacked in a multilayered circuit configuration. Switching at the element level would allow to connect each element to the desired BFN, and thus generate the four beams, one at a time. Such BFNs can be straightforwardly derived from the previous design presented for Modes A and B (see Fig. A.5) by simply adding the piece of line needed to achieve the  $\pm 45$  deg phase delays between the pairs of elements. The second strategy consists in designing a single BFN (in a single layer) with four inputs and four outputs. Each input fed independently would provide the required phase sequence as reported in Tab. A.3 to generate one of the beams.

The adopted solution is an intermediate case between the two aforementioned strategies. Indeed, it consists of two distinct BFNs, each one having two inputs to achieve two opposite tilted beams. A BFN is used to generate beams 1 and 3; a second identical BFN rotated of 90 deg and located in another layer generates beams 2 and 4. Switches are still required to connect each element to one BFN or the other. The layout of the BFN is shown in Fig. A.12, while the associated S-parameters are illustrated in Fig. A.13: return and insertion losses are acceptable, while the required phase shift for the two beams are correctly produced. It is worth noticing that the solution based on an hybrid coupler works only because the required phase shift between element pairs is equal to 90 deg. With a different phase shift, another coupler would be necessary, probably with a less good matching.

#### A.4. The Proof-Of-Concept

The complete antenna system consists of six faces sub-arrays illustrated in Fig. A.14a. For the generation of the omnidirectional mode, the elements are connected to a 6-to-1 Wilkinson power divider (Fig. A.14b). By using this type of divider, a similar matching between the face antenna sub-arrays is ensured, while minimizing the mutual coupling between them. The

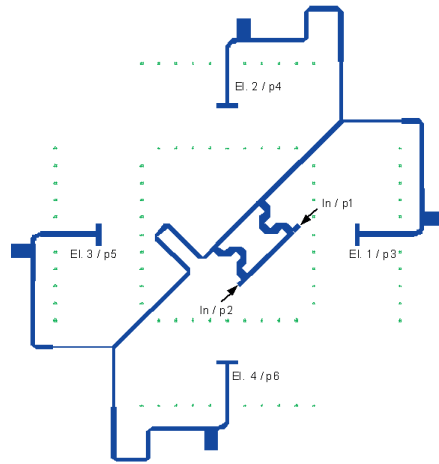


**Figure A.12.:** The Beam Forming Network used for Mode C.

single sub-array is also used to generate Mode B and, fed through a different BFN (Fig. A.14c), Mode C.

A complete view of the satellite is presented in Fig. A.14d.  $\ddot{i} > \grave{c}$

## A.5. Measurement setup

The three antenna modes generated by the POC were measured in EPFL-LEMA anechoic chamber. The setup is presented organized by antenna mode and measurements are shown and commented in the next section.

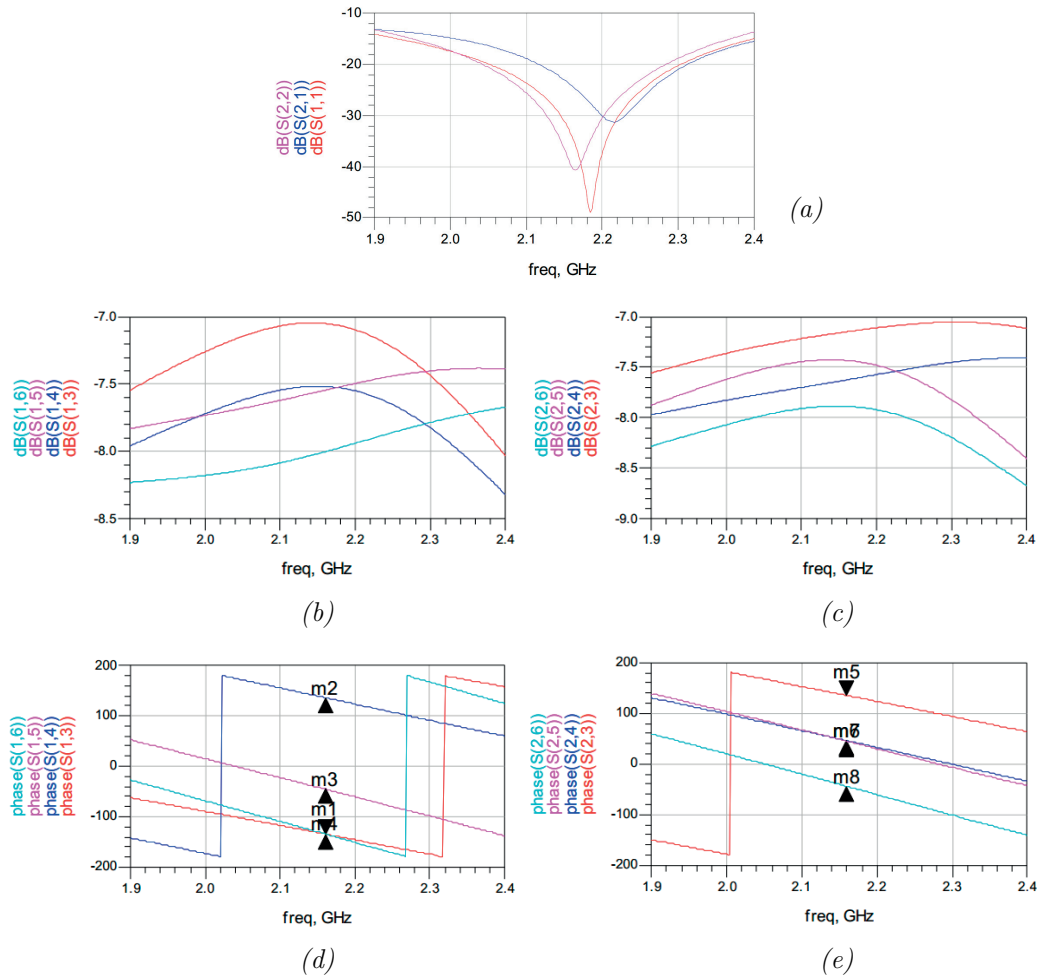
### Mode A

A total of five measurements were performed along three different cuts:

- Plane “R”: the satellite lies on a LHCP face (Fig. A.15a): the face sub-arrays on the four lateral faces are RHCP. The cut is along the azimuth plane.
- Plane “RL”: the satellite lies on a RHCP face (similar to Fig. A.15a) but the lateral faces sub-arrays are alternately R- and L-HCP polarized. The cut is along the azimuth plane.
- Plane “V”: the satellite is fixed to a platform by its vertex (Fig. A.15b). The cut is again along the azimuth plane and interests all the faces.

### Mode B

Mode B pattern is produced by one of the face sub-arrays of Mode A. Therefore, only one face sub-array of the POC, mounted on its satellite face, was measured in one of the two



m1 Freq = 2.160 GHz phase(S(1,3)) = 135	m2 ind Delta = 0.000 dep Delta = 270.866 Delta Mode ON
m3 ind Delta = 0.000 dep Delta = 89.192 Delta Mode ON	m4 ind Delta = 0.000 dep Delta = 0.113 Delta Mode ON

m5 Freq = 2.160 GHz phase(S(2,3)) = 134.5	m6 ind Delta = 0.000 dep Delta = -89.2 Delta Mode ON
m7 ind Delta = 0.000 dep Delta = -90.151 Delta Mode ON	m8 ind Delta = 0.000 dep Delta = -179.2 Delta Mode ON

**Figure A.13.:** Beam Forming Network used for Mode C: (a) input reflection and isolation, (b) and (c) insertion losses for the two input ports, (d) and (e), phase shifts. Port 1 (b,d) generates beam 1, port 2 (c,e) generates beam 3.

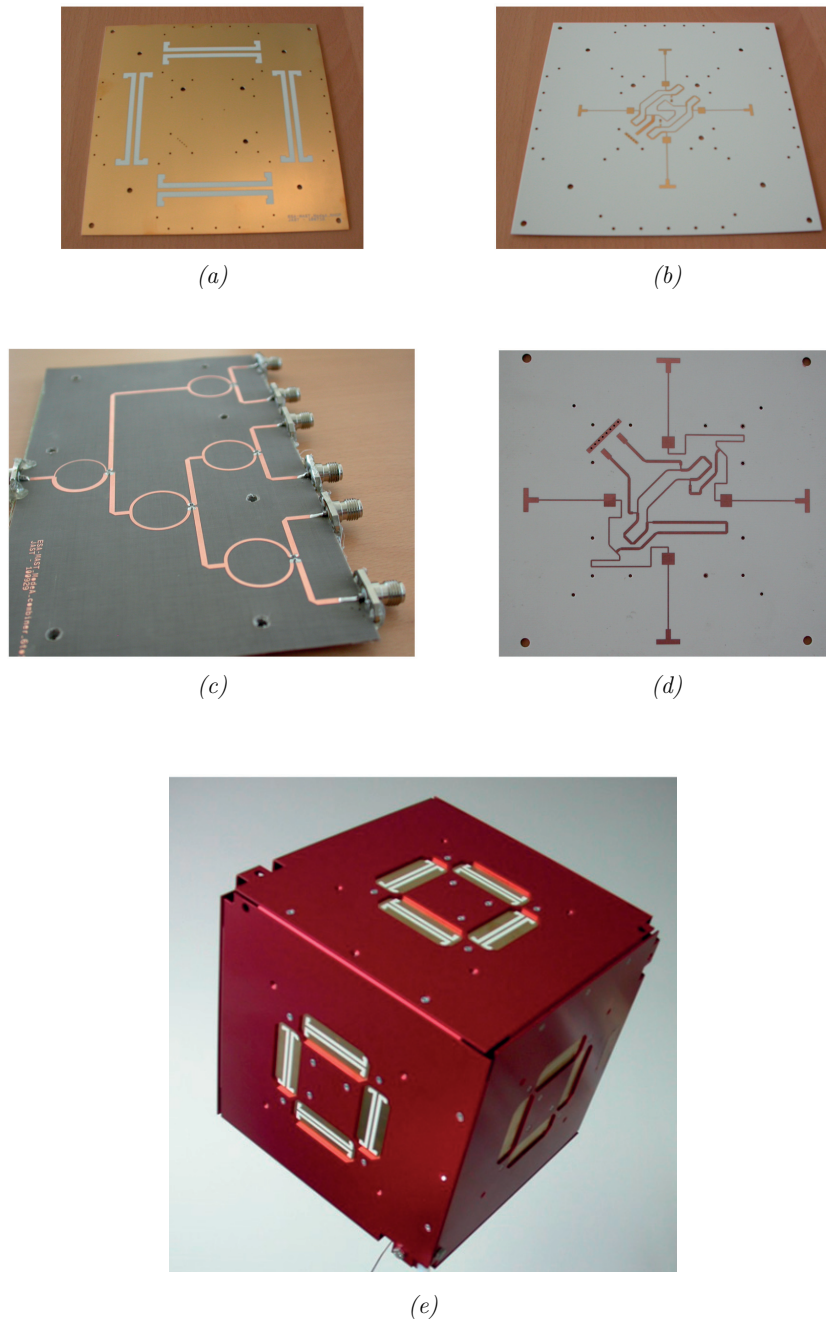


**Figure A.14.:** The realized components of the POC. (a), (b) top and bottom views of the manufactured PCB showing respectively the four radiating elements sub-array and the BFN; (c) the power combiner designed to combine the Mode A sub-array antennas; (d) Mode C BFN integrated on the bottom side of the slots PCB and (e) MAST POC satellite final assembly.

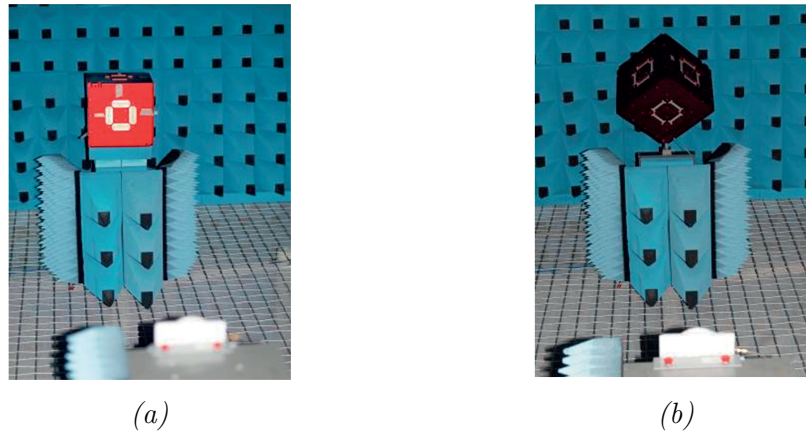


**Figure A.15.:** The measurement setup for (a) R and RL cuts and (b) V cut.

orthogonal elevation cuts ( $\varphi = 0$ ), given the symmetry of the configuration.

### Mode C

Also Mode C pattern is generated by the same sub-array as Mode B, differently fed. In this case, since the four tracking lobes generated for Mode C point towards the vertices of the face ( $\pm 45, \pm 135$  deg), it was necessary mounting the satellite on the proper angle in order to be able to measure two of the four lobes contained into one of the planes.

## A.6. Measurements

### A.6.1. Mode A

Design specifications state that Mode A radiation pattern shall have a minimum gain of  $-3$  dBi with a maximum ripple of 6 dB. This requirement was extended to the concept of “coverage”, extensively used through this document and meaning the portion (in percentage) of the 3D radiation pattern fulfilling the specifications.

The measured input matching of the whole Mode A system: six sub-array face antennas, plus the correspondent BFN of each sub-array, plus the power combiner, are provided in Fig. A.16. A maximum value of  $-12.9$  dB was measured within the whole operation band. It is also important to point out that, as previously mentioned, all the face sub-arrays which lay on each face of the satellite have been connected via a power combiner (1 input to 6 outputs) (see Fig. A.14c in Sec. A.4). The measured S-parameters of the power combiner are shown in Fig. A.17: the reflection coefficient is lower than  $-16$  dB within the whole band of interest, while the  $S_{1n}$  response was rather similar for all the outputs; also the phase difference between the outputs is lower than 10 deg.



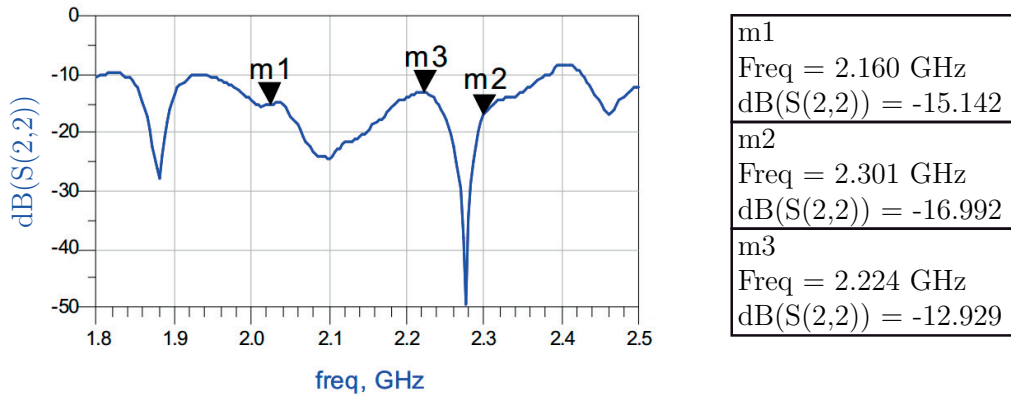


Figure A.16.: Measured reflection coefficient of the entire Mode A system.

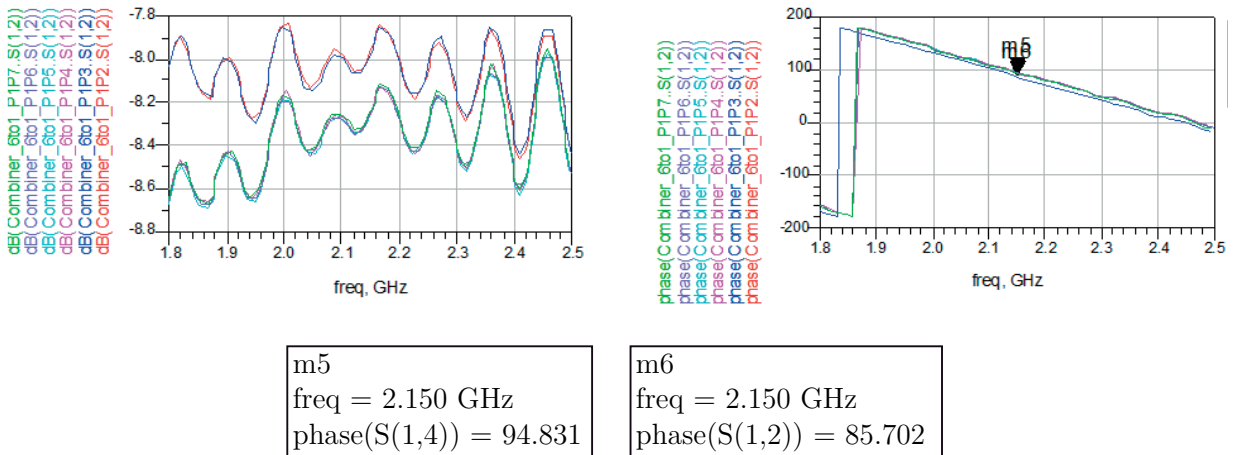
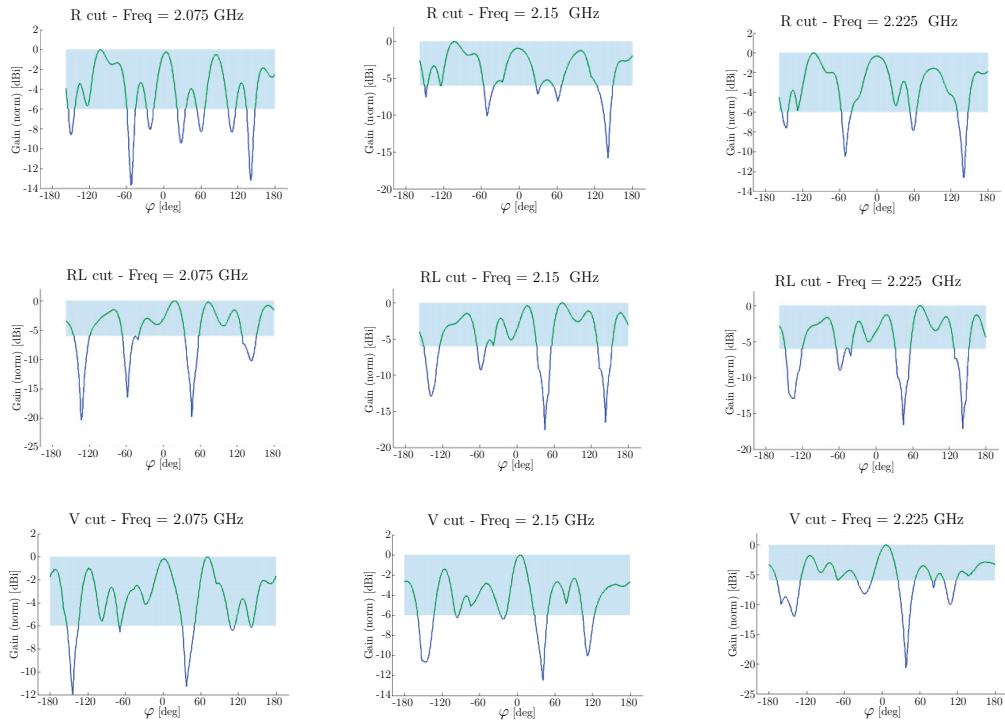


Figure A.17.: Measured reflection coefficient of the 6-to-1 power combined utilized to connect the 6 face sub-array antennas.



**Figure A.18.:** Measured radiation pattern of Mode A, strongest R-/L-HCP component. “R” setup (first row), “RL”, (second row) and “V”, (third row). The three frequencies correspond to lower bound, center and upper bound of the operative band.

The measured radiation patterns on the three cuts R, RL and V, as described in Sec. A.5, are presented hereafter in Fig. A.18. The diagrams on the left column show separately the normalized gain for RHCP and LHCP components of the radiated fields, renamed CO- and X-POL. As the specifications require the *strongest* of the two circular polarizations to be within a range  $-6$  dB from the maximum gain, on the right for better readability, it is shown the strongest of the two polarization and the range where patterns are within the specifications. The degree of coverage ranges from 70% up to 90% in all the patterns shown and can be retained overall satisfying. This holds in particular not only at center frequency, but also in the adjacent frequencies within the operation bandwidth dictated by the antenna reflection coefficient.

### A.6.2. Mode B

Regarding Mode B specifications, it was stated that a single directive beam of a minimum directivity of 5 dB within a 60 deg cone should be achieved. The face sub-array employed to obtain Mode A is also used for Mode B: the measured input matching is shown in Fig. A.19 and the radiation pattern on the elevation cut is depicted in Fig. A.20.

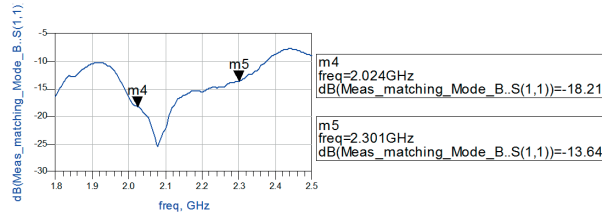


Figure A.19.: Measured reflection coefficient of the face sub-array.

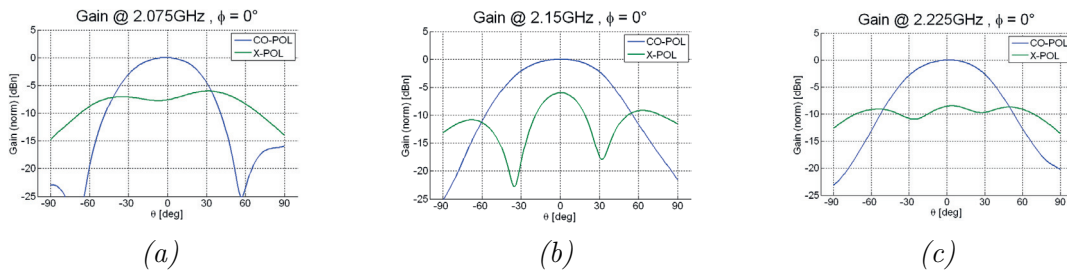


Figure A.20.: Measured radiation pattern of Mode B on the o, strongest R-/L-HCP component. “R” setup (first row), “RL”, (second row) and “V”, (third row). The three frequencies correspond to lower bound, center and upper bound of the operative band.

### A.6.3. Mode C

One of the two main planes, containing two of the four tracking lobes, was measured. The measured results of the first beam which points at  $-15$  deg, approximately, at the three main frequencies are presented in Fig. A.21, while the results of the second lobe pointing at around  $+15$  deg are depicted in Fig. A.22. As occurred with the Mode B, the co-polar component behavior is satisfactorily similar to the simulation results, however the cross-polar measurement shows a higher than expected value. The negative impact of this component is something which could be refined.

It can also be pointed out that, mainly due to the fact of re-using the same elements arrangement, the beamwidth of the lobes turned out to be not as narrow as desired. Although the

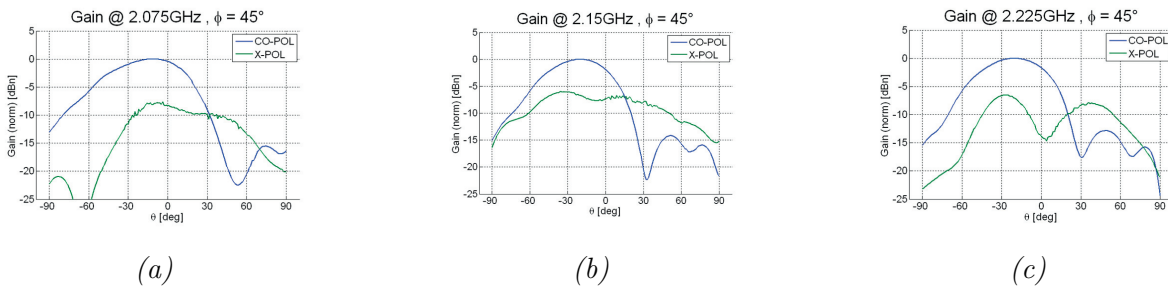
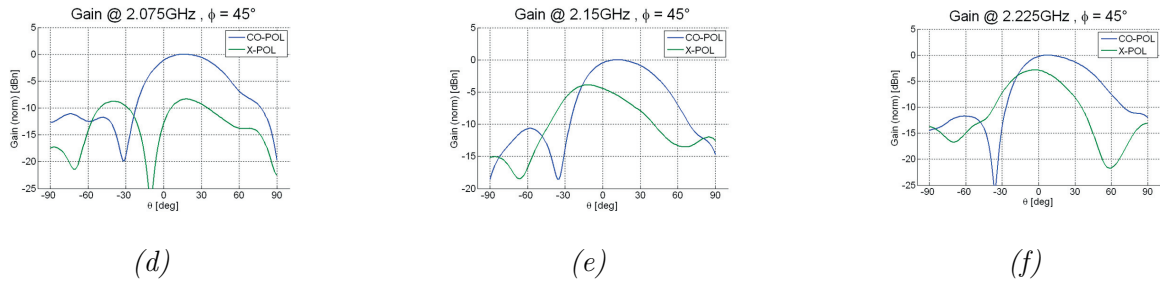


Figure A.21.: Measured first tracking lobe at (a) 2.075 GHz, (b) 2.15 GHz, (c) 2.225 GHz.



**Figure A.22.:** Measured second tracking lobe at (a) 2.075 GHz, (b) 2.15 GHz, (c) 2.225 GHz.

maximum of the lobe is found at around  $\pm 15 \sim 20$  deg, it would have been desired to obtain a more directive beam. This could be an aspect to be refined and improved in a future version of the antenna system.  $\ddot{i} \gg j$

## A.7. Final assessment

The Proof-Of-Concept architecture that was selected in the course of the project has been successfully realized and characterized through the planned measurement campaign. The outcome is that performance generally confirms simulations predictions and satisfies project specifications, even though some aspects, typical of realization processes, have been identified as responsible for perturbations.

Comments and issues can be summarized by antenna mode:

- Mode A: the measurements performed show that coverage ranges around 70-90 % on all the plane cuts, while a comparison between measurements and predicted results highlights an overall similar behavior. The fact that some of the measurements were expressly performed on critical planes, and the presence of a modest cross-polarization (absent in simulations), should justify the deviations that sometimes occur in the comparisons.
- Mode B: The co-polar field component matches rather well the expected results and the specifications; on the contrary, the cross-polar field component measurement turned out to be higher than desired, resulting into an aspect to be eventually refined in a future design.
- Mode C: again, the co-polar component behavior is satisfactorily similar to the simulation results, however the cross-polar measurement shows a higher than expected value. The negative impact of this component is something which could be refined.

The compliance matrix is shown in Tab. A.4.

**Table A.4.:** Specifications matrix of the measured elements for the different modes.

Mode	Frequency	Return loss	Polarization	Gain $G$ [dB]
A Omnidirectional	S-band 2025 – 2300 MHz	$\leq -12.9$ dB	RHCP or LHCP	$-6 \leq G \leq 0$ $\sim 75\%$ Coverage (*)
B Directional (60 deg cone)		$\leq -13.6$ dB		TBM (**) Gain Ripple < 3 dB
C RF-Tracking (4 lobes within a 60 deg cone)		$\leq -12.1$ dB		TBM (**) Gain Ripple < 1 dB

(\*) Coverage is defined as the percentage of 3D space fulfilling the specifications.

(\*\*) TBM = To be Measured. It is important to note that, by the time the measurements were realized, no measurement of gain could be performed due to unavailability of a proper third antenna for the three-antenna-method.



## B. SatAF source code

We include in this appendix the SatAF source code for the treatment of the rotations and translations related to the 3D Array Theory on the basis of the mathematical formulation illustrated in Par. 2.3.2

```
1 function f_0 = RotSigma_Handle(func,Pts0,TransfSigma,TypeFunc)
2
3 % Author:
4 %
5 %   Gabriele Rosati, EPFL-LEMA, November. 2009
6
7 %%%%%%%%%%%%%%%%%%%%%%%%%%%%%%%%%%%%%%%%%%%%%%%%%%%%%%%%%%%%%%%%%%%%%%%%%
8
9 % Let Sigma_1 be a "local" coordinate system function of a "global"
10 % coordinate system Sigma_0, with Sigma_1 = TransfSigma * Sigma_0
11
12 % [ x1 ]      [ x1_x0  x1_y0  x1_z0 ]   [ x0 ]
13 % [ y1 ] =    [ y1_x0  y1_y0  y1_z0 ] * [ y0 ]
14 % [ z1 ]      [ z1_x0  z1_y0  z1_z0 ]   [ z0 ]
15
16 % [ P1 ] =      [ TransfSigma ]   *      [ P0 ]
17 % [ P1 ]' =      [ P0 ]'         * [ TransfSigma ]'
18
19 % Evaluates the function "func", passed as an handle and with
20 % components along ^theta1, ^phi1 in every point [theta0,phi0]
21 % and returns its components along ^theta0, ^phi0
22
23 % The function func can be either:
24 %   TypeFunc = 'rDep'
25 %       func(r,theta1,phi1) = [ func_r , func_theta1 , func_phi1 ]
26 %   TypeFunc = 'rInd'
27 %       func(theta1,phi1)   = [ func_theta1 , func_phi1 ]
28
29 % THE FUNCTION IS EVALUATED IN SIGMA_0 - This case is useful when
30 % the function is available as an handle. The plot volume is defined
31 % in terms of Sigma_0
32
33 switch TypeFunc
34     case 'rInd'
35         theta0 = Pts0{1};
36         phi0   = Pts0{2};
37     case 'rDep'
```

```

38     r      = Pts0{1};
39     theta0 = Pts0{2};
40     phi0   = Pts0{3};
41 end
42
43 for i=1:3
44     TransfSigma(i,:) = TransfSigma(i,:) ./ norm(TransfSigma(i,:));
45 end
46
47 % Sigma1_Coord_Cart = { [x1] ; [y1] ; [z1] }(theta0,phi0) =
48 % = [TransfSigma] * { [x0] ; [y0] ; [z0] } =
49 % = [TransfSigma] * {coord_s2c(theta0,phi0)}
50 Sigma1_Coord_Cart = MatCell_Mult(TransfSigma, coord_s2c(theta0,phi0));
51 x1 = Sigma1_Coord_Cart{1,1};
52 y1 = Sigma1_Coord_Cart{2,1};
53 z1 = Sigma1_Coord_Cart{3,1};
54
55 % [theta1 phi1](theta0,phi0)
56 Sigma1_Coord_Sph = coord_c2s(x1, y1, z1);
57 theta1 = Sigma1_Coord_Sph{1,1};
58 phi1   = Sigma1_Coord_Sph{2,1};
59
60 % The function is passed as an handle (or a cell of handles)
61 switch TypeFunc
62     case 'rInd'
63         if length(func) == 2
64             f_theta1 = func{1}(theta1,phi1);
65             f_phi1   = func{2}(theta1,phi1);
66         else
67             f = func(theta1,phi1);
68             f_theta1 = f{1};
69             f_phi1   = f{2};
70         end
71     case 'rDep'
72         if length(func) == 3
73             f_r      = func{1}(r,theta1,phi1);
74             f_theta1 = func{2}(r,theta1,phi1);
75             f_phi1   = func{2}(r,theta1,phi1);
76         else
77             f = func(r,theta1,phi1);
78             if iscell(f)
79                 f_r      = f{1};
80                 f_theta1 = f{2};
81                 f_phi1   = f{3};
82             else
83                 f_r      = f(1,:);
84                 f_theta1 = f(2,:);
85                 f_phi1   = f(3,:);
86             end
87         end
88 end

```



```

89
90 %           { [theta0_x0] [phi0_x0] }
91 % Sph0_Sigma0 = { [theta0_y0] [phi0_y0] }
92 %           { [theta0_z0] [phi0_z0] }
93 % Sigma0 spherical versors decomposed along Sigma0 cartesian versors
94 Sph0_Sigma0 = vers_c2s(theta0,phi0);
95 vers_theta0 = Sph0_Sigma0(:,1);
96 vers_phi0   = Sph0_Sigma0(:,2);
97
98 %           { [theta1_x1] [phi1_x1] }
99 % Sph1_Sigma1 = { [theta1_y1] [phi1_y1] }
100 %           { [theta1_z1] [phi1_z1] }
101 % Sigma1 spherical versors decomposed along Sigma1 cartesian versors
102 Sph1_Sigma1 = vers_c2s(theta1,phi1);
103
104 % { Sph1_Sigma0 } = [TransfSigma] * { Sph1_Sigma1 }
105 % Sigma1 spherical versors (same as Sph1_Sigma1) but decomposed along
106 %   Sigma0 cartesian versors
107 % { [theta1_x0] [phi1_x0] }   [           ]' { [theta1_x1] [phi1_x1] }
108 % { [theta1_y0] [phi1_y0] } = [TransfSigma] * { [theta1_y1] [phi1_y1] }
109 % { [theta1_z0] [phi1_z0] }   [           ]' { [theta1_z1] [phi1_z1] }
110 Sph1_Sigma0 = MatCell_Mult(TransfSigma',Sph1_Sigma1);
111 vers_theta1 = Sph1_Sigma0(:,1);
112 vers_phi1   = Sph1_Sigma0(:,2);
113
114
115 % The cell "f_sigmal" contains the Sigma1 components of function "func",
116 % both decomposed along Sigma1 cartesian components
117 %           { f_theta1 * [ theta1_x1 ] + f_phi1 * [ phi1_x1 ] }
118 % f_sigmal = { f_theta1 * [ theta1_y1 ] + f_phi1 * [ phi1_y1 ] }
119 %           { f_theta1 * [ theta1_z1 ] + f_phi1 * [ phi1_z1 ] }
120 f_sigmal = CellCell_Sum(MatCell_ElemProd(f_theta1,vers_theta1) , ...
121                        MatCell_ElemProd(f_phi1 ,vers_phi1 ) );
122
123 % The final theta0 and phi0 components of function "func"
124 % The scalar product is performed by "CellCell_Mult" function
125 % f_theta0 = vector[f_sigmal] * versor[theta0]
126 % f_phi0   = vector[f_sigmal] * versor[phi0]
127 f_theta0 = CellCell_Mult(f_sigmal',vers_theta0);
128 f_phi0   = CellCell_Mult(f_sigmal',vers_phi0);
129
130 switch TypeFunc
131     case 'rInd'
132         f_0 = { f_theta0 , f_phi0 };
133     case 'rDep'
134         f_0 = { f_r , f_theta0 , f_phi0 };
135 end
136
137
138 function CartC = coord_s2c(theta,phi)
139 % { [x] ; [y] ; [z] } = [coord_s2c]( [theta] [phi] )

```

```

140 CartC{1,1} = sin(theta).*cos(phi);
141 CartC{2,1} = sin(theta).*sin(phi);
142 CartC{3,1} = cos(theta);
143
144 function SphC = coord_c2s(x,y,z)
145 % [ [theta] ; [phi] ] = [coord_c2s]([x] [y] [z])
146 SphC{1,1} = atan2(sqrt(x.^2 + y.^2) , z);
147 SphC{2,1} = atan2(y , x);
148
149 function SphV = vers_c2s(theta, phi)
150 % [          ] [ [^theta_x] [^phi_x] ]
151 % [ vers_c2s ] = [ [^theta_y] [^phi_y] ]
152 % [          ] [ [^theta_z] [^phi_z] ]
153 SphV{1,1} = cos(theta).*cos(phi);
154 SphV{2,1} = cos(theta).*sin(phi);
155 SphV{3,1} = -sin(theta);
156 SphV{1,2} = -sin(phi);
157 SphV{2,2} = cos(phi);
158 SphV{3,2} = 0;

```

```

1 function VectField_sph0 = ...
2     RotSigma_Table(TransfSigma,VectField,OutMeshgrid,varargin)
3
4 % Author:
5 %
6 %   Gabriele Rosati, EPFL-LEMA, November. 2009
7
8 %%%%%%%%%%%%%%%%%%%%%%%%%%%%%%%%%%%%%%%%%%%%%%%%%%%%%%%%%%%
9
10 %%%%%%%%%%%%%%%%%%%%%%%%%%%%%%%%%%%%%%%%%%%%%%%%%%%%%%%%%%%
11 %
12 % Let Sigma_1 be a "local" coordinate system, function of an "global" %
13 % coordinate system Sigma_0, with Sigma_1 = TransfSigma * Sigma_0. %
14 %
15 % The function interpolates the values of the vectorial field %
16 % vec_field(theta1,phi1), passed as a TABLE and with components along %
17 % ^theta1 and ^phi1, in every point [theta0 phi0] and returns its %
18 % components along ^theta0, ^phi0. %
19 %
20 % THE VECTORIAL FIELD IS EVALUATED IN SIGMA_1 cs - %
21 % This case is useful when data is available as a table. %
22 %
23 %%%%%%%%%%%%%%%%%%%%%%%%%%%%%%%%%%%%%%%%%%%%%%%%%%%%%%%%%%%
24
25 % TransfSigma is the 3x3 matrix: Sigma_0 = TransfSigma * Sigma_1
26 %
27 % The coordinates theta,phi can be passed as:
28 %   NxM MESHGRID - 2 elements: they are [theta phi] meshgrid and
29 %                               VectField's elements have the same size as them.

```

```

30 % 3xN VECTOR - 1 element : it is a [r theta phi] points array and VectField
31 % is 3xN matrix [ $\hat{r}$  ;  $\hat{\theta}$  ;  $\hat{\phi}$ ].
32 %
33 % VectField is a 2x1 cell whose elements are the components of VectField along
34 %  $\hat{\theta}_1$  ,  $\hat{\phi}_1$ . It has the same form as [theta, phi].
35 %
36 % OutMeshgrid is a cell containing the meshgrids in Sigma0 cs where
37 % the vectorial field is to be evaluated. If left empty, the output mesh has
38 % the same form as the input one.
39 %
40 % VectField_sph0 is a 2x1 cell whose elements are  $\hat{\theta}_0$  ,  $\hat{\phi}_0$  components
41 % of VectField, sorted according to Sigma0
42 %
43 % -----
44
45 global tol
46 tol = 1e-12;
47 OverSampling_Factor = 1.2; % Controls how much the known values are replied
48 % beyond the 0,2pi limits.
49
50 if nargin == 5 % [theta phi] are meshgrid
51     size_in = size(varargin{1});
52     Npts_in = prod(size_in);
53     if isempty(OutMeshgrid)
54         theta0_out = varargin{1}; phi0_out = varargin{2};
55     else
56         theta0_out = OutMeshgrid{1}; phi0_out = OutMeshgrid{2};
57     end
58     size_out = size(phi0_out);
59
60     % VectField is a 2x1 cell and contains  $\hat{\theta}_1$  ,  $\hat{\phi}_1$ 
61     % components in meshgrid form
62     % It is transformed to a 3xN matrix [ $\hat{r}$  ;  $\hat{\theta}$  ;  $\hat{\phi}$ ]
63     [sph1_coord,f_theta1,f_phi1] = ...
64         Mesh2Array(ones(size_in),varargin {1},varargin {2} , ...
65                 VectField{1},VectField{2} );
66     f_sph1 = [zeros(1,Npts_in) ; f_theta1 ; f_phi1];
67
68 else % [theta phi] is a 3xN [r theta phi] points array
69     f_sph1 = VectField;
70     size_out(1) = length(find(varargin{1} == varargin{1}(2,1)));
71     size_out(2) = size(varargin{1},2)/size_out(1);
72 end
73
74 % Redundant points (0,phi) and (pi,phi) are removed
75 ind_0phi = find(sph1_coord(2,:) < tol);
76 if length(ind_0phi) > 1
77     sph1_coord(:,ind_0phi(2:end)) = [];
78     f_sph1(:,ind_0phi(2:end)) = [];
79 end
80

```

```

81 ind_piphi = find(abs(sph1_coord(2,:) - pi) < tol);
82 if length(ind_piphi) > 1
83     sph1_coord(:,ind_piphi(2:end)) = [];
84     f_sph1(:,ind_piphi(2:end)) = [];
85 end
86
87 % Normalization and inversion of TransfSigma
88 for i=1:3
89     TransfSigma(i,:) = TransfSigma(i,:) / norm(TransfSigma(i,:));
90 end
91 TransfSigma = TransfSigma';
92
93 % cart1_coord = [Pts_x1 ; Pts_y1 ; Pts_z1 ](theta1,phi1)
94 cart1_coord = Sph2Cart_Coord(sph1_coord);
95
96 % cart0_coord = [Pts_x0 ; Pts_y0 ; Pts_z0 ](theta1,phi1) =
97 %               = [TransfSigma] * [Pts_x1 ; Pts_y1 ; Pts_z1 ] =
98 %               [TransfSigma] * cart1_coord
99 cart0_coord = TransfSigma * cart1_coord;
100
101 % sph0_coord = [Pts_r0 ; Pts_theta0 ; Pts_phi0]
102 [r, theta0,phi0] = Cart2Sph_Coord(cart0_coord,tol);
103 phi0(phi0<0) = phi0(phi0<0) +2*pi;
104
105 %               { [ r_x0] [theta0_x0] [phi0_x0] }
106 % sph0_vers_cart0 = { [ r_x0] [theta0_y0] [phi0_y0] }
107 %               { [ r_x0] [theta0_z0] [phi0_z0] }
108 % sph0_vers_cart0 = Sigma0 spherical versors decomposed
109 % along Sigma0 cartesian versors
110 f_cart1 = Sph2Cart_Vect(f_sph1,sph1_coord);
111 f_cart0 = TransfSigma * f_cart1;
112 f_sph0 = Cart2Sph_Vect(f_cart0,theta0,phi0);
113
114 os.lim_th = pi/10;
115 os.lim_ph = pi/10;
116 os.nphi = size(theta0_out,2)-1;
117 VectField_sph0 = {zeros(size_out) zeros(size_out)};
118 start = true;
119 while start || any(any(isnan(VectField_sph0{1}))) || ...
120     any(any(isnan(VectField_sph0{2})))
121     start = false;
122     [r, theta0_int,phi0_int,f_sph0_int] = OverSample(theta0,phi0,f_sph0,os);
123     os.lim_th = os.lim_th * OverSampling_Factor;
124     os.lim_ph = os.lim_ph * OverSampling_Factor;
125
126     for i=1:2
127         Fr = ...
128             TriScatteredInterp(theta0_int',phi0_int',real(f_sph0_int(i+1,:))');
129         Vr = Fr(theta0_out,phi0_out);
130         Fi = ...
131             TriScatteredInterp(theta0_int',phi0_int',imag(f_sph0_int(i+1,:))');

```

```

130     Vi = Fi(theta0_out,phi0_out);
131
132     VectField_sph0{i} = (Vr + li*Vi);
133     end
134 end
135
136 end
137
138
139 function [r0_tot,theta0_tot,phi0_tot,f_sph0_tot] = ...
    OverSample(theta0,phi0,f_sph0,os)
140
141 % 00) Generates points (0,:) from (0,0)
142 % pi0) Generates points (pi,:) from (pi,0)
143 % t1) Duplicates points from 0 < theta0 < lim_rep.th
144 %           to pi < theta0 < pi+lim_rep.th
145 % t2) Duplicates points from pi-lim_rep.th < theta0 < pi
146 %           to -lim_rep.th < theta0 < 0
147 % p1) Duplicates points from 0 < phi0 < os.lim_ph
148 %           to pi < phi0 < pi+os.lim_ph
149 % p2) Duplicates points from pi-os.lim_ph < phi0 < pi
150 %           to -os.lim_ph < phi0 < 0
151
152 global tol
153
154 [var_sort , f_sph0] = TrueSort([theta0 ; phi0 ] , [1 2] , f_sph0);
155 theta0 = var_sort(1,:); phi0 = var_sort(2,:);
156 cond_red = abs(diff(theta0)) < tol & abs(diff(phi0)) < tol;
157 theta0(cond_red) = [];
158 phi0(cond_red) = [];
159 f_sph0(:,cond_red) = [];
160
161 % Add points from (0,0) to (0,phi)
162 cond_00 = find(abs(theta0)<tol & abs(phi0)<tol);
163 switch length(cond_00)
164     case 1
165         ft_00 = f_sph0(2,cond_00);
166         fp_00 = f_sph0(3,cond_00);
167         theta0_add_00 = zeros(1,os.nphi);
168         phi0_add_00 = 2*pi*(1/os.nphi:1/os.nphi:1);
169         f_sph0_add_00 = [ ones(1,os.nphi) ; ...
170             ft_00*cos(phi0_add_00) + fp_00*sin(phi0_add_00) ; ...
171             -ft_00*sin(phi0_add_00) + fp_00*cos(phi0_add_00) ];
172     case 0
173         theta0_add_00 = [];
174         phi0_add_00 = [];
175         f_sph0_add_00 = [];
176 end
177
178 % Add points from (pi,0) to (pi,phi)
179 cond_pi0 = find(abs(theta0-pi)<tol & abs(phi0)<tol);

```

```

180 switch length(cond_pi0)
181     case 1
182         ft_pi0 = f_sph0(2,cond_pi0);
183         fp_pi0 = f_sph0(3,cond_pi0);
184         theta0_add_pi0 = pi*ones(1,os.nphi);
185         phi0_add_pi0 = 2*pi*(1/os.nphi:1/os.nphi:1);
186         f_sph0_add_pi0 = [ ones(1,os.nphi) ; ...
187             ft_pi0*cos(phi0_add_pi0) - fp_pi0*sin(phi0_add_pi0) ; ...
188             ft_pi0*sin(phi0_add_pi0) + fp_pi0*cos(phi0_add_pi0) ];
189     case 0
190         theta0_add_pi0 = [];
191         phi0_add_pi0 = [];
192         f_sph0_add_pi0 = [];
193 end
194
195 theta0_add_t = [ theta0  theta0_add_00  theta0_add_pi0 ];
196 phi0_add_t = [ phi0  phi0_add_00  phi0_add_pi0 ];
197 f_sph0_add_t = [ f_sph0  f_sph0_add_00  f_sph0_add_pi0 ];
198
199 % Duplicating points from 0 < theta0 ≤ os.lim_th
200 % to pi < theta0 ≤ pi+os.lim_th
201 ind_t1 = find(tol < theta0_add_t & theta0_add_t ≤ os.lim_th);
202 theta0_add_t1 = -theta0_add_t(ind_t1);
203 phi0_add_t1 = pi + phi0_add_t(ind_t1);
204 phi0_add_t1(phi0_add_t1 ≥ 2*pi) = phi0_add_t1(phi0_add_t1 ≥ 2*pi) - 2*pi;
205 f_sph0_add_t1 = -f_sph0_add_t(:,ind_t1);
206
207 % Duplicating points from pi-os.lim_th < theta0 < pi
208 % to -lim_rep-th < theta0 < 0
209 ind_t2 = find(pi-os.lim_th ≤ theta0_add_t & theta0_add_t < pi);
210 theta0_add_t2 = 2*pi - theta0_add_t(ind_t2);
211 phi0_add_t2 = pi + phi0_add_t(ind_t2);
212 phi0_add_t2(phi0_add_t2 ≥ 2*pi) = phi0_add_t2(phi0_add_t2 ≥ 2*pi) - 2*pi;
213 f_sph0_add_t2 = -f_sph0_add_t(:,ind_t2);
214
215 theta0_add_t = [theta0_add_t  theta0_add_t1  theta0_add_t2 ];
216 phi0_add_t = [phi0_add_t  phi0_add_t1  phi0_add_t2 ];
217 f_sph0_add_t = [f_sph0_add_t  f_sph0_add_t1  f_sph0_add_t2 ];
218
219 % Adding points for phi<0 and phi≥2pi
220 ind_p1 = find(tol < phi0_add_t & phi0_add_t ≤ os.lim_ph);
221 theta0_add_p1 = theta0_add_t(ind_p1);
222 phi0_add_p1 = phi0_add_t(ind_p1) + 2*pi;
223 f_sph0_add_p1 = f_sph0_add_t(:,ind_p1);
224
225 ind_p2 = find(2*pi-os.lim_ph ≤ phi0_add_t & phi0_add_t < 2*pi);
226 theta0_add_p2 = theta0_add_t(ind_p2);
227 phi0_add_p2 = phi0_add_t(ind_p2) - 2*pi;
228 f_sph0_add_p2 = f_sph0_add_t(:,ind_p2);
229
230 % Concatenate vectors

```

```

231 theta0_tot = [ theta0_add_t  theta0_add_p1  theta0_add_p2 ];
232 phi0_tot   = [ phi0_add_t    phi0_add_p1   phi0_add_p2   ];
233 f_sph0_tot = [ f_sph0_add_t  f_sph0_add_p1 f_sph0_add_p2 ];
234
235 r0_tot = ones(size(theta0_tot));
236
237 end
238
239
240 % -----
241
242 % Footnotes
243 % -----
244
245 % [ x0 ]      [ x0_x1  x0_y1  x0_z1 ]   [ x1 ]
246 % [ y0 ] =   [ y0_x1  y0_y1  y0_z1 ] * [ y1 ]
247 % [ z0 ]      [ z0_x1  z0_y1  z0_z1 ]   [ z1 ]
248
249 % [ P0 ] =      [ TransfSigma ]      * [ P1 ]
250 % It is also: [P0]' = [P1]' * [ TransfSigma ]'
251
252 % -----
253
254 % Functions f_theta0, f_phi0 are mapped according to Sigma_1:
255 %   f(p,q) corresponds to f_ applied to the point
256 %   (theta1(any,p),phi(q,any)).
257 %
258 % The theta0,phi0 meshgrid points instead are not ordered and
259 % represent the new coordinate system Sigma0.
260 % In this way, plotting f_ versus Sigma0 makes the function
261 % "appear" rotated, while what is rotated is only the
262 % coordinate system. This makes impossible plotting the pattern
263 % generated by two elements differently rotated: the f_ matrix
264 % will contain the proper ^theta,^phi components but its ordering
265 % is "frozen" to Sigma_1, so the pattern obtained is the one
266 % generated by two elements with the same orientation.
267 % The arrange function tries to map f function according to Sigma_0
268 % coord system. This is done by defining a new, ordered meshgrid
269 % (theta0,phi0 is not ordered) and by coherently reordering f_ .
270 % The value of f_ will in general not be available in every point
271 % of the ordered meshgrid, so an approximation the available values
272 % is required. If instead the coordinate system is rotated of an
273 % angle included in the function table, then Sigma_0 points will all
274 % be available.
275 % After this process, the field generated by two elements differently
276 % oriented can be summed.
277 % An alternative could be not defining a new grid, but keeping the
278 % theta0,phi0 one. However, when adding two plots, values of f_ will
279 % be availables in different points.

```





## Bibliography

- [1] B. Klofas, J. Anderson, and K. Leveque, “A survey of cubesat communication systems,” 2008.
- [2] I. S. S. International Academy of Astronautics, R. Sandau, H. Röser, and A. Valenzuela, *Small Satellites for Earth Observation: Selected Contributions*. Springer Science+Business Media B.V., 2008.
- [3] D. J. Barnhart, T. Vladimirova, and M. N. Sweeting, “Very-small-satellite design for distributed space missions,” *Journal of Spacecraft and Rockets*, vol. 44, pp. 1294–1306, Nov. 2007.
- [4] J. Padilla, G. Rosati, A. Ivanov, F. Bongard, S. Vaccaro, and J. Mosig, “Multi-functional miniaturized slot antenna system for small satellites,” in *EuCAP 2011, Proceedings of the 5th European Conference on Antennas and Propagation*, Apr. 2011, pp. 2170–2174.
- [5] G. Marrocco, L. Mattioni, A. Potenza, F. Milani, A. Giacomini, and M. Sabbadini, “Distributed multi-function antenna system for micro- and nano-satellites,” in *EuCAP 2010, Proceedings of the 4th European Conference on Antennas and Propagation*, Apr. 2010, pp. 1–4.
- [6] J. Mueller, H. Goldberg, and L. Alkalai, “Micro-inspector spacecraft testbed: Breadboard subsystem demonstrations,” in *Space Technology and Applications International Forum-STAIF 2007*, ser. American Institute of Physics Conference Series, M. El-Genik, Ed., vol. 880, Jan. 2007, pp. 742–759.
- [7] F. C. Bruhn, P. Rathsman, and L. Stenmark, “Nanospace-1: Spacecraft design using advanced modular architecture (AMA),” *AIAA Journal of Spacecraft and Rockets*, 2005.
- [8] N. Raj, “Satellites built by universities,” 2008.
- [9] O. Montenbruck, M. Markgraf, S. Santandrea, and J. Naudet, “GPS orbit determination for micro-satellites - the PROBA-2 flight experience,” in *AIAA/AAS Astrodynamics Specialist Conference*, 2010.
- [10] R. Sandau, H. Roeser, and A. Valenzuela, *Small Satellite Missions for Earth Observation*. Springer, 2008.
- [11] M. Cutter, “A small satellite hyperspectral mission,” in *Small Satellites, Systems and Services*, ser. ESA Special Publication, B. Warmbein, Ed., vol. 571, Nov. 2004.

- 
- [12] “<http://www.esa.int/specials/education/sem4dlpr4cf/0.html>.”
- [13] K. Wincza, M. Osys, L. Dudzifiski, and P. Kabacik, “Lightweight low gain microstrip antennas for use in minisatellites,” in *15th International Conference on Microwaves, Radar and Wireless Communications, MIKON-2004.*, vol. 1, May 2004, pp. 314 – 317 Vol.1.
- [14] E. Arnieri, L. Boccia, G. Amendola, and G. Di Massa, “A compact high gain antenna for small satellite applications,” *IEEE Transactions on Antennas and Propagation*, vol. 55, no. 2, pp. 277 –282, Feb. 2007.
- [15] L. Alminde, M. Bisgaard, N. Melville, and J. Schaefer, “The SSETI-Express mission: from idea to launch in one and a half year,” in *Proceedings of 2nd International Conference on Recent Advances in Space Technologies (RAST), 2005*, Jun. 2005, pp. 100 – 105.
- [16] “<http://www.esa.int/specials/sseti/express/sem1az708be/0.html>.”
- [17] H. Zebker, T. Farr, R. Salazar, and T. Dixon, “Mapping the world’s topography using radar interferometry: the TOPSAT mission,” *Proceedings of the IEEE*, vol. 82, no. 12, pp. 1774 –1786, Dec. 1994.
- [18] J. Lohn, “Advanced antenna design for a NASA small satellite mission,” in *22nd Annual AIAA/USS conference on small satellites*, 2008.
- [19] D. Speer, G. Jackson, and D. Raphael, “Flight computer design for the Space Technology 5 (ST-5) mission,” in *Journal of Spacecraft and Rockets*, vol. 1, Nov. 2002, pp. 255–269.
- [20] “<http://www.utias-sfl.net/nanosatellites/aissat-1/>.”
- [21] “<http://swisscube.epfl.ch/>.”
- [22] G. Rosati, “Miniaturised multi-functional antenna systems for micro/nano satellites - Technical Note 01,” LEMA-EPFL, Lausanne, Switzerland, Tech. Rep., Apr. 2009.
- [23] —, “Miniaturised multi-functional antenna systems for micro/nano satellites - Baseline Design Review,” Tech. Rep.
- [24] —, “Miniaturised multi-functional antenna systems for micro/nano satellites - Preliminary Design Review,” LEMA-EPFL, Lausanne, Switzerland, Tech. Rep., Nov. 2009.
- [25] —, “Miniaturised multi-functional antenna systems for micro/nano satellites - Critical Design Review,” LEMA-EPFL, Lausanne, Switzerland, Tech. Rep., Jun. 2010.
- [26] —, “Miniaturised multi-functional antenna systems for micro/nano satellites - Final Review,” LEMA-EPFL, Lausanne, Switzerland, Tech. Rep., Dec. 2010.

- [27] G. Rosati and J. Mosig, "An efficient analysis & design methodology for slot antennas on microsatellites," in *15th International Symposium on Antenna Technology and Applied Electromagnetics (ANTEM)*, Jun. 2012, pp. 1–7.
- [28] —, "Simplified point-wise schemes for integral equations in electromagnetics," in *12th Mediterranean Microwave Symposium*, Sep. 2012.
- [29] —, "An alternate point-wise scheme for electric field integral equations," *Accepted for publication in International Journal of RF and Microwave Computer Aided Engineering*, 2013.
- [30] A. Dastranj, A. Imani, and M. Naser-Moghaddasi, "Printed wide-slot antenna for wide-band applications," *IEEE Transactions on Antennas and Propagation*, vol. 56, no. 10, pp. 3097–3102, Oct. 2008.
- [31] J. Guterman, Y. Rahmat-Samii, A. Moreira, and C. Peixeiro, "Quasi-omnidirectional dual-band back-to-back e-shaped patch antenna for laptop applications," *Electronics Letters*, vol. 42, no. 15, pp. 845–847, Jul. 2006.
- [32] S.-M. Deng, "A study on the special characteristic of near isotropic or ball-like radiation pattern," in *Antennas and Propagation Society International Symposium, 2005 IEEE*, vol. 2A, Jul. 2005, pp. 284–287.
- [33] M. Hanqing and W. Dakui, "A wideband E-plane omnidirectional antenna," in *7th International Symposium on Antennas, Propagation EM Theory, 2006. ISAPE '06.*, Oct. 2006, pp. 1–2.
- [34] P. Kabacik, M. Kulig, P. Gorski, and M. Jagoda, "The omnidirectional coverage of low-profile ttc antennas onboard minispacecraft," in *Antennas and Propagation Society International Symposium, 2005 IEEE*, vol. 2B, Jul. 2005, pp. 222–225.
- [35] K. Muchalski, M. Jagoda, M. Tomasiak, P. Gorski, A. Akonom, M. Kulig, W. Barecki, and P. Kabacik, "Optimizing TT&C antenna placement on minisatellites," in *15th International Conference on Microwaves, Radar and Wireless Communications, MIKON-2004.*, vol. 2, May 2004, pp. 489–492.
- [36] T. Maleszka, P. Gorski, and P. Kabacik, "On omnidirectional coverage with minimum number of circularly polarized patch antennas placed on minisatellites," in *Antennas and Propagation Society International Symposium, 2007 IEEE*, Jun. 2007, pp. 3037–3040.
- [37] C. A. Balanis, *Antenna Theory: Analysis and Design*. John Wiley & Sons Inc., 1996.
- [38] Ansoft HFSS - <http://www.ansoft.com/products/>, Ansoft Corporation.
- [39] CST Microwave Studio - <http://www.cst.com/Content/Products/MWS/Overview.aspx>, Computer Simulation Technology.

- 
- [40] FEKO - <http://www.feko.info/>, FEKO. Comprehensive electromagnetic simulation software.
- [41] Advanced Design System Momentum Simulator - <http://home.agilent.com/>, Agilent Technologies.
- [42] S. Vaccaro, "Solant: study and development of planar antennas integrating solar cells - Thesis Nr. 2689," Ph.D. dissertation, EPFL-LEMA, 2002.
- [43] C. Balanis, *Engineering Electromagnetics*. John Wiley & Sons, 1989.
- [44] R. Harrington, *Time-harmonic electromagnetic fields*. McGraw-Hill, 1961.
- [45] J. Wang, *Generalized moment methods in electromagnetics: formulation and computer solution of integral equations*. J. Wiley, 1991.
- [46] W. Gibson, *The Method of Moments in Electromagnetics*. CRC PressINC, 2008.
- [47] L. Felsen and N. Marcuvitz, *Radiation and Scattering of Waves*. Wiley, 1994.
- [48] R. Collin, *Field Theory of Guided Waves*. Wiley, 1990.
- [49] K. Michalski and J. Mosig, "Multilayered media Green's functions in integral equation formulations," *IEEE Transactions on Antennas and Propagation*, vol. 45, no. 3, pp. 508–519, Mar. 1997.
- [50] M. Aksun and G. Dural, "Clarification of issues on the closed-form Green's functions in stratified media," *IEEE Transactions on Antennas and Propagation*, vol. 53, no. 11, pp. 3644–3653, Nov. 2005.
- [51] V. Kourkoulos and A. Cangellaris, "Accurate approximation of Green's functions in planar stratified media in terms of a finite sum of spherical and cylindrical waves," *IEEE Transactions on Antennas and Propagation*, vol. 54, no. 5, pp. 1568–1576, May 2006.
- [52] A. Polimeridis, T. Yioultsis, and T. Tsiboukis, "A robust method for the computation of Green's functions in stratified media," *IEEE Transactions on Antennas and Propagation*, vol. 55, no. 7, pp. 1963–1969, Jul. 2007.
- [53] K. Michalski, "Extrapolation methods for Sommerfeld integral tails," *IEEE Transactions on Antennas and Propagation*, vol. 46, no. 10, pp. 1405–1418, Oct. 1998.
- [54] J. Mosig, *Numerical Techniques for Microwave and Millimeter-Wave Passive Structures*. Wiley, 1989.
- [55] ———, *Integral-equation techniques for three-dimensional microstrip structures*. Review of Radio Science, R. Stone, Ed. Oxford: URSI-Oxford Science Publications, 1998.

- [56] A. Peterson, S. Ray, and Mittra, *Computational methods for electromagnetics*. IEEE Press, 1998.
- [57] P. Yla-Oijala and M. Taskinen, "Calculation of CFIE impedance matrix elements with RWG and  $n \times$  RWG functions," *IEEE Transactions on Antennas and Propagation*, vol. 51, no. 8, pp. 1837 – 1846, Aug. 2003.
- [58] J. Mosig and F. Gardiol, "General integral equation formulation for microstrip antennas and scatterers," *IEEE Proceedings on Microwaves, Antennas and Propagation*, vol. 132, no. 7, pp. 424 – 432, Dec. 1985.
- [59] J. Mosig, "Arbitrarily shaped microstrip structures and their analysis with a mixed potential integral equation," *IEEE Transactions on Microwave Theory and Techniques*, vol. 36, no. 2, pp. 314 – 323, Feb. 1988.
- [60] M. Cloud and D. Nyquist, "A note on the mixed potential representation of electric fields in layered media," *IEEE Transactions on Microwave Theory and Techniques*, vol. 37, no. 7, pp. 1150 – 1152, Jul. 1989.
- [61] G. Vandenbosch and A. Van de Capelle, "Mixed-potential integral expression formulation of the electric field in a stratified dielectric medium-application to the case of a probe current source," *IEEE Transactions on Antennas and Propagation*, vol. 40, no. 7, pp. 806 – 817, Jul. 1992.
- [62] J. Sercu, N. Fache, F. Libbrecht, and P. Lagasse, "Mixed potential integral equation technique for hybrid microstrip-slotline multilayered circuits using a mixed rectangular-triangular mesh," *IEEE Transactions on Microwave Theory and Techniques*, vol. 43, no. 5, pp. 1162 – 1172, May 1995.
- [63] M. Sancer, K. Sertel, J. Volakis, and P. Van Alstine, "On volume integral equations," *IEEE Transactions on Antennas and Propagation*, vol. 54, no. 5, pp. 1488 – 1495, May 2006.
- [64] B. Usner, K. Sertel, M. Carr, and J. Volakis, "Generalized volume-surface integral equation for modeling inhomogeneities within high contrast composite structures," *IEEE Transactions on Antennas and Propagation*, vol. 54, no. 1, pp. 68 – 75, Jan. 2006.
- [65] S. Makarov, S. Kulkarni, A. Marut, and L. Kempel, "Method of moments solution for a printed patch/slot antenna on a thin finite dielectric substrate using the volume integral equation," *IEEE Transactions on Antennas and Propagation*, vol. 54, no. 4, pp. 1174 – 1184, Apr. 2006.
- [66] W. Chew, *Waves and fields in inhomogeneous media*. IEEE Press, 1999.
- [67] R. E. Hodges and Y. Rahmat-Samii, "The evaluation of MFIE integrals with the use of vector triangle basis functions," *Microwave and Optical Technology Letters*, vol. 14, no. 1, pp. 9–14, 1997.

- 
- [68] N. Morita, N. Kumagai, and J. Mautz, *Integral Equation Methods for Electromagnetics*. Artech House, 1990.
- [69] M. Sadiku, *Numerical Techniques in Electromagnetics, Second Edition*. CRC PressINC, 2001.
- [70] S. Rao, D. Wilton, and A. Glisson, “Electromagnetic scattering by surfaces of arbitrary shape,” *IEEE Transactions on Antennas and Propagation*, vol. 30, no. 3, pp. 409 – 418, May 1982.
- [71] W. Chew, *Fast and Efficient Algorithms in Computational Electromagnetics*. Artech House, 2001.
- [72] E. Nyström , “Über die praktische auflösung von integralgleichungen mit anwendungen auf randwertaufgaben,” *Acta Mathematica*, vol. 54, pp. 185–204, 1930.
- [73] R. Kress, *Linear Integral Systems*. Springer-Verlag GmbH, 1999.
- [74] S. Gedney, “On deriving a locally corrected Nyström scheme from a quadrature sampled moment method,” *IEEE Transactions on Antennas and Propagation*, vol. 51, no. 9, pp. 2402 – 2412, Sep. 2003.
- [75] L. F. Canino, J. J. Ottusch, M. A. Stalzer, J. L. Visher, and S. M. Wandzura, “Numerical solution of the Helmholtz equation in 2D and 3D using a high-order Nyström discretization,” *Journal of Computational Physics*, vol. 146, no. 2, pp. 627 – 663, 1998.
- [76] D. Wilton, S. Rao, A. Glisson, D. Schaubert, O. Al-Bundak, and C. Butler, “Potential integrals for uniform and linear source distributions on polygonal and polyhedral domains,” *IEEE Transactions on Antennas and Propagation*, vol. 32, no. 3, pp. 276 – 281, Mar. 1984.
- [77] WIPL-D. Electromagnetic modeling of composite metallic and dielectric structures - <http://www.wipl-d.com/>.
- [78] M. S. Tong and W. C. Chew, “Superhyper singularity treatment for solving 3d electric field integral equations,” *Microw. Opt. Tech. Lett*, vol. 49, no. 6, pp. 1383–1388, Mar. 2007.
- [79] —, “On the near-interaction elements in integral equation solvers for electromagnetic scattering by three-dimensional thin objects,” *IEEE Transactions on Antennas and Propagation*, vol. 57, no. 8, pp. 2500 –2506, Aug. 2009.
- [80] M. Yuan, T. Sarkar, and M. Salazar-Palma, “A direct discrete complex image method from the closed-form Green’s functions in multilayered media,” *IEEE Transactions on Microwave Theory and Techniques*, vol. 54, no. 3, pp. 1025 – 1032, Mar. 2006.

- 
- [81] R. R. Boix, F. Mesa, and F. Medina, "Application of total least squares to the derivation of closed-form Green's functions for planar layered media," *IEEE Transactions on Microwave Theory and Techniques*, vol. 55, no. 2, pp. 268–280, Feb. 2007.
- [82] K. Michalski and D. Zheng, "Electromagnetic scattering and radiation by surfaces of arbitrary shape in layered media. I. Theory," *IEEE Transactions on Antennas and Propagation*, vol. 38, no. 3, pp. 335–344, Mar. 1990.
- [83] A. Polimeridis, T. Yioultsis, and T. Tsiboukis, "Fast numerical computation of Green's functions for unbounded planar stratified media with a finite-difference technique and gaussian spectral rules," *IEEE Transactions on Microwave Theory and Techniques*, vol. 55, no. 1, pp. 100–107, Jan. 2007.
- [84] F. Demuyneck, G. Vandebosch, and A. Van de Capelle, "Analytical treatment of the Green's function singularities in a stratified dielectric medium," in *23rd European Microwave Conference*, Sep. 1993, pp. 1000–1001.
- [85] A. Polimeridis and T. Yioultsis, "On the direct evaluation of weakly singular integrals in Galerkin mixed potential integral equation formulations," *IEEE Transactions on Antennas and Propagation*, vol. 56, no. 9, pp. 3011–3019, Sep. 2008.
- [86] L. Gray, J. Glaeser, and T. Kaplan, "Direct evaluation of hypersingular Galerkin surface integrals," *SIAM Journal on Scientific Computing*, vol. 25, no. 5, pp. 1534–1556, 2004.
- [87] L. Gray, A. Salvadori, A. Phan, and V. Mantic, "Direct evaluation of hypersingular Galerkin surface integrals II," *Electronic Journal of Boundary Elements*, vol. 4, no. 3, 2007.
- [88] R. Graglia, "On the numerical integration of the linear shape functions times the 3-D Green's function or its gradient on a plane triangle," *IEEE Transactions on Antennas and Propagation*, vol. 41, no. 10, pp. 1448–1455, Oct. 1993.
- [89] T. Eibert and V. Hansen, "On the calculation of potential integrals for linear source distributions on triangular domains," *IEEE Transactions on Antennas and Propagation*, vol. 43, no. 12, pp. 1499–1502, Dec. 1995.
- [90] A. Tzoulis and T. F. Eibert, "Review of singular potential integrals for method of moments solutions of surface integral equations," *Advances in Radio Science*, vol. 2, pp. 93–99, 2004.
- [91] C. Schwab and W. Wendland, "On numerical cubatures of singular surface integrals in boundary element methods," *Numerische Mathematik*, vol. 62, pp. 343–369, 1992.
- [92] Ismatullah and T. Eibert, "Adaptive singularity cancellation for efficient treatment of near-singular and near-hypersingular integrals in surface integral equation formulations," *IEEE Transactions on Antennas and Propagation*, vol. 56, no. 1, pp. 274–278, Jan. 2008.

- 
- [93] S. Chakraborty and V. Jandhyala, "Evaluation of Green's function integrals in conducting media," in *Antennas and Propagation Society International Symposium, 2003. IEEE*, vol. 3, Jun. 2003, pp. 320 – 323.
- [94] H.-X. Zhou, W. Hong, and G. Hua, "An accurate approach for the calculation of MoM matrix elements," *IEEE Transactions on Antennas and Propagation*, vol. 54, no. 4, pp. 1185 – 1191, Apr. 2006.
- [95] P. Fink, D. Wilton, and M. Khayat, "Simple and efficient numerical evaluation of near-hypersingular integrals," in *Antennas and Propagation Society International Symposium, 2007 IEEE*, Jun. 2007, pp. 4849 – 4852.
- [96] M. E. Cabot Barja, "Characterization techniques for antennas with highly convoluted topologies - Thesis Nr. 3152," Ph.D. dissertation, EPFL-LEMA, 2004.
- [97] J. M. Rius, J. M. G. Arbesu, J. R. Mosig, and E. C. et al., "Conclusions and results of the fractalcoms project: Exploring the limits of fractal electrodynamics for the future telecommunication technologies," in *ACTAS del 27TH ESA Antenna Technology Workshop on Innovative Periodic Antennas: Electromagnetic Bandgap, Left-Handed Materials, Fractal and Frequency Selective Surfaces*, 2004, pp. 229 – 233.
- [98] K. E. Atkinson, *The Numerical Solution of Integral Equations of the Second Kind*. Cambridge University Press, 1997.







# Gabriele Rosati

---

CONTACT 15, Rue du Villars *Mobile: +41 76 251 44 19*  
INFORMATION CH-1024, Ecublens, Switzerland *E-mail: gabriele.rosati@epfl.ch*

BIO SKETCH *Date - place of birth:* June 16, 1981 - Prato, Italy  
*Gender:* Male  
*Marital status:* Single  
*Citizenhsip:* Italian

RESEARCH Numerical methods for Electromagnetics, with emphasis on Integral Equations and Method  
INTERESTS of Moments. Analysis and design of antenna systems for space applications and printed microwave circuits.

PROFESSIONAL & ACADEMIC EXPERIENCES **Ecole Polytechnique Fédérale de Lausanne**, Lausanne, Switzerland  
Laboratory of Electromagnetics and Acoustics (LEMA)  
*Ph.D. Degree* in Electrical Engineering **Jan. 2009–Jan. 2013**

- Research in numerical methods for electromagnetics.
- Development and implementation of accelerated formulations of the Method of Moments.
- Design of a multi-functional antenna systems for micro-satellites.
- Participation in the ESA project MAST.
- Contribution to project proposals for the European Space Agency (ESA) (MASSA, MILAS, MAST-X)
- Teaching assistance and students supervision.

**TNO Defence Security & Safety**, The Hague, Netherlands  
Department of Antennas and Propagation  
*Research internship* **Oct. 2002–Apr. 2003**

- Electromagnetic Band-Gap technology.
- Substrate Integrated Waveguides.

EDUCATION **Ecole Polytechnique Fédérale de Lausanne**, Lausanne, Switzerland  
Laboratory of Electromagnetics and Acoustics (LEMA)  
*Ph.D. Degree* in Electrical Engineering, **Jan. 2013.**

- Thesis Title: *Numerical Analysis and Design of a Antenna Systems for Micro/Nano Satellites.*
- Advisor: Prof. Juan R. Mosig.
- Areas of study: numerical methods for electromagnetic problems, Integral Equations, Method of Moments; implementation and development of simulation software. Multi-functional, 3D antenna arrays, omni-directional radiation in circular polarization. Space applications.

**Università degli Studi di Firenze**, Florence, Italy  
*Master Degree* in Electronic Engineering, **Dec. 2007.**  
*Score:* Summa cum laude  
*Specialization:* Electromagnetism, integrated high-frequency circuit design, signal processing.

- Thesis Title: *Design of an EBG-based feed for a cylindrical reflector antenna using PCB technology.*
- Advisor: Prof. Angelo Freni.
- Area of study: planar stratified media, Electronic Band Gap technology, Substrate Integrated Waveguides, measurements and calibration techniques.

ADVANCED  
TRAINING &  
GRADUATE  
COURSES

**From the European School of Antennas (ESoA)**

- *Advanced Computational EM for Antenna Analysis.* EPFL, Lausanne, Switzerland. **Oct. 2010**
- *Advanced Mathematics for Antenna Analysis.* Dubrovnik, Croatia. **May. 2010**

**From the Antenna Center of Excellence (ACE)**

- *Phased Arrays and Reflectarrays.* TNO, The Hague, Netherlands. **May. 2007**

**From the EPFL PhD program (EDOC)**

- *Integral Equations in Electromagnetics*, Prof. Juan R. Mosig. **2011**
- *Optimization and Simulation*, Prof. Michel Bierlaire. **2009**
- *Advanced topics in Electromagnetic Compatibility*, Prof. Farhad Rachidi-Haeri. **2008**
- *Advanced microwaves for wireless communications*, Prof. Anja K. Skrivervik. **2007**

TEACHING  
EXPERIENCE

**Ecole Polytechnique Fédérale de Lausanne**, Lausanne, Switzerland

Teaching assistant for the courses of *Radiation and Antennas* and *Electromagnetics* (Exercise Sessions, Bachelor Level).

In charge of the LEMA introductory seminars for the students of first year of Bachelor (*Laboratoires Répartis*).

Technical advisor for student projects:

- Thesis Title: *Radiation patterns for 3D distribution of antennas*
  - Author: A. Banda
  - Supervisors: Prof. J.R. Mosig and G. Rosati (LEMA)
  - Area of study: 3D array theory, elementary sources propagation, *MATLAB* programming language.
- Thesis Title: *Problèmes électrostatiques résolus avec la matrice de Green* (in French).
- Semester Project
  - Author: N. Perraudin
  - Supervisors: Prof. J.R. Mosig and G. Rosati (LEMA)
  - Area of study: Static Green's functions, *MATLAB* programming language and User Interface design, computing and plotting capabilities for educational and scientific applications.

RESEARCH  
PROJECTS

“MAST: *Miniaturized Multi-functional Antenna Systems for Micro-/Nano Satellites*”, European Space Agency (ESA), ESA-ESTEC/Contract No. AO/1-5822/08/NL/ST. Prime: EPFL-LEMA, PI. Prof. J.R. Mosig. Subc: JAST Antenna Systems, Lausanne (Switzerland), 2009-2010.

SOFTWARE SKILLS	<ul style="list-style-type: none"> <li>• Electromagnetic (CAD) Tools: <i>Ansoft HFSS &amp; Designer</i> (advanced user); <i>FEKO</i>, <i>CST Microwave Studio</i> (intermediate user).</li> <li>• Computing Environments: <i>Matlab</i> (advanced) and <i>Maple</i> (advanced).</li> <li>• Programming Languages: <i>C</i>, <i>C++</i>, <i>Visual Basic</i> (basics).</li> <li>• Operating Systems: <i>Windows</i> (advanced).</li> <li>• Text editors for scientific documents: <i>LaTeX</i>, <i>MS Office</i>, <i>MathType</i>, <i>OpenOffice</i>.</li> <li>• Graphic Editors: <i>Adobe Illustrator</i> (frequent user) and <i>Corel Draw</i> (basics).</li> <li>• Recent Programming Experiences: <ul style="list-style-type: none"> <li>- Development of the electromagnetic simulation software SatAF (Satellite Array Factor), including User Interface</li> </ul> </li> </ul>
HARDWARE SKILLS	<ul style="list-style-type: none"> <li>• <b>Scattering parameters:</b> Basic experience in the use of the Vector Network Analyzers (<i>HP8510XF</i> and <i>HP8720D</i>).</li> <li>• <b>Radiation parameters:</b> Basic experience in the use of LEMA Anechoic Chamber (from 0.5 to 20 GHz, azimuth/elevation positioner with 0.05° resolution).</li> </ul>
SCIENTIFIC PRODUCTION	<ul style="list-style-type: none"> <li>• 1 journal paper.</li> <li>• 3 conference papers.</li> <li>• 4 technical reports.</li> </ul>
LANGUAGE SKILLS	<ul style="list-style-type: none"> <li>• Italian: native.</li> <li>• English: fluent (reading, writing, verbal skills).</li> <li>• French: fluent (reading, writing, verbal skills).</li> <li>• German: intermediate (reading, writing, verbal skills).</li> </ul>
PERSONAL HIGHLIGHTS	<p>Great passion for learning, marked sense of responsibilities, cooperative attitude, good ability to adapt to multi-cultural environments, organized, attention to detail.</p> <p>Sport activities: swimming, biking, running. Interested in classic and modern literature, music and cinema. Playing chess.</p>
REFERENCES	<p><b>Prof. Juan R. Mosig</b>  Director of Laboratory of Electromagnetics and Acoustics (LEMA)  Ecole Polytechnique Fédérale de Lausanne (EPFL), Switzerland  email: <a href="mailto:juan.mosig@epfl.ch">juan.mosig@epfl.ch</a> <span style="float: right;">Tel: +41 216 934 628</span></p> <p><b>Prof. Angelo Freni</b>  Università degli Studi di Firenze  email: <a href="mailto:angelo.freni@unifi.it">angelo.freni@unifi.it</a> <span style="float: right;">Tel: +39 055 4796522</span></p>



# List of Publications

## Journal Publications

- G. Rosati**, J.R. Mosig, “An alternate point-wise Scheme for the Electric Field Integral Equation”, Accepted for publication in *International Journal of RF and Microwave Computer Aided Engineering*.

## Conference Publications

- J. Padilla, **G. Rosati**, A. Ivanov, F. Bongard, S. Vaccaro, J.R. Mosig , “Multi-functional miniaturized slot antenna system for small satellites” , *Proceedings of the 5th European Conference on Antennas and Propagation (EuCAP)*, pp.2170-2174, 11-15 April 2011.
- G. Rosati**, J.R. Mosig , “An efficient analysis & design methodology for slot antennas on micro-satellites” , *2012 15th International Symposium on Antenna Technology and Applied Electromagnetics (ANTEM)*, pp.1-7, 25-28 June 2012.
- G. Rosati**, J.R. Mosig , “Simplified point-wise schemes for Integral Equations in Electromagnetics” , *12th Mediterranean Microwave Symposium*, Istanbul, Turkey, September 1–5, 2012.

## Technical Reports

- G. Rosati**, “Miniaturised multi-functional antenna systems for micro/nano satellites - Baseline Design Review” , LEMA (EPFL), Lausanne, Switzerland, Jun. 2009.
- G. Rosati**, “Miniaturised multi-functional antenna systems for micro/nano satellites - Preliminary Design Review” , LEMA (EPFL), Lausanne, Switzerland, Nov. 2009.
- G. Rosati**, “Miniaturised multi-functional antenna systems for micro/nano satellites - Critical Design Review” , LEMA (EPFL), Lausanne, Switzerland, Jun. 2010.
- G. Rosati**, “Miniaturised multi-functional antenna systems for micro/nano satellites - Final Review” , LEMA (EPFL), Lausanne, Switzerland, Dec. 2010.

